



ScuDo
Scuola di Dottorato ~ Doctoral School
WHAT YOU ARE, TAKES YOU FAR

Doctoral Dissertation
Doctoral Program in Electronic Engineering (29th Cycle)

Development of new nanostructured electrodes in Microbial Fuel Cells (MFCs)

By

Giulia Massaglia

Supervisor(s):

Prof. C.F Pirri
Prof. M.G Ajmone
Dr. M. Quaglio

Doctoral Examination Committee:

Prof. S. Licoccia Referee, University of Rome Dipartimento di Chimica
Prof. S. Bordiga, Referee, University of Turin, Dipartimento di Chimica
Prof. E. Tresso, Referee, Politecnico of Turin, Dipartimento di scienza applicata e tecnologia
Prof. C. Barolo, Referee, University of Turin, Dipartimento di Chimica
Prof. C. Francia, Referee, Politecnico of Turin, Dipartimento di scienza applicata e tecnologia

Politecnico di Torino
2016

Declaration

I hereby declare that, the contents and organization of this dissertation constitute my own original work and does not compromise in any way the rights of third parties, including those relating to the security of personal data.

Giulia Massaglia

2016

* This dissertation is presented in partial fulfillment of the requirements for **Ph.D. degree** in the Graduate School of Politecnico di Torino (ScuDo).

Acknowledgments

I wish to thank all the persons who have supported me during these three years of PhD.

First of all, I would like to express my gratitude to Prof. Fabrizio Pirri for having given the opportunity to work on this interesting subject and to Dr. Marzia Quaglio and Dr. Valentina Margaria for the constant help and their scientific support that they gave me in every moment.

I wish acknowledged the scientific contribution of all people of the Italian Institute of Technology (IIT- Center for sustainable Future Technologies CSFT@Polito) with who I had the honor of working: Matteo Gerosa, Valeria Agostino, Valentina Margaria, Adriano Sacco, Nadia Garino, Angelica Chiodoni, Micaela Castellino, Stefano Bianco and Marzia Quaglio. Among them, I special thank goes to my important friend Matteo Gerosa who has shared with me all the work during these three years.

I would like all the persons who supported my scientific work with our measurements and characterizations: Adriano Sacco, Nadia Garino, Stefano Bianco, Micaela Castellino, Angelica Chiodoni and Valentina Margaria.

Moreover, I would like to thank all the people working at the Center of Sustainable Future of IIT; in particular, I wish to thank all my colleagues and friends Matteo Gerosa, Valeria Agostino and Michela Di Girolamo for the funny lunchtimes and coffee breaks.

Last but not least, a special thank goes to Alain and my parents who supported me lovely all through the different stages of my life.

Abstract

The aim of my thesis work is to investigate new nanostructured materials, obtained by the electrospinning technique, in order to design 3D arrangement of the electrodes, leading thus to improve the energy efficiency of energy production devices, such as microbial fuel cells (MFCs). The carbon nanofibers reveal to be the most promising material in the field of bio electrochemistry; in fact, up to now the best performing microbial fuel cells are fabricated using carbon and carbon based material electrodes. To further enhance the performances of bio anodes and bio cathodes, a set of properties are then required to be overcome, such as a proper surface morphology and chemistry, good biofilm adhesion and electron transfer, and a good electrical conductivity.

This work aims to demonstrate that the electrospun nanofibers own all the necessary properties, revealing themselves as the most innovative and promising structures for anodes and cathodes for microbial fuel cells. The nanofibers ensure all the properties listed above; in particular, during my Ph.D. I have investigated and studied the carbon based nanofibers to be applied as cathode and as anode in these kind of the devices. In this thesis, it will be demonstrated that the nanostructured electrodes improve the efficiency devices thanks both to the low impedance and to the interaction with the microorganisms.

The high micrometric porosity characteristics of the realized anodic material create the ideal habitat for the microorganism's proliferation.

Moreover, different solution for the cathode material have been developed using ceramic nanofibers, such as Mn_xO_y nanofibers and carbon nanofibers, in order to improve the performance of the devices. The layer made of these nanofibers, in fact, catalyzes the oxygen reduction reaction if the oxygen is used as terminal electron acceptor in the devices; thus these catalysts can substitute the platinum layer, which is the most used today, granting a cheaper and eco friendlier material.

Contents

Aims of the work.....	17
1 Chapter 1 Microbial Fuel Cells (MFCs)	22
1.1 Introduction.....	23
1.2 Bioelectricity generation using MFC	25
1.3 Voltage generation.....	36
1.3.1 Anode Voltages	37
1.3.2 Cathode Voltages	39
1.3.3 Factors affecting the MFC voltage	41
1.4 Power Generation and Columbic Efficiency.....	44
1.4.1 Polarization curves, power density curves and internal resistance definition.....	47
1.5 Materials.....	51
1.5.1 Anode Materials.....	52
1.5.2 Cathode Materials.....	55
1.5.3 Membrane materials and its uses.....	59
1.6 MFCs Applications	60
1.6.1 Waste water treatments.....	60
1.6.2 Electricity generations	61
1.6.3 Biosensors	62
1.6.4 Bio Hydrogen.....	63
2 Chapter 2 State of art on Electrospinning.....	65
2.1 Nanofibers definition and introduction of different technique to obtain fibers.....	65
2.2 History of the electrospinning.....	69
2.3 Electrospinning process.....	73
2.4 Physical phenomena that control the deposition of nanofibers	76

2.4.1	Droplet formation at the tip of needle	77
2.4.2	Development of rectilinear jet and onset of bending instabilities	83
2.4.3	Deposition on counter electrode	90
2.5	Electrospinning process parameters and their influence of the nanofibers properties	96
2.5.1	Viscosity, concentration and polymeric weight.....	97
2.5.2	Voltage, Flow rate, and Gap distance between the tip of the needle and the counter electrode	103
2.6	Applications	106
2.6.1	Biomedical applications of nanofibers.....	107
2.6.2	Nanofibers sensors and filter	111
2.6.3	The applications of carbon and catalytic nanofibers	112
3	Chapter 3 The new 3D electrodes based on carbon nanofibers for Single Chamber Microbial Fuel Cells (SCMFCs)	121
3.1	Introduction.....	122
3.2	Experimental section: materials and nanofibers synthesis	125
3.3	Characterization on the carbon nanofibers	128
3.3.1	Morphological, Optical and Electrical characterization.....	128
3.3.2	Electrochemical characterizations	129
3.3.3	Biological characterizations on the nanofibers studied as anode	130
3.4	Single chamber MFC architecture and operation mode.....	132
3.5	Results and Discussion	135
3.5.1	Optical, physical and electrical characterizations results	135
3.5.2	Electrochemical characterizations results	146
3.5.3	Morphological properties of carbon nanofibers	150
3.6	MFC performances evaluated with nanofibers as anode	153

3.7	MFC performances obtained with PAN_900 nanofibers as cathode.....	157
3.8	Conclusion	159
4	Chapter 4 Mn _x O _y catalysts nanofibers for Oxygen Reduction Reaction using Multi Wall Carbon Nanotubes as conductive filler.....	161
4.1	Introduction.....	161
4.2	Experimental section: materials and methods	165
4.2.1	Manganese oxide nanofibers synthesis.....	165
4.2.2	Composite nanofibers based on PEO and Multiwall carbon nanotubes synthesis ...	165
4.3	Characterizations on the nanofibers.....	166
4.3.1	Morphological, optical and electrochemical characterizations performed on the Manganese oxide nanofibers.....	166
4.3.2	Characterizations performed on composite nanofibers PEO/MWCNTs	168
4.4	Results and Discussion	169
4.4.1	Manganese oxide nanofibers Results	169
4.4.2	Composite nanofibers based on PEO/MWCNTs.....	176
4.5	Conclusions.....	189
5	Thesis Conclusion.....	191
6	References	196

LIST OF FIGURES

Figure 1 US energy consumption by energy sources in 2015 [2]	18
Figure 2 The world increased demand of energy [Wikipedia].....	24
Figure 3 Total energy consumption by source (2013) [Wikipedia].....	25
Figure 4 scheme of working principle of a MFC.....	26
Figure 5 Representation of an example of biofilm formation.	28
Figure 6 principal representation of the energy flux and production in Microbial Fuel Cells [22] ...	29
Figure 7 scheme of the direct electron transfer pathway through A) the membrane bound cytochromes and B) nanowires self- produced by bacteria	30
Figure 8 The representation of one of the main electron transfer processes: this mechanism is based on the direct electron transfer to the electrode through the self -produced redox mediators	32
Figure 9 represents two different electrochemical schemes describing two different architectures of MFCs; a) shows the dual chamber MFCs where the reduced species in the cathode is hexacyanoferrate of potassium; b) represents the single chamber MFCs where, on the contrary, the oxygen in the cathode is reduced into the water.	34
Figure 10 proposes the theoretical power losses due to the overpotentials related to the cathode and anode	47
Figure 11 represents an example of polarization and power density curves. The curve a) represents the variation of voltage related with the measured current; while the curve b) represents the power density versus the measured current	48
Figure 12a) the trend line to define the dimension of the nanofibers related to the some other elements, such as red blood cell or DNA filament; b) shows the correlation between the surface area of mat of nanofibers related to the diameter of the fibers.....	65
Figure 13 Model of wet spinning technique [92].....	67
Figure 14 the setup of dry spinning [93]	68
Figure 15 represents a scheme of melt spinning technique [94]	68
Figure 16 shows the definition of the angle of the Taylor's cone	71
Figure 17 number of publications on electrospinning (1995-2010) source Research Gate.....	73

Figure 18 represents the electrospinning setup (sources www.intechopen.com) and an example of Field Electronic Scanning Microscopy (FESEM) of no woven mat of nanofibers, obtained in our laboratory. In particular, the nanofibers are obtained starting from an electrospun solution of Polyethylene oxide (PEO) and Deionized water.75

Figure 19 deformation of the droplet according to the variation of electric field, until the formation of the Taylor' cone and then the formation of polymeric jet [126] 79

Figure 20 Hyperbolic coordinates used to describe the electric field and the equipotential lines near the tip of a fluid cone an instant before its instability and a jet issued from the tip [127, 128]..... 80

Figure 21 The looping part of the jet. This figure represents the bending instabilities of the jet [128]85

Figure 22 viscoelastic dumbbell representation used to explain from a theoretic point of view the viscous and elastic contributions on the electrified jet86

Figure 23 electrostatic forces applied by two charges elements to a neighboring third charge element [131, 132]..... 88

Figure 24 a schematic representation of electrospinning setup with a rotating drum collector92

Figure 25 represents an example of aligned collagen and PGA electrospun nanofibers92

Figure 26 Schematic of the disk collector used for fiber collection. The SEM micrograph shows the alignment of the fibers obtained using the disk collector. Better alignment of the fibers is observed compared to the rotating drum. [142] 93

Figure 27 alignment distribution of nanofibers, starting from an electrospun Polyvinilpirrolydone PVP. A) a schematic representation of the modified counter electrode. Two strips of gold are deposited on an insulated substrate. B) the FESEM analysis to confirm the alignment distribution of nanofibers across the gap between the gold strips [143]95

Figure 28 A) schematic illustration of the patterns obtained through the deposition of 4 gold electrodes on quartz wafers B, C, D) FESEM characterizations of PVP nanofibers which are aligned in a different way, according to the patter [143].96

Figure 29 definition and representation from theoretical point of view the Laplace's Law. T is the named Wall Tension; P is the pressure difference and R is the radius of the circular section of the tube 98

Figure 30 Morphological differences induced by the presence or not of salts in the polymeric solutions [109].	100
Figure 31 Morphological differences induced by the increasing of viscosity of the polymeric solutions [109].	100
Figure 32 represents how the distribution of the beads into the mat of nanofibers decreases as the charge density in the jet increases [109].	101
Figure 33 demonstrates the power law relationship between the fiber diameter distributions and the polymeric concentration (wt%) [95].	103
Figure 34 The different values of applied voltage on the 7 wt% PEO in distilled water. The volume of droplet decreases as the applied voltage increases and the distribution of the beads in the mat of nanofibers increases with the increasing of the voltage intensities [132].	104
Figure 35 Many potential applications of the nanofibers [112].	107
Figure 36 Experimental setup for the electrodeposition/photo-polymerization process [186].	119
Figure 37 Field Electron Scanning Microscopy (FESEM) characterization to demonstrate the coating of the TiO ₂ with the photopolimerized layers, electrodeposited on it with a time process of $t_e=45s$ [186].	120
Figure 38 3D polymeric single chamber microbial fuel cell (SMFC). a) anodic chamber; b) intermediate space and c) cathode chamber and d) represents an example of cathode electrode obtained cutting a piece 3x3 cm ² of CF.	132
Figure 39 represents the formation of a cyclic structure occurring during the oxidative stabilization in air atmosphere at 280°C [206].	135
Figure 40 is a schematic representation of dehydrogenation occurring when the heating treatment is defined up to 600°C under inert atmosphere [191].	136
Figure 41 [215] shows how the different types of nitrogen were distributed in the graphitic sheets. The red dots represent the graphitic nitrogen, which is trapped in the sheet; the pyridinic N, represented by the green dot, is at the edge of the plain and it was a free bond, incrementing the reactivity of the samples; the pyrrolic N, (yellow dot), has all bond saturated; finally, the dark yellow dot represents the graphitic nitrogen.	137
Figure 42 The survey spectra of carbon nanofibers at different temperature a) 280°C, b)600°C, c) 900°C.	138

Figure 43 represents the high resolution spectra respectively a) C1s and b) N1s for the nanofibers treated at different temperature (@280°C, @600°C and @900°C) 140

Figure 44 shows the comparison between the FTIR spectra for PAN_900 (light blue line), and the ATR spectra for PAN_600 (dark blue line). FTIR spectra demonstrates that the intensities of peaks related to the nitrogen bonds on the surface of PAN_900 are smaller than the PAN_600 ones, which have the same weight of 4mg..... 143

Figure 45 Raman Spectroscopy performed on the nanofibers pyrolyzed at 600°C and on PAN_900 samples. The definition of D-band and G-band confirm the presence of graphitic features in the mat of nanofibers; in particular, the degree of graphitization is higher in the PAN_900 than one obtained in the PAN_600 sample..... 145

Figure 46 represent the Cyclic voltammetry conducted on the different samples. a) represents the comparison between the PAN_600 nanofibers (light blue curve) and the PAN_600 with the adhesion of microorganisms (pink curve); b) show the cyclic voltammetry conducted on the PAN_900 carbon nanofibers, with (green curve) and without (red curve) the biofilm formed on the carbon nanofibers. Finally, it is possible to confirm how the trends of CV's curves are similar to the curve characterizing the CF materials (Grey curve) 148

Figure 47 Comparison of electron transfer number (left axis) and peroxide percentage (right axis) evaluated from RRDE measurements of the different samples at 2500 rpm rotation speed and different potentials. The samples are respectively PAN_600 and PAN_900 nanofibers 150

Figure 48 Morphological characterization of PAN_600 at different magnification. a) the mat of no woven nanofibers of PAN precursor before the heated treatment; b) a mat of nanofibers of PAN precursor with a higher magnification; c) mat of no woven pyrolyzed nanofibers; d) the mat of nanofibers of PAN_600 pyrolyzed with a higher magnification to evaluate the formation of bundled carbon nanofibers and e) the fibers of carbon felt..... 151

Figure 49 Field Scanning Electron Microscopy (FESEM) images related to the interconnected biofilm on respectively: a) shows the interaction between the bacteria , obtained from the fresh water sediment and CF b) shows the biofilm growth on PAN_600 using an inoculum obtained from freshwater sediment. The development of a densely connected biofilm results better in the mat of PAN_600 than in CF. 152

Figure 50 Power Density trends represented as function of time and normalized respect the projected area. a) represents the power density values obtained from PAN_600: dark grey line represents the power density reached with an external load of 47Ω , while dark cyan one represents that reach under $1k\Omega$; b) reports the power density curve obtained from CF material. The light grey line report the values of power density obtained with 47Ω of external resistance and the blue one that reached under $1k\Omega$ 154

Figure 51 represents two different EIS related with two different SCMFCs with different anodes. The pink curve represented the EIS curve obtained with carbon nanofibers (PAN_600) used as anode, while the black one represents the EIS obtained with a CF anode electrode. 156

Figure 52 the LSV characterizations performed on PAN_600 and on CF materials, used as anode in SCMFCs..... 157

Figure 53 Power Density trends represented as function of time and normalized respect the projected area. a) represents the power density values obtained from PAN_900 catalyst cathode. The dark blue line represents the power density from the PAN_900, higher than one obtained with the CP modified with Pt as catalyst, represented by the pink curve..... 158

Figure 54 reports the TGA plot of a polymeric solution based on 5wt% PEO ($M_w=600$ kDa) dissolved into the deionized water..... 170

Figure 55 Morphological properties before and after the calcination treatment. In particular, a) shows the morphological properties of the PEO/manganese acetate nanofibers mat; b) show the morphological characteristics of Mn_xO_y nanofibers, when the PEO is completely removed. 171

Figure 56 TEM images of the calcinated nanofibers in (A) bright field, (B) dark field, SAED pattern in the inset (C) (HR)TEM micrograph and its corresponding (D) FFT..... 172

Figure 57 XRD pattern of the manganese oxide nanofibers supported on Si after calcination. In the graph are reported the experimental measure (black curve), the fitting results (red curve) and their difference (grey curve)..... 173

Figure 58 Ring current (a) and Disk current (b) obtained from the RRDE measurements of Mn_3O_4 -based and reference Pt/C samples at a rotating speed of 2500 rpm and a potential of the ring electrode of 0.2 V. (c) Comparison of electron transfer number (left axis) and peroxide percentage (right axis) evaluated from RRDE measurements of manganese oxide-based samples and of the reference Pt/C catalyst at 2500 rpm rotating speed and different potentials. 175

Figure 59 The shear viscosity is reported as a function of the shear rate. All the polymeric solutions have been analyzed, both with and without MWCNTs.178

Figure 60 In a) FESEM images of nanofiber mats obtained from 600 kDa PEO in i) and ii), and from 1000 kDa PEO in iii) and iv). The mats have been processed at two different voltages: i) and iii) refer to 18 kV, while ii) and iv) to 23 kV. In b) the distribution of the diameters is analysed as a function of the Mw, the voltage and the flow rate (for 600 kDa PEO only).179

Figure 61 In a) and b) FESEM images of samples 5PEO_600 and 5PEO_1000 respectively, with different concentrations of MWCNTs. Two values are reported for each PEO Mw, i.e. 1.5 and 3.5 wt%, in the upper and lower line respectively of each picture. Morphology is investigated as function of voltage: pictures refers to 18 kV in the left column and 23 kV in the right column. Processing the 5PEO_1000 with MWCNTs nanonetting appears, as highlighted in b).181

Figure 62 In a) the electrospinning/netting process due to MWCNTs is sketched, with both the NFN and the nanobeaded-NFN represented. In b) TEM analysis of nanocomposite nanofibers with 1.5 wt% MWCNTs is proposed, showing MWCNTs well aligned with the main axis of the nanofibers. In c) a TEM picture of NF and NFN is reported, showing MWCNTs present also in the very small size secondary nanofibers. In d) a TEM picture of a NFN a nanobeaded-NFN is shown.183

Figure 63 a) Raman spectra of nanofiber mats containing 1.5wt% and 3.5 wt% of MWCNTs. b) Thermogravimetric analysis (TGA) of samples with different MWCNTs loading. In the inserted graph the decomposition temperature (Td) is represented as a function of the concentration of MWCNTs: the higher the concentration, the higher the resulting Td.185

Figure 64 Experimental values of the electrical conductivity of composite nanofibers and nanofiber/nets for different concentration of MWCNTs. Three sets of samples are represented: red = 5PEO_600 with MWCNTs; blue = 5PEO_1000 with MWCNTs processed at 18 kV; red =5PEO_1000 with MWCNTs processed at 23 kV.187

Figure 65 the relative differential resistance for the NF, NFN and dense NFN.189

LIST OF TABLES

Table 1 summarizes the main examples of redox mediators self-produced by bacteria, guaranteeing the electron transfer between them and the anode electrode	31
Table 2 reports some standard anode potential defined versus SHE. Most common organic matters are considered, such as methane, acetate, hydrogen and glucose, which are oxidized into the anode compartment guaranteeing thus a certain value of anode voltages. In the table, moreover, the number of electrons, produced during the oxidation of each substrate, is defined.	38
Table 3 some cathode potentials for different reduction reaction occurred. E_{cat0} values are defined for value of pH=7 at T=298K	39
Table 4 report some examples of different polymeric nanofibers used as sensor [166].....	112
Table 5 summarize of the electrospinning parameters defined in order to obtain a mat of nanofibers of PAN, used a precursor for carbon nanofibers and of the heated treatment parameters to have a final mat of carbon nanofibers.	127
Table 6 Atomic percentage of carbon, oxygen and nitrogen obtained from the XPS characterization and related to the carbon nanofibers obtained from the same precursor PAN but heated ad different pyrolysis temperature [213].	141
Table 7 summarizes maximum values of current density and power density reached with PAN_600 and CF used as anodic electrode	154
Table 8 The names and the main properties of the examined PEO based solutions are listed.....	177

This page is intentionally left blank

Aims of the work

Nevertheless, the nanotechnologies were discovered many years ago, until now there is not a unique accepted international definition of this science.

Nanotechnologies define the design, the analysis and the application of structures, molecular materials, inner interfaces and surfaces with dimensions in the range from 100 nm to 1 μm .

The nanostructures can enhance the properties of the materials in a complete different way, which is not even thinkable considering only their macroscopic structure.

In the last years, the fields of engineering and science increase their interest in the development and investigation of new forms of energy technologies, in order to improve the life quality all over the world [1]. In particular, the discovery and the improvement of nanotechnologies allowed to enhance the energy efficiency of the existing devices, and to obtain the new renewable energy technologies, optimizing the energy production.

The nanotechnologies play a decisive role nowadays regarding the conventional energy sources and the renewable energy devices, such as fuel cells in general and photovoltaic systems (for example dye sensitize solar cells) [1]. The conventional energy sources based on oil, coal, and natural gas are damaging economic progress, environment and human life; as represented in Figure 1, the conventional energy sources are widely used respect to the renewable energy that is only 10% of U.S energy consumption in 2015 [2].

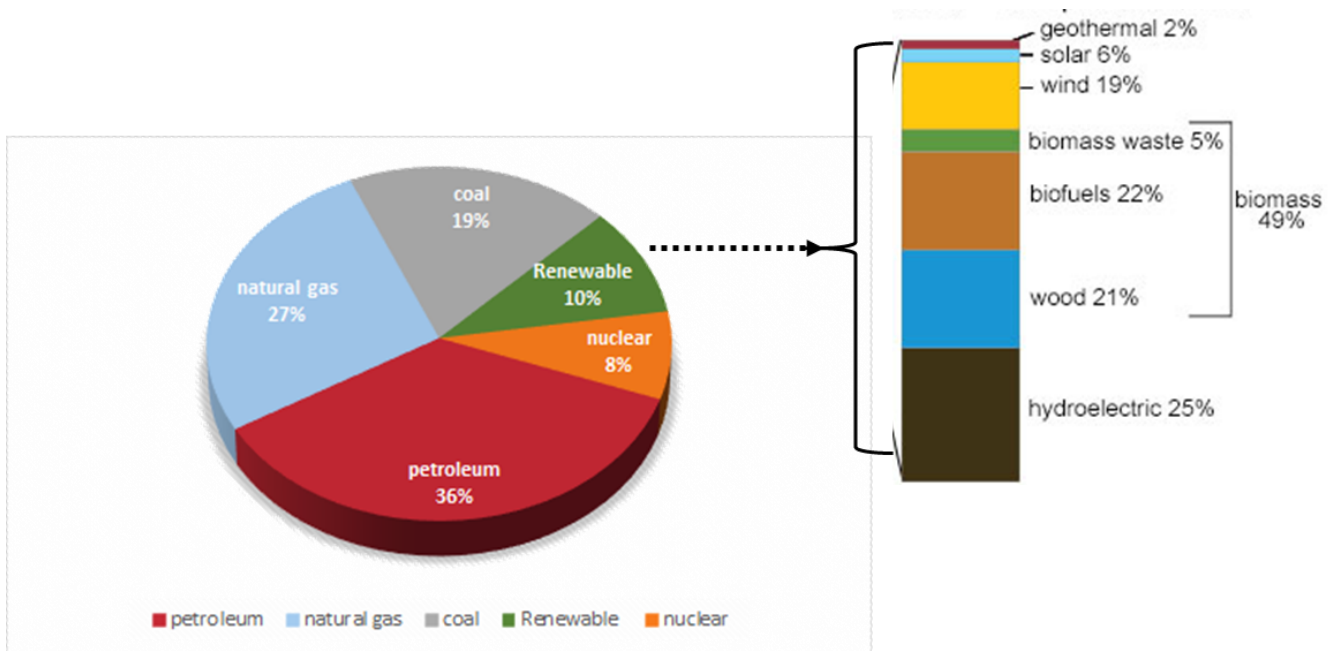


Figure 1 US energy consumption by energy sources in 2015 [2]

These traditional fossil fuel based energy sources increase the current high level of greenhouse gas emissions (GHG), which must be reduced as confirmed by the Kyoto Protocol [3, 4]. Renewably energy sources can give between 15% and 20% of the total amount of energy demand. According to the European Commission “Renewable energy can be produced from a wide variety of sources including wind, solar, hydro, tidal, geothermal, and biomass. By using more renewables to meet its energy needs, the EU lowers its dependence on imported fossil fuels and makes its energy production more sustainable. The renewable energy industry also drives technological innovation and employment across Europe”.

The targets of EU’s Renewable Energy Directive are to obtain 20% final energy consumption from renewable energy sources by 2020 [5] and, moreover, all EU countries must adopt national energy action plans demonstrating what things they are going to take in order to achieve their renewables targets. Renewable energy plays an important role in reducing greenhouse gas emissions. When renewable energy sources are used, the demand for fossil fuels is reduced. Unlike fossil fuels, non-biomass renewable sources of energy (hydropower, geothermal, wind, and solar) do not directly emit greenhouse gases. In the last years the renewable sources are developed leading to the studies of solar energy, wind energy, geothermal energy and bio-energy, which can supply in the second

half of the 21st century the 50% of energy demand [6]. New materials, developed with nanotechnologies, are investigated in order to design innovative anode and or cathode able to improve the overall energy efficiency of the devices, which use these renewable energy sources.

One of the possible example of nanotechnology is represented by the electrospinning process.

The electrospinning is a unique technique that produces continuous polymer fibers with diameters in the range between few micrometers and some nanometers, through an applied voltage on a polymeric jet. This process uses high voltage electric field to obtain solid nanofibers starting from the polymeric solutions. In particular, through the electrospinning technique, it is possible to obtain a mat of nanofibers, whose thickness is related to the time of the process [7].

In contrast with the fibers obtained with the conventional spinning methods, such as wet, dry, melt and gel spinning, the nanofibers show very interesting morphological characteristics like high surface area to volume ratio, small size pores guaranteeing high value of porosity; all these characteristics are fundamental and mandatory in a wide interesting variety of applications, making the electrospun materials the ideal choice.

It is possible to consider the nanofibers as the conjunction point between the nanometric world and macroscopic one, thanks to the diameters of fibers, which is in the nanometric range, and their length that is of some kilometers.

Furthermore, this technique guarantees the formation of different kind of nanofiber materials, such as ceramic mat, carbon based materials or graphitic ones, depending on the initial polymeric precursor selected and on the proper definition of the heated treatment [8].

In the field of energy conversion, the nanotechnology is used to optimize the efficiency of the devices. Taking into account the fuel cells, starting from a chemical source, the energy is transduced into electrical output, which can be increased by nanostructured electrodes; these new nanomaterials, indeed, help the design of portable devices, able to produce, to convert and to store the energy, with higher efficiencies than ones reached with commercial bulk materials.

Carbon based nanomaterials have been applied in the energy production devices, such as fuel cells and Microbial fuel cells, in order to optimize the power supply providing a higher power production.

The fibers represent a preferential path for the electrons movements, minimizing the impedance of the materials; moreover, their high surface area to volume ratio grant an extremely good electrons exchange with adjacent environment.

Considering the microbial fuel cells, which are bio-electrochemical devices, where the conversion of the chemical energy into the electrical energy is driven by the bacteria that are able to oxidize the organic matter, the nanofibers could improve some of the key component of the device: the anode and the cathode [9]. Both the anode and cathode material must have the following properties:

- a proper value of electrical conductivity ensuring the electron transfer among the electrodes;
- a high porosity with a micrometric sizes distribution enhancing the diffusion of the chemical species, such as the organic matter in to the anode chamber and the chemical species to be reduced into the cathode one;

In addition, the anode must have a very good biocompatibility in order to guarantee the bacteria growth, while the cathode needs good electro-catalytic properties in order to catalyze the electrolyte reduction reaction. Further developments in the field of bio electrochemistry require innovative approaches to the design and the engineering of materials for highly performing bio-electrodes, applied in the Microbial fuel cells.

The aim of my thesis work is then to investigate new nanostructured materials, obtained by the electrospinning technique, in order to design 3D arrangement of the electrodes and to improve the energy efficiency of microbial fuel cells. The carbon nanofibers reveal to be the most promising material in the field of bio electrochemistry, in fact, up to now the best performing microbial fuel cells are fabricated using carbon and carbon based material electrodes [10].

To further enhance the performances of bio anodes and bio cathodes, a set of properties are then required to be overcome, such as a proper surface morphology and chemistry, good biofilm adhesion and electron transfer, and a good electrical conductivity.

This work aims to demonstrate that the electrospun nanofibers own all the necessary properties, revealing themselves as the most innovative and promising structures for anodes and cathodes for microbial fuel cells.

The nanofibers ensure all the properties listed above; in particular, during my Ph.D. I have investigated and studied the carbon based nanofibers to be applied as cathode and as anode in these kind of the devices. In this thesis it will be demonstrated that the nanostructured electrodes improve the efficiency devices thanks both to the low impedance and to the interaction with the microorganisms.

The high porosity characteristics of the realized anodic material create the ideal habitat for the microorganism's proliferation.

Moreover, different solution for the cathode material have been developed using ceramic nanofibers, such as Mn_xO_y nanofibers and carbon nanofibers, in order to improve the performance of the devices. The layer made of these nanofibers, indeed, catalyzes the oxygen reduction reaction if the oxygen is used as terminal electron acceptor in the devices; thus these catalysts can substitute the platinum layer, which is the most used today, granting a cheaper and eco friendlier material.

1 Chapter 1

Microbial Fuel Cells (MFCs)

A fuel cell is an electrochemical device that produces electricity through a chemical reaction between a source fuel and an oxidant agent. The source fuel is any reagent able to be oxidized, such as hydrogen, methane, propane, methanol, diesel fuel or gasoline, while the oxidant agent is any reagent that causes the oxidation, such as platinum powder and bacteria. If the oxidizer agent used is the oxygen contained in the air, the reaction products are water [11]. Fuel cells can be used to power many different devices, such as cars, mobile phones and even space vehicles [12]. In February 2010 Bloom Energy launched into the market the bloom boxes: modular energy servers consisting of stacks of Bloom's solid oxide fuel cell able to produce the correct amount of energy for a given application [www.bloomenergy.com]. In 2015 Toyota started selling the Toyota Mirai, one of the first commercially produced hydrogen fuel cell automobiles [<https://ssl.toyota.com/mirai/fcv.html>] Fuel cell presents different advantages with respect to the conventional power sources, like fossil fuels, petroleum, natural gas, coal and so on, such as:

- Long useful life;
- High efficiency;
- Relative safety;
- Reduced pollution, in particular carbon emissions;
- Low maintenance costs

How do fuel cells work?

The most common representation of fuel cell is the hydrogen fuel cell, in which the hydrogen is the anodic electrode, (positive electrode). Inside the anodic part, the hydrogen is oxidized and electrons and protons are released. The protons flow through the electrolyte solution and migrate into the cathode chamber thanks to a proton exchange membrane (PEM). Electrons flow through an external load applied from the anode electrode into cathode one, providing current and then power to the connected device. Within the cathode part, the oxygen is reduced by generated electrons together with protons, in order to obtain water as product of oxygen reduction reaction. Single PEM hydrogen

fuel cell generates a voltage up to 0.6V- 0.7V [11, 13]. A fuel cell can be recharged by filling a tank or from a continuously external recipient of source fuel. Different combinations of cells, connected in series or in parallel, can produce higher voltage and higher current than a single cell. Fuel cells can then be used to provide power for the most electrical or electronic devices designed to be powered from batteries or from conventional utility power sources.

A microbial fuel cell (MFC) is a bio-electrochemical device that converts the chemical energy into the electrical energy by the action of microorganisms [14]. These electrochemical cells are based on a bioanode and/or a biocathode. Most MFCs contain a proton exchange membrane to separate the anode chamber, where oxidation takes place, and the cathode one, where the reduction occurs. The electrons, produced during oxidation, are directly transferred to an electrode or to a redox mediator species, which are chemical species able to move the electrons from the bacteria into the anode electrode. The electrons then flow into the cathode, through the external load applied, while the charge balance among all elements is guaranteed by the flux of the protons through the electrolyte (also named substrate), usually across an ionic (cationic/ anionic) membrane. Most MFCs use an organic electron donor (i.e. organic matter as carbon energy source like sodium acetate, glucose, peptone) that, once oxidized, produces CO₂, protons and electrons. Other electron donors have been reported in the literature, such as Sulphur compounds or hydrogen. The cathode reaction uses a variety of electron acceptors and among all, the oxygen reduction is the most studied process. However, other electron acceptors have been studied in past, including metal recovery by reduction, water reduction to hydrogen, nitrate reduction and sulfate reduction [15].

In the following paragraphs, the working principles of Microbial Fuel Cells and their main possible applications will be widely explained and investigated.

1.1 Introduction

There are over six billion people on the planet with 9.4 billion projected for 2050 [16]. Nowadays the human technologies are mainly based on the oil, natural gases and fossil fuel in general, but they are doomed to extinguish. The request of the different types of fuels increases every year, but the Countries are not able to establish a long term plan to sustain their global economy. Usually

plans are time limited from 3 to 5 years. Figure 2 shows the consumption trends of all the power sources in the world during the last 40 years [15].

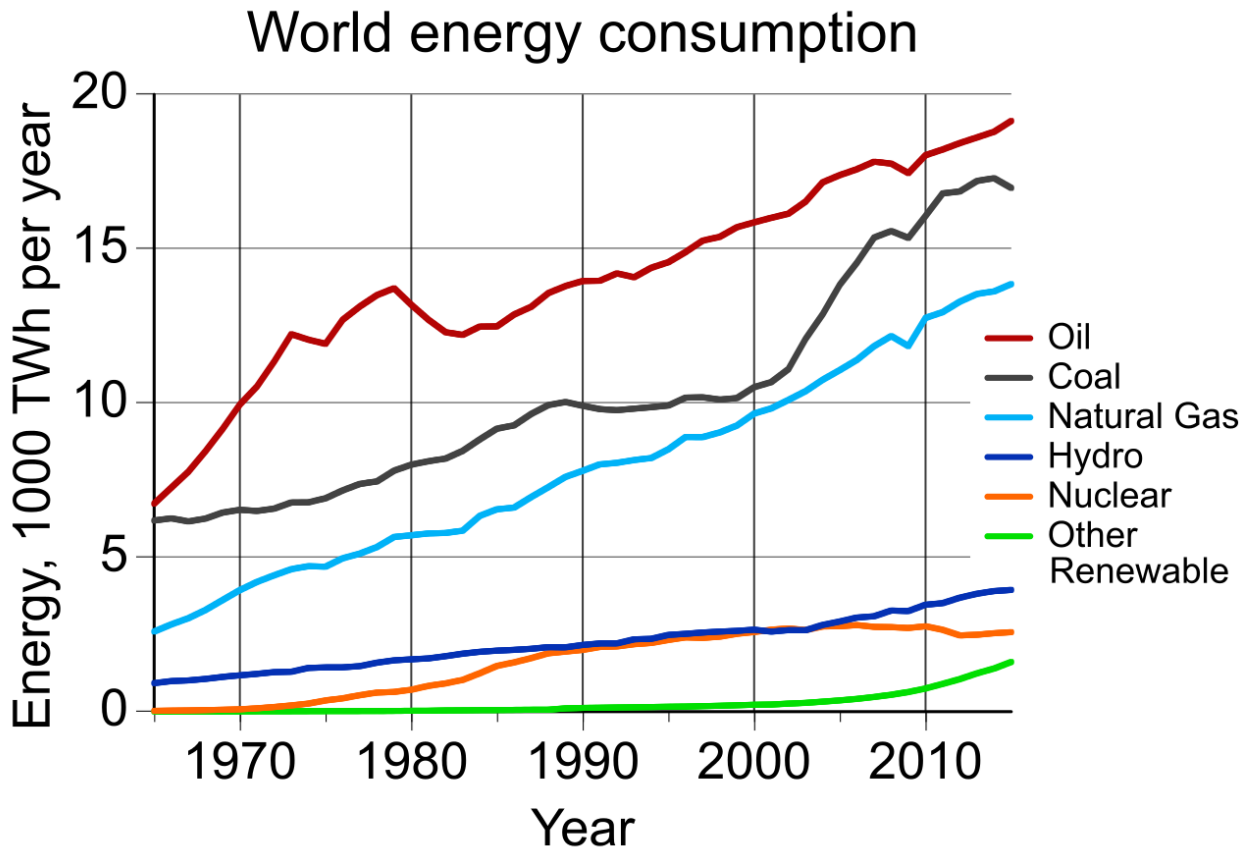


Figure 2 The world increased demand of energy [Wikipedia]

In order to define the total annual energy consumption of the countries, institutions, such as the International Energy Agency (IEA), the U.S. Energy Information Administration (EIA), and the European Environment Agency (EEA), periodically record and publish energy data. All the information may reveal systemic trends and patterns, which could help to frame current energy issues and encourage movement towards collectively useful solutions.

The IEA estimated that, in 2013, total world energy consumption was 390 GJ equal to an average power consumption of 12.3 terawatts, as represented in Figure 3 [17]. From 2000–2012 coal was the source of energy with the largest growth; the use of oil and natural gas also had considerable growth, followed by hydro power and renewable energy. The renewable energy, during this period,

grew faster than any other time in history, which can possibly be explained by an increase in international investment in renewable energy. Moreover, the demand for nuclear energy decreased, possibly due to the accidents at Chernobyl and Three Mile Island.

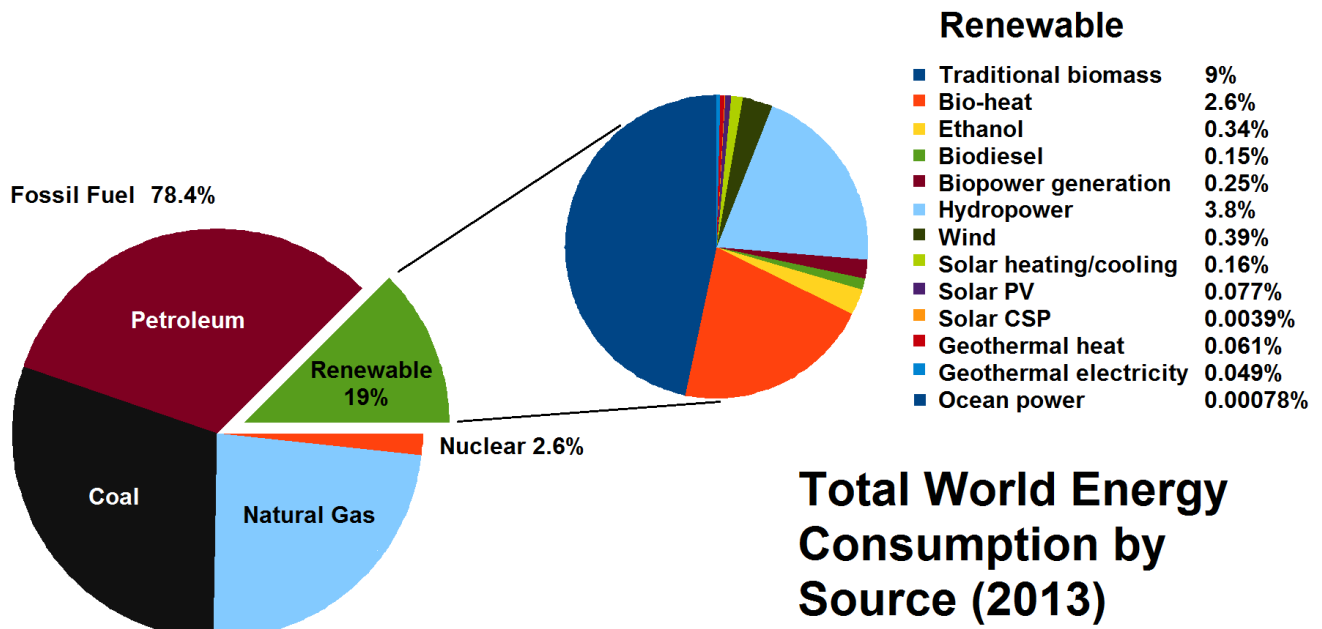


Figure 3 Total energy consumption by source (2013) [Wikipedia]

In the last 2 decades the problem of pollution and the CO₂ emissions became a key factor in the energy plans for developed countries. In addition to the common renewable power sources, many research centers around the world are investigating the development of novel green renewable power sources. Among all those new technology, the MFCs shine as the newest and more environmental friendly devices to obtain energy from microorganism. The MFCs are bio-electrochemical transducers that transform chemical energy into the electrical energy mimicking bacterial interactions found in nature.

1.2 Bioelectricity generation using MFC

The Microbial fuel cell (MFC) permits the generation of bioelectricity starting from a biomass using bacteria [18].

In 1911 Potter observed for the first time the electricity produced by the bacteria, but only in the early 1990s the MFCs became of more interest and research in their field increases [18].

Chapter 1 Microbial Fuel Cells (MFCs)

More generally, the MFCs present three main parts as proposed in Figure 4: the anode chamber, where the bacteria grow and they oxidize the organic matter present in the electrolyte, (such as sodium acetate in laboratory conditions); the cathode chamber into which the released electrons flow and reduce the electron terminal acceptors and the proton exchange membrane (PEM), which separates the anode and cathode, but it is not indispensable.

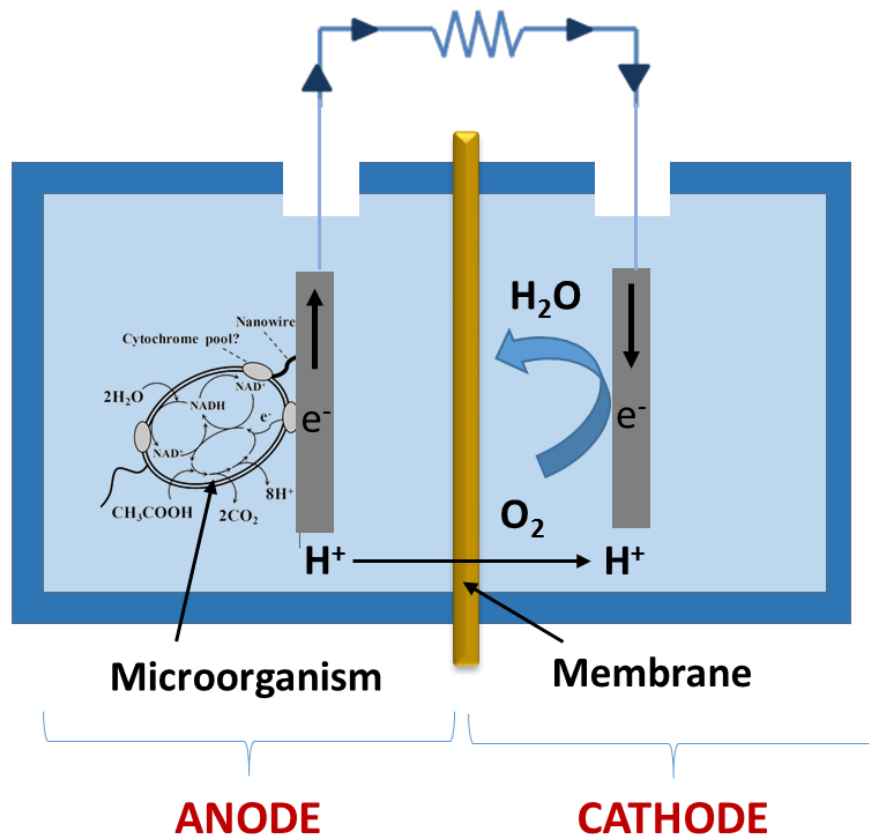


Figure 4 scheme of working principle of a MFC

During those years, the conducted experiments required the use of chemical mediator, or electron shuttles, to transfer the electrons inside the microorganisms' cell to the electrodes. In 1999 Kim et al. [19] demonstrate that the mediators are not needed.

In MFCs, microorganisms are able to oxidize the organic matter [20], producing electrons that flow into the anode and then they flow, through an external load applied, into a terminal electron acceptor (TEA), which acquire the electrons and becomes reduced (see Figure 4).

There are some bacteria in natural environments, indeed, which are able to directly transfer electrons outside their cells exogenously.

These bacteria are called exoelectrogens, “exo” for extracellular and “electrogens” based on the ability to directly transfer electrons to a chemical or material that it is not the immediate electron acceptor [14].

The exoelectrogenic bacteria are different from some anaerobes microorganisms (i.e. Escherichia Coli, Clostridium genus and Bacteroides Species), which, by contrast, can only transfer the electron to soluble compounds such as nitrate or sulfate, that can diffuse across the cell membrane and into cell. These electrogenic bacteria can be used to produce power in the MFCs [20]. Consequently, the process, which uses this type of bacteria in the MFCs reactor in order to produce power, is defined as electrogenesis.

Bacterial reactions can occur at several different temperatures, related to the tolerance of different species of bacteria, ranging from the room temperature (18-35°C) to higher temperature (50-60 °C), tolerated by the thermophiles, and lower temperature (< 15°C), tolerated by the psychrophiles.

In particular, in the anode chamber the bacteria grow on the electrode leading to the formation of the so called biofilm.

✓ **Biofilm and Electron transfer process definition**

The IUPAC defined the biofilm as an” Aggregate of microorganisms in which cells that are frequently embedded within a self-produced matrix of extracellular polymeric substance (EPS) adhere to each other and/or to a surface.” [21]

In general, the biofilm is defined as any group of microorganisms in which cells attach to each other and often these cells adhere to a surface. The adhesion of these microorganisms to the surface is initially induced through weak, reversible adhesion via Van der Waals forces and hydrophobic effects. If the microorganisms are not immediately separated from the surface, they can anchor themselves more permanently using cell adhesion such as pili, based on a self-produced matrix of extracellular polymeric substance. The occurring formation of biofilm is different from planktonic microorganisms, which, on the contrary, float or swim in a liquid medium. Electrochemically active biofilms have great importance in the natural environment taking parts in many process, principally

in metal oxidation and reduction and the associated effects on mineral dissolution, the carbon cycle, and the sorption and complexation of the phosphorous and heavy metals.

An example of electrochemically active biofilm formation on the material surface is represented in Figure 5. The analysis of deeply interconnections between the bacteria and the materials is performed through the Scanning Electron Microscopy.

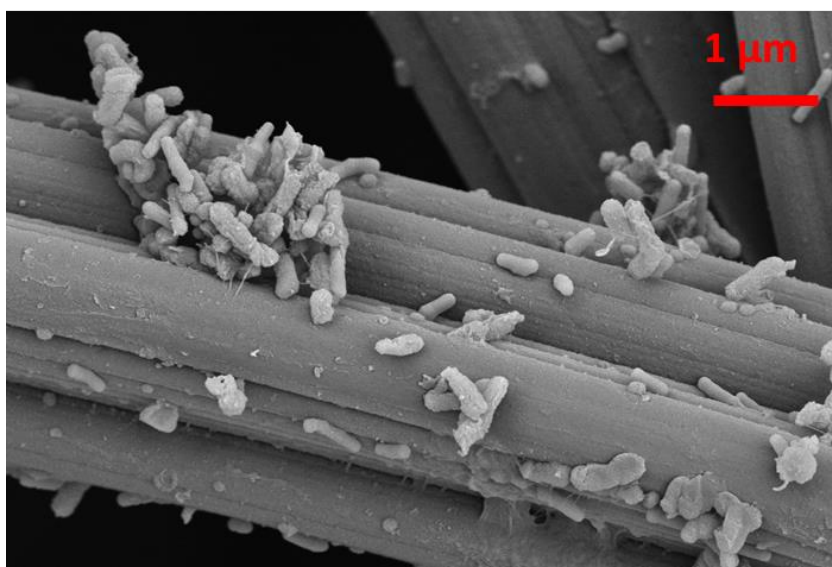


Figure 5 Representation of an example of biofilm formation.

More in general, the microorganisms can guarantee the conversion between the chemical energy, contained in an organic substrate, into the electricity energy, but they retain a portion of the Gibbs free energy $\Delta G^{\theta}_{bacteria}$ for their own reproduction [22].

Gibbs free energy of the MFCs is defined according to the Eq 1

$$\Delta G^{\theta}_{MFC} = \Delta G^{\theta}_{tot} - \Delta G^{\theta}_{bacteria} \quad \text{Eq 1}$$

Where ΔG^{θ}_{tot} is the total free energy involved in the bioelectrochemical process and ΔG^{θ}_{MFC} can be defined as the portion of free Gibbs energy of the devices. In particular, the portion of biological free energy $\Delta G^{\theta}_{bacteria}$ allows the maintenance of the bacterial vitality, granting not only the durability of the process operation, but leading to occur the electron transfer mechanisms ensured from microorganisms. It is important to highlight that if the $\Delta G^{\theta}_{bacteria}$ becomes too large, the energy efficiency, defined as the electricity energy output, of MFCs decreases. A linear relationship

between the free Gibbs energy and the standard potentials of the different reactions, occurred in the MFCs, can be introduced as shown in Figure 6.

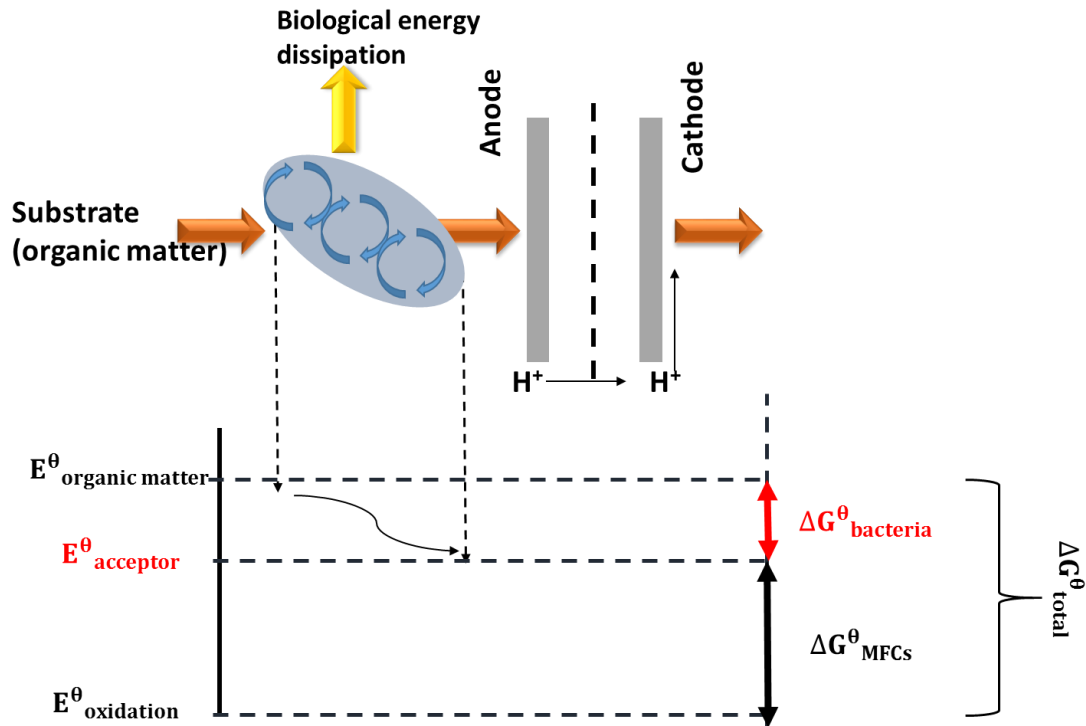


Figure 6 principal representation of the energy flux and production in Microbial Fuel Cells [22]

In particular total Gibbs free energy is defined by the following Eq 2. The $\Delta G^{\theta}_{total}$ linearly depends on the difference potential between the electron donor, as the organic matter and the electron acceptor.

$$\Delta G^{\theta}_{total} = -nF[E_{acceptor}^{\theta} - E_{organic\ matter}^{\theta}] \quad \text{Eq 2}$$

Where n is the electron number involved in the oxidation reaction and F is Faraday constant ($F=96485 \text{ Cmol}^{-1}$).

The process of electron transfer by bacteria can be divided in two mainly different ways [23, 24]:

- 1) electron shuttling via self-produced mediators [25, 26]
- 2) nanowires produced by some bacteria which are used as endogenous mediators [27, 28].

Gorby et al. [27] studied the formation of conductive attachments for both *Geobacter* and *Shewanella* species which were defined bacterial nanowires. They demonstrated the nanowires conductivity and consequently their ability to directly transfer the electron, produced by bacteria,

to the electrode. These self-produced nanowires ensure a direct electron transfer pathways from the microorganisms to electrode. Another direct electron transfer pathway is also ensured when there is a physical contact of a redox active bacterial membrane organelle, such as cytochromes, with the anode electrode [22]. These methods of direct electron transfer are represented in the Figure 7.

Figure 7A) shows the direct electron transfer occurred through the direct contact of bacterial cytochromes and the anode electrodes; while Figure 7B) is a schematic representation of the direct electron transfer pathway guaranteed by the ability of the microorganism to produce nanowires connecting themselves with the electrodes in MFCs. The conductive nanowires connected with the material surface represent the recently point of view for the electron transfer process.

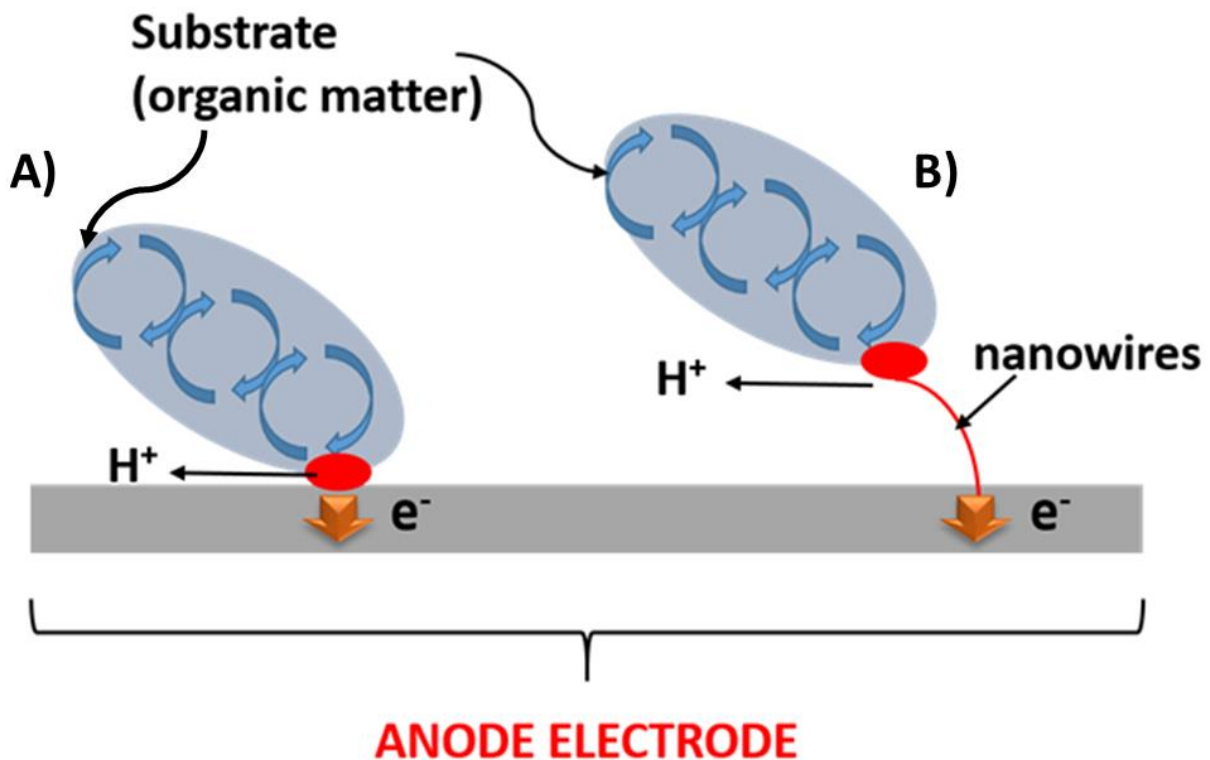


Figure 7 scheme of the direct electron transfer pathway through A) the membrane bound cytochromes and B) nanowires self-produced by bacteria

On the contrary, Rabaey et al. [25, 26] demonstrated that there are some bacteria able to generate exogenous redox mediators, which not have to be added to a culture. These self-produced mediators permit to shuttle the electrons to an electrode, inducing the power generation in a MFC.

The examples of these exogenous mediators are summarized in the Table 1. One of them is pyocyanine produced by *Pseudomonas Aeruginosa* [25].

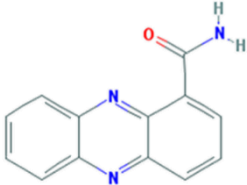
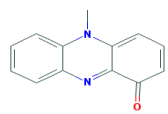
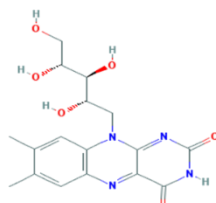
Name of redox mediator	Structure
Phenazine-1-carboxamide [29]	 <p>The structure shows a phenazine ring system (three fused benzene rings with two nitrogen atoms at the 10 and 11 positions) with a carboxamide group (-C(=O)NH₂) attached to the 4-position. The nitrogen atoms in the ring and the amide group are highlighted in blue.</p>
Pyocyanine [25]	 <p>The structure shows a phenazine ring system with a methyl group on the nitrogen at position 10 and a carbonyl group (=O) at position 4. The nitrogen atoms in the ring are highlighted in blue.</p>
Riboflavin [30]	 <p>The structure shows a riboflavin molecule, which consists of a ribityl side chain attached to an isoalloxazine ring system. The nitrogen atoms in the ring and the carbonyl groups are highlighted in blue.</p>

Table 1 summarizes the main examples of redox mediators self-produced by bacteria, guaranteeing the electron transfer between them and the anode electrode

Figure 8 shows a schematic representation of these electron transfer processes, the self-produced redox mediators, attached on the material surface, defines a more traditional idea of electron transfer mechanism.

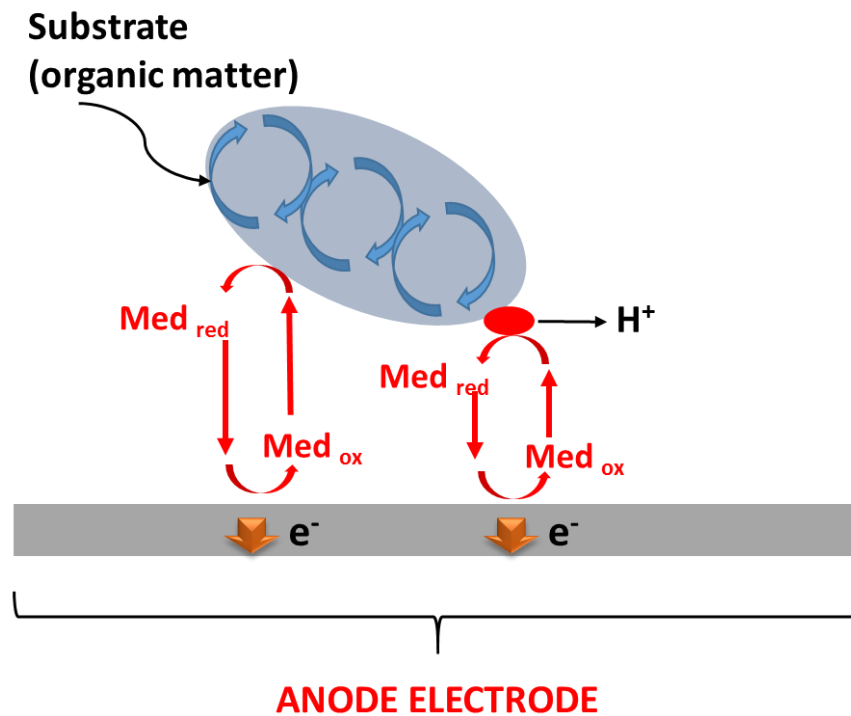


Figure 8 The representation of one of the main electron transfer processes: this mechanism is based on the direct electron transfer to the electrode through the self-produced redox mediators

Some factors, like electrode material, how the electrochemical active biofilm grown on the electrode and the devices configuration where the biofilm is formed, have a great impact on the ability of electroactive grown biofilm to participate in extracellular electron transfer process.

The development of the processes that can use bacteria to produce electricity represents a fantastic method for bioenergy production, since the bacteria are self-replicating and thus catalysts for organic matter oxidation are self-sustaining.

In conclusion, the bacteria, interconnected with the anode material forming the biofilm, are mainly the anaerobic exoelectrogenic species; due to the anaerobic metabolism of these bacteria, it is important/fundamental to design a device able to keep the bacteria separated from the oxygen as much as possible.

Regarding the electrolyte in the cathode of MFCs, there are many different chemical species that accept the electron and then are reduced. One of them is the oxygen, which can be reduced into the water through a catalyzed reaction of the electron with the protons.

Many TEAs, such as oxygen, nitrate, sulfate and others, accept the electrons making some products that can diffuse outside the devices.

✓ **MFCs Architectures**

There are mainly two architectures of Microbial Fuel Cells, studied in the literature; Figure 9 shows a bioelectrochemical schemes describing the principal components of these architectures [15]. Figure 9 a) shows a dual chamber MFC (DCMFC), in which the electrolyte inside the cathode is based on chemical solutions, like hexacyanoferrate of potassium. This architecture requires the presence of a cationic membrane, which allows the protons transfer between the anode and cathode and create two different and separate compartments: the anode chamber and the cathode chamber. In this way the produced electrons, which flow into the cathode, can be recombined with protons. Figure 9 b) represents the Single Chamber MFCs (SCMFCs) configuration, characterized by only one chamber. The electrolyte is unique and common with anode and cathode; moreover, it contains the oxidizing organic matter. In this configuration, there is not the cationic exchange membrane and the final electron acceptor is the oxygen. Moreover, in order to use oxygen dissolved in the electrolyte as unique terminal electrons acceptor, the SCMFCs are designed; this configuration is usually defined also as air open cathode MFCs.

The SCMFCs, developed and widely studied during my Ph.D. period, ensures the proper oxygen diffusion from the external environment into the device, limiting, at the same time, the direct contact/interaction between the anodic biofilm and oxygen. Moreover, all SCMFCs are inoculated using an environmental mixed culture (freshwater sediment) from a river in Valle D'Aosta. The inoculum can be defined as "A small amount of substance containing bacteria from a pure or mixed culture which is used to start a new culture or to infect an experimental animal" [31].

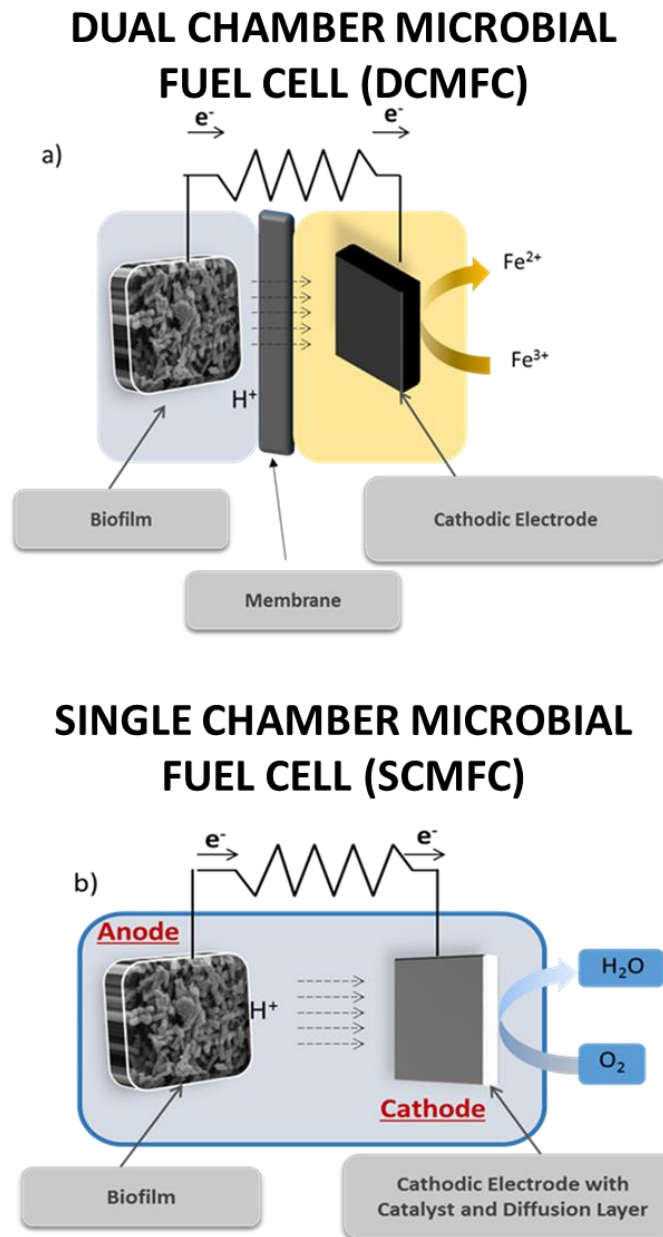


Figure 9 represents two different electrochemical schemes describing two different architectures of MFCs; a) shows the dual chamber MFCs where the reduced species in the cathode is hexacyanoferrate of potassium; b) represents the single chamber MFCs where, on the contrary, the oxygen in the cathode is reduced into the water.

These two described configurations show different advantages and disadvantages [14]. The main advantage of the Dual Chamber configuration is represented by the fact that the terminal electron acceptors are normally soluble in the deionized water and, if the electrolyte is based on

hexacyanoferrate of potassium, the standard reduction potential is very low, close to 0.361V, favouring the reduction reaction. In contrast the disadvantages are represented by the use of chemical electrolyte in the cathode, which constrains the environmental applications of the devices for safety reasons and because a continuous refreshment of the solution is needed. Moreover, the low standard reduction potential induces lower performances of this device with respect the one achieved by single chamber configuration. On the contrary, the key features and benefit of the SCMFCs is the use of oxygen as terminal electron acceptor that does not require any chemical species to run the cathode, ensuring consequently the environmental application of these devices. Due to the high standard reduction potential of oxygen, close to 1.23V or close to 0.805V when the oxygen is dissolved in water, the reached power generation is higher if compared with the double chamber. Moreover, the SCMFCs configuration ensure the diffusion of oxygen into the devices, limiting as much as possible the contact between the biofilm on the anode material and the oxygen itself. As introduced above, the anaerobic metabolism of bacteria, used in order to produce energy, can be invalidated by the oxygen. Finally, this configuration can guarantee reduced dimension of the reactors. The main disadvantage of SCMFC is represented by the mandatory presence of the catalyst on cathode surface, in order to favour the direct oxygen reduction reaction (ORR) producing water, minimizing simultaneously the intermediate reaction, which produces the hydrogen peroxide as the final products. This latter reaction requires low constraint to be performed, but its product results to be toxic for the microorganisms and corrosive for electrode material, and then it undesired. In paragraph 1.3.2 both these reactions will be deeply investigated. The schematic resistor which connects the anode and cathode in both the schemes of Figure 9 is the external load applied to the cells and represents the device to be powered up. The variety of molecules and compounds that can be used as organic matter, such as volatile acids, carbohydrates, proteins, alcohols and other relatively recalcitrant materials like cellulose, represents one of the great aspects of the MFC's employment as power generator [14]. In general, the waste water can be used as an oxidizing organic matter in MFCs. The waste waters, and the other waste in general, contain the physical organic matter, which can be removed by bacteria metabolism, leading the MFCs bioremediations systems [32]. The bioremediation is defined as the process during which the contaminants are removed by the biological actions, such as the oxidation of the organic matter.

Indeed, many works in the literature underline that the MFCs are able to remove compounds such as trichloroethylene, dichlorethen and uranium from waste water and soil [32]. In this way, it is possible to conjugate together the use of MFCs as a bioelectrochemical generator and wastewater treatment application; waste products can be then used as organic matter to be oxidized by bacteria in MFC. The first application of MFCs as water treatment devices was made at the end of 1999, by Kim and his coworkers, who observed and demonstrated the use of MFCs not only to generate electricity but also to detect the concentration of lactate inside industrial wastewater [33]. In 2004 Liu et al. [34] confirmed this new application producing an amount of electricity several order of magnitude higher than the previous one, using the domestic wastewater as organic matter. Once demonstrated the possibility to create a power generator through the use of wastewater, the following goal of the research was to develop a practical application of a MFC with a scalable technology for the treatment of domestic, industrial and other types of wastewaters [14].

During my Ph.D. period, I was mainly focused on the Single Chamber Microbial Fuel Cells configuration, due to the features and benefit of this architecture described above.

1.3 Voltage generation

MFCs commonly achieved a maximum working voltage of 0.3-0.7 V [15].

According to the first Ohm's Law, the voltage depends on the external load applied R_{ext} and the current, I , as represented in the Eq 3:

$$V = I * R_{ext} \quad \text{Eq 3}$$

The current produced by a single MFC is usually small, in fact, when a MFC is constructed in the laboratory the current cannot be measured, but it is calculated from the measured voltage drop across the resistor. The highest voltage experimentally produced by an MFC is the open circuit voltage (OCV), which can be measured with no external load applied; the voltage reduces if the value of the external load decreases.

The voltage generated by MFCs is generally more difficult to be predicted than the one obtained by other kinds of fuel cells, because of the dependence between the voltage generation and the bacteria growth.

In fact, the voltage is correlated with the catabolic activity of the bacteria (more generally microorganisms) growth on the anode electrode defined as biofilm, with the enzymes or structures needed to transfer the electrons outside the bacteria and, if there is a mixed culture of microorganisms, with the different bacteria species and their way of grow, which can set different potentials [14].

The maximum potential cell that can be theoretically produced by a fuel cell is the overall cell electromotive force (E_{emf}). It can be generally described as the difference between the anode and cathode potentials, as proposed in the Eq 4 [35].

$$E_{emf} = E_{cat} - E_{An} \quad E_{emf}^{0/} = E_{cat}^{0/} - E_{An}^{0/} \quad \text{Eq 4}$$

Where E_{emf} is the maximum electromotive force; E_{cat} is the potential value in the cathode and finally E_{An} is the potential value in the anode. $E_{cat}^{0/}$ and $E_{An}^{0/}$ are, respectively, the standard reduction potential of electrolyte in the cathode and the standard oxidation potential of electrolyte in the anode. The standard potential is referred to a standard hydrogen electrode under conditions of neutral pH and of temperature equal to 25°C.

The maximum E_{emf} that can be generated by a MFC strictly depend on the organic matter used at the anode, as the fuel, and on the TEA selected to close the reduction at the cathode.

Analysis of the anode and cathode voltages is presented in the following paragraphs.

1.3.1 Anode Voltages

The anodic voltage depends on the organic matter used in the MFCs. Usually in laboratory conditions, the organic matter is made of sodium acetate, used as the carbon-energy source, and necessary as the fuel for the bacteria. Sodium acetate ensures the production of a certain amount of electrons equal to 8, when the microorganisms oxidize it. The other compound, which is not strictly correlated with the production of electron, is ammonium chloride, selected as the nitrogen sources, and needed to accelerate the bacteria growth and their colonization of the anodic electrode. Most MFCs, despite operating on various substrates, produce an Open Circuit Voltage (OCV) approaching -0.3V [14]. According to the IUPAC definition, standard potentials (at 298 K, 1 bar, 1 M) must be described as a reduction potential, for example reactions must be written as

consuming electrons [35]. Acetate oxidation to HCO_3^- expressed as reduction is defined into the Eq 5:



Acetate standard potential referred to the standard hydrogen electrode (SHE) is $E^0 = 0.187 \text{ V}$.

For typical working conditions defined in MFC [35], according to which the devices operates under neutral pH=7 conditions and where the oxidation of sodium acetate (with a concentration of 1g/l) to bicarbonate HCO_3^- (with a concentration equal to 5mM) occurs, the anode potential is defined by Nernst Equation, represented into the Eq 6:

$$E_{An} = E_{An}^0 - \frac{RT}{8F} \ln \frac{[\text{CH}_3\text{COO}^-]}{[\text{HCO}_3^-]^2[\text{H}^+]^9} = -0.300\text{V}(\text{vs SHE}) \quad \text{Eq 6}$$

Where R is the gas constant, $R = 8.314 \text{ J/mol} \cdot \text{K}$; F is the Faraday constant, $F = 96487 \text{ C/mol}$ and T is the temperature defined in Kelvin. The E_{An}^0 define the standard oxidation potential of the selected organic matter and the all other elements in the equation represent the concentration of the ionic species. Since that the anode voltages strictly depend on the organic matter used in the devices, it is important to know different E_{An}^0 versus SHE of the distinct possible substrates and the number of electrons produced after the substrate oxidation, as represented in the Table 2.

Oxidation reaction into anode	Standard Potential $E^0_{An}(\text{V})$	Electrons produced
$\text{H}_2\text{O}/\text{O}_2$	0.82	$4e^-$
Methane/ HCO_3^-	-0.24	$8e^-$
Acetate/ HCO_3^-	-0.28	$8e^-$
H_2/H^+	-0.41	$2e^-$
Glucose/ HCO_3^-	-0.41	$24e^-$

Table 2 reports some standard anode potential defined versus SHE. Most common organic matters are considered, such as methane, acetate, hydrogen and glucose, which are oxidized into the anode compartment guaranteeing thus a certain value of anode voltages. In the table, moreover, the number of electrons, produced during the oxidation of each substrate, is defined.

1.3.2 Cathode Voltages

The cathode voltage depends on the standard potential reduction E_{cat}^0 of the different electrolytes, which must be reduced. The value of standard reduction potential is usually referred to a standard hydrogen electrode (SHE) under conditions of neutral pH and of temperature equal to 25°C. The final performances of the device are also correlated with the different reduction potentials required by the several electrolytes used in the cathode; the standard reduction potential of some different reactions are summarized in the Table 3 and, in particular, the all values of voltage are defined for pH = 7 at T = 298K.

Reduction reaction into the cathode	Standard Potential $E_{cat}^0(V)$	Number of electrons used
$O_2 + 4H^+ + 4e^- \rightarrow 2H_2O$	0.805	4e ⁻
$O_2 + 2H^+ + 2e^- \rightarrow H_2O_2$	0.328	2e ⁻
$H_2O_2 + 2H^+ + 2e^- \rightarrow H_2O$	0.867	2e ⁻
$Fe(CN)_6^{3-} + e^- \rightarrow Fe(CN)_6^{4-}$	0.361	1e ⁻
$MnO_2 + 4H^+ + 2e^- \rightarrow 2H_2O + MnO_2^{2+}$	0.470	2e ⁻

Table 3 some cathode potentials for different reduction reaction occurred. E_{cat}^0 values are defined for value of pH=7 at T=298K

For a single chamber microbial fuel cell (SCMFC), using dissolved oxygen as TEA, the maximum value of cathode standard potential is $E_{cat}^0 = 0.805 V$ versus SHE under condition of neutral pH and of temperature equal to 25°C [20].

As explained above, the standard potential of the oxygen reduction reaction is higher than others related to different electrolytes, ensuring in this way a high power generation produced by the devices, where the final terminal acceptor is the oxygen. For an air cathode MFC with 1g/L of acetate as substrate and a concentration of $HCO_3^- = 5mM$, the maximum cell potential, according to the Eq 7, is :

$$E_{emf}^{0/} = (0.805) - (-0.300) = 1.105V \quad \text{Eq 7}$$

The oxygen reduction reaction (ORR) in aqueous solutions involves 2 different pathways: the direct 4-electron reduction pathway from O_2 to H_2O , and the 2 electron reduction pathway from O_2 to H_2O_2 (hydrogen peroxide) [36]. The direct reduction of oxygen to water requires 4-electrons transfer, but when the 4 electrons are not achieved, the oxygen reduction produces hydrogen peroxide as result, for which only 2 electrons are needed. The two oxygen reduction reactions were defined by the Eq 8 and Eq 9, representing respectively the direct and intermediate reactions.



The standard potential for H_2O_2 is theoretically equal to 0.695V; however, since the MFCs doesn't work under standard conditions (pH=7, T= 298K), the experimental data established that the 2 electron reduction pathway occurred in MFCs at a potential of about $E_{cat}^{0/} = 0.328V$.

Although the intermediate oxygen reduction reaction is thermodynamically advantageous thanks to a lower potential reduction (equal to 0.695V versus SHE) and the 2 electron pathway requested, in MFCs the production of H_2O_2 is problematic as oxidizer, because of it can result in degradation of electrode or a membrane and it results to be toxic for the microorganisms.

For all these reasons, when the oxygen is used as reduced species, the cathodes must be modified to ensure its diffusion from outside to inside the MFC and to catalyze the oxygen reaction reduction (ORR).

The cathode modification is performed as following: on one side of the carbon based electrode, such as carbon felt (CF), were applied 4 layers of polytetrafluoroethylene (PTFE), known as Diffusion Layers (DLs), while on the opposite side was deposited a layer based on Platinum and Nafion, defined as catalyst layer (CLs) [37].

Each layer of PTFE (built by a deposition of a solution of 60wt% PTFE dissolved in deionized water, purchased from Fuel Cell EARTH LLC, USA) was dried at 370°C in air for 15 min. The catalyst layers were based on a mixture of Platinum/Carbon (Pt/C 0.5 mg/cm², purchased from Sigma Aldrich), Nafion (5wt% Nafion purchased from Sigma Aldrich) and isopropanol and were dried in air at room temperature for 1 day.

The mixture of Nafion and Isopropanol has been used to ensure the adhesion of Platinum/carbon on the cathode. Platinum is widely known as the best performing catalyst for ORR. However, due to the very expensive cost of platinum for making commercially viable microbial fuel cell, some works in the literature studied and investigated other possible cheaper catalysts, which must guarantee the same performances in terms of oxygen reduction reactions [38, 39].

While the oxygen is predicted to have a higher cathode potential than potassium ferricyanide, in practice the potentials achieved using oxygen are much lower than its theoretical value.

Oh and Logan (2006) [40] demonstrated how the power produced by the cell increases by 1.5 to 1.8 times, when the oxygen is substituted by potassium ferricyanide.

Rabaey et al. (2004) [25] obtained the highest power equal to 4.1 W/m² using the ferricyanide as electrolyte in cathode of MFCs. Some works use iron, manganese and permanganate as catholyte [41, 34].

1.3.3 Factors affecting the MFC voltage

The cell voltage produced at any specific current is considered to be the result of voltage losses due to electrode overpotentials and Ohmic losses, as defined in the Eq. 10

$$E_{emf} = E^0 - \left(\sum OP_{An} + \left| \sum OP_{cat} \right| + IR_{\Omega} \right) \quad \text{Eq 10}$$

$\sum OP_{An}$ e $\left| \sum OP_{cat} \right|$ are the overpotentials of the anode and the cathode respectively and the IR_{Ω} includes all ohmic losses, which are proportional to the current generated (I) and the resistance of the system R_{Ω} .

The overpotentials define the drops of voltage occurring in order to enhance the charge transport of the released electrons and protons, respectively.

In general, the first Ohmic's Law is used to define the ohmic overpotential η_{ohmic} , Eq 11 :

$$\eta_{ohmic} = i * R_{\Omega} \quad \text{Eq 11}$$

The overpotentials of the electrodes are more evident at low current densities, where the voltage rapidly decreases; moreover, the magnitude of overpotentials at any specific point is current dependent, as defined by the previous equation.

Electrode overpotentials are thought to arise from 3 basic losses [35]:

The Activation losses are due to the energy lost, i.e. heat, to start the oxidation or reduction reactions and the energy lost through the transfer of electrons from the cell terminal protein or enzyme to the anode surface. These losses are apparent at low current densities. They can be reduced improving catalyst at the cathode, using different bacteria at the anode or by enhancing the electron transfer between bacteria and the anode.

The Bacterial metabolisms cause voltage losses which are inevitable and due to the fact that the bacteria derive energy to sustain from the same substrate oxidation process.

The Mass transports losses arise when the flux of reactants to the electrode, or the flux of the products from the electrode are insufficient and therefore limit the reaction rate. Mass transport, in addition to limit the proton transport to the cathode, can also limit power generation resulting in an elevated pH at the cathode. It is important to maintain sufficient buffer capacity in the system and to minimize the build-up of material on the cathode that can hinder proton diffusion. The buffer capacity is defined as the ability of the salts mixture to compensate the pH value in the electrolyte; the pH value, indeed, must be in the range from 7 to 11, in order to guarantee good performance of the device.

Ohmic losses represented by R_{Ω} are the most important losses to be overcome for an optimum design of the MFC architecture.

They arise from all the elements that contribute to increase the internal resistance of the cell such as the ions, the protons, the solution electrolyte, the membrane, the contact points between the electrodes and any internal electrical connection.

Ohmic losses can be limited in many ways, such as by reducing the electrode spacing, choosing membranes or electrode characterized by low resistance materials and ensuring a good contact between the circuit and the electrodes.

As explained above, the ohmic losses, due to the solution electrolyte conductivity between the reference electrode and a bipolar membrane, are defined by Eq 12:

$$\Delta V_{\Omega} = \frac{\delta_w I}{\sigma} \quad \text{Eq 12}$$

δ_w is the distance between the reference electrode and a bipolar membrane (cm), I is the current density (A/cm²) and σ is the electrolyte conductivity (S/cm).

It is possible to notice that there is a linear relationship between the voltage produced and the current density that can be expressed by Eq 13:

$$E_{emf} = OCV^* - IR_{int} \quad \text{Eq 13}$$

IR_{int} indicates the sum of all internal losses in the MFC, which are proportional to the internal resistance of the cell and the produced current. This linear relationship between potential and the current is a defining characteristic of MFCs due to the relatively high internal resistance.

It is important to underline that the microbial fuel cell performances have been affected by the cathode ohmic overpotentials, also defined as internal resistances.

The cathode resistance, in particular, is defined as a combination of ionic resistance, R_{ionic} and electronic one, R_{elec} [15].

Many studies demonstrate how the ionic conductivity is order of magnitude higher than electrical one and so it is possible consider the ionic resistance negligible with respect to the electrolyte one, as described in the Eq 14 .

$$R_{elec} = \frac{l}{AK} \quad \text{Eq 14}$$

Where l is the distance between the electrolyte and the cathode (cm), A is the surface area where the ionic transports occur and K is the specific conductivity ($\Omega \cdot \text{cm}$)⁻¹ of the electrolyte. According to the definition of the cathode internal resistance R_{elec} , the decreasing of the MFCs dimensions, limiting the distance l between the cathode electrode and electrolyte, induce a lower value of R_{elec} reducing the cathode losses.

The cathode ohmic losses are directly proportional to the current densities, and consequently reducing the cathode losses, the MFCs performances increase.

Moreover, it is needed to consider the mass transport losses at the cathode.

The mass transport losses are defined as the voltage required to drive mass transport phenomenon at the cathode and it is related to as the chemical species concentration decreases at the cathode. An insufficient mass transport can induce a limitation of the reduction reaction or a product accumulation into the cathode chamber.

Many characteristics, such as the presence of mediators, the use of modified electrode with a deposition of catalyst layer on the electrode surface, and the optimization of operational conditions within the cathode, induce a limitation of the cathode activation losses. These approaches will be examined later when the cathode voltages will be explained.

1.4 Power Generation and Columbic Efficiency

The power output by an MFC can be calculated from the measured output voltage across the load, E_{MFC} , and the current that flows inside it (I), as following Eq 15 [15]:

$$P = I \cdot E_{MFC} \quad \text{Eq 15}$$

The current produced (I) is calculated measuring the potential across the load as defined by Eq 16:

$$I = \frac{E_{MFC}}{R_{ext}} \rightarrow P = \frac{E_{MFC}^2}{R_{ext}} \rightarrow P = I^2 \cdot R_{ext} \quad \text{Eq 16}$$

The size of the anode surface, which is available for the microorganisms growth, can affect the amount of power generated by the cell. It is common to normalize the power production by the surface area of the anode, A_{an} . The power density produced by the MFC is represented by the Eq 17:

$$P_{An} = \frac{E_{MFC}^2}{A_{an} R_{ext}} \quad \text{Eq 17}$$

In reactor where the anode is suspended in H_2O , the available area, described by Eq 18 is defined as the projection of the geometric surface area based on both sides of the electrode

$$A_{an} = 2l_{an}w_{an} \quad \text{Eq 18}$$

where l_{an} and w_{an} are respectively the length and the width of the rectangular shaped electrode.

In general the A_{an} is the surface area that includes all the microbe accessible area.

Calculating the total area using the gas absorption, for example Argon, causes an overestimation of the useful amount of surface area, because portions of material with pore sizes much less than $1\mu\text{m}$ might be inaccessible to the microbes. In systems with the 2 electrode chambers separated by the membrane, it is also possible to normalize the power based on the membrane projected surface area, A_m .

It is then possible to assert that the power production depends on the relative size of anode, cathode and proton exchange membrane (PEM). The relative performance of the system can be evaluated with equally sized anodes, cathodes and membranes. As MFCs are designed to maximize the power output, the most important factor is the power production on the basis of the total reactor volume. The volumetric power [15] is defined by the equation Eq 19:

$$P_v = \frac{E_{MFC}^2}{vR_{ext}} \quad \text{Eq 19}$$

Where P_v is the volumetric power [W/m^3] and v is the total reactor volume [m^3].

Sometimes, the MFCs reactors produce a power density of few milliwatts per reactor volume, which is very low [15]. The main reason is related to the internal resistance of the device, which limit the intrinsic maximum voltage reaching it only the theoretical reactions at anode and cathode were considered.

It is possible to model the MFC as an equivalent resistor, which take into account all the internal resistances, linked in series with the external load.

The total maximum power theoretically possible is described by the Eq 20:

$$P_{t,emf} = \frac{E_{emf}^2}{R_{int} + R_{ext}} \quad \text{Eq 20}$$

The power directly increases with the square of the maximum potential. The maximum power achievable is calculated on the measured OCV and is equal to the following Eq 21; this value will be always less than the power obtained with the E_{emf} .

$$P_{t,OCV} = \frac{OCV^2}{R_{int} + R_{ext}} \quad \text{Eq 21}$$

The maximum power output possible is summarized by the Eq 22:

$$P_{max,emf} = \frac{E_{emf}^2}{R_{int} + R_{ext}} \cdot \frac{R_{ext}}{R_{int} + R_{ext}} = \frac{E_{emf}^2 \cdot R_{ext}}{(R_{int} + R_{ext})^2} \quad \text{Eq 22}$$

The OCV is a more useful measure of voltage to compute the maximum power, defined through the Eq 23:

$$P_{max} = \frac{OCV^2}{R_{int} + R_{ext}} \cdot \frac{R_{ext}}{R_{int} + R_{ext}} = \frac{OCV^2 \cdot R_{ext}}{(R_{int} + R_{ext})^2} \quad \text{Eq 23}$$

It is easy to observe that the maximum power is obtained with the smallest internal resistance; the target is then to minimize the internal resistance. The electrons recovery is referred to as Columbic efficiency, and it is defined as the ratio or the percentage of electrons recovered as current with respect to the electron in the starting organic matter.

$$C_E = \frac{\text{Coulombs recovered}}{\text{Total coulombs in substrate}}$$

If the current obtained is integrated over time, it is possible to define the total Coulombs transferred in the system, according to the Eq 24:

$$C_E = \frac{M_s \int_0^{t_b} I dt}{F b_{es} v_{An} \Delta c} \quad \text{Eq 24}$$

Δc is the variation of the substrate concentration over the batch cycle during a time period= t_b ; M_s is the molecular weight of the substrate; F is the Faraday constant; and v_{An} is the volume of liquid in the anode compartment.

The energy efficiency of an MFC is based on energy recovered in the system compared to the energy content of the starting material; it is defined as the ratio between the power produced by the cell over a time interval t and the heat of combustion of the organic substrate, according to the Eq 25:

$$\eta_{MFC} = \frac{\int_0^t E_{MFC} I dt}{\Delta H n_s} \quad \text{Eq 25}$$

Where ΔH is the heat combustion [J/mol] and n_s is the amount of substrate added. Usually, the value of the MFC efficiency is inside the range $2\% \leq \eta_{MFC} \leq 50\%$ when easily biodegradable substrates are used.

1.4.1 Polarization curves, power density curves and internal resistance definition

A polarization curve, represented in Figure 10, is used to characterize the current as a function of the voltage. There are 3 characteristic regions of voltage decrease in the MFC, as also represented in Figure 10 and as deeply explained into the paragraph 1.3.3:

- 1) Rapid voltage drops as current flows through the circuit;
- 2) A nearly decrease in voltage;
- 3) A second rapid voltage decrease at high current densities.

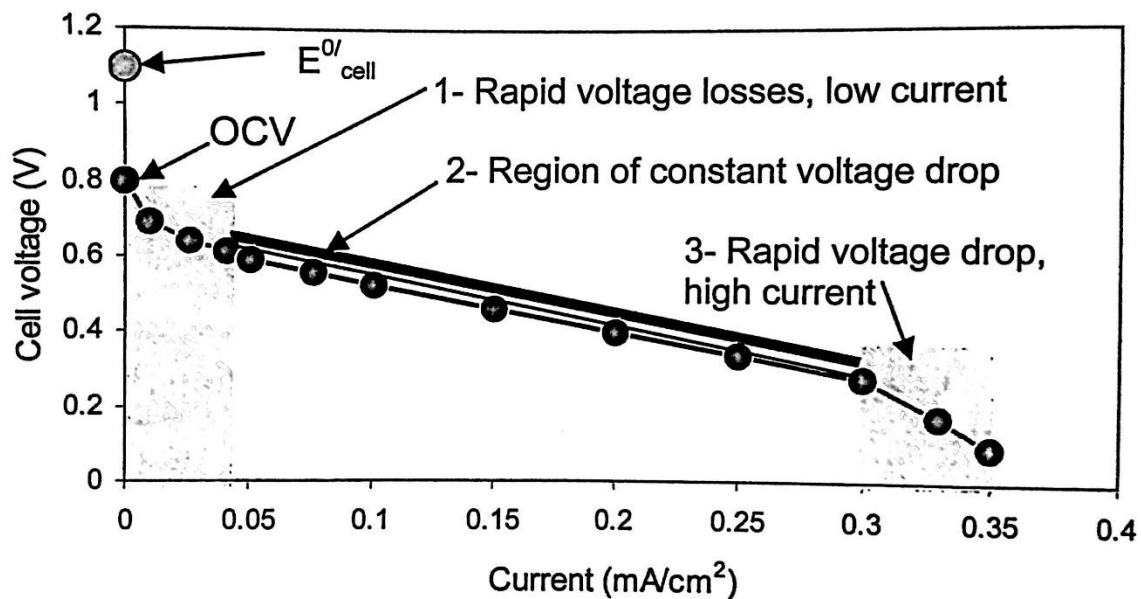


Figure 10 proposes the theoretical power losses due to the overpotentials related to the cathode and anode. To obtain the polarization curve, it is necessary to change the applied load using different resistances, measuring the different voltages across each resistance and obtaining the current value $I = \frac{E}{R_{ext}}$ and the current density by normalizing the current (I) over the surface area, as represented in Figure 11. The power density curve is defined from the measured voltage according to the Eq 26

$$P = \frac{E_{emf}^2}{R} \text{ or } (P = I^2 R) \quad \text{Eq 26}$$

Usually this curve is used to define the maximum value of power density achievable with the MFCs, as shown in Figure 11.

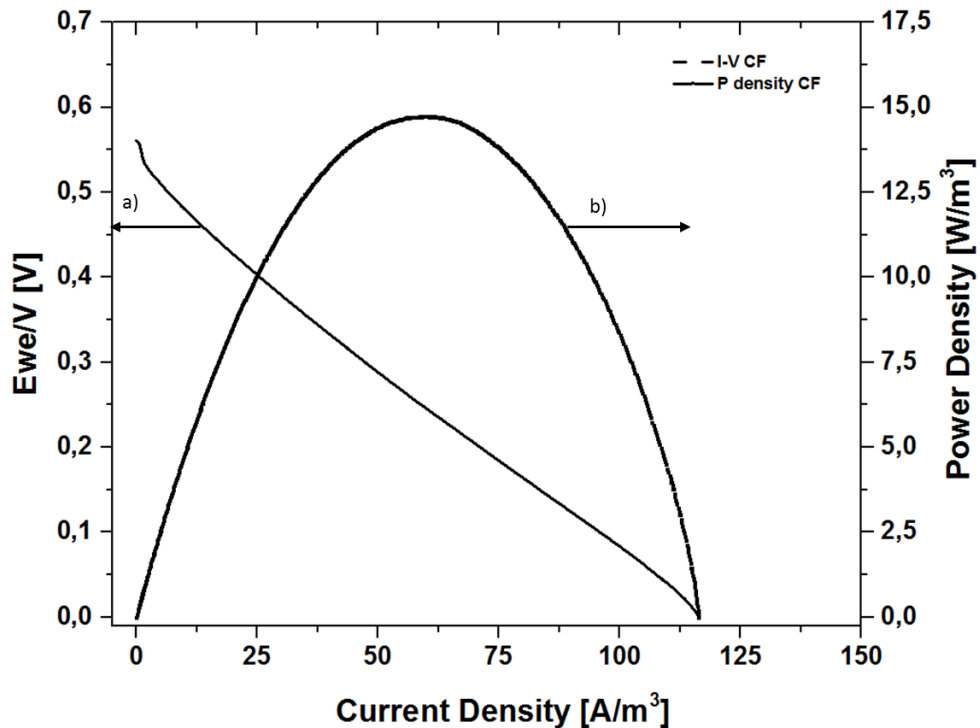


Figure 11 represents an example of polarization and power density curves. The curve a) represents the variation of voltage related with the measured current; while the curve b) represents the power density versus the measured current

It is possible to define a direct linear relationship between the voltage produced and the current density, as beforehand described by Eq 13:

$$E_{mfc} = OCV - IR_{int} \quad \text{Eq 13}$$

Where the term IR_{int} indicates all the internal losses of the MFC and it is proportional to the internal resistance of the cell and the current. The internal resistance R_{int} includes also the electrode overpotentials that change with the current. It is quite difficult to distinguish the concept of ohmic losses from the overpotentials.

The condition needed to define the internal resistance of microbial fuel cells and the power polarization curve is not uniformly defined and then it is quite difficult to optimize it, in order to obtain the most accurate measurements.

Usually, the MFCs are set up in OCV configuration for some hours before the characterizations; during this period of time it is important to verify that the cell reach the steady state conditions with an applied external resistance. The steady state conditions can be defined in different ways according to the operational mode implemented. In particular, it is possible to consider two different ways to feed the MFCs: the first one is called fed batch mode, in which with a constant time period, the all volume of the reactor is changed, for example every two days, or when the voltage drop reaches a very low value of voltage; on the contrary for the second mode, known as continuously fed mode, the moto syringe pumps or peristaltic pumps are used to define a constant value of flow rate in order to change all electrolyte volume of the device. The definition of the flow rate, consequently, determined a retention time, which is defined as the recovery time of the liquid inside of the reactor, related to the devices' volume.

In fed batch mode, it can be assumed that the steady state conditions are reached when two or three cycles shows a quite similar value of power. On the contrary, during the continuously fed mode, the steady state conditions are achieved when the cell provide a sustained power over several hydraulic retention time.

To obtain the polarization curves, 2 different methods can be used. The first one requires the use of potentiostat, which change the values of the applied voltage starting from the OCV value to the short circuit one with a fixed sample rating (i.e. equal to 1mVs^{-1}); this method is defined the Linear Sweep Voltammetry and it is deeply investigated in the Chapter 3 [42].

The second one required to manually change the external load applied. In this case, the period of time, during which the applied external resistance is kept constant, is defined by the time interval needed by the bacteria to consume their food, while the voltage remains quite constant.

The resistors are normally changed increasing their value from the lowest to highest in order to reach the external load that guarantees the maximum power output, which can be assumed equal to the internal one. There are many works in the literature that used the last method to define the

polarization curves. Menicucci et al. 2006 [43] maintained the external resistors for 3 minutes; 15 minutes were defined from Logan et al. 2006 [44] while Heilman and Logan 2006 [45] investigated the effects of a much longer period, equal to 7 hours. Despite all these investigation, there is not a clear indication to define which period is better than others.

Moreover, there are different methods to evaluate the internal resistance of an MFC:

1) Polarization slope method

According to the previous equation, the slope of the curve I-V is R_{int} (see Figure 10). The Curve I-V is usually defined by the Linear Sweep Voltammetry characterization. The current, flowing into the MFCs devices is measured and it is correlated with the relative voltage value applied. This characterization permits also to indirectly define the Power density peak.

2) Power density peak method

Starting from Eq 23, defining the maximum power, the OCV and the applied R_{ext} , it is possible to evaluate R_{int} . Starting from the polarization curve if and only if the polarization curve is a symmetric curve, it is possible to define that the maximum power occurs when the internal resistance is equal to the external one.

Thus it is possible to identify the internal resistance knowing the value of applied external resistance that produced the peak power output.

3) Electrochemical impedance spectroscopy (EIS):

Impedance spectroscopy is a powerful method in order to analyse the complex electrical internal resistance of the Microbial Fuel Cells and simultaneously the analysis of the system response contains information about the interfaces, its structure and the reactions taking place there [46, 47]. This method is based on the measured dynamic response of the cell, using the potentiostat to obtain the data.

All the aspects of impedance spectroscopy, such as the description of this characterization, the analysis of the results and how the characterization has to implement, are widely explained in the following Chapters (see Chapter 3).

4) Current interrupt method

This method requires the use of potentiostat and accurate determination of the potential after interrupting current requires a very fast recording of potential [13]. The MFC should be operated under steady state conditions without any concentration losses. In the OCV configuration the electrical circuit is opened producing zero current, an infinite resistance and an initial voltage steep rise. The voltage increases until the potential value equal to the OCV is reached. The ohmic losses are proportional to the current and so they became zero in OCV configuration. This effect produces the steep rise in the potential, E_R , which is proportional to R_Ω and the current I produced before the interruption. The ohmic resistance is defined by the equation $R_\Omega = E_R / I$, according to the first Ohmic's Law .

This method, differently from the EIS and LSV, defines approximately the internal resistance of the device without the possibility to distinguish the different interfaces among the anode, the electrolyte and the cathode, considering also the ionic diffusion in electrolyte solution. Since that the evaluation of dynamic response of the device cannot be defined with this method, in this thesis electrochemical characterizations performed are EIS and LSV.

1.5 Materials

The main target design for MFCs is to identify the materials and the scalable architectures able to maximize the power generation and the columbic efficiency, minimizing costs.

As explained before, the three main parts of MFCs are anode, cathode and eventually the membrane to separate the two chambers. The anode requires the capacity to induce the development of biofilm on the electrode; the membrane must help the ionic transport from anodic chamber into the cathode, increasing the internal resistance of cells; finally, the cathode must properly catalyze the reduction reactions.

As explained before, I investigated and studied the power generation reached using the SCMFCs.

The main aim of this work is, indeed, the development of new materials to be applied as electrodes in the devices, in order to enhance their performances.

1.5.1 Anode Materials

The anode material must have the following properties [15]:

- High conductivity;
- High chemical resistance;
- High specific area to volume ratio;
- High porosity with proper pore dimension of order of micrometer in order to improve the bacteria's growth on the anodic electrode;
- Non bio-fouling (the bacteria do not fill it up)
- Cheap, the production of the anodic electrode should be not expensive;
- Easily to be made and scalable according to the cell dimensions

In addition to all these properties, probably the most important characteristic, that the anode must guarantee, is its compatibility for the bacteria growth. The anodes must not be cytotoxic for the bacteria proliferation. In fact, when new materials are developed, first of all it is mandatory to conduct a test in agar plates in order to establish the no cytotoxicity properties of the sample. During this test, the material is put into the agar plates, which are a mixture based on agar, inoculum and bacteria's feeding, such as sodium acetate. The no cytotoxicity of the material is verified by the proliferation of the bacteria on the sample and around and it; on the contrary, if the material results to be cytotoxic, around the sample appear the so-called "cytotoxic ring", an empty area in which the bacteria are unable to grow. More details on this characterization are provided into the Chapter 3. The ring can be formed, for example, around a samples covered by silver, whereof cytotoxicity properties for the microorganisms are well known.

Another important property of the material is the electrical conductivity in order to ensure a low value of material's resistance and allowing a good charge transfer into the cell; the high value of electrical conductivity, consequently, guarantees the high produced electrons, which flow between the biofilm and the anode and then between the anode and the cathode.

The conductivity of the materials such as copper is 0.1 Ω/cm , for carbon paper is 0.8 Ω/cm , for graphitic fibers is 1.6 Ω/cm , for carbon cloth is 2.2 Ω/cm and for conductive polymer sheet is 130 Ω/cm [15].

For the fabrication of electrodes in the energy application fields, carbon in its various forms like powder, fibers and mats, has been found as most promising material. Many studies report the comparison between Microbial Fuel Cells based on different carbon anodic materials.

Indeed, the anodes currently used are often made of carbon built by carbon paper, felt and carbon cloth or whereas built by graphite rods, plates and felt [48].

The most representative work has been done by Liu et al. [34] in which the authors investigate a SCMFCs with eight graphite rods as anodes and an air cathode. The maximum value of power density, reached with this configuration, is of 26 mW/m². The limit of graphite rods is related to their low value of porosity and surface area that reduce the bacteria proliferation on anodic electrode. The graphite brush shows a higher value of porosity and surface area, enhancing the interaction with bacteria and consequently improving the performances. Logan [49] designed a single air chamber MFC with a graphite brush at the anode, obtaining a maximum value of power density of 422 mW/m². Finally, carbon paper and carbon cloth are used in MFCs as a flat plate electrode [50].

Some works in the literature developed a single air chamber microbial fuel cells using carbon cloth as anodic electrode and brewery wastewater as the anode substrate, the maximum power density reached is of 483 mW/m² [51].

Among all these works, this kind of carbon-based materials has not shown the fundamental properties of high porosity. As already said, the high porosity guarantees the provide habitat for bacteria proliferation, maximizing their penetration into the samples and minimizing, at the same time, the quantity of the materials needed to reach the target performances. The high porosity, moreover, enhance the diffusion of organic matter into the anode.

In conclusion, in order to generate electricity using bacteria in MFCs, highly conductive and chemical resistant materials are needed; those materials must have a high specific surface area and an open structure to avoid biofouling [52].

Nanostructured materials ensure a very high micrometric porosity, in particular the porous nanofibers have an extremely high length to diameter ratio, with a nanoscale diameter and an ultrahigh specific surface area if compared to other carbon materials [53, 54]

The nanofibers have been obtained through the electrospinning technology, as described into the Chapter 2.

The electrospinning is a unique technology that allows fibers with diameter in the range from a few nanometers to several microns to be obtained.

The mat of nanofibers, obtained as result of this process, is characterized by a very high value of micrometric porosity and a larger surface area to volume ratio.

In a small number of works in the literature, the carbon nanofibers have been obtained starting from an electrospun polymeric solution and then conducting a proper pyrolysis treatment on the mat.

In particular, these carbon nanofibers have been obtained through the carbonization of electrospun Polyacrylonitrile (PAN) nanofibers; the PAN was used as a precursor thanks to its high yield of carbonization. The pyrolysis treatment is conducted until a value of temperature ranging from 900°C to 1000°C under inert atmosphere [55, 56, 57].

Moreover, many works in the literature report a subsequent activation process used to compensate the losses of important element, such as ammonia, which occurs during the pyrolysis. The activation of nanofibers is possible according to different treatments, such as ammonia treatment, steam activation; all of them improve the electrocatalytic properties of these materials and enhance the bacteria growth on nanofibers [56, 58].

The activated carbon nanofibers improve the performances of MFCs, reaching a maximum power density of 758 W/m³, (the normalization is defined with respect to the volume of mat of nanofibers in order to deeply investigate the properties of materials) [56].

During my PhD period, I developed carbon nanofibers starting from electrospun PAN precursor, dissolved in N-N dimethylformamide used as the only solvent. One of the aims of this thesis is the development of innovative anodes in SCMFCs based on nanofibers. The innovation provided by my materials consist in the definition of a partial carbonization treatment, stopping the process once reached a lower final temperature, in order to guarantee an optimized nitrogen doping in the carbon nanofiber. The nitrogen doped nanofibers exhibits an optimized surface chemistry and a positive charged surface, improving the bacteria growth on the electrode, without the necessity of the

successive activation treatments [57]. Chapter 3 provides the detailed carbon nanofibers development process and the results obtained.

1.5.2 Cathode Materials

As in the anodic chamber, also in the cathode one the voltage losses occur due to the over potentials.

To decrease this phenomenon, it is necessary to develop a catalyst, or some mediators, which must be able to transfer the electrons from the cathode to the chemical species, such as oxygen or other ones, for the reduction reaction.

If the oxygen reduction reaction (ORR) occurs in the device, a catalyst, in general, must be used in order to speed up the ORR kinetics; in general, the catalyst is made of the conductive material, such as noble or no noble metals [36] .

When the single chamber configuration is considered, the cathode must be exposed at the same time at the air and the water based electrolyte and, because of that, in these conditions, the protons and electrons can reach the same active reaction sites.

The same materials, previously analyzed as anode, can be considered for the cathode development, such as carbon paper, carbon cloth, carbon felt, graphite brushes, graphite granules, nonwoven graphite and so on [38, 59].

Also the materials used as cathode require the same characteristics previously analyzed for the anodes. In particular, the high porosity enhances the diffusion of the final electron acceptor, incrementing the reduction reaction into the cathode. If oxygen is used as chemical species to be reduced, the cathode must have a catalyst that allows the reaction described by the Eq 8 and minimizing, at the same time, the intermediate reaction, defined by the Eq 9. Many studies investigate the performances obtained with a chemical cathode, in which the electrolyte is the potassium ferricyanide; in this case the presence of catalysts is not required.

✓ **Carbon based cathode with Platinum (Pt)**

The platinum is widely used as catalyst for cathodes. The commercial carbon based materials, used as cathode, present Platinum layer on their surface to catalyze the oxygen reduction reaction.

When the oxygen reduction reaction occurred into the cathode, the cathodes must be functionalized to ensure the oxygen diffusion from outside to inside the MFC, through a diffusion layers, and to catalyze the reduction reaction of oxygen (ORR), through the catalyst layers [38].

In particular, the diffusion of oxygen from outside into inside the device was ensured by diffusion layers, obtained as described into the paragraph 1.2.

While, the catalyst layer, deposited on internal side of electrode, allow the ORR [37]. As previously defined, the commercial catalyst layer is made of Platinum and Nafion, the first one is used to catalyze the ORR, while the second one is used as a binder in order to ensure the adhesion of platinum to the electrode.

The water is the final product of the oxygen reduction reaction, represented by the Eq 8.

There are many studies in the literature that investigate the different performances obtained with different amounts of diffusion layers. The power production obtained with 4 diffusion layers is equal of 766mW/m^2 with 4 diffusion layers, which is higher than one obtained without any diffusion layers of about $538\pm 16\text{mW/m}^2$ [38]. Moreover, it is quite important to establish the proper number of diffusion layers because if the number of layers is too high the diffusion of oxygen into the MFCs is reduced.

In fact, with 8 layers of PTFE, the power density decreases as a consequence of an insufficient oxygen transfer at the cathode part [15].

The catalyst layers were based on a mixture of Platinum/C ($\text{Pt/C } 0.5 \text{ mg/cm}^2$, purchased from Sigma Aldrich), Nafion (5wt% Nafion purchased from Sigma Aldrich) and isopropanol.

Also in this case the mixture of Nafion and Isopropanol was used to ensure the adhesion of Platinum on the cathode electrode.

The catalyst layers were dried in air at room temperature for 1 day.

✓ **Carbon cathode without Pt**

There are some works in the literature that don't use the precious metal such as platinum as a catalyst. Park and Zeikus (2002) [60] used an iron cathodes obtained starting from a ferric sulfate, fine graphite, kaolin (as a binder) and Nickel chloride. The cathodes are heated at $1100 \text{ }^\circ\text{C}$ for 12 h under N_2 . In this study the power density obtained is up to 3.8 times as much power as plain carbon

based materials. This obtained performance is not comparable with the one obtained with a carbon based cathode with Pt [61].

Recent works investigate the use of transition metal carbon cathodes to substitute the platinum and to obtain the better, or at least the same, performances occurred with the platinum as catalysts.

Zhao et al. [62] demonstrate, through electrochemical test, that two different transition metals, such as iron (II) phthalocyanine (FePc) and cobalt tetramethoxyphenylporphyrin (CoTMPP), could reach good performances, which result to be higher than ones obtained with the carbon based cathodes with platinum. Cheng et al [39], moreover, analyzed the performances of a single air chamber MFCs, using the CoTMPP as catalysts; the power density obtained reached a value of 369 ± 8 mW/m², which is only 12% lower than the with platinum, but it is largely higher than the one obtained without any catalysts. This can be an optimum compromise between the good performances obtained and the costs, which are reduced due to the presence of a non-precious metal as catalyst. Some ceramic materials can be applied as catalyst on the cathode electrodes. Many works are focused on the development of TiO₂ or MnO₂ to catalyze the ORR [63, 64].

✓ **Bacteria biofilms as catalyst for the ORR**

One of the newest approaches is the development of bio-cathodes; those cathodes, according to the typology of the bacteria which growth on their surfaces, are able to properly catalyze the reduction reaction in the cathode compartments.

Clauwaert et al. [65] are the first research group, which used the nitrate as electrolyte in MFC.

In this work, the acetate is oxidized in the anodic chamber and the nitrate was completely reduced by the bio cathodes and transformed in nitrogen gas. The maximum power density obtained with this configuration is of 4 W/m³, the cell voltage is 0.214 V and the current density is of about 35 A/m³.

Some works in the literature investigate the possibility to use the biofilm, growth on the cathode electrode, in order to catalyze the ORR to water on stainless steel [66]. In particular, the aerobic bacteria are able to donor the electrons to TEA reducing the oxygen in the cathode. Furthermore, cathode biofilms can contribute to preserve the anaerobic conditions in the media in the absence of a membrane, consuming oxygen incoming from the porous cathode. Until now, all the studies in

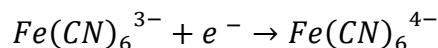
the literature on the development of biofilms as cathode catalyst lead to conflicting results: some works demonstrate the improved performances of MFCs using bacteria as catalyst for ORR; on the contrary, other studies establish lower energy production when a cathodic biofilm catalyzed the ORR.

In this thesis, I study the organic catalyst able to perform the oxygen reduction reaction allowing the improvement of the SCMFCs performances.

✓ **Other cathodes and different electrolytes**

Some works in the literature underlines the possibility to increase the MFCs efficiency changing the electrolyte into the cathode, for example from ferricyanide to permanganate [41].

Different materials and setup are required when the oxygen is not used as electron acceptor at the cathode, but different electrolytes into the cathode are chosen. In this configuration, the cathode electrode can be the plain carbon based materials. Moreover, there are many different aqueous electrolytes, but the most commonly used is the ferricyanide or the hexacyanoferrate of potassium, which is reduced according the following reaction:



One of the main disadvantages of these electrolytes is the necessity to chemically replaced them during the cell lifetime, in order to guarantee the proper working performances. Usually, the certain concentration of ferricyanide is dissolved in the same buffer used for the anodic chamber. Some works consider the possibility to aerate the electrolyte solution, [67, 68]; of course the frequency of the oxygen reduction reaction into the electrolyte at the cathode, without any catalyst, will be lower than the reduction of the ferricyanide. One of the problems related to a high amount of oxygen in the electrolyte is the possibility that the oxygen diffusion from cathode to anode deteriorates the anoxic conditions needed for high anodic performances.

Rabaey et al. [67] underlined high performances, in terms of power densities, occurred with ferricyanide as electrolytes. The high power densities are obtained in terms of high open circuit voltages and relatively small over potentials, lower than the ones obtained with the oxygen.

Few works in the literature used platinum plates or platinum coated metals as cathode. Independently from the performances of the cell, the platinum plates show prohibitive costs and for this reason, it is impossible to widely use it as electrodes [15].

1.5.3 Membrane materials and its uses

The membrane used in MFCs is a proton exchange membrane (PEM). PEM is used mainly in the two chamber MFCs to separate the anode from the electrolyte contained into the cathode, avoiding the mix of the potassium ferricyanide or the oxygen dissolved in the water with the liquid present in the anode.

In this configuration, one of the goals of the PEM is to ensure the proton transfer from anode to cathode. The PEM must be permeable to proton and for example a simple foil placed between the two compartments doesn't enhance the proton flux. At the same time, the membranes must be impermeable for other species contained into the cathode, such as the oxygen, which must not flux from cathode to the anode.

Normally the PEM is made of Nafion, which is able to transfer the protons from anode into the cathode chamber and contemporary block the anionic flux.

One of the disadvantages of these membranes is their high costs. Another one is due to the fact that the presence of the PEM increases the internal resistance of the MFCs and then reduces the power production.

In a single chamber MFCs, in which there are not two different compartments of anode and cathode, the PEM is always useless. Sometimes, under this configuration, the membrane electrode assemblies (MEAs) is used. The MEAs is a particular configuration, in which the membrane directly coats the catalyst side of the cathode electrode limiting the oxygen diffusion from cathode to anode. Liu and Logan [69] demonstrated that the power density obtained from the MFCs without the membrane is higher than the one reached by a MFCs with the membrane whether PEM or MEAs.

1.6 MFCs Applications

1.6.1 Waste water treatments

It is possible conjugate the use of MFCs as bioelectric generator and the wastewater treatment application, due to the fact that the waste products of the water can be used as organic matter to be oxidized by the bacteria. Once demonstrated the possibility to create a power generator through the use of wastewater, the following goal of the research was to develop a practical application of a MFC for the treatment of domestic, industrial and other types of wastewaters [14].

In the 1991 Habermann and Pommer investigate the possibility to apply the MFCs in the waste water treatment. The metropolitan water, used in this experiment, contains many organic compounds that could feed the MFCs. The first application of MFCs as water treatment devices was made at the end of 1999, by Kim and his coworkers, which observed and demonstrated the use of MFCs not only to generate electricity but also to detect the concentration of lactate inside industrial wastewater [33]. In 2004 Liu et al. [34] confirmed this new application producing an amount of electricity several order of magnitude higher than the previous one, using the domestic wastewater as organic matter. The amount of power generated by MFCs in the wastewater treatment process can potentially have the electricity needed if compared to conventional treatment processes, which consumes a lot of electric power aerating the activated sludge.

One of the important advantages of using MFCs in these applications is the possibility to apply a mixed inoculum that can biodegrade a higher amount of organic compounds if compared with a pure culture of bacteria.

Rabaey et al. [70] studied specific microbes, which are able to reduced sulfides, as required in the wastewater treatment.

Moreover, the use of MFCs can conjugate the effective treatment of the water and with the growth of the bio electrochemically active biofilm in the devices, enhancing the performances of the MFCs and increasing the power density.

The continuous flow, single-compartment and membrane-less MFCs are favored for the wastewater treatment due to their better scaling-up [71, 72, 73].

Sanitary wastes, food processing wastewater and swine wastewater are all great biomass sources for MFCs thanks to their abundance of organic matters [74, 34, 75, 76] .

Up to 80%of the COD can be removed in some cases [34, 75] and a 80% Columbic efficiency has been reported [77].

1.6.2 Electricity generations

As explained above, the MFCs transduce the chemical energy, stored in the chemical compounds and in a biomass, into the electrical one through the microorganisms.

The microorganisms oxidize the fuel molecules, contained in the biomass, and through this process, the bacteria convert the chemical energy into the electrical energy.

One of the limits of the MFCs is represented by their very low power generation [78, 79], and consequently the flux of electron produced is very low.

To solve this problem, Ieropoulos et al. [80] investigate the possibility to store the electricity in rechargeable devices and then distribute the electricity to end-users.

Capacitors were used in their biologically inspired robots named EcoBot I to accumulate the energy generated by the MFCs and worked in a pulsed manner.

The power generated by MFCs can be used to power small telemetry systems and wireless sensors that have low power requirements.

For example, some works develop the MFCs as supply energy to temperature sensors, which must transmit the measured signal to receivers in remote locations [81].

Some researchers consider the MFCs as a suitable devices to power robots, which are realistic energetically autonomous and equipped with MFCs utilizing different fuels like sugar, fruit, dead insects, grass and weed [82].

One of the main results, obtained with MSC as energy supply, is represented by the development of EcoBot-II.

The robot is exclusively powered by MFCs and it is able to perform some behavior, such as motion, sensing, computing and communication [81].

Another possible and amazing application of MFCs is in a spaceship, where they can produce electricity, oxidizing and degrading wastes generated on board, which became the feed for the microorganisms.

The future developments can be regarded the application of MFCs as implantable medical devices [83].

The MFC technology is particularly favored for sustainable long-term power applications.

However, only after solving the potential health and safety issues brought by the microorganisms contained in the MFC, they could be widely applied for this purpose.

1.6.3 Biosensors

Another application of the MFCs is their use as sensors for pollutant analysis and in situ processes of monitoring and control [84]

The development of MFCs as biosensor is based on the proportional correlation between the Columbic efficiency and the strength of the wastewater. In order to define the organic matter concentration in wastewater, its biological oxygen demand (BOD), achieved in a five day tests, or its chemical oxygen demand (COD), evaluated by a rapid chemical oxidation test, have to define. This aspect ensures the MFCs devices used as possible biological oxygen demand (BOD) sensors [85].

Wang et al. 2013 demonstrate that the MFCs have a great potential as biosensor for water quality. As explained before, the current generated can be correlated with the metabolic activity of the microorganisms. Indeed, the chemical energy, contained in the organic compound, was transformed into the electrical one from the oxidation of biomass; the oxidation of organic matters is directly dependent on the metabolic activity of the bacteria growth in the anode.

If the devices work under non-saturated condition, all the variations in the feed concentration inside the MFCs are directly proportional with the number of electrons produced and consequently with the current density generated.

This is the theoretical principle, which explains the application of MFCs device as BOD sensor in wastewater. Differently from the other traditional BOD method, the MFCs permit to have a completely screening tool in situ, to work on-line, to guarantee real time measurements with good

operational stability [86, 87]. If the devices work under fuel saturated concentration and the other parameters, such as pH, salinity, temperature and anode potentials, remain constant, the variations in the measured current output can be totally related to the presence of toxicant element into the feeding stream [88].

Indeed, the metabolism of bacteria can be inhibited by the presence of some toxicant compounds in the environment, causing a lower electron transfer between anodic and cathode. If a toxic compound flows through the anodic electrode, the biosensor will react with a drop of the voltage (or on a drop of current density) measured over the MFCs. These sensors can then be used for example to identify the toxicants in the rivers in correspondence of wastewater treatment plants, in order to detect unwanted pollution or illegal dumps [89].

1.6.4 Bio Hydrogen

MFCs can be readily modified to produce hydrogen instead of electricity. Under normal operating conditions, the protons released by the anodic reaction migrate to the cathode to be combined with oxygen producing water.

The hydrogen generation starting from the protons and the electrons produced by the metabolism of microbes in an MFC is thermodynamically unfavorable and so more difficult to be achieved if compared with the water production.

Liu et al. (2005c) [90] applied an external potential to the cathode to increase its potential in the MFC circuit and thus overcame the thermodynamic barrier. In this way, protons and electrons produced by the anodic reaction can be combined at the cathode to form hydrogen. The required external potential for an MFC is theoretically only 110 mV, much lower than the 1210 mV required for the direct electrolysis of water at neutral pH; this is mainly due thanks to the energy that already comes from the biomass oxidation process in the anodic chamber. MFCs can potentially produce about 8–9 mol H₂/mol glucose compared to the typical 4 mol H₂/mol glucose achieved in conventional fermentation [90].

In the bio-hydrogen production with MFCs, the oxygen is no longer needed in the cathode chamber. Thus, the MFC efficiency improves because the oxygen leaks into the anodic chamber are no longer an issue. Another advantage is represented by the fact that hydrogen can be accumulated and

Chapter 1 Microbial Fuel Cells (MFCs)

stored for later usage, partially overcoming the inherent low power feature of the MFCs. Therefore, MFCs provide a renewable hydrogen source that can contribute to the overall hydrogen demand in a hydrogen economy.

2 Chapter 2

State of art on Electrospinning

2.1 Nanofibers definition and introduction of different technique to obtain fibers

Nanofibers are defined as fibers with diameters less than 100 nanometers. In general, the fiber can be defined as natural or synthetic substance that is significantly longer than its wide characterized by a circular cross section. The nonwoven industry generally considers nanofibers as fibers having a diameter of less than one micron, although the National Science Foundation (NSF) defines nanofibers as having at least one dimension of 100 nanometer (nm) or less. Figure 12 reports on the trend line the dimension of nanofibers, which is smaller than the dimension of elements such as red blood and human hair, in contrast it is close to the dimension of DNA filament. Moreover, Figure 12 b) represents the correlation between the nanofibers diameters and the surface area to the volume ratio. It is possible to define how the surface area of nanofiber mats increases dramatically as the fiber diameters decreases.

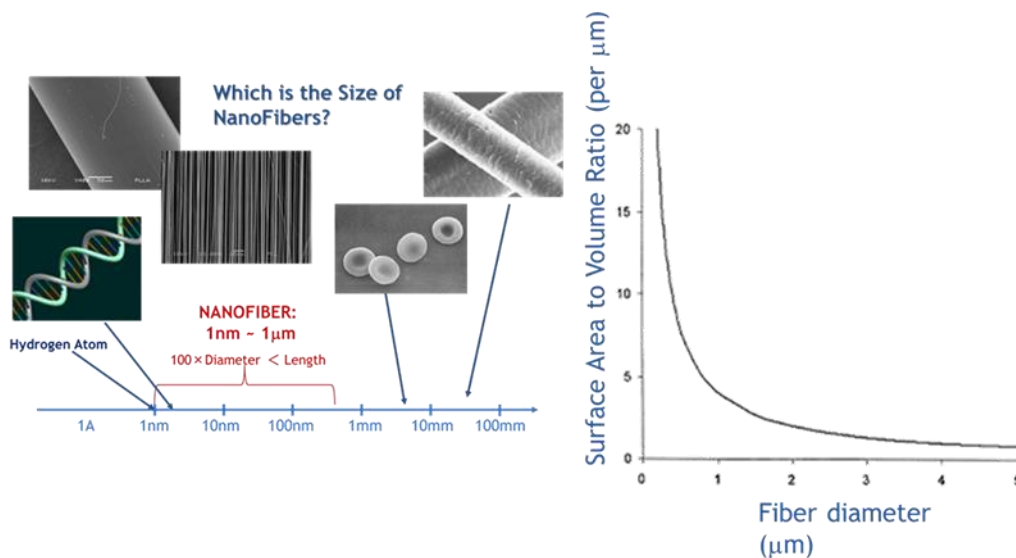


Figure 12a) the trend line to define the dimension of the nanofibers related to the some other elements, such as red blood cell or DNA filament; b) shows the correlation between the surface area of mat of nanofibers related to the diameter of the fibers.

There are conventional spinning techniques to produce fibers starting from polymeric solutions such as wet spinning, dry spinning, melt spinning, gel spinning. All these techniques are capable to produce fibers with a distribution of diameters less than a micrometer. The spinning technique is a specialized form of extrusion that uses a spinneret to form multiple continuous polymeric fibers [91]. All these techniques are based on the use of the spinneret, which may have from one to several hundred holes. The tiny openings are very sensitive to impurities and corrosion, and so the liquid feeding them must be carefully filtered (not an easy task with very viscous materials) and, in some cases, the spinneret itself must be made of very expensive, corrosion-resistant metals. The maintenance is also a critical task because the spinnerets must be removed and cleaned on a regular basis in order to prevent clogging. As the filaments emerge from the holes in the spinneret, the liquid polymer is converted firstly into a rubbery state and then solidified. This process of extrusion and solidification of endless filaments is called spinning.

- **Wet spinning**

This process is used for polymers that require to be dissolved in a solvent to be spun. It is called wet spinning because the fibers are extruded directly into a liquid bath, based on a non-solvent liquid for the polymeric solution, where the spinneret is submerged. The presence of the spinneret in the liquid bath permits to obtain the precipitation of the fibers, which are successively dried in air. One of the fundamentals parameters is the rate at which this technique occurs; indeed, if it occurs too quickly, the bath liquid can create micro-voids into the fiber, which will be the weak points of the spun material. Figure 13 represents an example of wet spinning model [92].

The fiber spun using this technique is obtained starting from a polymeric solution based on Acrylic, rayon, aramid, monoacrylic, and spandex.

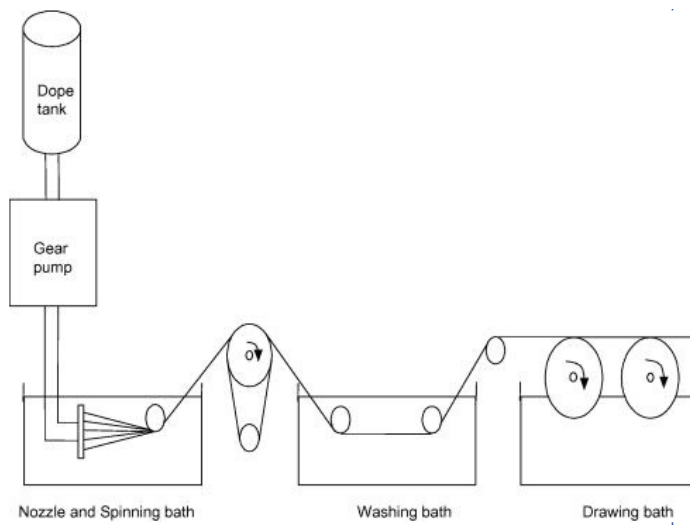


Figure 13 Model of wet spinning technique [92].

- **Dry spinning:**

This extrusion technique is used when the polymer must be dissolved in a solvent. The fibers are extruded and emerge through the spinneret in the evaporation chamber, as represented in Figure 14. In the evaporation chamber, the solvent evaporates off with hot air, such as steam of air or inert gas. In some cases, the solvent can be re used in future. The dry spinning is also required for polymers with a melting temperature lower or close to their thermal degradation temperature [93]. Acetate, triacetate, acrylic, modacrylic, polybenzimidazole fiber, spandex, and vinyon are examples of materials produced through this process.

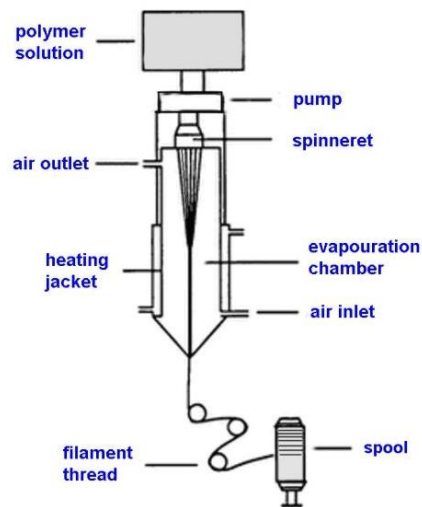


Figure 14 the setup of dry spinning [93]

- **Melt spinning**

This spinning technique is used for polymers that can be melted. The polymer granules are melted and then the melting liquid, whose feed is controlled by a pump, has been extruded through the spin head with a controlled pump. During this phase of the process, the liquid must also be filtered because of all the not melted parts could induce the formation of weak points in the fibers. After the extrusion the polymer solidifies by cooling thanks to the quench air. Figure 15 shows a schematic representation of this technique [94]. Nylon, olefin, polyester, saran, and sulfar are materials produced via this process.

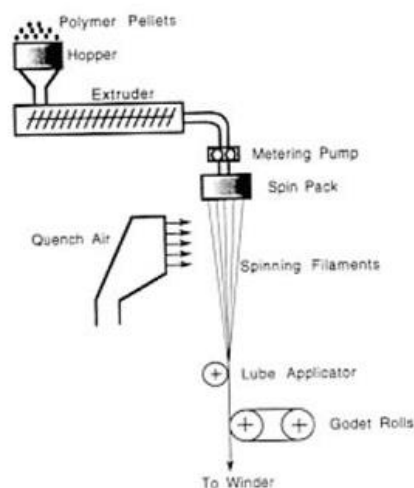


Figure 15 represents a scheme of melt spinning technique [94]

The electrospinning, instead, is the unique technique capable to produce fibers with diameters down to the nanometer range.

Nanofibers are the ultrafine solid fibers with the diameters in the range between few micrometers and 100 nanometers. Nanofibers present high value of length related to the small diameter. Indeed, the nanofibers show extraordinary properties, such as high surface area to the volume ratio, high surface area per unit mass and small pore size.

All these properties made the nanofibers suitable and appropriate for many different applications, such as in aerospace, capacitors, transistors, drug delivery systems, battery separators, energy storage, fuel cells, and information technology [95]. Moreover, low density, large surface area to mass, high pore volume, and tight pore size make the nanofiber nonwoven appropriate for a wide range of filtration applications [95].

2.2 History of the electrospinning

The term “Electrospinning” derives from electrostatic spinning.

Electrospinning roots from the earliest electrospray, used for painting in early nineteenth century. In the late 16th century, William Gilbert [96] set out to describe the behavior of magnetic and electrostatic phenomena. He observed that, when a suitably electrically charged piece of amber was brought near a droplet of water, it would form a cone shape; moreover, he also defined how the small droplets would be ejected from the tip of the cone. This is the first recorded observation of **electrospraying**.

In 1887 C. V. Boys described “the old, but little known experiment of electrical spinning”. Boys’ apparatus consisted of “a small dish, insulated and connected with an electrical machine” [97].

He found that, as his stock liquid reached the edge of the dish, the fibers could be drawn from a number of materials including shellac, beeswax, sealing-wax, gutta-percha and collodion. During 1934 and 1944 the early patent for electrospinning was submitted by Formhals [98].

Formhals designed an electrospinning setup able to produce polymer fibers, characterized by size and dimensions much larger than the today’s nanofibers. His contributions also included the production of fibers starting from polymer blend system and the alignment of these fibers in a

parallel structure. Since then, the electrospinning has seemed to be dormant until 1966 when a new apparatus was designed by Simons [99]. In his patent, he demonstrated the production feasibility of ultra-thin and light non-woven fabrics through electrospinning, moreover, he found that less viscous solutions could produce shorter and finer fibers, while, on the contrary, more viscous solutions could produce thicker and relatively continuous fibers.

Between 1964 and 1969, Sir Geoffrey Ingram Taylor drew up the theoretical bases of electrospinning [100, 101, 102], studying the shape of the initial charged droplet during the electrospinning process. Taylor's work defined, through a mathematic modeling, the shape of the cone formed by the fluid droplet under the effect of an electric field. The droplet of solution, under the action of the applied electric field, is deformed assuming a conical shape. This characteristic droplet shape is known nowadays as the Taylor cone. Taylor further worked with J. R. Melcher to develop the "leaky dielectric model" for conducting fluids. In his studies, he used as electrode the tip of the syringe needle, where the polymeric solution was loaded. In particular, he found that the solution droplet starts to become cone-shaped when the needle potential increases. The critical angle for the stable cone is equal to $\phi=49.3^\circ$, as represented in Figure 16. Beyond this angle, the jet will break due to the maximum instability of the fluid surface induced by the electrical field. The theory developed by Taylor also defined the concept of critical voltage. The critical voltage is the value of voltage applied between the tip of the needle and the counter-electrode, above which the charges repulsion forces overcome the viscoelastic forces.

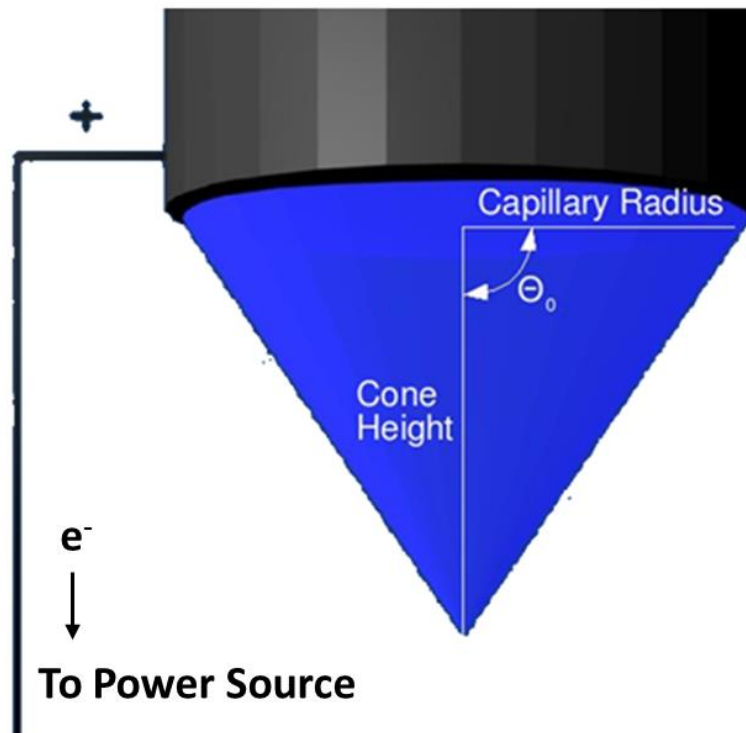


Figure 16 shows the definition of the angle of the Taylor's cone

The Taylor's theory was proved later by the production of sub-micron fibers by Baumgarten in 1971 [103]. When the voltage reaches its critical value, the relative viscous solution (1.7-215 Poise in his experiments) did not break into droplet but into a fluid stream. Baumgarten found, moreover, that the relation between the solution viscosity and the fiber diameter can be approximated as following Eq 27:

$$\phi = \sqrt{\varphi} \quad \text{Eq 27}$$

Where the ϕ and φ are respectively the diameters of nanofibers and the flow rate.

In the 1980's Larrondo and Manley [104] devised the first melt electrospinning setup. They studied the jet formation from polyethylene/paraffin solution and, more important, molten polyethylene. Their studies greatly extended the application of electrospinning. However, due to the lack of temperature control in the spinning region, they were able to produce only 50 μm fibers. Nevertheless, they demonstrated that the desired fiber diameter can be obtained controlling the temperature of the spinneret and the spinning voltage. Since 1995, there have been further

theoretical developments of the driving mechanisms of the electrospinning process; Reznik et al. described the shape of the Taylor cone and the subsequent ejection of a fluid jet [105].

Hohman et al. investigated the relative growth rates of the numerous proposed instabilities in an electrically forced jet once in flight [106]. In this work, the authors described the most important instability that occurs during the electrospinning process; this phenomenon was defined by them as the bending (whipping) instability.

Reneker and coworkers re-explored this processes providing a great contribute to the development of this field [107, 108, 109, 110, 111].

Numerous experiments and a number of theoretical works have been carried out to better understand the electrospinning process and to develop the technique in order to obtain nanofibers for more applications. This trend can be clearly sensed from the number of publications between 1995 and 2010 Figure 17.

Most of current studies deal with organic polymers or biopolymers. However, also inorganic filaments attracted a huge focus, due to some special applications in which some properties, such as high values of temperature and mechanical strength, were required. Some of them are quite interesting, for example, carbon nanotubes on carbon fibers and Vanadium Oxide whiskers on Titanium oxide fibers [112, 113].

The composite polymeric fibers, which are based on the modification of polymeric nanofibers by strengthening agents, such as carbon nanotubes, silica nanoclays and graphite, are also hot topics in the field of electrospinning [114, 115].

Finally, the coaxial electrospinning is another branch of electrospinning, which can produce fibers with multiple layers [116, 117] or hollow fibers [118].

The current research on electrospinning can be categorized into five categories:

- electrospinning of different materials;
- functionalization of as-spun fibers;
- various applications of electrospun fibers;
- structural studies of electrospun fibers;
- simulation of the electrospinning process.

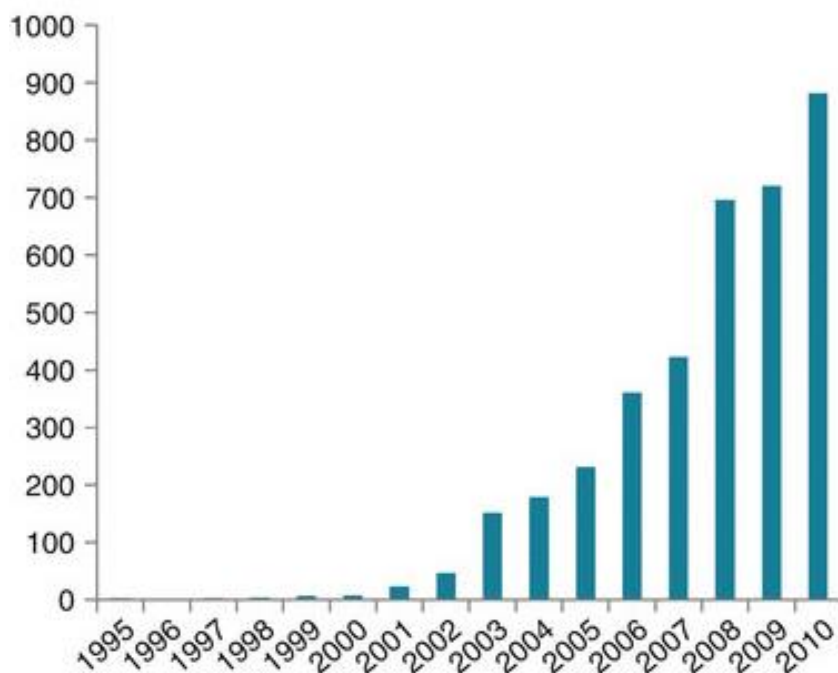


Figure 17 number of publications on electrospinning (1995-2010) source Research Gate

2.3 Electrospinning process

The Electrospinning process constitutes the unique technique for the production of nanofibers with diameters in the range between few nanometers and some microns.

The process is based on a self-assembly process driven by the Columbic interaction between charged elements of the polymeric fluids, allowing the formation of nanofibers; this process is in strong contrast to conventional fibers producing techniques. The transition from a microscopic fluid element, such as the droplet formed at the beginning of the process, to a solid nanofiber is ensured by a series of jet instability. All the jet instabilities give rise to an extremely high extensional deformation and, at the same time, they induce the strain rates during fiber formation; all these physical aspects enhance, among other effect, a high orientation order in the nanofibers, improving the mechanical properties.

Electrospinning process is applied predominantly to polymer-based material including both natural and synthetic polymers; however, it is also possible to obtain metallic, ceramic and carbon

nanofibers starting from an electrospun polymeric solution by means of successive treatment, such as calcination, pyrolysis and so on.

The schematic setup of electrospinning is based on three major components [119], as represented in Figure 18:

- a) an high-voltage power supply
- b) a spinneret, which constitutes one of the two electrodes supporting the metallic needle
- c) a collector, also defined grounded counter electrode, which is the second electrode. The nanofibers are collected on this component or on a specific substrate, selected according to the applications. If the counter electrode is planar, the nanofibers are randomly deposited on it, with no preferred fiber direction in the plane. Consequently, with a planar counter electrode the deposition generates a no woven mat of nanofibers. Usually, the diameters distributions are not homogeneous during the process also if the values of all spinning parameters remain constant [120].

Other types of counter electrodes can be used, such as tips, rotating cylinders or discs, counter electrodes composed of two parallel bars, cross gratings composed of conductive wires and many more [120, 121]. In each specific case, a particular typology of fiber deposition was achieved. It is possible theoretically to predict the correlation between the different types of counter electrodes and the voltage applied. This aspect will be discussed in the following paragraph.

The voltage is applied directly between the two electrodes. Indirectly it is also possible to define the electric field intensity as the ratio between the voltage and the distance between the two electrodes: the tip of the needle and the grounded collector. This distance is usually defined as gap distance or working distance.

The spinneret is connected to a syringe in which polymer solution (or melt solutions) is loaded. With a syringe pump, the solution flows from the spinneret with a controlled and constant rate, which is known as flow rate. When a high voltage (typically from 1 to 30 kV) is applied, the drop at the tip of the needle will become highly electrified and the charges are distributed uniformly on its surface. The mutual charge repulsion causes a force directly opposite to the surface tension. As the intensity

of the electric field increases, the hemispherical surface of the solution at the tip of the capillary tube elongates to form a conical shape, known as the Taylor cone.

When the electric field reaches the critical value, the repulsive electric force overcomes the surface tension and a charged jet of the solution is ejected from the tip of the Taylor cone. As the jet travels in air, the solvent evaporates, leaving behind a charged polymer fiber, which deposits randomly on the counter electrode, as represented in Figure 18. Thus, it is quite important to define the correct value of working distance in order to ensure the complete evaporation of the solvent, and consequently to obtain the deposition of the dried nonwoven mat of nanofibers.

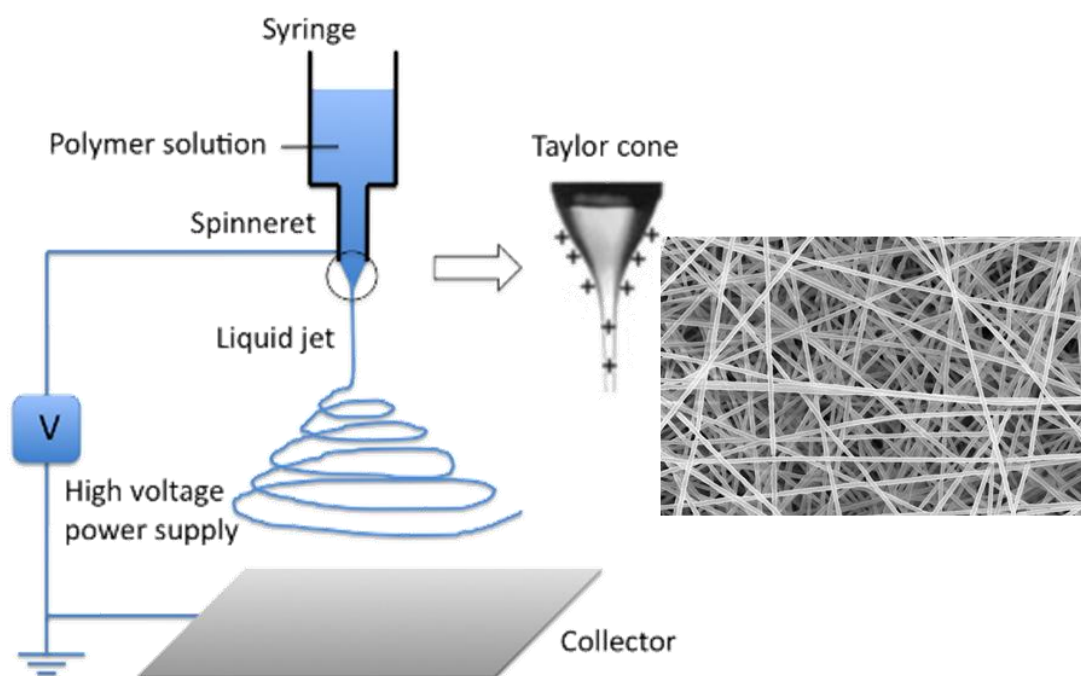


Figure 18 represents the electrospinning setup (sources www.intechopen.com) and an example of Field Electronic Scanning Microscopy (FESEM) of no woven mat of nanofibers, obtained in our laboratory. In particular, the nanofibers are obtained starting from an electrospun solution of Polyethylene oxide (PEO) and Deionized water.

The electrified jet then undergoes a stretching and whipping process, leading to the formation of a long and thin thread. The liquid jets are continuously elongated and the solvent evaporates. For this

reasons, the nanofibers' diameters can be greatly reduced from hundreds of micrometers to as small as tens on nanometers. These concepts will be deeply explained in the following paragraphs.

2.4 Physical phenomena that control the deposition of nanofibers

The fiber formation during electrospinning process is controlled by different physical phenomena, as described below [122, 123, 112, 119, 124, 125].

The different phenomena can be defined in the following way:

- Droplet formation at the tip of the needle, onset of jetting;
- Development of rectilinear jet;
- Onset of bending deformations with looping, spiraling trajectories;
- Deposition on the counter electrode.

Rayleigh deeply investigates and describes the electrical driven axisymmetric instability that influences the shape of the jet, resulting into nanofibers formation. The instabilities will be further described below. The simplest electrospinning setup, introduced above, is considered to theoretically model the fiber formation.

Finally, a polymer solution is pumped through the tip of the needle at the beginning of the electrospinning process.

The fiber formation during electrospinning process is controlled by different physical phenomena, as described below [122, 123, 112, 119, 124, 125].

The different phenomena can be defined in the following way:

- Droplet formation at the tip of the needle, onset of jetting;
- Development of rectilinear jet;
- Onset of bending deformations with looping, spiraling trajectories;
- Deposition on the counter electrode.

2.4.1 Droplet formation at the tip of needle

Before the formation of electrified jet, the first step consists in the formation of a droplet at the tip of the needle, where the polymeric solution is pumped. Without any applied electric field, the drop equilibrium presents a spherical shape; in particular, it is suspended by surface tension and by viscoelastic stresses at an orifice in the form of a hole, smaller than the base of the droplet, in the bowl of a small aluminum spoon.

An electrical potential difference is then applied between the fluid and a flat electrically conducting plate, which is the counter electrode; subsequently the droplet becomes electrically charged. The interaction of the charged droplet with the external electric field induces the deformation of the droplet itself, which assumes a deformed shape. This deformed shape corresponds to an equilibrium state, based on the balance between the electrical forces and the surface tension.

In the electrospinning process the gravity effects are usually neglected thanks to the very small process time, which is in the range of few nanoseconds. With the increment of electric field, the shape of the droplet changes becoming progressively longer, while the repulsion forces, among the charges, increase as well. As explained before, the average electric field in the absence of a jet is defined as the ratio between the electrical potential difference applied and the working distance. The working distance is defined as perpendicular to the plate.

A critical voltage value is reached when the repulsion forces intensity results equal to the surface tension. Indeed, closes to the critical value of applied voltage, the droplet assumes the shape of the Taylor Cone, with a characteristic half vertex angle of $49,3^\circ$ at the tip of the droplet. Some experimental observations define the values of this angle in the range of 30° - 38° [95].

Finally, when the electric field overcomes the critical value of voltage, and consequently when the charged repulsion forces overcome the surface tensions, the electrified jet is formed from the tip of the Taylor cone. The initial diameter of the jet is a parameter in mathematical models but the experimental measurement is clearly difficult, because the diameter may vary rapidly near the beginning, labeled as 2 ns. Figure 19 represents the different phases of the formation of polymeric jet, starting from the statement of the droplet. All images were acquired by using video recording every 2 ms.

In conclusion, below a critical electrical field, the droplet acquires a steady state shape with no jet. On contrary, above the critical electrical field, a jet initiates and the entire droplet is pulled off the surface in a very short time.

Taylor showed that the critical voltage V_c (expressed in kilovolts), above which, the maximum jet fluid instability develops, is given by Eq 28 [95]:

$$V_c^2 = 4 \frac{H^2}{L^2} \left(\ln \frac{2L}{R} - 1,5 \right) (0,117\pi R\gamma) \quad \text{Eq 28}$$

where

- H is the distance between the electrodes (the capillary tip and the collecting screen), defined also working distance;
- L is the length of the capillary tube, which connects the syringe with the polymeric solution and the needle;
- R is the radius of the tube
- γ is surface tension of the fluid.

Usually in spinning, the flow, beyond the spinneret, is mainly elongated.

While on the contrary, when the process conditions and the solution's properties are not sufficient to ensure the formation of polymeric charge jet, the minimum spraying potential of a suspended hemispherical conducting drop in air can be calculated through the Eq 29:

$$V = 300\sqrt{20\pi r\gamma} \quad \text{Eq 29}$$

where r is the jet radius.

If the surrounding medium is not the air but a nonconductive liquid immiscible with the spinning fluid, the drop distortion will be greater at any given electric field and, therefore, the minimum spinning voltage will be reduced. This means that if the electrospinning process is encapsulated in vacuum, the required voltage will be lower.

It is also possible to observe two different features. The first one is related to the flow pattern around the jet in the cone region, the presence of tangential electrical shear stresses induces a circulation of the fluid, generating a strong flow that takes place toward the apex of the surface of

the cone. The second feature is represented by the fact that the shape of the cone becomes strongly modified at elevated values of electrical field.

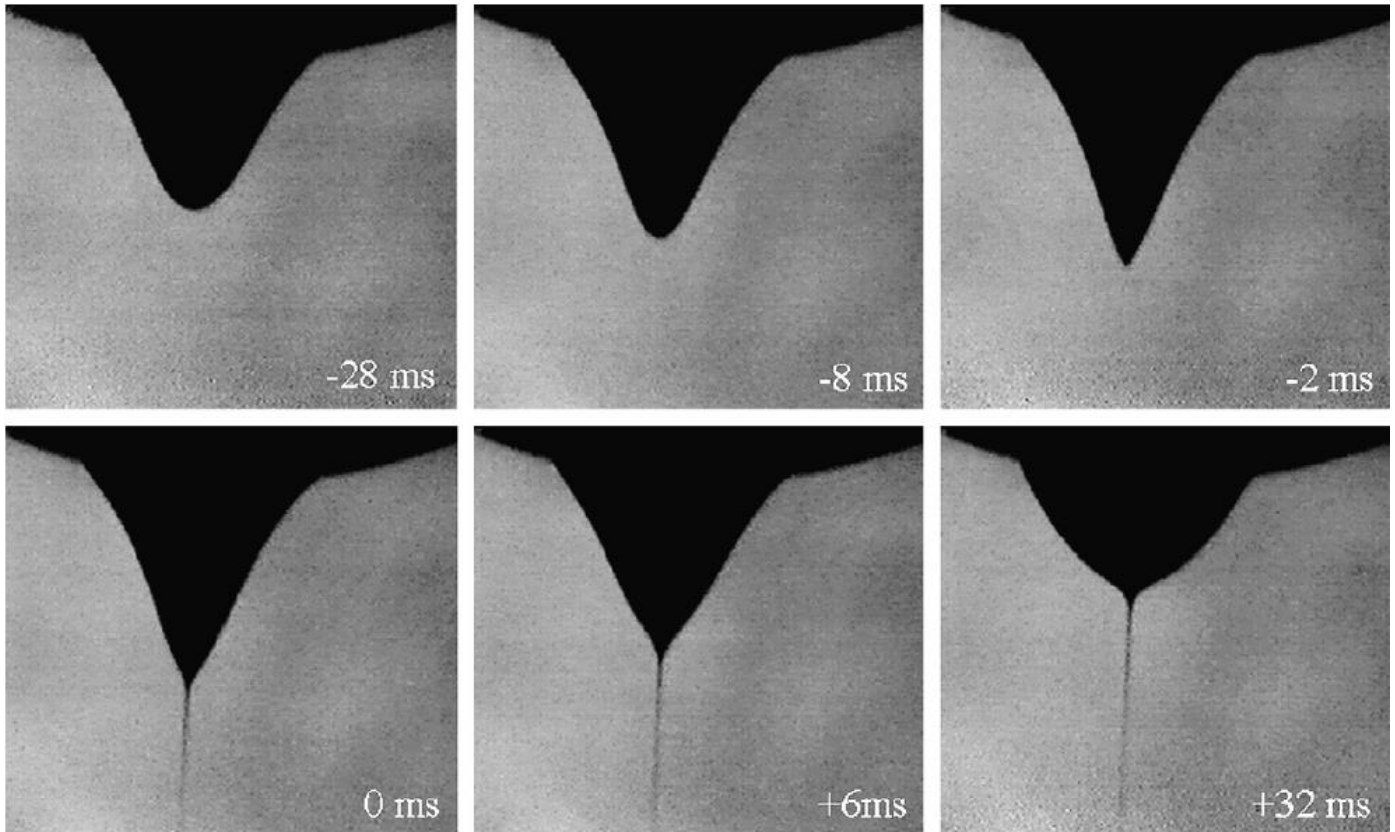


Figure 19 deformation of the droplet according to the variation of electric field, until the formation of the Taylor' cone and then the formation of polymeric jet [126]

One of the mainly reasons, which cause a difference between the experimental observations done and the Taylor prediction, is related to the accepted assumptions related to the definition of the droplet's shape. Moreover, the electric field and the shape of the droplet depend on each other simultaneously.

As explained before, there is a direct correlation between the shape of the droplet and the electric field. For this calculation, Taylor defined the shape of the droplet as a spheroid. The prolate results from the rotation of an ellipsoid around his major axis.

Yarin et al. [127] represented the shape of the droplet, which is induced by the electric field, as a hyperboloid of revolution. This description may assume a cone-like shape at high field strength with

a vertex cone angle close to those observed experimentally. These geometric objects can be represented by general formulae, as defined by Eq 30:

$$x^2 + y^2/a^2 + z^2/b^2 = 0$$

b > a for a spheroid with a prolate geometry and

$$x^2 + y^2/a^2 - z^2/b^2 = 0$$

for a hyperboloid of revolution

Eq 30

Figure 20 represents the curve connecting the points B, C, and D, which describes the surface of the droplet at the end of the tip of the needle, in polar coordinates (z, ρ). The distance between the tip of the droplet and the flat equipotential surface at z=0 is defined as a₀. It is important to underline that z=0 is the position of the matching boundary and not the position of the counter electrode, which is of the order of several cm distant from the tip of the droplet. The magnitude of a₀ indicates the distance over what the tip of the cone extends. The magnitude of a₀ is of the order of 1000 nm.

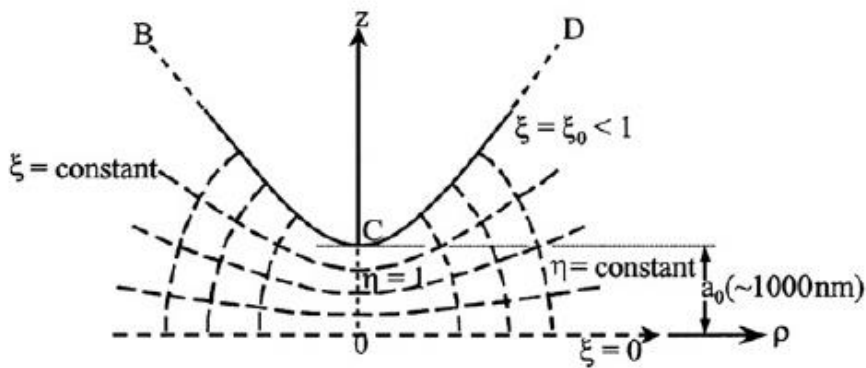


Figure 20 Hyperbolic coordinates used to describe the electric field and the equipotential lines near the tip of a fluid cone an instant before its instability and a jet issued from the tip [127, 128].

The dimension labeled a₀, which is 1 mm, shows the scale of this drawing. The shape of the tip is a hyperboloid of revolution traced by the line BCD.

The enhancements of the electric field, which occur on the radius of curvature of the tip of the cone, are dramatically important in the transformation of the tip of the fluid cone into a flowing jet.

The surface of the hyperboloid described by the line BCD can be defined in terms of cylindrical coordinates by Eq 31:

$$z^2/a_0^2 - \rho^2/b_0^2 = 1 \quad \text{Eq 31}$$

To analyze the hyperboloid geometries, it is necessary to introduce the prolate spherical coordinates (μ, ν, ϕ) , according to the Eq 32

$$\begin{cases} x = a \sin(h) \mu \sin(\nu) \cos(\phi) \\ y = a \sin(h) \mu \sin(\nu) \sin(\phi) \\ z = a \cos(h) \mu \cos(\nu) \end{cases} \quad \text{Eq 32}$$

Where μ is a not negative real number, ν is in the interval $[0, \pi]$ and ϕ is the azimuthal angle in the interval $[0, 2\pi]$. Another set of prolate spheroidal coordinates (η, ξ, ϕ) is used and it is represented by Eq 33

$$\begin{cases} \eta = \cos(h) \\ \mu = \xi = \cos(\nu) \end{cases} \quad \text{Eq 33}$$

In this case, the curves with a constant η are prolate spheroids, whereas the curves with a constant ξ are hyperboloids of revolution. The lines with a constant ξ represent both the surface of hyperboloid droplet (ξ_0) as well as the lines of constant potentials in the range between $z=0$ and $z=a_0$.

It is also necessary to define a mathematical approach to describe the balance between the electric field and surface forces. It is assumed that the space-charged effects can be neglected. Thus the electric potential of the surface of the droplet satisfy the Laplace Equation (Eq 34)

$$\Delta\Phi = 0 \quad \text{Eq 34}$$

The first step involves the representation of the Laplace equation in the coordinate system chosen, as defined by Eq 35:

$$\frac{\partial}{\partial \xi} \left((1 - \xi^2) \frac{\partial \Phi}{\partial \xi} \right) + \frac{\partial}{\partial \eta} \left((\eta^2 - 1) \frac{\partial \Phi}{\partial \eta} \right) = 0 \quad \text{Eq 35}$$

Selecting for the potential defined by Eq 36 [105, 95]

$$\phi_0 = \varphi_0 + const \quad \text{Eq 36}$$

At the surface of the hyperboloid that is for $\xi = \xi_0$, and introducing appropriate boundary conditions and approximations, it is possible to obtain the solution represented by the Eq 37

$$\phi = \varphi_0 \ln[(1 + \xi)/(1 - \xi)] / \ln[(1 + \xi_0)/(1 - \xi_0)] \quad \text{Eq 37}$$

Based on this equation, it is possible to derive the normal stress acting on the hyperboloid droplet surface generated by the electrical potential, through the Eq 38

$$\sigma_{nn} = 1/8 \pi (\partial\phi/\partial n)^2 \text{ for } \xi = \xi_0 \quad \text{Eq 38}$$

Which yields, at $\xi = \xi_0$, the Eq 39:

$$\sigma_{nn}(\xi = \xi_0) = \frac{\varphi^2}{2\pi \ln^2 \left[\frac{1 + \xi_0}{1 - \xi_0} \right]} * \frac{1}{\left[\left(\frac{z^2}{\xi_0^2 - a_0^2} \right) (1 - \xi_0^2) \right]} \quad \text{Eq 39}$$

When $z=a_0$, close to the tip of the cone shaped geometry, the maximal stress is obtained.

The stress originated by the electrical potential is smaller further away from the tip. It is also possible to define the characteristic relation for the balance between the electrical forces and the surface tensions trough the Eq 40:

$$\sigma K_{at z=a_0) - \Delta p = \sigma_{nn at z=a_0)} \quad \text{Eq 40}$$

Where Δp is the pressure difference between inside and outside of the droplet and K is the curvature derived from the hyperboloid shape.

Assuming that the pressure difference is constant among all the locations of the hyperboloid surface, and substituting the obtained results for the surface and electric forces in the Eq 38, it is possible to obtain a general equation for infinite hyperboloids. The obtained Eq 41 relates the surface potential of a stable charged droplet in equilibrium to the surface tension all along the surface of the droplet.

$$\varphi_0 = (\sigma a_0)^{1/2} (4\pi)^{1/2} \ln[(1 + \xi_0)/(1 - \xi_0)] (1 - \xi_0^2)^{1/2} \quad \text{Eq 41}$$

This expression permits to define a correlation between the shape parameters ξ_0 and the electrical potential. The analysis predicts that the maximum potential, able to guarantee a stationary shape, corresponds to $\xi_0=0.834$; this value of ξ_0 corresponds to the critical hyperboloid. An envelope cone for this particular hyperboloid is characterized by a half angle of 33,5°.

All the described phenomena are valid for viscous and viscoelastic fluid, as polymeric solution needed for electrospinning process.

2.4.2 Development of rectilinear jet and onset of bending instabilities

As discussed before, when the repulsion charged forces overcome the electrical ones a straight jet, originated from the tip of the droplet, is generated. The electrified jet follows a straight path directed towards the counter electrode until the formation of instabilities of the jet, which are analyzed below. When the formation of instability occurs, the jet starts to originate a series of coils and lateral movements.

At the beginning of the electrospinning process, the electrostatic forces accelerate the polymeric jet away from the tip of the needle to the grounded counter electrode. This phenomenon induces the generation only of the longitudinal stress along the axis of the jet, which is able to stabilize the jet and ensure the formation of linear path. The principal parameter, which controls the straight path of the jet, is the longitudinal force applied on the fluid.

Indeed, it is possible to demonstrate that the electrified jet is stretched along its axis by the external electric field applied and by the Coulomb repulsions among all the equally charged segments of the jet [106, 129, 130]. At a certain distance from the tip of the needle, which is strongly depending on the intensity of applied voltage (or on the strength of the electric field), the jet starts to undergo a stress relaxation effect. When the stress relaxation occurs, the electrostatic interactions among the charges distributed in the polymeric originated jet become predominant inducing then chaotic motions of the jet towards the counter electrode. The viscoelastic stresses, moreover, neutralize the effect of stretching, induced by the electrostatic forces. It is possible to describe the jet as a distribution of charges connected by a viscous medium, whose one extremity is fixed at the point of the origin, while the other is free. The free end of the jet can be characterized by the deviation from the linear path of the jet, generated by the bending instabilities. All the interactions, not completely known, between the external electric field, the surface tension and the Columbic repulsions through the charges within the jet, induce the instabilities. The charge transport in the liquid jet is induced after the electric field application; moreover, the consequently interactions, among the charges and the external applied electric field, cause the formation of circular loops in the jet, which lead to the instauration of instabilities. The electrostatic forces, defined between paths of polymeric jet with the same charges' distributions, induce the instauration of the radial charge repulsion forces.

These repulsion forces, in particular, involve the splitting of the primary jet into multiple sub-jets, known as **Bending (whipping) instabilities** [131]; these types of instability can be repeated in self-similar way on a smaller and smaller scale, with the decreasing of the diameters of the jet. Thus, the bending instabilities induce the reduction of fiber diameter from micrometer to nanometer. These concepts are clearly represented in Figure 21, taken from the literature [128]. The key role in reducing the jet diameter from a micrometer to a nanometer is played by a whipping instability, which causes the bending and the stretching of the jet. Regarding the fluid jet diameters, the definition is represented by the following Eq 42:

$$r_0^3 = \frac{4\varepsilon\dot{m}_0}{k\pi\sigma\rho} \quad \text{Eq 42}$$

where ε is the permittivity of the fluid (C/V*cm), \dot{m}_0 is the mass flow rate (g/s) when r_0 (cm) is calculated, κ is a dimensionless parameter related with the electric currents, σ is electric conductivity (A/V*cm), and ρ is the density (g/cm³) of the electrospun material.

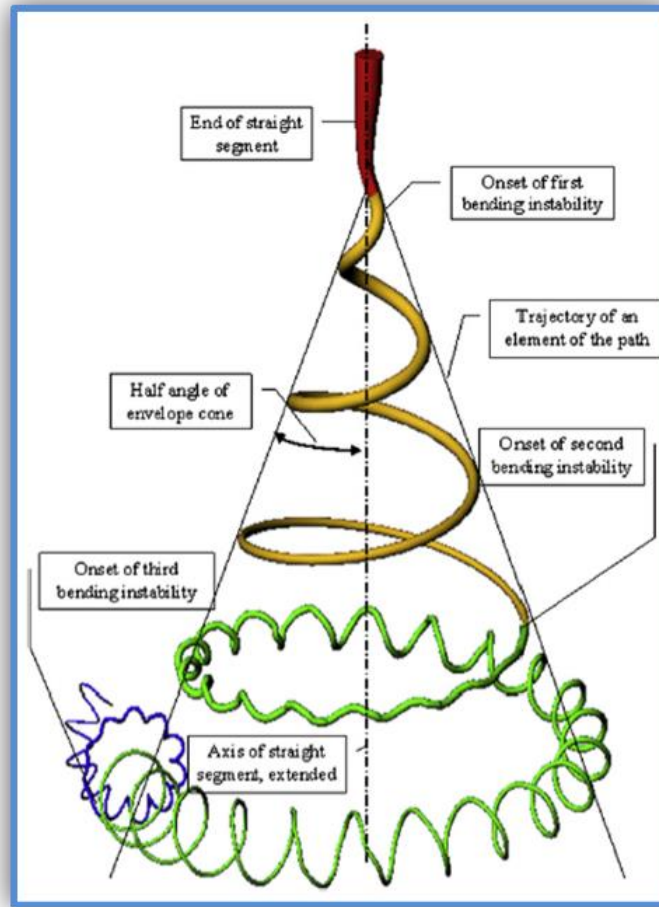


Figure 21 The looping part of the jet. This figure represents the bending instabilities of the jet [128]

Yarin and Reneker [131] designed a viscoelastic dumbbell model, as represented in Figure 22.

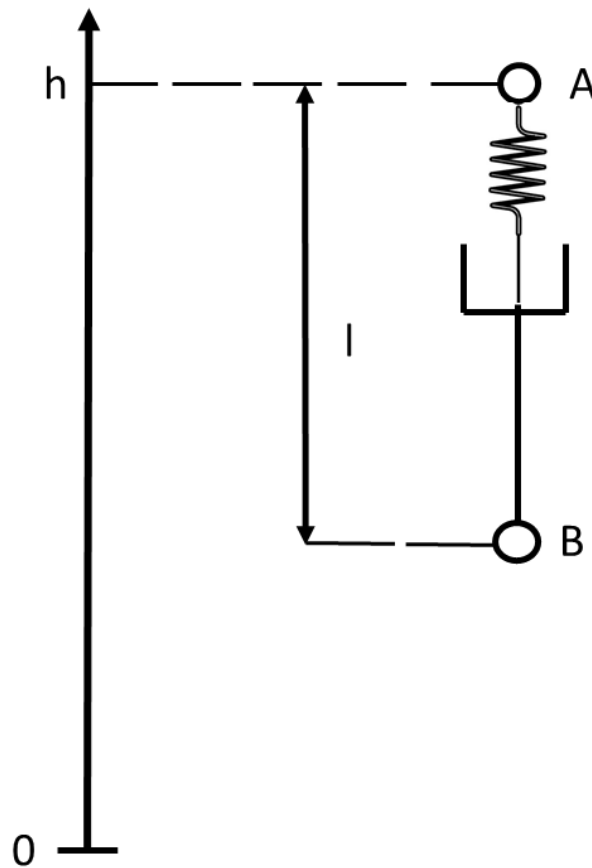


Figure 22 viscoelastic dumbbell representation used to explain from a theoretic point of view the viscous and elastic contributions on the electrified jet

The viscoelastic dumbbell was implemented in order to define the length of the linear path of the jet, to correlate the linear path itself with the external electric field and, finally, to investigate the onset of instabilities. The viscoelastic model, according to the Maxwellian fluid theory, shall be represented as the serial connection of a spring (elastic modulus G (GPa)) and of the viscous component a dumper (viscosity μ (Pa*s)). According to the Maxwellian model the total deformation is due to the deformation of the elastic modulus and to the viscous response, as described by Eq 43:

$$d\sigma/dt = G dl/dt - \sigma G/\mu \quad \text{Eq 43}$$

In particular, the second term describes the viscous deformation of the fluid, which is opposite to the elastic one, and it is function of the viscoelastic relaxation time $\tau = \mu/G$.

The Eq 44 defines the forces inducted in the linear path:

$$\left\{ \begin{array}{l} -\frac{eU_0}{h} \\ e^2 \\ -\frac{1}{l^2} \end{array} \right. \quad \text{Eq 44}$$

Where the first equation in the system is related to the external electric field and h is the distance between the tip of the needle and the counter electrode; while the second one is related to the coulombic repulsion forces that are present through all the equally charged segment of the jet.

The total momentum balance acting on the droplet B, including the viscous stress σ (Pa) applied on the surface area πa^2 of the droplet B, is defined by Eq 45:

$$m \frac{dv}{dt} = -\frac{e^2}{l^2} - \frac{eU_0}{h} + \pi a^2 \sigma \quad \text{Eq 45}$$

To explain the onset of the beginning instabilities, Reneker et al. considered three elements with equal charges, two positive charges are distributed on the axis of the jet, while the third one is placed perpendicularly to the axis of the polymeric jet [131, 132], as represented in Figure 23.

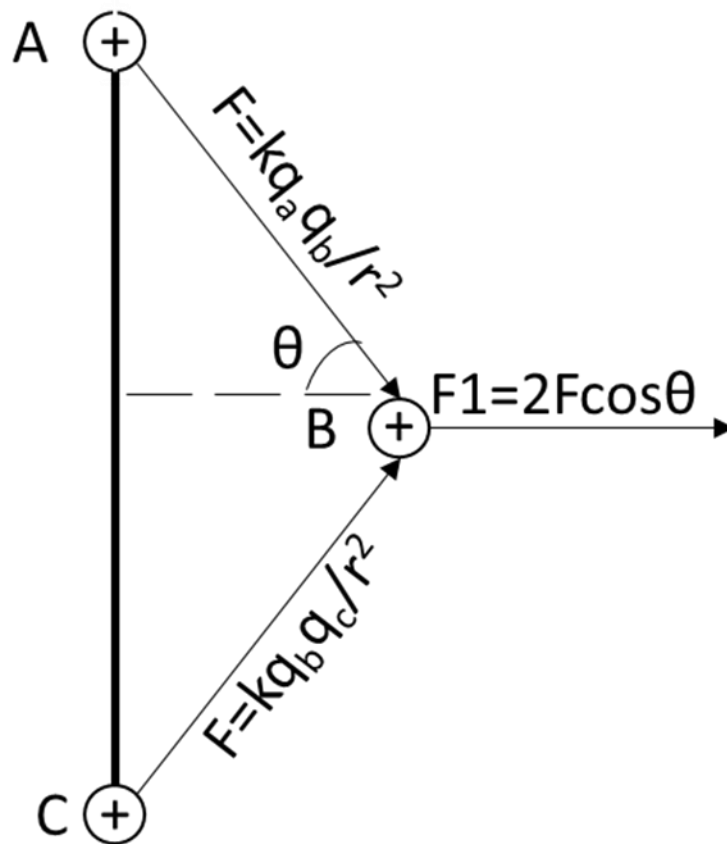


Figure 23 electrostatic forces applied by two charges elements to a neighboring third charge element [131, 132].

The charges A and C generate a couple forces with equal magnitude and opposite direction acting on the third charge B. The magnitude of the force is defined by the Eq 46:

$$F = k * (q_a * q_b) / r^2 = k * (q_b * q_c) / r^2 \quad \text{Eq 46}$$

Where q_a , q_b and q_c are the values of the three charges, r is the distance between the charges A and C respect to the charge B and k is the Coulombic constant.

As a consequence of the two electrostatic forces F , the resultant force $F_1 = 2F \cos \theta$ induces a lateral movement of the charged point B.

The resultant force F_1 induces an instability predicted by the Earnshaw's theorem. The Earnshaw's theorem states that: a collection of point charges cannot be maintained in a stable stationary equilibrium configuration only by the electrostatic forces between the charges [133, 134].

The resultant force F_1 can be considered as one of the principal causes of instabilities of the jet, also according to the Earnshaw's theorem.

The description made by Reneker suggests how the instability shall be reduced if the distribution of electric field, applied between the electrodes, can be controlled. Moreover, in this way the deposition of the nanofibers on the counter electrode could be managed.

The most important result of the theoretical analysis of the linear path and of the onset of bending instabilities, are that:

- The viscoelastic stresses decrease according with the time as the jet becomes deformed. The jet becomes deformed when the radial electrically repulsion forces induce the formation of secondary jets from the primary one.
- The length of the linear path increases linearly with the augment of applied voltage. In particular, the linear jet is stable for high values of forces and stress. When the longitudinal forces and stresses reach a maximum value, and after they decrease strongly, the jet become so small that instabilities, in particular whipping ones, become dominant.

Finally, one example of whipping instability was investigated in some works in the literature. This instability was defined as **branching effect** [135, 128]. Depending on the chosen electrospinning parameters and on the charges distributions into the polymeric jet, the occurrence of jet branching happens. The branching jet is characterized either by isolated or by regular arrangements of the branches that extend perpendicularly to the main jet. In particular, the secondary jet is generated from the principal one along an axis perpendicular to the one of the main jet. Moreover, the average diameters of the secondary jet are smaller than the ones of the primary jet.

Normally, the branching effect is a direct consequence of the interaction among the charges distributed into the polymeric jet and the applied electric field. This interaction induces the static undulations on the surface of a charged jet. These kind of undulations are not stable when an electric field is applied, leading to the increasing of their curvature radius, near the highest peaks of these static undulations. In this way, starting from the undulations of the polymeric jet, the branches were obtained.

2.4.3 Deposition on counter electrode

The deposition of the dried nanofibers on the counter electrode represents the final step of the electrospinning technique.

As explained previously, the elongation and thinning of the fiber occurs in the linear pathway and in the looped one, at the same time with the evaporation of the solvent. All these factors induce the reduction of the diameter of the jet, allowing the nanofibers deposition that is characterized by a diameter distribution significantly thinner than the initial jet. The time needed to obtain the first deposition of solid nanofibers on the counter electrode after the elongation phase of the droplet, the linear path of the jet, the instauration of whipping instabilities and the die trough the tip of the needle and the collector, is estimated of about 10^{-1} s.

During the electrospinning process, the polymeric chain tends to become more oriented inside the jet, which is confirmed by formation of crystal morphology [136].

Moreover, during the initial phase of linear path of the jet, the mechanical deformation applied on the polymeric jet, can be reflected in the stiffness and strain of nanofibers. In general, solid fibers are deposited on the collector with a time less than a second, which is enough to guarantee the complete evaporation of the volatile solvent (for example Deionized water). When the polymeric materials present a glass transition temperature close to or lower than the room temperature, soft fibers are deposited and the coalescence effects are introduced. The coalescence effects are given by the not complete evaporation of the solvent during the die of nanofibers, by the intersection among the nanofibers or when the nanofibers close in contact. The coalescence process induces the presence of the junction points between the nanofibers of the mat. The junction points show different geometrical characteristics, depending on the diameter of the nanofibers in contact one with each other and on the contact angle itself [137].

The counter electrode is a conductive electrode, which is connected to the ground potential in order to maintain stable the potential difference between the tip of the needle and the collector.

Many works in the literature investigate the relation between the architecture counter electrodes and the morphological and physical properties of the nanofibers. Different types of collectors are

used such as: plane plate collector, rotating drum collector, rotating wheel with edge, multifilament thread, parallel bars, simple mesh collector [112].

Usually, the same substrate is used as collector of the nanofibers among all the experiment, operating in the same condition of the counter electrode.

- **Plane plate collector**

A plane plate collector is usually covered by an aluminum foil during the tests. The plate collector induces the formation of a no woven mat of nanofibers, obtaining a layer-by-layer deposition on the planar arrangements.

The electrospinning technique is not limited to the only random distribution of nanofibers on a planar counter electrode. In particular, in order to obtain a specific alignment among the nanofibers, the use of different type of counter electrode is required.

- **Drum rotating collector:**

Parallel nanofibers can be organized using the rapid rotating cylindrical collectors, as represented in Figure 24. The collector, usually, has a cylinder shape, which rotates at very high speed up to thousands rpm (round per minute). Clearly, the linear tangential velocity of each surface point is directly proportional with angular velocity and the radius of the cylinder. When tangential velocity is enough to guarantee the full evaporation of the solvent of the jet, the fibers deposited on the collector surface assume a circular shape. In this case, the rotating velocity of the counter electrode is defined as an alignment speed. On the contrary, if the tangential velocity is lower than the one that guarantee the jet deposition, the distributions of the nanofibers on the collector tend to be randomly generated. Finally, if the tangential speed is too high, the continuous fibers cannot be collected since the over fast take-up speed will break the fiber jet. In conclusion, it is quite difficult to obtain a proper alignment of the nanofibers due to the only motions of the jet during the die towards the counter electrode.

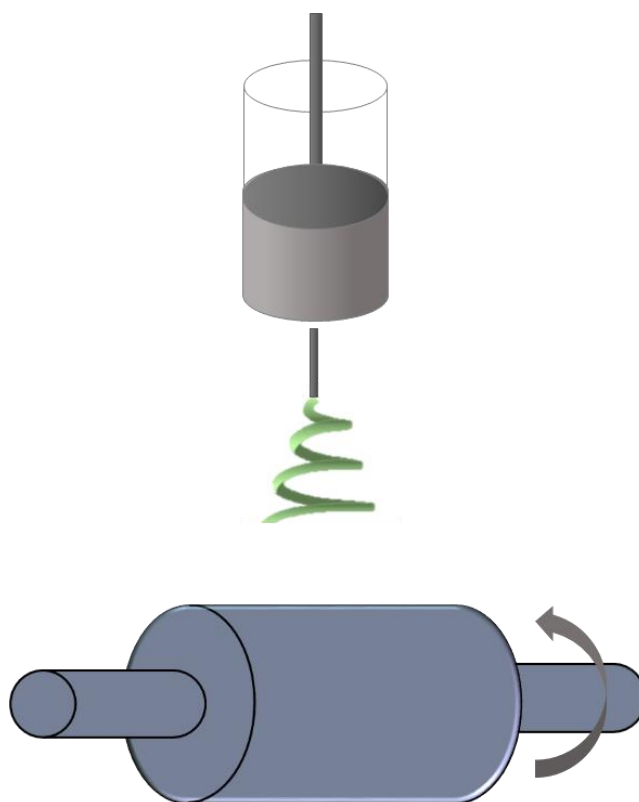


Figure 24 a schematic representation of electrospinning setup with a rotating drum collector

An example of aligned nanofibers with the above-mentioned method is represented in Figure 25, which shows the mats of nanofibers were obtained by researches of Virginia Commonwealth University. Figure 25, in particular, represents the alignment of nanofibers obtained starting from a polymeric solutions of poly(glycolic acid) (PGA) and Type I collagen with a rotating speed of drum collector of 1000 rpm and 4500 rpm respectively [138, 139].

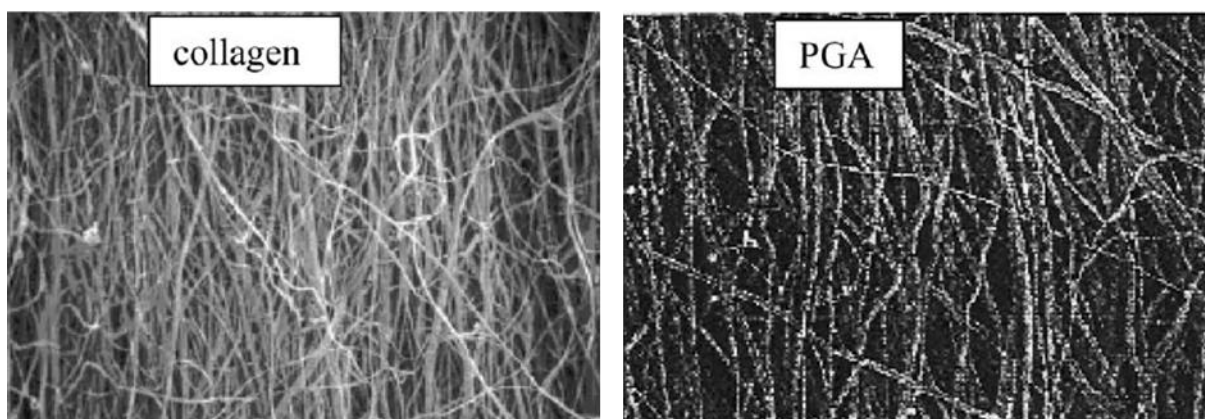


Figure 25 represents an example of aligned collagen and PGA electrospun nanofibers

- **Rotating disk collector**

It is a variation of the drum collector and it is used to obtain uniaxial aligned nanofibers.

The rotating disk collector is a setup variation of the rotating drum collector and is used to obtain uniaxial aligned fibers. The rotating disk is thinner than the drum collector and, consequently, the nanofibers tends to be deposited on its edge. For this reason, the nanofibers result to be more aligned than the ones obtained on the drum collector [112, 140, 141, 142]. The nanofibers intercept the edge of rotating disk, as represented in Figure 26

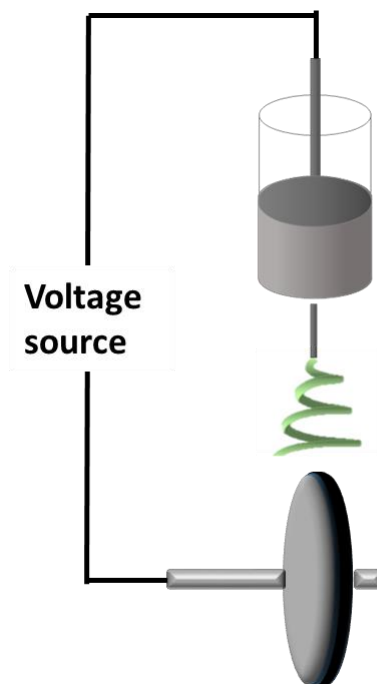


Figure 26 Schematic of the disk collector used for fiber collection. The SEM micrograph shows the alignment of the fibers obtained using the disk collector. Better alignment of the fibers is observed compared to the rotating drum. [142]

It is possible to notify a sort of symmetry within the jet die. The conical shape, which characterizes the initial linear path of the jet is quite equal to the one obtained above the rotating disk after all the instabilities occurred.

During the first stage, the jet follows the usual envelope cone path caused by the instabilities that influence the jet. At a certain distance from the disk, the diameter of the loop decreases as the conical shape of the jet starts to shrink. This induces the inverted cone appearance whose apex of the cone remains on the disk.

The inverted conical shape is due to the concentration of the electric field on the small edge of the disk, which attract and pull the jet on this region of the wheel.

The rotation of the disk induces a tangential force, which act on the fibers and leads the deposition of the mat of nanofibers only on the edge of the disk.

Moreover, this force further stretches the fibers and reduces their diameter. The quality of the fiber alignment obtained using the disk is much better than the one obtained with the rotating drum; on the contrary, the main limitation of this collector is that only a small quantity of aligned fibers can be obtained.

In addition to the different types of counter electrodes, there are many different ways to guarantee the formation of oriented nanofibers, which mainly involve the modulation of external field by means of a specific geometry of counter electrode.

The following example is only one of the many possible solutions.

- **Conducting patterns on the counter electrode**

On the planar counter electrode, two metallic strips, such as gold, are deposited on an insulated substrate, as represented in Figure 27.

This arrangement induces an aligned distribution of nanofibers across the gap of the two metal depositions; moreover, their longitudinal axes are perpendicular to the edge of metallic strips [143]. This behavior is represented in Figure 27.

On the contrary, the nanofibers deposited on the metallic conductive strips shows a random distribution [121, 143].

As explained before, during the die of jet, there are three electrostatic forces that control the motion, the first one is related to the external field, the second one to the counter electrode and the last is related to any adjacent charged fibers. Thus, when the counter electrode is represented by a conductive grounded plane, the distribution of the electric field results to be homogeneous, inducing a random distribution of the nanofibers. In contrast, in correspondence of the insulated gap the electric field is modified and the directions of the electrostatic forces, applied on the nanofibers across the insulated gap, are altered. In particular, it is mandatory to consider that the charges of the nanofibers induce an opposite force on the polymeric jet.

These electrostatic phenomena attract the nanofibers towards the edges of two electrodes, enhancing the alignment distributions across the gap.

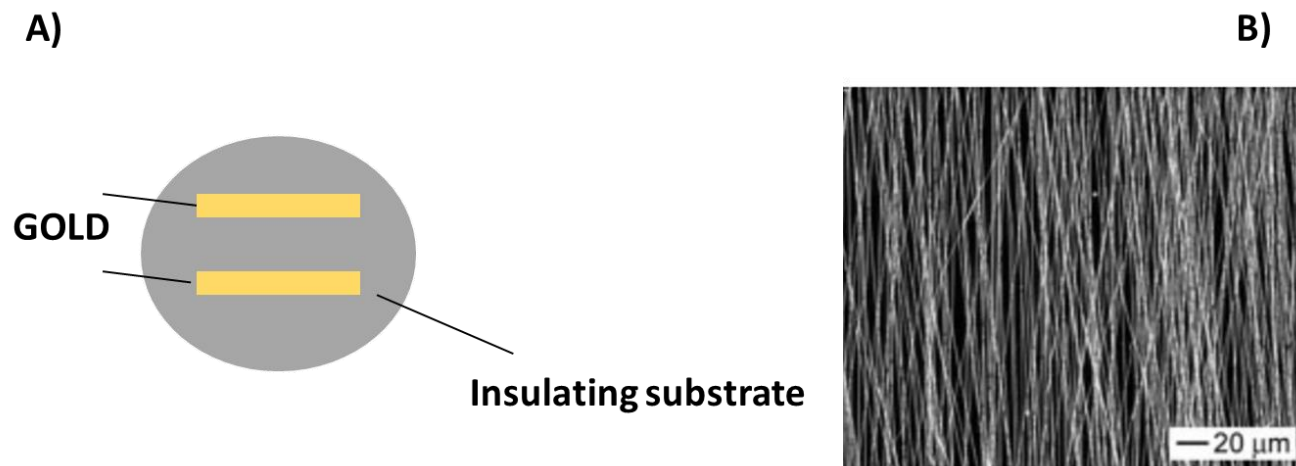


Figure 27 alignment distribution of nanofibers, starting from an electrospun Polyvinylpyrrolidone PVP. A) a schematic representation of the modified counter electrode. Two strips of gold are deposited on an insulated substrate. B) the FESEM analysis to confirm the alignment distribution of nanofibers across the gap between the gold strips [143]

The arrangement can be modified introducing four-electrodes of gold deposited on a quartz wafer [143]. During the collection the electrodes couples 1-3 and 2-4 were alternatively grounded for 5s, as shown in Figure 28. Through the FESEM characterizations, it is possible to demonstrate that the alignment of the nanofibers is present between the closest corners of the adjacent electrodes, as demonstrated by Figure 28 B). While only few fibers were aligned between the couples of electrode to form a single layered mesh in the center of the region of the pattern, represented by Figure 28 C-D).

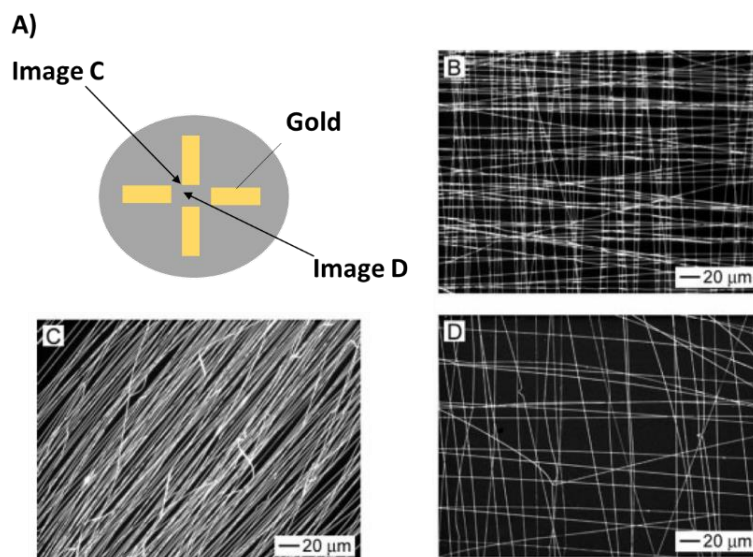


Figure 28 A) schematic illustration of the patterns obtained through the deposition of 4 gold electrodes on quartz wafers B, C, D) FESEM characterizations of PVP nanofibers which are aligned in a different way, according to the patten [143].

2.5 Electrospinning process parameters and their influence of the nanofibers properties

In order to widely investigate and understand the complexity of the electrospinning technique, it is important to deeply analyze the parameters process, from which the modulation of morphological properties of the final nanofibers mat is dependent on.

There are some parameters that influence the final morphology of the mat of nanofibers obtained through the electrospinning technique [135, 144, 145]. According to an engineering point of view, these parameters can be divided in different categories:

- The parameters referring to polymer solution or polymer melt properties, such as viscosity concentration and polymer molecular weight;
- The parameters related to the electrospinning process, such as voltage, flow rate, distance between the tip of the needle and the counter electrode;
- Parameters related to the external environment, such as humidity and room temperature, due to the fact that the inner environment of the electrospinner is the same of the room;

- The parameters related to the morphology of the surface of the chosen substrate, such as conductivity, roughness, smooth, porosity, displaying curvature and so on.

2.5.1 Viscosity, concentration and polymeric weight

The solution parameters, such as viscosity solution, conductivity, dielectric constant and surface tension, deeply influence the morphology properties of the mat of nanofibers.

Many works in the literature investigate how these solution properties determine the formation of nanofibers or the formation of droplets [128, 112, 108, 128].

- **The solution viscosity and the surface tension of the solution influence the formation of the nanofibers with or without defects:**

The solution viscosity is defined as the measure of its resistance to gradual deformation by shear stress or tensile stress. Viscosity is a property arising from collisions between neighboring particles in a fluid that are moving at different velocities. When the fluid is forced through a tube, the particles which compose the fluid generally move more quickly near the tube's axis and more slowly near its walls; therefore, some stress (such as a pressure difference between the two ends of the tube) is needed to overcome the friction between particle layers to keep the fluid moving. For a given velocity pattern, the stress required is proportional to the fluid's viscosity.

Instead, the surface tension is defined as the elastic tendency of a fluid surface, which makes it acquire the least surface area possible. The cohesive forces among liquid molecules are responsible for the phenomenon of surface tension. In one liquid, each molecule is pulled equally in every direction by neighboring liquid molecules, resulting in a net force of zero. The molecules at the surface do not have the same neighboring molecules on all sides of them, therefore are pulled inwards. This induces an internal pressure that forces liquid surfaces to contract to the minimal area. In the electrospinning process, the surface tension is responsible for the liquid droplets shape. Although easily deformed, droplets of water tend to be forced into a spherical shape by the imbalance in cohesive forces of the surface layer, in the absence of other forces, including gravity. The spherical shape minimizes the necessary "wall tension" of the surface layer according to Laplace's law, defined in Figure 29.

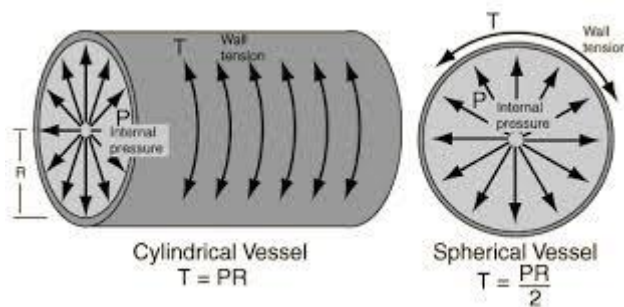


Figure 29 definition and representation from theoretical point of view the Laplace's Law. T is the named Wall Tension; P is the pressure difference and R is the radius of the circular section of the tube

Indeed, a molecule in contact with a neighbor is in a lower state of energy than if it were not in contact with anything. In contrast, the boundary molecules are missing neighbors, compared to interior molecules, and their state of energy is higher; in order to minimize its energy state, the number of these boundary molecules must be minimized, resulting in a minimal surface area.

There is a direct correlation between the viscosity of a polymer and its concentration, in particular, the solution viscosity increased as the polymer concentration increased.

In order to ensure the formation of the mat of nanofibers starting from an electrospun polymeric solution, the viscosity solution must be into the following range (Eq 47) [95, 132, 146]:

$$(0.02 \leq \eta \leq 300) \text{ Pa} \cdot \text{s} \quad \text{Eq 47}$$

The different values of viscosity induce two distinct processes.

In particular, at low values of viscosity ($\eta \leq 0.1 \text{ Pa} \cdot \text{s}$), the surface tension overcomes the viscoelastic forces and consequently the polymeric jet is broken up into the droplets with different diameters and with different concentrations. This process is defined **electrospray** [132, 95].

While, on the contrary, at higher values of concentration, and then viscosity ($\eta \geq 2 \text{ Pa} \cdot \text{s}$), the correct electrospinning process is guaranteed and the formation of nanofibers are ensured. For this value of the solution viscosity, indeed, the polymeric jet is not broken up, but it travels as a continuous jet to the counter electrode, inducing the formation of a dried mat of nanofibers.

The increment of solution viscosity, induced by the augment of concentration, guarantees the formation of a uniform mat of nanofibers, without the presence of beads [132].

The presence of beads in the mat of nanofibers is due to a combination of surface tension, charge density and the viscoelastic forces. The surface tension, as explained before, minimizes the surface area of the droplet at the tip of the needle, inducing a modification of the shape of the droplet in spheres; a zero value net charge density and a value of viscoelastic force lower than the opposite surface tension one ensure the formation of thinner jets. This combined phenomenon favors the formation of the beads in the nanofiber mats.

While, on the contrary, if the net charge density is different from zero and, at the same time, the viscoelastic forces increase, the nanofibers formation is induced. Indeed, a charge density increment, which can be obtained using some proper additives such as salts or cationic surfactants, ensures a surface tension decrement and consequently the formation of nanofibers with a lower concentration of beads or even without any bead [147, 132, 126, 109].

Fong and colleagues [109] analyze the morphological differences between the mat of nanofibers, obtained starting from a polymeric solution based only on Polyethylene oxide (PEO) and the nanofibers formed by an electrospun polymeric solution based on PEO with the addition of NaCl. For both the solutions, the solvent used is distilled water. The addition of NaCl to the PEO solution increases the charges distribution into the polymeric solution and consequently, the net charge density, flowing into the jet during the electrospinning process, increases as well. This higher net charged induces an increment of the force applied on the jet and consequently the formation of thinner jet without beads. The FESEM images, in Figure 30, demonstrate how the distribution of beads into the nanofibers decreases as the content of NaCl increases.

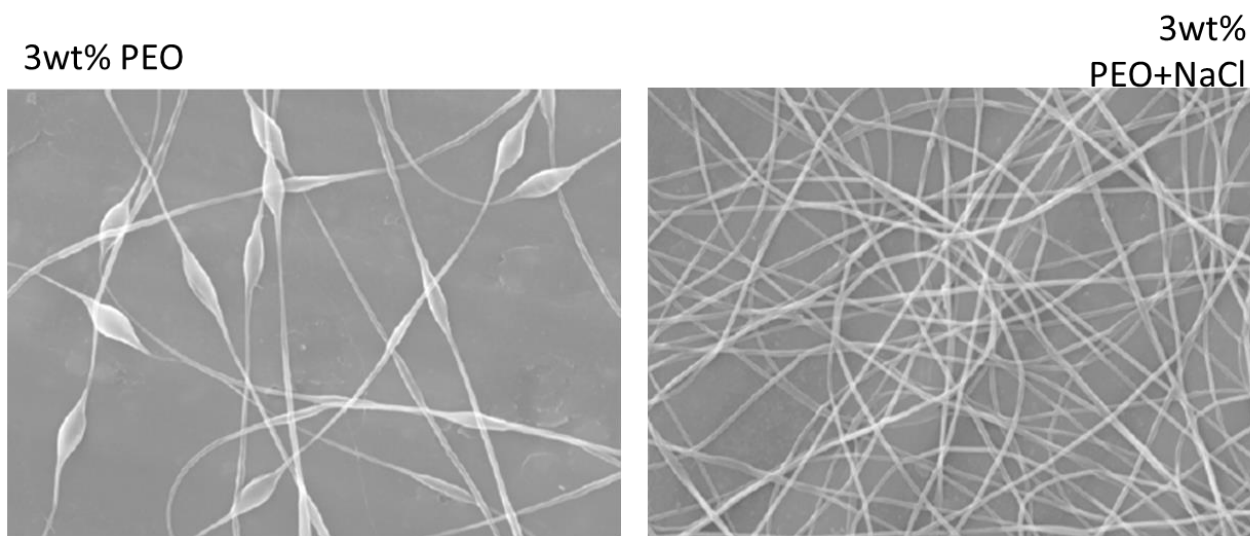


Figure 30 Morphological differences induced by the presence or not of salts in the polymeric solutions [109].

The same correlation is defined between the solution viscosity and the surface tension: the higher is solution viscosity, the lower is surface tension intensity. Consequently, the increment of viscosity supports the formation of smooth fibers minimizing the formation of the beads, as clarified by Figure 31.

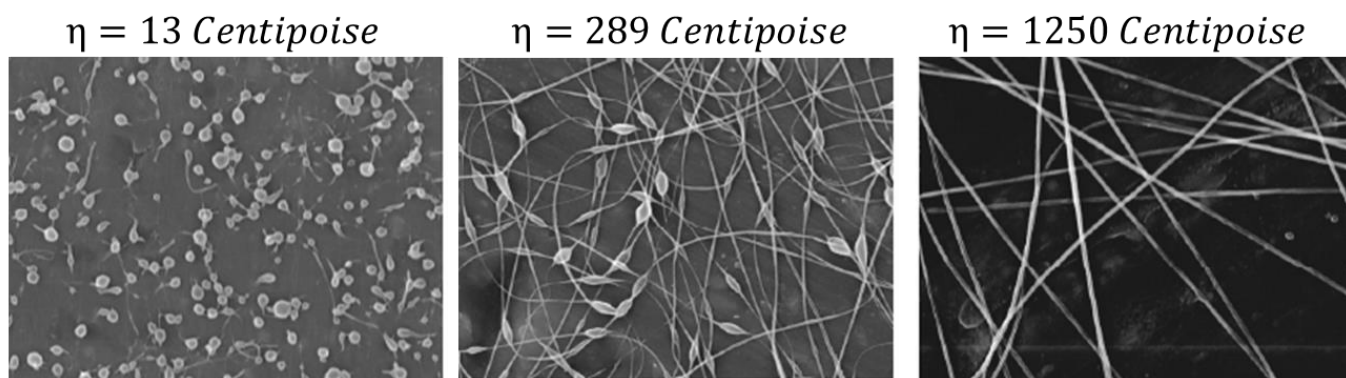
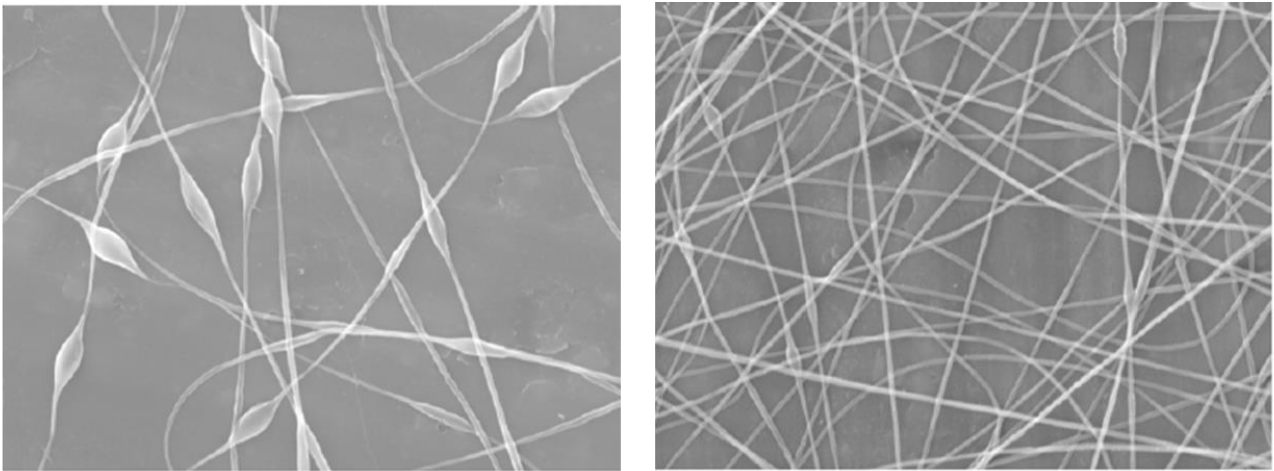


Figure 31 Morphological differences induced by the increasing of viscosity of the polymeric solutions [109].

Moreover, the surface tension is a function of the solvent and not only of the polymeric concentration. The formation of the beads decreases also by changing the solvent from distilled water to a water/ethanol mixture, although the PEO concentration remains constant. This behavior is due to the fact that the ethanol induces an increment of viscosity and so a lower value of surface tension.

As explained before, a net charge density equal to zero, neutralized by the presence of the same number of the ions with the opposite polarity in the jet, induces the formation of the beads.

The electrical forces on the jet are reduced by the neutralizing charge, so the jet start to present more instabilities and the formation of the beads as represented in Figure 32



INCREASING THE NET CHARGE DISTRIBUTION INTO THE JET

Figure 32 represents how the distribution of the beads into the mat of nanofibers decreases as the charge density in the jet increases [109]

- **The effect of molecular weight and of the polymeric concentration on the morphology of nanofiber mats**

The molecular weight of polymer (M_w), dissolved into the solution, influences not only the distributions of beaded defects into the mat of nanofibers, but at the same time it varies the diameters distributions of nanofibers.

Some works in the literature demonstrate that as the molecular weight increases, the number of beads and droplet is reduced.

The effect of molecular weight is quite pronounced on the distribution of the diameters, too. Indeed, increasing the molecular weight, the instability of the jet can be strongly enhanced, causing the spread of the diameters of the collected nanofibers; in particular, the higher the molecular weight is, the more disperse the values of resulting diameters.

Also the polymeric concentration influences the diameter of the mat of nanofibers formation. A low polymer concentration induces a shrinkage of the fiber diameter due to the evaporation of the solvent [132].

The major effects of the polymeric concentration variations are the modification of the solution viscosity and the variation of the jet deformations to the viscoelastic forces applied during the electrospinning.

In particular, as previously explained, a lower value of polymeric concentration induces a lower value of solution viscosity; consequently, the surface tension is predominant during the process, and so, the electrospray results to be the electrified main process.

While, if the polymeric concentration is too high, the control and the maintenance of the flow rate of the polymeric jet can become difficult, due to the cohesive and viscoelastic forces, which increase together with the solution viscosity. If the viscosity value is too high, it can be very difficult to force the polymeric solution through the tip of the needle, causing the instability of the flow rate.

Experimental data in the literature confirm that at low concentration [132], the fibers have an irregular and undulating morphology, with a high variation of the diameters distributions and many junctions and beads. Instead, at high value of concentration, the nanofibers have a regular and cylindrical morphology, with a more uniform diameter distribution into the mat and a lower amount of the junctions and the beads defects. In particular, it is possible to observe that the relationship between the fiber diameters and the concentration is the following Eq 48:

$$Diameter \propto \sqrt{Concentration} \quad \text{Eq 48}$$

This relationship is represented in Figure 33 [132].

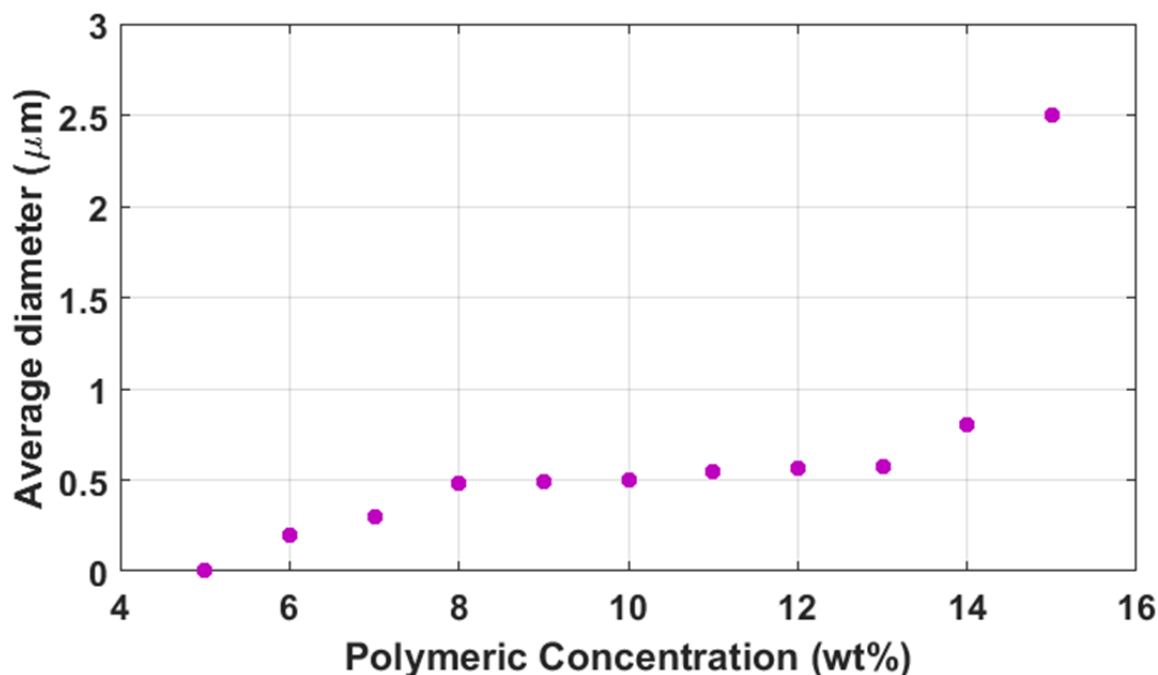


Figure 33 demonstrates the power law relationship between the fiber diameter distributions and the polymeric concentration (wt%) [95].

2.5.2 Voltage, Flow rate, and Gap distance between the tip of the needle and the counter electrode

The electrospinning parameters influence the diameters distribution in the nanofiber mats. As explained before the diameters of the nanofibers influence the porosity distributions and the surface area of the mat. Therefore, it is quite important to establish what parameters can directly influence the diameters distribution.

- Effect of the voltage on morphology of nanofibers

Although the correlation between the voltage applied and the fiber morphology is ambiguous, the voltage is an important process parameter in order to define, for each solution, the proper threshold above which a continuous jet is originated. Moreover, the current induced by the applied voltage, can flow only through the charged polymeric jet during electrospinning process. Consequently, the increment of the flowing current causes an increment of net charge distribution in the polymeric jet, and so, a decrement of the quantity of beads in the nanofiber mats.

Deitzel and coworkers [132, 95] analyze the effects of the current during the electrospinning process of mats of PEO nanofibers, applying different values of voltage.

They observed how the position of Taylor cone, related to the tip of the needle, changes as the voltage is modified. They investigated three different voltage values: 5.5, 7 and 9 kV. In presence of a low value of voltage (5.5 kV), the droplet remains suspended at the end of the tip of the needle and the jet starts from the cone at the bottom of the droplet. In this case, they observed that the value of the semi vertical angle of cone was of about 50° . The nanofibers produced in these conditions show a cylindrical morphology and few beads defects. With an applied voltage of 7 kV, the cone receded and the jet was originated from the polymeric droplet in the tip of the needle. In this case, a major quantity of beads defects into the mat of nanofibers was observed. Finally, with the highest applied voltage of 9 kV, the solution jet appears to be originated starting from the tip of the needle with no external formation of the droplet or cone. Due the strongly instability of the charged polymeric jet obtained under these conditions, the mat of the nanofibers present a higher density of beads defects. In conclusion, they demonstrated that the presence of beads defects can be correlated with the value of the applied voltage during the electrospinning process: lower density of the beads, lower voltage applied

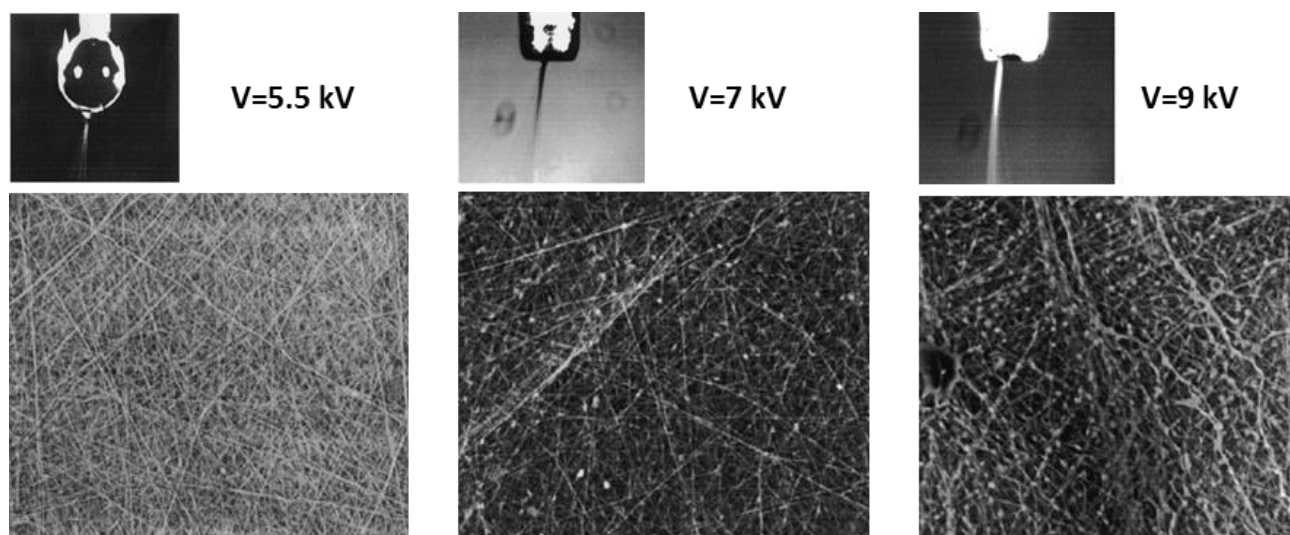


Figure 34 The different values of applied voltage on the 7 wt% PEO in distilled water. The volume of droplet decreases as the applied voltage increases and the distribution of the beads in the mat of nanofibers increases with the increasing of the voltage intensities [132]

- **The effect of the working distance of the morphology of the nanofibers**

The working distance is a fundamental parameter to ensure the completely evaporation of the solvent. It is important to define the minimum value of the required distance to allow the fiber sufficient time to dry before reaching the collector. It has been observed that both too close and too far working distances generate defects.

- **The effect of the flow rate on the morphology of nanofibers**

The flow rate is the rate at which the polymer solution is pumped into the tip of the needle, defining the flowing mass of solution and consequently the replenishment of the Taylor's cone. The flow rate determines also the length of linear path of the charged jet, before the instauration of bending instabilities, correlated with the electric field strength [95].

At lower values of flow rate, electrospinning may only be intermittent, due to the fact that the Taylor's cone is formed inside the needle; on the contrary, when the flow rates becomes too high, the charge polymeric jet is continuous but the final nanofibers are characterized by the presence of beads and by a diameter distribution less uniform. Experimental results, moreover, underline and demonstrate a correlation between the flow rate and the diameters distributions. As the flow rate increases, the diameters of nanofibers mat increase [95].

To model these correlations, it is necessary to consider that the diameters distribution must have a limit, which is defined as the balance between surface tension and charge repulsion forces into the polymeric jet.

The mass flow rate Q is characterized by an intensity current I , which flows into the polymeric jet during the electrospinning process and by a surface tension γ of the fluid [95]. Considering the assumption that, further along the jet, the electric current only contributes to the surface charges, the surface charge σ_0 can be defined with the following Eq 49:

$$\sigma_0 = \frac{hI}{2Q} \quad \text{Eq 49}$$

Where h is the diameter of the jet. Through the definition of the balance between the charge repulsion and the surface tension, it is possible to define the limit value of the jet diameter h , described by the equation Eq 50:

$$h = \left(\frac{2\varepsilon\gamma Q^2}{l^2\pi(2 \ln \zeta - 3)} \right)^{1/3} \quad \text{Eq 50}$$

ε is the electric constant, ζ is the dimensionless wavelength of instability, which normally is assumed equal to 100.

It is then possible to approximate the definition of h with the following Eq 51:

$$h \sim \left(\frac{Q}{I} \right)^{2/3} \gamma^{1/3} \quad \text{Eq 51}$$

In order to take in consideration, the solvent evaporation occurring during the electrospinning process, it is necessary to correlate the limit of the jet diameter h with the concentration of the solvent, which leaves the polymeric solution. The Eq 52 describes this relationship:

$$d_t = c^{1/2}h \quad \text{Eq 52}$$

Obviously, the solution's properties, such as conductivity, surface tension and the current induced by the electric field, also depend on the type of the solvent; this model can then be considered as an approximation, according to which the flow rate is a limitation of diameter jet h and thus of final fiber diameter. The experimental measurements indicate that the volume charge density q_v on the jet to decrease exponentially with feed rate, confirming the theoretical prediction [145, 148]. It is assumed that the higher flow rate is, the lower is the rate of replenishment of charges on the surface of the droplet. Theron et al. (2004) [145], however, suggest that the charge replenishments are governed by the drift velocity of ions and therefore are independent of flow rate. The lower values of q_v are therefore likely to be a result of high rates of withdrawal of charges as well as polymer solution from the droplet surface at the higher feed rates.

2.6 Applications

Many application fields, based on electrospun polymer nanofiber, have been steadily extended especially in recent years. Figure 35 reports some of the many potential applications of the nanofibers.

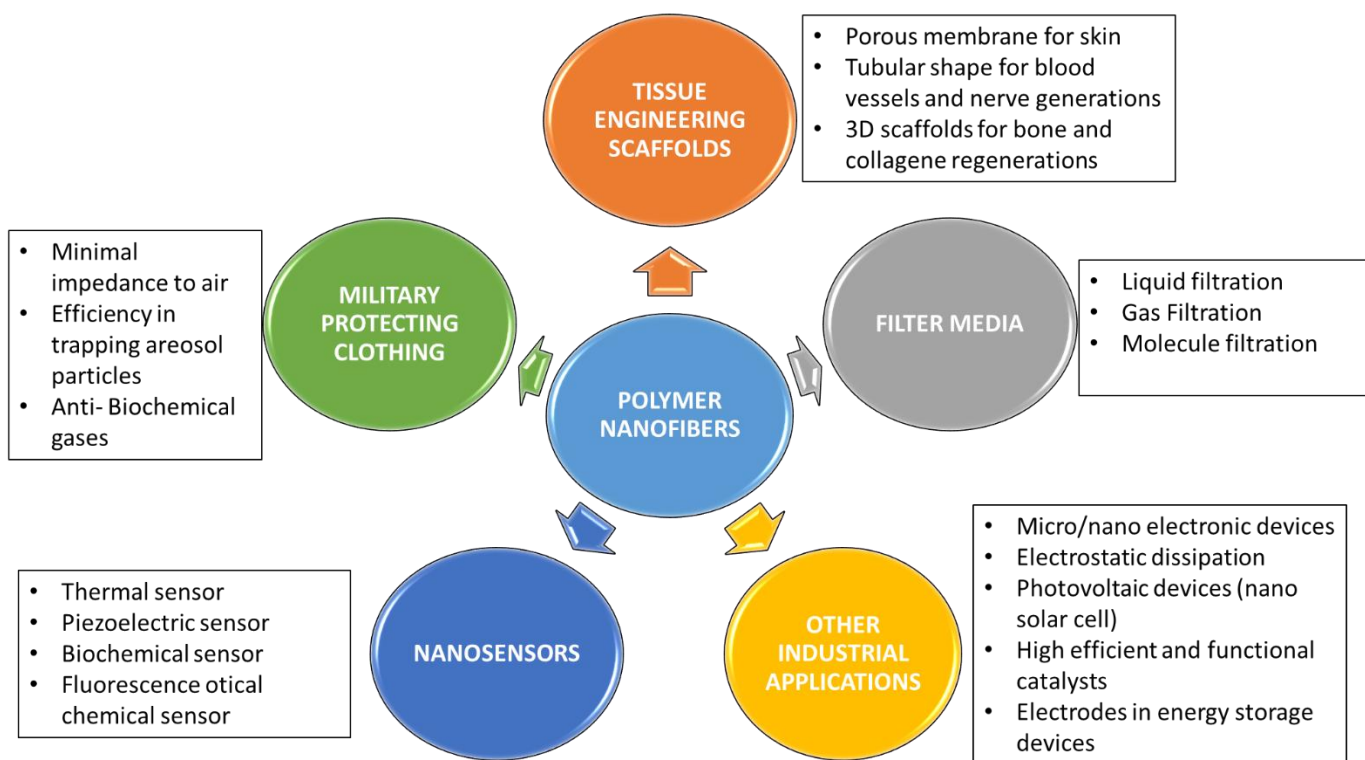


Figure 35 Many potential applications of the nanofibers [112]

2.6.1 Biomedical applications of nanofibers

Nanofibers can provide a great contribute in different emerging medical areas, such as organogenesis, genomic medicine, high throughput screening, rapid bedside clinical tests, and smart wound dressings [116, 149, 150, 151]. In particular, two main biomedical fields could be improved by using nanofibers: the first one it is the development of 3D scaffolds for tissue engineering; while, the second one is the design of devices for controlled pharmaceuticals delivery [152]. Due to the dimensions, which are very close to the structural features dimensions present in the human body, due to the high porosity and due to the readily tailorable surface chemistry, the polymer nanofibers are ideal to realize the biomedical scaffold [153]. Moreover, it is possible to obtain different polymeric solutions based on biodegradable, biocompatible and bio-inert polymers obtaining different synergies with the mat of nanofibers. These requirements are fundamental in order to develop biomedical systems.

➤ **Drug delivery applications**

According to the conventional drug delivery [116], during all the time of the therapies the drug concentration trend in the blood (or other tissue phase) must fluctuates around the proper value.

The provided drug concentration must be lower than a maximum admitted value C_{max} , in order to avoid any risk of bio-toxicity; moreover, at the same time it must be also higher than a minimum admitted value C_{min} , in order to guarantee the correct effect of the therapy. Therefore the optimum value of concentration C , belonging the range $[C_{min};C_{max}]$, must be defined and maintained in the body during the whole therapy. The nanofibers could be developed in order to properly release antibiotics or drugs [154], ensuring a low release drug time and the capacity to locally diffuse the correct concentration of the drug in the body region. Many works in the literature investigate the possible methods of drugs releasing occurring with the nanofibers and the two manly used are: the diffusion or chemical control. Regarding the chemical controlled method, the drug can be released through bio-erosion of the matrix or with biodegradation of the linkages between the remedy and the nanofibers [155, 156]. The drug can be dissolved in high concentration or suspended as particles in the cylindrical polymer nanofibers. The releasing system of the drug from the mat of nanofibers may occur into different ways:

1. The diffusive transfer from the polymer matrix to the surrounding tissue.
2. The release of the dissolved or suspended drug through the slow biodegradation or erosion of the surface layers of the fiber.
3. The slow release of covalently bonded drug via hydrolytic cleavage of the linkages.
4. The rapid delivery of the drug due to dissolution of the fiber.

Among all these methods, the most commonly used mechanism to release the drug from the nanofibers, is the diffusive transfer through the polymer matrix to the surrounding tissue.

Moreover, the use of melting spun water soluble fibers guarantee further improvements, permitting to release the drug only if the mat of nanofibers is dissolved in water or if it is heated at a proper temperature [157].

Another advantages of the use of nanofibers to dissolve the correct amount of the drugs in the body, is the possibility to obtain a uniform distribution of the correct dosage manipulating the mat of

nanofibers in a proper way. There are many works in the literature, and even some patents, regarding the development of nanoscale fibers used as carrier for pharmaceutical components [152, 158, 159]. The study of the drug diffusion kinetic through the polymers has been widely discussed by Crank (1980).

The Fick's Law is used in order to describe the drugs diffusion through the polymers; the concentration gradient between inside and outside the mat of nanofibers is directly correlated with the diffusion flux, through the Eq 53:

$$J = -D\left(\frac{dc}{dx}\right) \quad \text{Eq 53}$$

where J is the local flux of the drug ($\text{g/cm}^2 \cdot \text{s}$), D is diffusion coefficient and (dc/dx) is the concentration gradient.

It is important to define the fraction of drug released by the polymer matrix (M_t/M_1) at the time t, where M_t is the amount of drug released at time t, and M_1 is the total amount released at infinite time.

Crank defined the relationship between (M_t/M_1) at the time t and the different geometric properties of the polymer release devices. Assuming to consider the simplest slice geometry of the samples, it is possible to obtain this Eq 54:

$$\left(\frac{M_t}{M_\infty}\right) = 4\sqrt{\left(\frac{D \cdot t}{\pi r^2}\right)} \quad \text{Eq 54}$$

where r is the thickness of the samples and D is the diffusion coefficient.

It can be observed that the rate of the drug release varies with the square root of the time.

Regarding the geometric morphology, it is possible to assume that the nanofibers spun is cylindrical, and then the mat of nanofibers has a circular cross section with r as the diameter of the section. Comyn [160] defined the rates of drugs released from the spun nanofibers. The Fick's second law for the diffusive release of pharmaceutical components from a device based on thinner mat of nanofibers well predicts the simplest kinetics.

Luong -Van [161] investigated the loading of heparin on a mat of nanofibers based on poly(1-caprolactone) (PCL). They demonstrated how the Fick's law could correctly identify the process of drugs releasing and, in particular, that the fraction of dosage released increases according to the

square root of the time. Moreover, Kissel et al. [162] proposed three different ways to dissolve the drugs in the polymeric matrix:

1. Drug dissolved in the polymer matrix at the molecular level.
2. Drug distributed in the polymer matrix as crystalline or amorphous particles.
3. Drug enclosed in the polymer matrix yielding a core of the drug encapsulated by a polymer layer (similar to a reservoir device).

With the nanofibers devices, the third way can be obtained through a coaxial spinning of core-shell nanofibers. Moreover, considering the type 1, because the drugs must be dissolved into the solution, their solubility limits their maximum available concentration. There are many works in the literature that investigate the type 1 to load the drug in the mat of nanofibers; in particular Zeng et al. (2003) [163] obtained an electrospun solution based on 3.9wt% of Poly(l-lactic acid (PLLA), dissolved into CHCl_3 : acetone (2:1 v/v) with rifampin varying the concentration in the range 5-100wt%. Nanofibers were obtained with a low drug load, whose average diameters are of 700 nm, showing no crystallinity inclusions. This characteristic can be explained by the complete diffusion of the drug in the initial polymeric solution. If the loading of the drugs increases, it is possible to observe a dispersion of the drugs as type 2; in this case, the releasing of the rifampin occurs thanks to the enzymatic biodegradation of the surface layers.

➤ **Tissue Engineering**

An important target of this field is to design new polymeric 3D scaffold populated with a mixture of different cells and tissue [153]. Live tissue comprises a collection of cells arranged in complex geometries within an extracellular matrix (ECM) that is in intimate association with the cells. The specific arrangement of cells in the tissue depends on the functional architecture of the organ. The ECM, however, plays a vital role in lending the structural integrity to most types of tissue and in the transduction of chemical signals able to direct tissue development and cellular differentiation. Polymeric scaffolds are an important substitute for the native ECM in the body. In particular, the nanofibers scaffolding systems, thanks to their high porosity, their small dimensions that are comparable with the cells, their distribution of the nanofibers in the space, can be an ideal three-dimensional environment for cell adhesion and proliferation, guiding the growth and the

organization of the cells into complex tissue. Min et al. [149] investigated and compared the cellular adhesion on 3 different scaffolds; the first one was based on the nanofibers ($d \approx 800 \text{ nm}$), the second one on micrometric fibers ($d \approx 800 \mu\text{m}$) and the third one the polymeric matrix. They demonstrated how the higher surface area of the nanofibers improve the adhesion and the proliferation of the cells on the scaffolds. Indeed, the high surface area to volume ratio and the exceptionally high porosity lead to the development of a support for the cell growth, allowing gas and nutrients to be exchanged and supporting the tissue. The relatively higher specific surface area of nanofibers, in comparison to other scaffolds, is expected to be able to enhance cell adhesion as well as adhesion-dependent phenomena such as migration during proliferation. Electrospun nanofiber scaffolds can be realized with many different precursors such as: natural polymers, synthetic polymers (PLLA, Polyglycolic acid PGA, Polycaprolactone PCL and copolymers) and polymer blends of natural or synthetic polymers. Using natural polymers, such as cellulose, collagen and elastin, generally ensures a proper degree of biocompatibility and biodegradability of the scaffold.

2.6.2 Nanofibers sensors and filter

The higher surface area of the nanofibers, with respect to flat films, guarantees their good performances in the sensors field. Many works demonstrate that nanofibers present a higher value of sensitivity and a quicker response to the variations if compared to the ones obtained with different types of materials. One of the possible applications of the nanofibers as sensors is the design of gas monitoring devices able to supervise the gas concentration in a certain area and detect, for example, the environmental pollution [164]. The sensor performances are evaluated through the definitions of parameters such as sensitivity, selectivity, time response, stability, durability, reproducibility, and reversibility; each of them are largely influenced by the properties of the sensing materials used inside the device.

In particular, different materials, such as semiconductors (semiconducting metal oxides such as TiO_2 , SnO_2 , ZnO), organic/inorganic composites, conducting polymers, carbon graphite, have been investigated to be applied as sensing element into devices based on electrospun nanofibers.

There are many works where different polymeric nanofibers are applied in the sensor devices, as summarized in the following Table 4:

Sensor class	Parameter measured	Nanofibers	Analyte	Reference
Gravimetric	Mass of analyte	PAA/PVA	NH ₃	Ding et al. (2004b,2005c)
Amperometric	Electric current	PEO/LiClO ₄	Humidity	Aussawasathein (2006)
		PANI/PEO/CSA	NH ₃	Liu et al.(2004) Virji (2004)
Conductometric	Electric resistance	PANI/PS/GOX	Glucose	Aussawasathein (2006)
		PANI/PVP/UREASE	NO ₂	Bishop and Gouma (2005)

Table 4 report some examples of different polymeric nanofibers used as sensor [165]

The sensitivity of the sensors depends on the interaction between the material and the analyte. The analyte is the element that have to be detected by the sensor. Consequently, it is reasonable to suppose that the surface interaction between the molecules of the analyte and the materials increases with the surface area of the sensing material. Thanks to their higher surface area, the mat of nanofibers can increase the performances of the sensor.

The more efficiency can also occur thanks to the higher porosity of the sample, which implies a quicker diffusion of the species into the mat of nanofibers.

2.6.3 The applications of carbon and catalytic nanofibers

Carbon nanofibers have been used for several applications of energy sources and storage systems, thanks to their conductivity and higher surface area to the volume ratio. Moreover, their mechanical properties in composite samples can improve the stiffness, the strength and induce a low electrical resistivity. Nanomaterials, moreover, are of recent interest as catalyst substrates due to their large surface area per unit mass and the feasibility for high catalyst loading. Nanofibrous catalysts could substitute catalytic nanoparticles in order to overcome the limitations of catalyst recovery. Jia et al. [166] prepared bioactive polystyrene (PS) nanofibers by chemical attachment of chymotrypsin on PS samples and they observed a high catalytic activity with improved enzyme stability over other forms of immobilized enzymes. Fibrous catalysts offer advantages, such as feasibility of adapting to any geometry and low resistance to the flow of liquids and gases. Though catalyst loading and mechanical properties limit the usage of fibrous catalysts, the advent of

nanofibrous materials as catalytic substrates alter the scope of its application. The activity of the catalyst, supported on a substrate, depends on its large active surface area. Nonporous substrates can be coated with a high surface area material like nanofibers to increase the surface area, thereby enhancing reactivity. Carbon nanofiber supports loaded with iron particles have shown high conversion of hydrocarbons in comparison with active carbon and alumina. It has been shown that the intrinsic catalyst effect is more pronounced when loaded in smaller diameter fibers such as nanofibers [167].

There are many applications of carbon nanofibers in energy production devices, such as:

- **Lithium- Ion batteries:**

Lithium ion batteries are characterized by three primary functional components, such as anode, cathode and electrolyte designed to control effectively the motion of the ions from the negative electrode to the positive one on discharge and back again on charging. Many works in the literature investigate the used of nanofibers and core shell nanofibers, developed as anodes in batteries.

One example can be carbon cobalt composite nanofibers with diameters ranging from 100 to 300 nm were prepared as anodes by electrospinning and subsequent thermal treatment [168].

The electrochemical properties of the mat of nanofibers are proper for the application in batteries and in particular they present a high value of reversible capacity of about $750 \text{ mA} \cdot \text{h} \cdot \text{g}^{-1}$. Another example is based on manganese oxide, obtained starting from manganese acetate mixed in the polymeric solutions and after a proper heated treatment, the crystal of manganese oxide, with diameters in the 20–25 nm range, were found on the carbon nanofibers. The functionalization with manganese oxide increases the reversible capacity [169, 170]

The increasing performances can be related to the porosity of the mat of nanofibers, which improves the diffusion of the liquid electrolyte. There are many studies on carbon nanofibers, obtained from heat treated composite PAN nanofibers, and functionalized by tin oxide nanoparticles. These composite samples present high charge and discharge capacities of about $1200 \text{ mA} \cdot \text{h} \cdot \text{g}^{-1}$, at elevated temperatures of around $800 \text{ }^\circ\text{C}$ [170, 171]

One of the key advantages of the electrospinning technology is represented by the possibility to control the amount of the oxidizing nanoparticles on the mat of nanofibers. Another possibility to

obtain anode for Li-ion batteries is the use of the coaxial electrospinning to have composite hollow nanofibers.

In general, anodes for Li-ion batteries, obtained through electrospinning technique, are characterized by the hollow nanofibers, where the core is oxide nanoparticles and the shell of carbon [172, 173].

There are few studies about the electrospun nanofibers used as cathode in lithium ion batteries [174, 175]. In these cases, vanadium oxide nanowires with diameters in the range of 100-200 nm and with a length of up to several millimeters, functionalized with vanadium nanorods on the nanofiber, have been developed as cathode in these batteries. The discharge capacity was reported to be in the range from 390 and 200 mA*h*g⁻¹. Vanadium pentoxide (V₂O₅) nanofibers were obtained by electrospinning of the sol gel precursor containing vanadyl acetylacetonate and Poly-Vinil Pyrrolidone PVP [175]. Electrospun nanofibers present diameters in the range of 300-800 nm and they are successively annealed in the air. The mat of nanofibers is characterized by porous polycrystalline vanadium oxide with a high surface area and they increase the storage capacity of the Li-ion batteries, close to 370 mA*h*g⁻¹; moreover, this kind of sample also increase the charge/discharge capacity with only small cyclic degradation.

- **Fuel cells**

As already introduced into the Chapter 1, fuel cells contain three principal part: anode, electrolyte and the cathode. The fuel cell transduces the chemical energy, contained into an inorganic or organic fuel, into electricity, through a chemical reaction with oxygen or other oxidizing agents. At the anode a catalyst agent oxidizes the fuel, occurring into a positively charged ion and electrons. Hydrogen is the most common fuel, but hydrocarbons such as natural gas and alcohols, like methanol, are also used.

The electrolyte must have the proper characteristics to permit the migration of positively ions only towards the cathode. To obtain this, frequently there is a proton charged polymer membrane, used to separate the anode and cathode. Electrons flow through an external applied load from anode to cathode. Electrons are recombined with the protons at the cathode, where the reduction reaction of chemical species, such as often oxygen, occurs producing water. The mat of nanofibers has been

studied to be applied as anodes and cathodes but also as proton exchange membranes (PEM). Usually, the PEM is composed by Nafion (*sulfonated tetrafluoroethylene based fluoropolymer-copolymer with ionic properties*), which presents excellent mechanical and thermal stabilities. The higher cost of PEM made of Nafion is one of the negative aspect for this material. Different composite nanofibers, obtained starting from the electrospun solutions, containing Poly-Vinil alcohol PVA, partially sulfonated poly (ether sulfone), sulfonated polystyrene, poly (phenyl sulfone) or inorganic materials such as sulfated zirconia (S-ZrO₂) with Nafion, are investigated. The resulting composite membranes have in general higher proton conductivities than pure Nafion membranes. The hypothesis is that the interfaces between the Nafion and the nanofibers improve the pathways of the protonic transport. There are two works in the literature, which investigate the preparation of composite membrane through the electrospinning of aqueous solution of PVA. The mat of nanofibers has a thickness around 19–97 μm containing Nafion, infiltrated into a porous membrane [176, 177, 178]. The diameters of nanofibers are in the range of 200–300 nm and their external surface is functionalized with sulfonic acid groups, in order to enhance proton conduction. The proton conduction of this composite membrane is defined by impedance spectroscopy of about 0.022 S/cm at 70°C. For the Nafion/PVA composite membranes, the resistance to methanol permeation showed a linear variation with the thickness. Another example of proton exchange membrane is based on the functionalization of the Nafion with the incorporation of the super acidic sulfated zirconia (S-ZrO₂) fibers [179]. The super acidic nanofibers introduction leads to the formation of protogenic groups, which are aggregated in the interfacial region between S-ZrO₂ nanofibers and the ionomer matrix; this nanostructured conformation enhances the continuous pathways for proton transport. The resulting hybrid membranes shows high proton conductivities, which could be controlled by the fiber diameters and fiber volume fraction. The use of electrospun 3D carbon fiber electrodes enhance significantly the efficiency of fuel cells. Regarding the Microbial Fuel Cell (MFC), which is a particular example of fuel cell, where the bacteria, inducing the oxidation of organic matter, transform the chemical energy into the electrical energy, the carbon nanofibers are studied to be applied as anode and cathode in the devices. All these aspects, in particular, the improvement of efficiency of the devices thanks to the nanostructured electrodes in MFCs, will be

widely described in Chapter 3. Electrospun nanofibers can be developed in order to design an innovative 3D anode and cathode electrodes, applying into the fuel cells and into the MFCs.

- **Dye sensitized solar cells (DSSC)**

Electrospinning investigations focusing on solar cells have primarily dealt with dye-sensitized ones (DSSCs) considered to be extremely promising, thanks to their high efficiency and low production costs. In the DSSC, the photosensitizers absorb light to generate excited electrode hole pairs, which next undergo interfacial charge separation. The electrons then flow through the photo-electrode, while the holes diffuse through an electrolyte solution to the counter electrode.

Charge collection is defined considering the charge recombination, occurring at the interfaces of photo-electrode/dye/electrolyte. To realize high device efficiencies, charge diffusion must be enhanced, minimizing charge recombination. One-dimensional (1D) nanostructures (e.g., nanowires, nanorods, nanotubes, nanobelts, nanofibers) present the better electron transport characteristics, if compared to the ones of conventional film; indeed, relatively low electronic junction densities are found in 1D nanostructures. In the DSSC, TiO₂ photo-electrodes are the most common materials. In many works, moreover, the effects of parameters, such as morphology, pore volume, the crystallinity of TiO₂ as well as of doping on charge transport and recombination processes have been evaluated [180, 181].

To have an higher energy conversion efficiencies, TiO₂ nanorods, obtained through the electrospinning starting from a solution made of titanium n-propoxide and poly(vinyl acetate) in dimethylformamide, are investigated [182]. The optimization of the nanorods morphology to improve and favor the charge transport, is fundamental to obtain a high value of efficiency of the DSSC.

A low-cost fabrication of TiO₂ nanorods photoelectrodes for DSSC application has been based on electrospinning with PEO, which is an amazing biocompatible and environmental friendliness material. It is used as a template for the fabrication of nonwoven mat of TiO₂ nanofibers. Moreover, PEO is completely removed in the calcination step. PEO is a good matrix polymer for prepare pure anatase TiO₂ due to the fact that its calcination temperature is 200°C, guaranteeing the completely decomposition of polymer [183, 184]. Anatase meso-porous TiO₂ nanofibers were prepared for

solid-state dye-sensitized solar cells with high surface areas of up to $112 \text{ m}^2 \cdot \text{g}^{-1}$ enhancing the dye uptake considerably.

While on the contrary, in order to obtain rutile TiO_2 nanofibers, a polymeric solution, containing Polyvinylpyrrolone (PVP), a titanium precursor and acid ethanol is electrospun. The final composite nanofibers were subsequently sintered at 800°C , inducing the completely removing of the polymer [185].

During my Ph.D. period, we investigated the effect of polymer matrix on the photo-voltage of DSSC by a combined approach of polymer electrolyte nano-growth in the photo-anode mesopores and photo-electrochemical measurements on the resulting devices. The obtained results are deeply explained in the following section.

✓ **Electrospray to module the electrolyte-photo-anode interface in the DSSC**

In the field of dye-sensitized solar cells, polymer electrolytes are among the most studied materials due to their ability to ensure both high efficiency and stability, the latter being a critical point of these devices.

In order to ensure these last two properties, during my Ph.D. period, I developed an electro spray process to optimize the photo-electrode/electrolyte interface in DSSC devices [186]. The nanostructured photo-anode was obtained through a nanoscale growth and through the crosslinking of a polymer electrolyte.

In particular, the selecting of the monomers with a low molecular weight and a combination, between electrodeposition and photo polymerization process, underline the increasing of the short-circuit current density J_{sc} of the DSSC devices.

A 35:65 weight of two liquid monomers, BEMA (Bisphenol A ethoxylate dimethacrylate average M_n of 1700) and PEGMA (poly(ethylene glycol) methyl ether methacrylate average M_n of 500), combined with a 3wt% of photo initiator (2-Hydroxy-2-methyl-1-phenyl-1-propanone Darocur® 1173), constituted the UV-curable reactive mixture for the electrodeposition process.

In this work, the substrate for the photo anodes was fluorine-doped tin oxide (FTO) glass plates (sheet resistance $7 \Omega \text{ sq}^{-1}$, purchased from Solaronix) cut into $2 \text{ cm} \times 2 \text{ cm}$ sheets. The FTO substrate was modified by the deposition of a thin film of TiO_2 on the top of conductive substrate. Then the

samples were heated at 100 °C for 10 min and then sintered at 525 °C for 30 min. The obtained photo-electrodes were soaked overnight in a 0.35 mM ethanolic N719 dye solution.

Finally, the electrodeposition and photo-polymerization of BEMA/PEGMA solution occurred on the top sides of the FTO glasses.

The electrodeposition was based on the electrospray process, thanks to the low values of viscosities characterizing the liquid solutions, described above. The electrospray induced, indeed, the formation of charged drops instead of the polymeric charged jet, typical of electrospinning process, was employed. To obtain the charged drops, the voltage applied was equal to 21 kV, the distance between the working electrode and the counter is of about 15 cm and consequently the electric field strength, defined as $E = \Delta V/d$, is equal to 1.4 kV/cm⁻¹. The electrodeposition time (t_e) was varied from 0 to 80 s, thus polymeric layers with different thicknesses were obtained.

During the electrodeposition process, moreover, the photo-polymerization occurred through an UV light; the UV irradiation inducing a crosslinking of the monomers in very close contact with the photo anode nanoparticles.

Thanks to the electrodeposition conditions, there was a perfect infiltration of the reactive mixture into the mesopores of the thin nanostructured film of TiO₂.

Figure 36 shows the electrodeposition setup used to obtain the nanostructured electrodes.

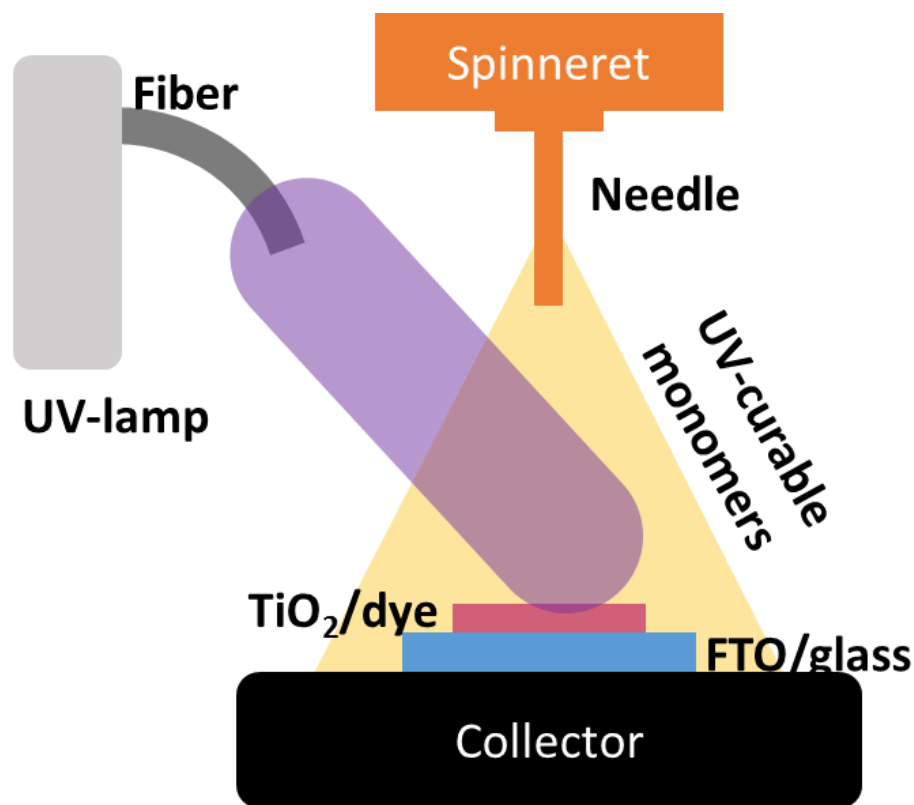


Figure 36 Experimental setup for the electrodeposition/photo-polymerization process [186]

Field emission scanning microscopy (FESEM) defined the thickness of the electrodeposited mixture, comparing the thickness of TiO₂ layer before and after the electro spray process.

These characterizations demonstrate not only the correlation between the thickness and the time of the process (higher thickness, higher time durability of the electro spray), but they also verify the different discontinuity of the coating of the TiO₂ nanoparticles.

In particular, the time process of $t_e = 45$ s allowed the formation of the polymeric layers, with a thickness closes to 20-25nm, coating the TiO₂ nanoparticles, as shown in Figure 37. This kind of coating would be ideal for application in DSSCs and, in particular, to maximize the dye regeneration process thanks to a close contact between the sensitizer molecules and the polymer electrolyte.

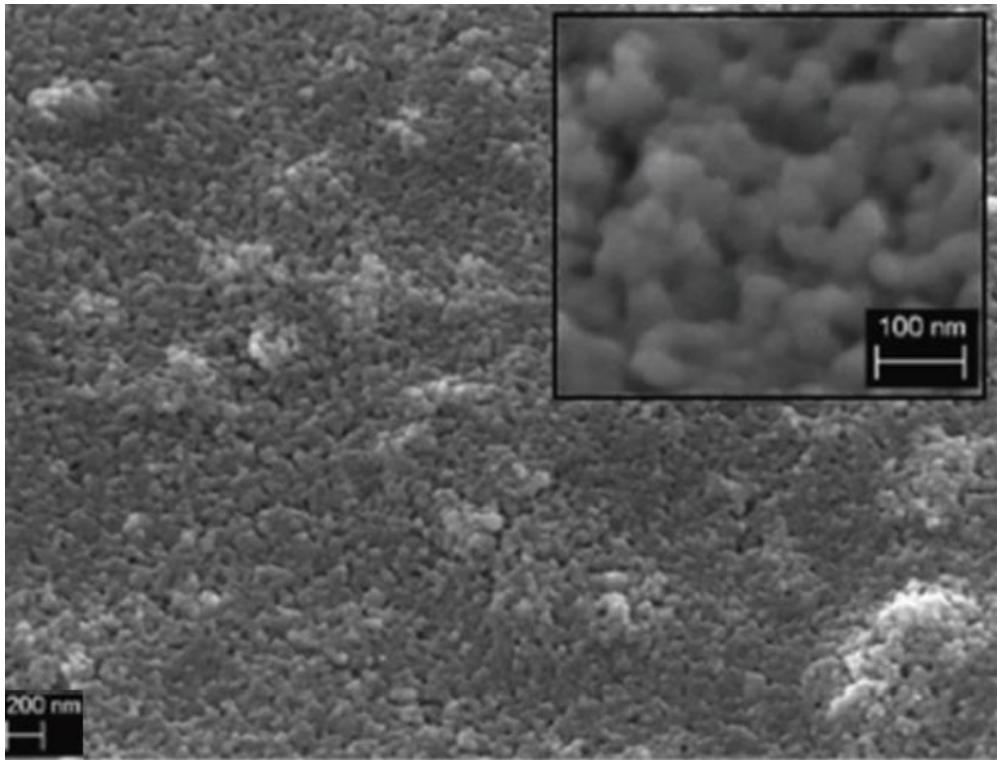


Figure 37 Field Electron Scanning Microscopy (FESEM) characterization to demonstrate the coating of the TiO_2 with the photopolymerized layers, electrodeposited on it with a time process of $t_e=45\text{s}$ [186].

By combining the photovoltaic, electrochemical and aging data, the existence of an optimal quantity of polymeric matrix able, at the same time, to ensure the fabrication of efficient and stable devices was demonstrated for the first time ever.

3 Chapter 3

The new 3D electrodes based on carbon nanofibers for Single Chamber Microbial Fuel Cells (SCMFCs)

One of the aims of my Ph.D. activity is the design of new electrodes able to improve the performances of Single Chamber Microbial Fuel Cells (SCMFCs). The SCMFCs are based on three different connected compartments which together form the inner chamber: the anode, the intermediate and the cathode compartments. As already explained, in the single chamber version of MFCs, in the present study, the cationic exchange membrane (PEM) is not present, the electrolyte, containing the oxidizing organic matter, is unique for both of anode and cathode and finally the diffusion of ions occurs into the liquid. The cathode in the open air configuration adopts the oxygen as the final electron acceptor. It is then necessary to modify the cathode in order to enhance the oxygen diffusion into the devices and to catalyze the oxygen reduction reaction.

The combination between the nanofibers, obtained through the electrospinning technique, and the commercial carbon based materials, used as electrodes in the energy field, open the doors to the investigation of these nanostructures as electrodes in microbial fuel cells.

The nanostructure provides an ideal habitat for the bacteria proliferations thanks to the high micrometric porosity nanofibers since that the bacteria dimensions are in order of some micrometer; in particular, the cross-linked nanofibers lead to the formation of 2D biofilm on them, which follow the connection among the nanofibers, improving the electron transfer from the bacteria to the electrode. Moreover, the high micrometric porosity of the materials, defined as the ratio between the volume of void spaces and the volume of bulk solid sample, enhances the penetration of bacteria and the diffusion of the chemical species, such as organic matter, used as a feed by the microorganisms in the anode compartment.

In particular, in my work, I obtained the carbon nanofibers by electrospinning process starting from a polymeric solution of polyacrylonitrile (PAN), used as a precursor of the carbon nanofibers thanks to its high yield of carbonization, its high intrinsic content of nitrogen and its templating role in order

to obtain the final mat of nanofibers. The N-N dimethylformamide (DMF) was selected as the solvent of the starting solution.

In order to design a carbon nanofibers mat applied as anode in SCMFCs, the carbonization was obtained by the pyrolysis treatment conducted under inert atmosphere until a final temperature of 600°C.

As deeply investigated below, this temperature permits to design a mat of nanofibers having a partial graphitization and a charge and surface chemistry proper to enhance the interaction with the microorganisms.

These kind of carbon nanofibers constitute a new 3D anode, leading to an improvement of the devices performances, which are greater than the ones obtained with the anode based on carbon based materials, like carbon felt (CF), or on activated carbon nanofibers [12,13]. As explained in the literature, the activated carbon nanofibers were obtained with a higher pyrolysis temperature and a successive necessary chemical treatment.

In order to design a carbon nanofibers mat applied as catalyst cathode in SCMFCs, the carbonization treatment was conducted until a temperature greater than or equal to 900°C, which was investigated in order to obtain a final mat of nanofibers with a high degree of graphitization.

3.1 Introduction

As widely investigated in the literature, the carbon in its various forms like powder, fibres and mats, has been found as the most promising material for the fabrication of electrodes for energy applications [187]. Many studies report the comparison between Microbial Fuel Cells based on different carbon anodic materials.

Indeed, the currently used anodes are often made of carbon paper, felt and cloth or built by graphite rods, plates and felt [188].

As deeply explained in the Chapter 1, the main limit of graphite rods is related to the low porosity value and surface area, which reduce bacteria proliferation on the anode. While, on the contrary, the use of graphite brush as anodes in a SCMFCs leads to a higher value of maximum power density

[188, 189]. Finally, carbon paper and carbon cloth are used in MFCs as a flat plate electrode [187, 190].

Moreover, many works in the literature underline how a higher amount of nitrogen content into the carbon based materials is mandatory to enhance the performances of MFCs [191, 192, 193]. Treatments, such as ammonia treatment or steam activation, induce a nitrogen doping into the materials, occurring consequently a positive surface charge, improving the interaction between the bacteria and the materials and then the devices performances.

In order to design a cathode in SCMFCs, many works in the literature modify the carbon based cathode with a proper catalyst layer, in order to guarantee the direct oxygen reduction reaction (ORR) [194, 195].

As already described, the direct ORR requires 4 electrons to fully reduce the oxygen and to produce water; if the cathode material is not able to sustain the 4 electrons reactions the intermediate one takes place, only partially reducing the oxygen and producing hydrogen peroxide, which results toxicant for the microorganisms and corrosive for electrode materials.

The catalyst cathode must then ensure a number of electrons as close as possible to the ideal value of 4, in order to minimize the hydrogen peroxide production and to favour the ORR kinetics. The Platinum is considered as the ideal catalyst for the ORR because it is able to guarantee a very high exchanged current density and consequently a number of electrons equal to 4 [196].

The main problem related to platinum is represented by its very high cost, so that many studies focus their attention to find a good and cheaper substitute [195, 197]. In order to achieve this goal, some works used no metal precious materials, such as iron, cobalt and copper phthalocyanine (FePc, CoPc, CuPc) [197], while others investigate materials based on graphene nanoparticles, nitrogen doped graphene nanosheets and graphene nanosheets modified with metal oxide [198, 199, 200].

One of the goal of my work is the development of carbon nanofibers, which can be applied as catalyst at the cathode in SCMFCs, leading to the complete ORR and constraining the intermediate one.

Among all the commercial carbon based materials applied both as anodes or cathodes, none exhibits all of the necessary characteristics. To generate electricity using bacteria in MFCs, highly conductive and non-corrosive materials are needed; those materials must have a high specific surface area and an open structure to avoid biofouling [201].

The required high porosity provides an ideal habitat for the bacteria, maximising their penetration into the electrode and, at the same time, increasing the diffusion of chemical elements, which can be organic substrate, if the materials are used as anode, or oxygen, if the samples were applied as cathode.

Porous carbon nanofibers have an extremely high length to diameter ratio, nanoscale diameter and ultrahigh specific surface area if compared to other carbon materials [202].

The carbon nanofibers applied as anode must have a proper value of conductivity to guarantee the electron flow among biofilm and anode, and between anode and cathode through an external load applied.

In my work, I obtained mat of nanofibers characterized by a high value of micrometric porosity and a large surface area to volume ratio. Usually, in the literature, all carbon nanofibers investigated as anode in MFCs, are treated until a values of temperature of 900°C or 1000°C under inert atmosphere [202] and then are successively activated with different treatments [202, 203, 204, 205] to ensure a nitrogen doped nanofibers in order to enhance bacteria growth on them and then the performances.

There are few works in the literature, which investigate the effect of nitrogen content already contained inside the materials, without any chemical treatments, and how this characteristic can improve the performances of SCMFCs [202, 203, 204, 205]

One of the goals of my work is to investigate and analyse the performances of single chamber microbial fuel cells (SCMFCs), realized using nitrogen doped carbon nanofibers as anode electrode; the nitrogen content was obtained defining conveniently the pyrolysis treatment, conducted up to a final temperature of 600°C.

This temperature, that theoretically ensures only a partial formation of the graphitic features, was selected to obtain a higher content of nitrogen without any functionalizing process needed. Moreover, the selected pyrolysis treatment guarantees a low cost process, able to ensure better morphological, chemical and electrical properties if compared with the commercial materials and with the activated carbon nanofibers analysed in the literature.

Regarding the cathode material, during my work carbon nanofibers treated at a final temperature of 900°C are applied, thanks to their high value of conductivity and electrocatalytic properties, which guarantee the ORR reactions.

This chapter will deeply investigate all the physical, optical and electrochemical characterizations performed on the materials, in order to demonstrate the achievement of all the characteristics stated before and the better performances in comparison with commercial material, such as carbon felt (CF) and carbon paper (CP). In this study, fresh water sediment from Valle D'Aosta was used as inoculum for SCMFCs. The characteristic of this sediment is the presence of a mixed bacteria culture, the derived biofilms were grown inside MFC with an external applied load of 47Ω. Then, in order to monitor the device performances, an external load of 1 k Ω was applied.

It will be demonstrated that the anode material results to have a better bio-electrochemical properties compared with the commercial one, evaluating that, the improved performances obtained, are due to the synthesis and properties of the carbon nanofibers [206].

Moreover, the cathode material shows a high graphitization features and consequently a major value of conductivity, enhancing the electrochemical behaviour of the material for the ORR.

All these results confirm the possibility to apply this kind of material as anode and cathode upgrading the performances of the device.

3.2 Experimental section: materials and nanofibers synthesis

The carbon nanofibers, developed as electrodes in SCFMCs, were obtained starting from a polymeric solutions based on polyacrylonitrile (PAN) in N-N Dymethylformamide (DMF).

PAN (average molecular weight $M_w=150,000$ kDa) and dymethylformamide DMF (assay 99.8%) were purchased from sigma Aldrich.

PAN in powder form was dissolved in a N-N dimethylformamide (DMF) solution at 60°C under continuous stirring to obtain a 12wt% stable solution that was then left at room temperature for 48 hours under continuous stirring for ageing.

The polymeric solution was loaded in a horizontal 6mL syringe connected, through a tube, to a spinneret vertically aligned with the needle (27 Gauge x 15 mm) and positioned into a NANON 01A electrospinning apparatus (MECC., LTD).

The spinneret, which constituted the first electrode in the electrospinning process, was powered with a high positive voltage provided by power supply (HVU-30P100) and connected to a feeding syringe pump setup operating with a flow rate ranging from 0.1 ml/h up to 99.9 ml/h.

During this process, a voltage of about 15kV was applied between the tip of the needle and the planar counter electrode plate, covered with a substrate, which is a carbon based material.

The working distance between the tip of the needle and the substrate was of 15 cm and the flow rate was defined of about 0.2 ml/h. The electrospinning process was performed for 3 hours.

As spun nanofibers were stabilized at 280°C in air for 120 minutes with a heating rate of 5°C/min. After stabilization phase, the nanofibers changed colour from white to a light brown.

After the stabilization, a second heating step was performed in a different way depending on whether the nanofiber have to be applied to the anode or the cathode.

In particular, in order to develop the new anode, the stabilized mat of nanofibers was then thermally treated up to 600°C under inert atmosphere, obtained through constant flow of Argon (equal to about 360 ccm), with a heating rate of 5°C/min.

This pyrolysis treatment was defined to ensure and demonstrate the higher formation of a nitrogen doped conductive carbon nanofibers and their correlation with the carbonization temperature.

While, the carbon nanofibers, built as cathode, were carbonized at a final temperature of 900°C under inert atmosphere with the same heating rate of the anodic ones. This more standard pyrolysis treatment was performed in order to obtain a higher graphitization degree of the material, optimizing the conductivity of the carbon nanofibers. The first sample was called PAN_600, treated at a less temperature and the second one was defined PAN_900, treated at a temperature of 900°C.

Moreover, for both mats of nanofibers, the electrospinning parameters were the same. The heated treatments were conducted by means of a vertical furnace (Carbolite, VST 12/300/3216). A summary of all defined parameters is reported in the Table 5 :

	Polymeric Precursor	Parameters	PAN_600	PAN_900
Electrospinning	Polyacrylonitrile (PAN):	Voltage	15 kV	
	The same polymeric precursor for both samples. PAN is template to ensure the nanofibers formations and for its high yield for carbonization	Working Distance	15 cm	
		Flow Rate	0.2 ml/h	
Pyrolysis		Max Temperature	600 °C	900 °C
		Heating Rate	5 °C/min	

Table 5 summarize of the electrospinning parameters defined in order to obtain a mat of nanofibers of PAN, used a precursor for carbon nanofibers and of the heated treatment parameters to have a final mat of carbon nanofibers.

The resulting samples are nonwoven mats of conductive carbon nanofibers with a high surface area. These samples are designed as 3D arrangement of the electrode and both of them are compared with commercial carbon based materials, respectively carbon Felt (CF, a commercial material purchased from Sigratherm, with a geometric area equal to 9 cm²) as anode and carbon paper (CP, a commercial material purchased from Fuel Cell Earth LLC) as cathode.

The final 3D arrangement of the electrode based on PAN_600 presents the following properties: a morphology closes to the scaffolds used in cell culture, good nitrogen content in the carbon nanofibers, a chemical surface able to favour the bacteria adhesion and electron transfer, and good electrical conductivity. All these characteristics are essential for the development of a performing bio anode. On the contrary, all the properties of carbon nanofibers PAN_900, like the superior electro-catalytic activities toward the ORR, the large specific surface area and excellent electrical conductivity, were satisfied leading to the application of carbon nanofibers as cathode.

3.3 Characterization on the carbon nanofibers

In order to confirm all fundamental properties that anode and cathode materials must satisfy, physical, morphological, electrical and electrochemical characterizations have been performed on both of carbon nanofibers (PAN_600 and PAN_900). Through the optical characterizations, such as Raman, Infrared spectroscopy (IR) and X-Ray Photoelectron spectroscopy (XPS), it is possible to define the properties of the materials depending on the chemical bonds between the elements, presented in the carbon nanofiber mats. These kind of characterizations, indeed, demonstrate the different content of nitrogen and its bonds with the nearby carbon atoms. The morphological characterizations, performed by Field Scanning Electron Microscopy, deeply show all the morphological information and properties of the nanofibers.

Finally, electrochemical characterizations, such as Cyclic Voltammetry, eventually performed using the RRDE setup, define the different electrochemical surface active area of PAN_600 and PAN_900 respectively and their electro-catalytic properties for ORR.

3.3.1 Morphological, Optical and Electrical characterization

The morphology of the samples was deeply analysed by Field Effect Scanning Electron Microscope (FESEM, ZEISS Merlin) technique, operating between 5 and 10 kV, equipped with an oxford energy dispersive X-ray detector.

Raman spectroscopy, obtained by means Renishaw 1000 spectrometer equipped with a 514.5 nm laser excitation, through a microscope objective (50×), was used to investigate the graphitic features of the samples.

Fourier Transform Infrared (FTIR) (Bruker Tensor 27) spectra were done in attenuated total reflection (ATR). Since both carbon nanofiber mats were electrospun on CF, which is not an IR-transparent material together with the possibility to preserve the nanostructures removing them from the substrate, the characterization was conducted in ATR mode. In particular, the ATR FTIR was performed on two different carbon nanofibers mats, PAN_600 and PAN_900 respectively, which have the same weight of 4 mg and the same thickness equal to 4 μm .

X-ray photoelectron spectroscopy (XPS), obtained by means A PHI 5000 Versaprobe scanning X-ray photoelectron spectrometer 169 (monochromatic Al K α X-ray source with 1486.6 eV energy), have been performed to define the chemical composition of both of PAN_600 and PAN_900.

Finally, electrical characterization was performed by polarising the samples applying different value of voltage (V) and measuring the current (I) that flows through the sample by means of a Keithley 2635A Source unit measure. The relation between voltage and current is exemplified by Ohm's Law, which permits the definition of bulk Resistance (R(V)) and consequently the conductance of PAN_600 and PAN_900.

3.3.2 Electrochemical characterizations

✓ Cyclic voltammetry (CV)

The cyclic voltammetry (CV) has been performed to investigate the different electrochemical surface active area of PAN_600 and PAN_900 respectively. The CV is performed with VSP biologic potentiostat. The characterizations were conducted in an electrochemical cell, containing a water based solution with 17mM (6.58g/l) of hexacyanoferrate of potassium (K₄Fe(CN)₆) and 34mM (13g/l) of sodium sulphate (Na₂SO₄). Inside the electrochemical cells, the tested materials are placed as working electrode, while a platinum wire was used as counter electrode and finally Ag/AgCl was applied as reference electrode. The CV characterizations were performed on PAN_600, PAN_900 and CF; all the samples were tested under two different conditions, in the first one the material was naked, without any bacteria on it, while in the second one the nanofibers were interconnected with the biofilm. All this tests are performed over the range of potential from -0.3 V to +0.9 V, replicating the procedures investigated in the literature [207, 208].

✓ Characterization by Rotating Ring Disk Electrode

The electrochemical characterizations, performed in order to establish the catalytic properties of the samples for the oxygen reduction reaction, were carried out by means of a CH Instrument 760D electrochemical workstation and an ALS RRDE-3A rotating ring disk electrode apparatus.

For all the measurements, the carbon nanofibers catalyst was fixed on the working electrode (a BioLogic glassy carbon disk/Pt ring, area 0.13 cm²).

For comparison purpose, commercial Pt/C (Sigma-Aldrich) was used as a reference catalyst. The commercial catalyst was dispersed in a solution containing 25 μl of water, 175 μl of Nafion[®] solution and 100 μl of 2-propanol. The mixture was ultra-sonicated for 2 min to form a uniform black dispersion. 10 μl of this formulation were cast-coated onto the disk surface to form a uniform film. The resulting deposition was dried at room temperature for one day. The final Pt loading was equal to 0.5 mg/cm^2 , used also for the catalyst layer, which is deposited on one side of the commercial carbon paper cathode.

The Pt wire was used as a counter electrode and Ag/AgCl as reference one. The electrolyte used was 0.1 M KOH O_2 -saturated aqueous solution and the experiments were conducted at room temperature.

For the rotating ring disk electrode (RRDE) measurements, the disk electrode was scanned from +0.2 to -0.8 V respect to the Ag/AgCl reference, with a rate of 5 mV/s and a fixed rotation speed of 2500 rpm, while the ring electrode was maintained at a fixed potential of 0.2 V. While scanning the disk potential at fixed rotation rate, the current disk and ring electrode is measured. The disk current is related to the four electrons ORR current, while the ring current is associated to the two electrons pathways. In particular, the ring electrode is made on platinum and it is applied a large potential value. The percentage of HO_2^- and the electron transfer number were calculated with the following Eq 55 and Eq 56, showing that the electron transfer number increases as the disk current increases:

$$\text{HO}_2^- \% = 200 \times \frac{I_R/N}{I_D + I_R/N} \quad \text{Eq 55}$$

$$n = 4 \times \frac{I_D}{I_D + I_R/N} \quad \text{Eq 56}$$

where I_R and I_D are the ring and disk currents, respectively, and N is the current collection efficiency of the Pt ring.

3.3.3 Biological characterizations on the nanofibers studied as anode

Regarding the samples applied as anodes, the cytotoxicity and the biofilm interaction with the mat of PAN_600 were investigated in comparison with carbon felt CF. The cytotoxicity of the samples is

analysed through the inclusion of materials within a gel made of agar, sodium acetate, peptone and microorganisms. The solution of Agar was based on 15g/l of agar, 1g/l of sodium acetate and 1.25 g/l of peptone in sterilized and deionized water. Then 100 µl of inoculum was diluted in 900 µl of sodium acetate solutions. The solution was then jellified leaving it to rest at room temperature, obtaining the agar plates in which the material has to be placed.

The anodes must not be cytotoxic for the bacteria proliferation. In fact, when new materials are developed, first of all it is mandatory to conduct a test in agar plates in order to establish the no cytotoxicity properties of the sample; in particular, the no cytotoxicity of the material is verified by the proliferation of the bacteria on the sample and around it; on the contrary, if the material results to be cytotoxic, around the sample appear the so-called “cytotoxic ring”, an empty area in which the bacteria are unable to grow.

The ring can be formed, for example, around a samples covered by silver, whereof cytotoxicity properties for the microorganisms are well known.

Moreover, to investigate the interaction between the bacteria and the materials, the samples have been put in a falcon containing a solution of 2.5g/l of sodium acetate and microorganisms. PAN_600 and CF have been left in this solution for 1 month. The consequently formation of biofilm, interconnected with the samples, is evaluated through morphological characterizations by (FESEM, ZEISS Merlin) technique, for which a standard fixation protocol, based on glutaraldehyde solution, is needed [209, 210]. Before the analysis of the microstructural morphological characteristics by FESEM, the fixation of the bacteria is mandatory to prevent alterations in their structure through decomposition. According to this protocol, the cross-linker used is the glutaraldehyde. The glutaraldehyde ($CH_2(CH_2CHO)_2$) reacts with some microorganisms 'proteins in order to form crosslinks between their proteins, fixing the biofilm on the samples.

A section of all samples is left in a solution containing 2wt% of glutaraldehyde dissolved in a phosphate buffer saline (PBS) solution for 1 hour at room temperature.

The samples are then washed three times in a PBS buffer solution, followed by stepwise dehydration in a series of five ethanol/water dilutions, with an incremental percentage of ethanol (30%, 50%,

70%, 80%, 90%). The samples remain in all the different solutions for 15 minutes and then they are placed into 100% ethanol solution overnight.

Finally, the materials were dried through a chemical way, based on mixed solutions of Hexamethyldisilazane (HDMS) and Ethanol with two different volume ratios, respectively 1:2 and 2:1. The chemical removal of water is necessary to further denature the proteins of the microorganisms. PAN_600, and CF remained in each solution for 15 min and then they were left in a solution of 100% HDMS for 1hour and 30 minutes.

3.4 Single chamber MFC architecture and operation mode

In this work, squared single chamber MFC devices, with an open air cathode configuration, is used. The devices have been realized by 3D printer (OBJET 30) and are composed by 3 different compartments: the anodic part, the intermediate compartment and the cathode one, as represented in Figure 38. The area of both anodic and cathode compartments is equal to 6.25 cm^2 , and the volume occupied by the electrolyte is 9 ml.

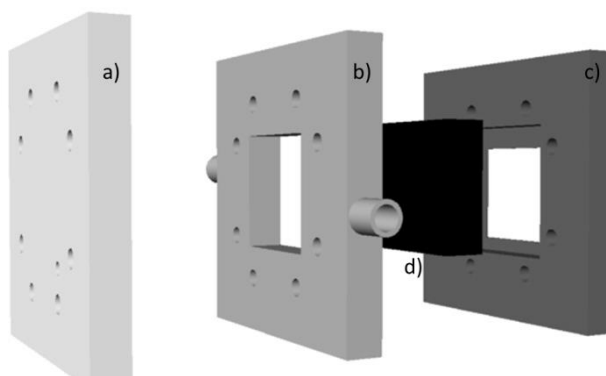


Figure 38 3D polymeric single chamber microbial fuel cell (SMFC). a) anodic chamber; b) intermediate space and c) cathode chamber and d) represents an example of cathode electrode obtained cutting a piece $3 \times 3 \text{ cm}^2$ of CF

As deeply explained previously, the carbon nanofibers PAN_600 are designed as anode, and they are compared with anode based on carbon felt (CF); on the contrary, the PAN_900 samples are applied as catalyst cathode with the flat carbon paper (CP) properly modified with the Catalyst Layer based on Pt/Nafion.

In particular, during this work, in the SCMFCs devices, where carbon nanofibers PAN_600 constituted the anode electrode, the cathode is based on the modified carbon felt (CF).

In this case, the cathode is properly modified, in order to ensure the diffusion of oxygen from outside to inside the MFC and the catalysis of oxygen reduction reaction (ORR). A squared shape of 3x3 cm of CF was cut. On one side of CF, 4 layers of polytetrafluoroethylene (PTFE) are applied, known as Diffusion Layers (DLs), while on the opposite side a layer based on Platinum and Nafion™ is deposited, defined as catalyst layer (CLs), usually based on platinum [38].

Each layer of PTFE (built by deposition of a solution of 60 wt% PTFE dissolved in deionized water, purchased from Fuel Cell EARTH LLC, USA) is dried at 370 °C in air for 15 min. While the catalyst layers are based on a mixture of platinum (Pt 0.5 mg/cm², purchased from Sigma Aldrich), Nafion™ (5wt% Nafion purchased from Sigma Aldrich) and isopropanol; the mixture of Nafion™ and isopropanol is used to ensure the adhesion of Platinum on the cathode. In particular, the CLs is dried in air at room temperature for 1 day.

On the contrary, the catalyst layer based on carbon nanofibers PAN_900, developed as catalyst cathode, is applied on the flat carbon paper.

Stainless steel wires are used to guarantee a good electrical contact; in particular, they are threaded in a grid in contact with the cathode and with the anode respectively. Two different values of external resistances have been applied: the first external load is equal to 47 Ω in order to ensure the formation of biofilm on the anode, while the second one is equal to 1000 Ω and it has been applied to evaluate the final device performances.

✓ **Electrochemical impedance spectroscopy (EIS)**

The internal ohmic resistances of the SCMFC have been evaluated through the electrochemical impedance spectroscopy (EIS). The EIS spectroscopy was performed by means VSP biologic potentiostat.

This method is based on the measured dynamic response of the cell, using the potentiostat to obtain the data. In particular, EIS sum a sinusoidal signal with small amplitude on the applied potential of the working electrode. By varying the frequency of the sinusoidal signal over a wide range, typically

from 10^{-4} to 10^6 Hz, the electrode impedance spectra can be obtained providing many detailed information of the system [14]. Usually the impedance measurements, that aim to define the internal resistance of the cell, is conducted under OCV conditions. The Nyquist plot, defined as the real impedance $Z_{\text{real}} (\Omega)$ versus the imaginary one $-Z_{\text{im}} (\Omega)$, is used to represent the data obtained. In the EIS-Nyquist plot, three different processes can be recognized. It is possible to define the value of the Ohmic resistance (R_s) as the intersection between the x-axis and the projection of the first semi arch that belong in the high frequency region. The charge-transfer resistance of the different anodes (R_{ct}) is defined as the intersection of the projected second semi arch with the x-axis, normally occurred in the middle frequency region. Finally, the straight line (on the right), that belong in the low frequency region, describes the resistance related to the interface between the electrolyte solution and the catalyst layer on cathode. In this work, EIS has been conducted in Open Circuit Voltage conditions (OCV) over the range of frequency between 150 MHz to 200mHz, summing a sinusoidal signal with an amplitude of 25 mV.

✓ **Linear Sweep Voltammetry**

Linear Sweep Voltammetry (LSV) is performed on the Single Chamber Microbial Fuel Cells containing the carbon nanofibers as anodes, compared with the anode based on CF, used as reference anode material. The target of the LSV is to estimate the polarization curves measuring the current density changes, when different values of voltage are applied [211]. In particular, the SCMFCs are set up in OCV configuration for some hours before this characterization in order to verify that the devices reach the steady state conditions. The LSV intrinsically estimates, through the direct correlation between the measured current and the applied voltage, the quality of biofilm and the ability to adapt itself to the different values of applied voltage. Moreover, through the LSV characterization, the power density curve is defined establishing the maximum value of power density achievable with SCMFCs. In particular, if and only if the power density curve is a symmetric curve, the maximum power density occurs when the internal resistance is equal to the external one, approaching an evaluation of the internal resistance of the devices [211]. It is important to perform this kind of characterization on the SCFMCs containing PAN_600 nanofibers as anode in order to deeply investigate the contribute of new nanostructured anode on the devices' performances. In this work,

the LSV is performed through the VSP biologic potentiostat that change the values of the applied voltage during time starting from the OCV value to the short circuit one with a fixed slope of 1mVs^{-1} and the current changes are measured.

3.5 Results and Discussion

3.5.1 Optical, physical and electrical characterizations results

Carbon nanofibers have been obtained starting from an electrospun polymeric solution and after carbonizing the mat of nanofibers through the definition of heating treatments based on two different steps, as explained previously and in some works in the literature [206, 212, 213, 214]. In particular, the first step is defined as oxidative stabilization of PAN, where the process is conducted in air and the final temperature is equal to $280\text{ }^{\circ}\text{C}$; one of the results of this step is the formation of double bond between the carbon atoms, occurred after the loss of two hydrogen atoms from the main carbon chains and so the resulting formation of a molecule of water, as shown in Figure 39. Moreover, at the same time, the second result was the formation of a cyclic structure allowed by the nitrogen, which break the nitrile bonds in the linear polymeric chain and makes a bond with a nearby carbon atom [206].

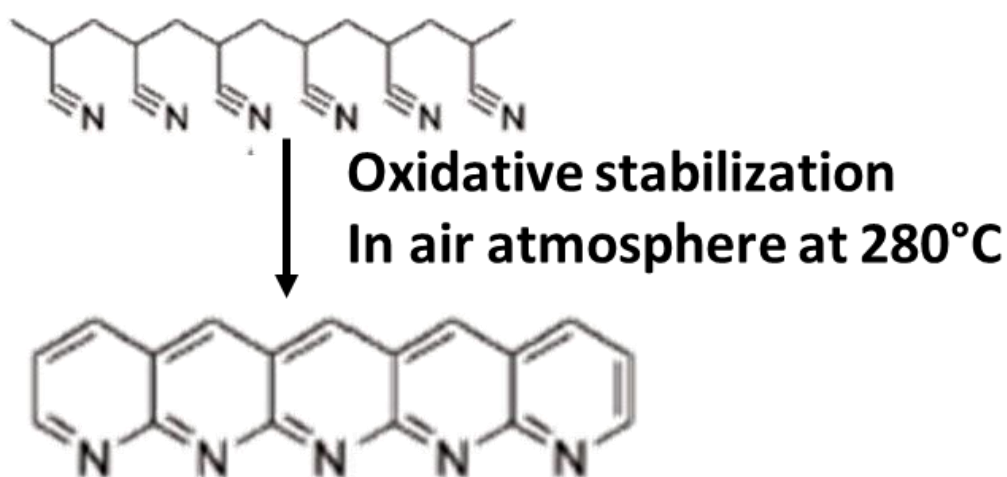


Figure 39 represents the formation of a cyclic structure occurring during the oxidative stabilization in air atmosphere at 280°C [206]

This stabilization phase is defined equal for both of two different samples, PAN_600 and PAN_900, while, on the contrary, the second step is quite different. Indeed, for PAN_600 samples the second step is conducted under inert atmosphere up to the final temperature of 600°C, while for PAN_900 the final temperature was equal to 900°C, as explained in the experimental section. It was deeply investigated in the literature, how for temperature lower or equal to 600°C, the process can be defined **carbonization (or dehydrogenation)**, in which the cyclic structure starts to arrange itself to get the formation of small size graphene sheets, as represented in Figure 40 [206, 212, 213, 214].

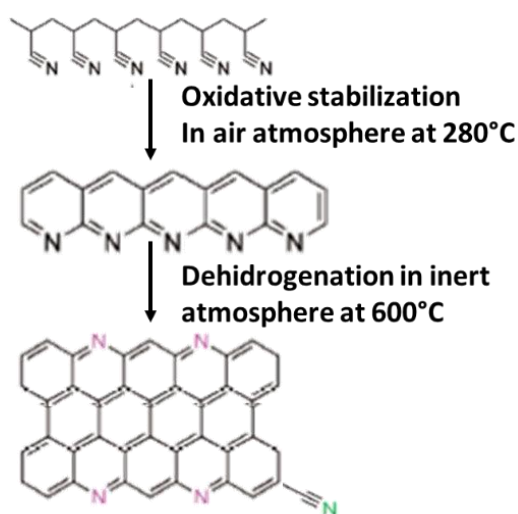


Figure 40 is a schematic representation of dehydrogenation occurring when the heating treatment is defined up to 600°C under inert atmosphere [191]

In these samples the amount of nitrogen is correlated, respectively, with the pyridinic-N, placing on the edge of the partial graphitic sheet, and with the pyrrolic one (see Figure 41). In particular, the pyridinic nitrogen is formed at the edge of the graphene sheet, when the cyclic carbon structure has been preserved. The pyridinic nitrogen is bonded with the two nearby carbon atoms and it donates one π -electron to the aromatic system and consequently it has a single electron pair in the plane of the carbon matrix. For this reason, the surface area of the materials exhibits a partial positive surface charge: the positive surface charge of the carbon nanofibers, due to the presence of the pyridinic nitrogen, can increase the adhesion with the bacteria [191]. The pyrrolic nitrogen, instead, is due to the nitrogen atoms that are bonded to two carbon atoms and contribute to the π -system

with two π - electrons. Differently to the pyridinic nitrogen, the pyrrolic one has all bonds saturated. The heating process obtained with temperatures greater than 600°C is known as **dehydrogenation** or carbonization; during this phase, in particular, a molecule of HCN broke out, a reduction of nitrogen content occurred and at the same time the graphitization of materials increases with the temperatures. In this case, the graphitic nitrogen results to be predominant in the graphitic sheets constituting the materials. The Graphitic-center N (III) and Graphitic-valley N (IV) are due to the trapped nitrogen in the main carbon chains during the graphitization steps. Both of two nitrogen types are called quaternary nitrogen. All these different kinds of nitrogen distributed into the PAN_600 and PAN_900 samples are represented in Figure 41.

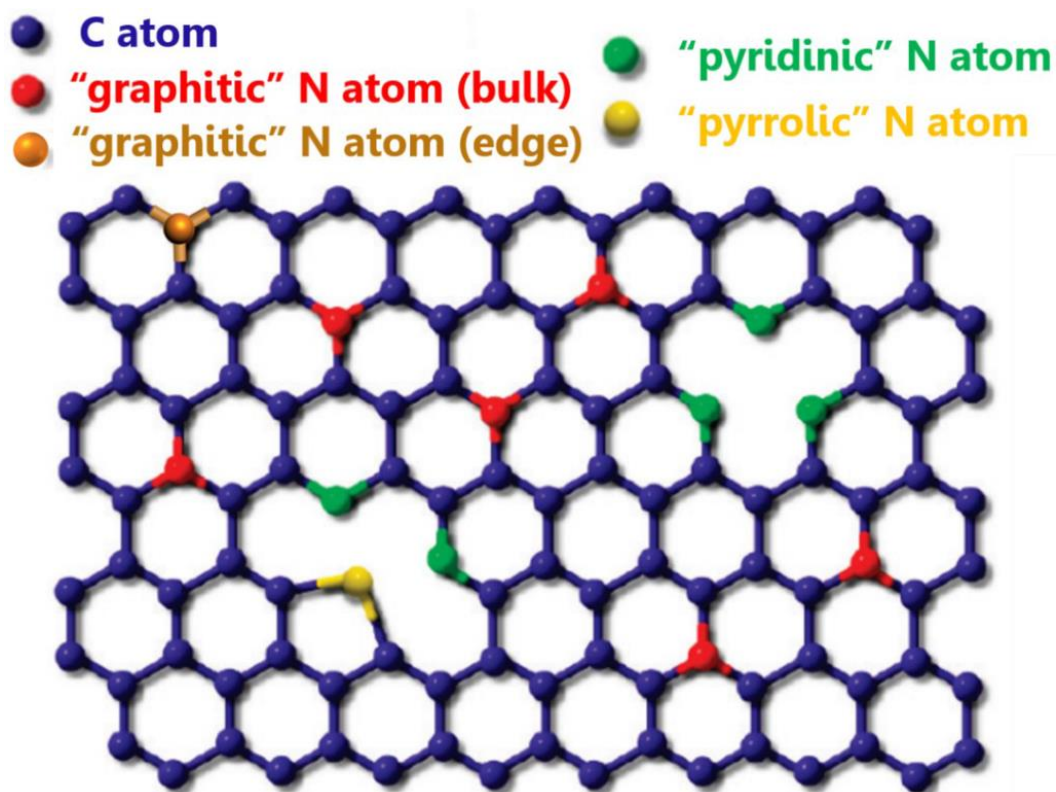


Figure 41 [215] shows how the different types of nitrogen were distributed in the graphitic sheets. The red dots represent the graphitic nitrogen, which is trapped in the sheet; the pyridinic N, represented by the green dot, is at the edge of the plain and it was a free bond, incrementing the reactivity of the samples; the pyrrolic N, (yellow dot), has all bond saturated; finally, the dark yellow dot represents the graphitic nitrogen.

The XPS spectroscopy is performed in order to investigate the content of nitrogen and its position related to the nearby carbon atoms in the main chains of both of samples, PAN_600 and PAN_900. The survey XPS spectra, shown in Figure 42, verify the presence of oxygen, nitrogen and carbon, as expected from the polymeric precursor used, and demonstrated the expected correlation between the temperature and the nitrogen content: the lower is the nitrogen content, the higher is the pyrolysis temperature. Indeed, the nitrogen content decrease from 15.1 at%, to 12.70 at% and to 1.95 at% as the temperature increases from 280°C, to 600°C and to 900 °C respectively.

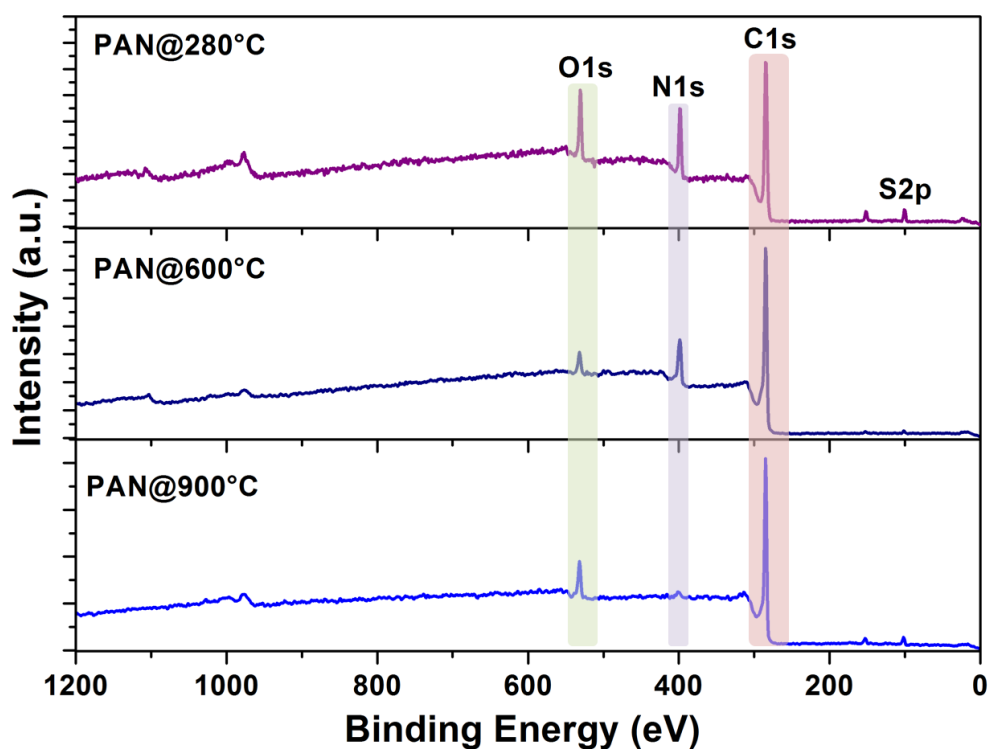


Figure 42 The survey spectra of carbon nanofibers at different temperature a) 280°C, b)600°C, c) 900°C

The high resolution XPS spectra of C1s, represented in Figure 43a), confirm how the degree of graphitization increases with the pyrolysis temperature. The intensity of the peaks related to the bond C-C (284.6 eV), which can be defined as Graphitic-C, is higher in the samples PAN_900 than one obtained for PAN_600 nanofibers.

Other two peaks are revealed by the high resolution C1s spectra, as shown in Figure 43a): the first peak at 286 eV corresponding to the C-H and/or C-N bonds , whose intensity decreases and

disappears for PAN_900 carbon nanofibers; the second one at 287.3 eV relating to the double bonds between oxygen and carbon atoms $C=O$, which there is only in the mat of nanofibers treated at a 280 °C.

The high resolution N1s spectra define the different content and species of nitrogen atoms and their bonds with the nearby carbon atoms, as represented in Figure 43 b).

In particular, N1s spectra define the presence of four different species of nitrogen [206, 212]: N1s (I) pyridinic (398.2 eV); N1s (II) pyrrolic (399.5 eV); Graphitic-center N (III) (403.2 eV); Graphitic-valley N (IV) or quaternary nitrogen (400.9 eV).

The carbon nanofibers PAN_600 are characterized by higher atomic percentage of pyridinic-N than one presents in the PAN_900 samples, as shown in Figure 43 b) and as summarized in the Table 6.

The higher content of pyridinic nitrogen should enhance the electrochemical activity of PAN_600 carbon nanofibers, evaluated by the Cyclic Voltammetry characterizations. Moreover, thanks to the presence of pyridinic nitrogen, the surface chemistry of PAN_600 improves the interaction between the bacteria and the carbon nanofibers and consequently increases the performances of SCMFCs.

N1s spectra confirm how the content of pyrrolic nitrogen is higher during the stabilization step conducted at 280°C, then it decreases in the PAN_600 samples and it almost completely disappears in the PAN_900 materials.

Figure 43 b) demonstrates that the content of both graphitic-center N and graphitic-valley N result higher in the PAN_900 samples than that present in the PAN_600 nanofibers, as also summarized in the Table 6.

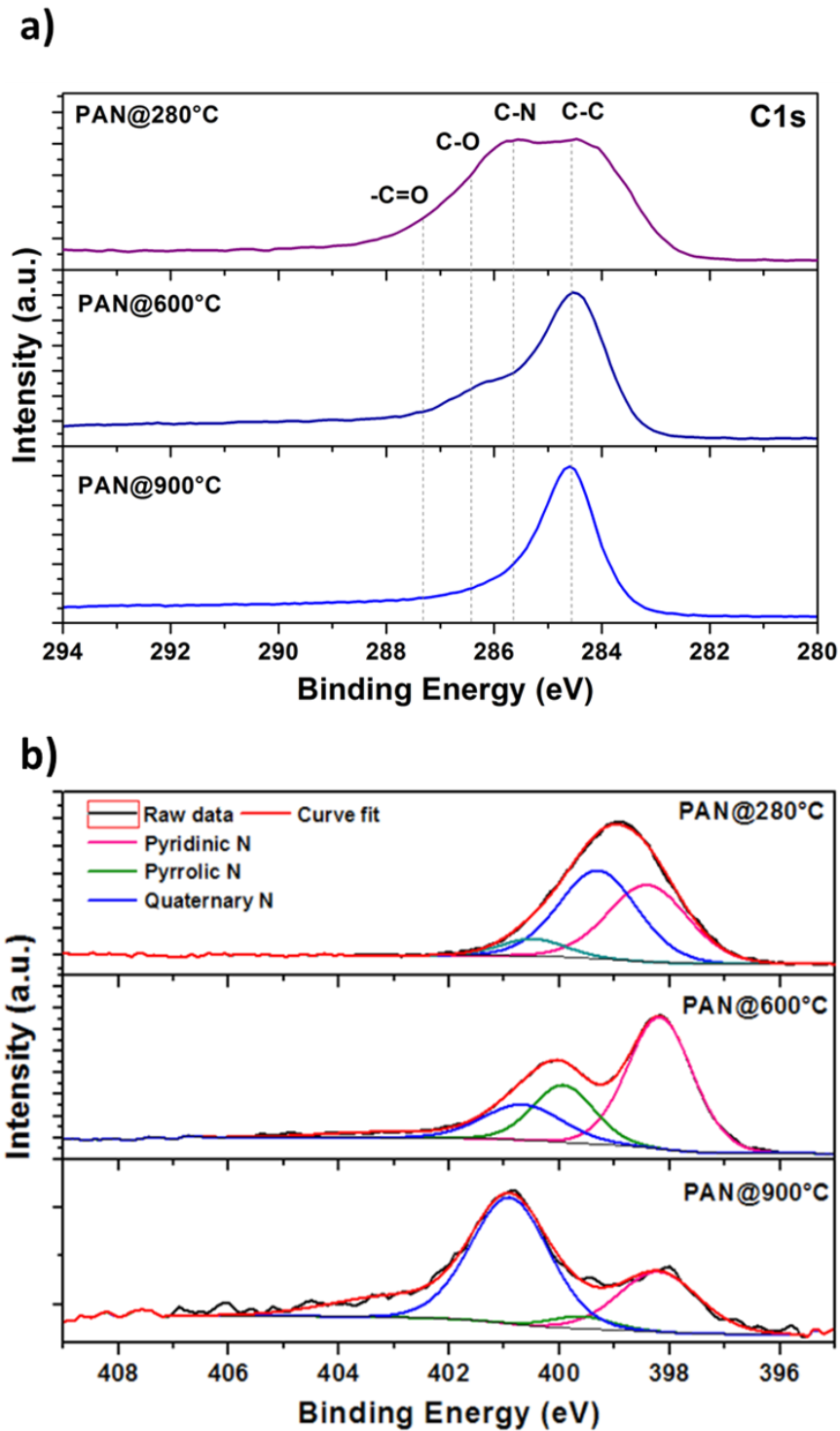


Figure 43 represents the high resolution spectra respectively a) C1s and b) N1s for the nanofibers treated at different temperature (@280°C, @600°C and @900°C)

Chapter 3
The new 3D electrodes based on carbon nanofibers for Single Chamber Microbial Fuel Cells (SCMFCs)

In line with the literature conclusions [206, 212, 213, 214], these results verify how the PAN_600 nanofibers are characterized by an initial graphitization phase, confirmed by the presence of graphitic-center N(III), and, at the same time their higher content of pyridinic and pyrrolic nitrogen allow to increase the electro-catalytic properties of the carbon nanofibers without other treatments. Thanks to the high content of pyridinic-N, the PAN_600 shows a positive charge distribution on its surface area, leading thus to the improvement of the bacteria growth on the sample. The PAN_900 nanofibers are characterized by a more evident graphitization phase confirmed by the higher value of conductivity of the samples, by a low content of pyridinic and pyrrolic nitrogen in the carbon nanofibers and by a greater amount of graphitic Center-N(III) and graphitic Valley-N(IV). In line with the finding results, the high conductivity of PAN_900, high content of graphitic nitrogen and an enough amount of pyridinic nitrogen should enhance its electro-catalytic property for ORR, since according to the literature, the N(III), N(IV) and pyridinic N(I) provide better ORR performances [191, 206].

Atomic concentration (at.%)	PAN@280 °C	PAN@600 °C	PAN@900 °C
C	71.8	83.0	88.8
O	9.9	3.5	6.7
N	15.0	12.7	2.0
Si	3.3	0.7	2.5
N1s components*			
Pyridinic-N (I)	43.4	55.1	26.7
Pyrrolic-N (II)	48.8	22.4	4.2
Graphitic-center N (III)	7.8	18.0	55.1
Graphitic-valley N (IV)	-	4.5	14.0

Table 6 Atomic percentage of carbon, oxygen and nitrogen obtained from the XPS characterization and related to the carbon nanofibers obtained from the same precursor PAN but heated ad different pyrolysis temperature [212].

The different content of nitrogen in the PAN_600 and PAN_900 is also demonstrated by the Infrared spectroscopy, conducted in ATR mode. This characterization is performed on both PAN_600 and PAN_900; the two samples are characterized by the same weight of 4 mg and the same thickness equal to 4 μm . The ATR-FTIR spectra of carbon nanofibers defines the absorption peaks related to stretching of different bonds between three elements, such as nitrogen, oxygen and carbon, whose content is dependent on the different temperature [216, 217]. The positions of adsorption bands are in a good agreement with the results explained in some works in the literature [216, 217].

In particular, in Figure 44 the two different spectra underline the presence of absorption peaks related to the bonds with nitrogen: N-H stretching vibration at 3400 cm^{-1} ; C-N stretching aromatic amine at 1294 cm^{-1} and the last one at 1570 cm^{-1} related probably with C=C or C= N.

The light blue line of Figure 44 represents the FTIR spectrum performed on the PAN_900, while the green one shows the FTIR spectrum, conducted on PAN_600. The higher intensity of peaks in the spectra related to PAN_600 demonstrate a larger amount of nitrogen bonds respect to the less nitrogen bonds related to the PAN_900 as underlined by its relative spectrum. These obtained results are in line with the key findings on the surface chemistry of carbon nanofibers obtained changing the temperature treatment [216, 217]; the nitrogen bonds on the surface of PAN_600 nanofibers are higher than ones on the surface of PAN_900.

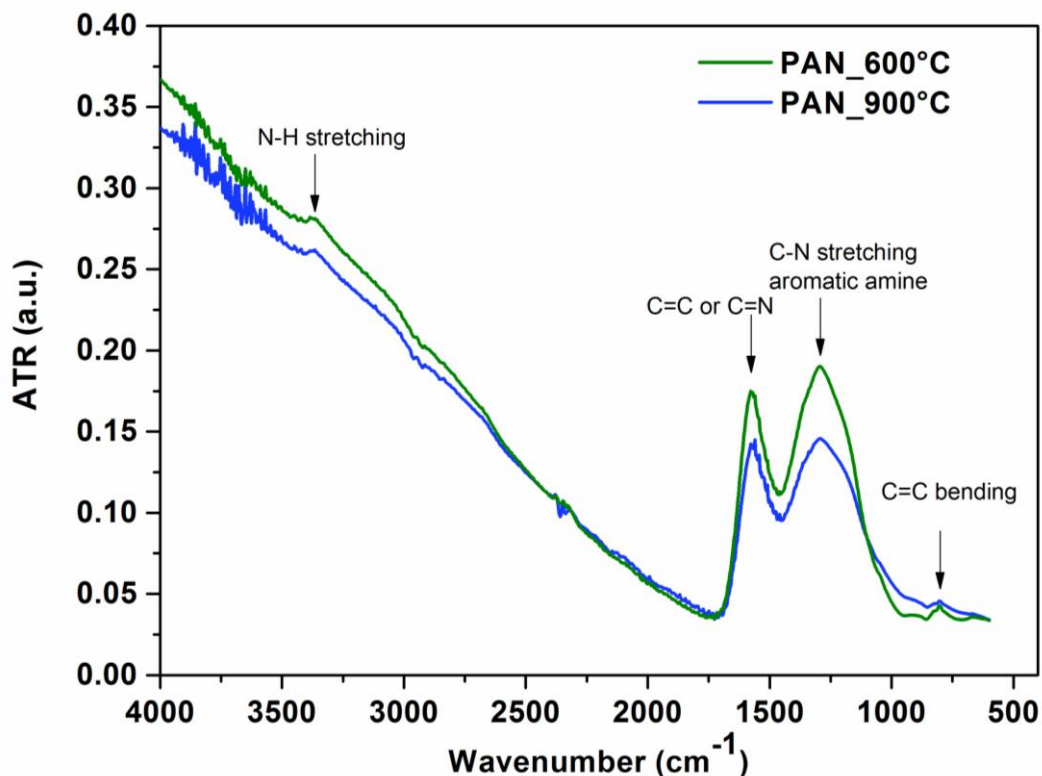


Figure 44 shows the comparison between the ATR-FTIR spectra for PAN_900 (light blue line), and the ATR-FTIR spectra for PAN_600 (dark blue line). ATR-FTIR spectra demonstrates that the intensities of peaks related to the nitrogen bonds on the surface of PAN_900 are smaller than the PAN_600 ones, which have the same weight of 4mg.

The initial graphitization phase, characterizing the PAN_600 carbon nanofibers, was confirmed by Raman spectroscopy.

The Raman spectroscopy was performed on both of samples, PAN_600 and PAN_900, as shown in Figure 45; it demonstrated that PAN_600 carbon nanofibers exhibit an initial and partial graphitization, while the graphitic features of PAN_900 are more evident. In particular, the green curve represents the Raman spectrum for PAN_600, while the light blue one shows the Raman spectrum for PAN_900; the D and G peaks regions, which are characteristics for the carbon based materials, are fitted through the Gaussian-Lorentzian mixed functions and, moreover, they are defined for both of 2 samples. The line centered near to 1360 cm^{-1} is due to the disordered portion

of the carbons; it is possible to observe how the peak of D-band is higher for PAN_600 samples than one characterizing the PAN_900. The second line centered close to 1581 cm^{-1} represents the graphitic part and it is more intense for PAN 900, confirming the higher graphitization of this material. It is also possible to define the ratio between the intensity of D and G peaks (Eq 57), known as

$$R = I_D / I_G \quad \text{Eq 57}$$

where I_D and I_G are the intensities of D and G peaks respectively. As explained in many works in the literature [218, 219], R is a measure of the ordering sp^2 phase. For PAN_600 the value of R is of about 1.2, which could represent a good but not complete graphitization phase, while for PAN_900 the value of R is very close to 1, in line with the properties demonstrated before. Finally, the dimensions of graphitic crystals can be defined through the following relation (Eq 58):

$$L_a(\text{nm}) = 4.4 / R \quad \text{Eq 58}$$

Where R is the ratio between the two intensity peaks defined previously by the Eq 57. As expected, the value of L_a is lower for PAN_600, which is about (3.7 nm), than that obtained for PAN_900, closes to (5 nm).

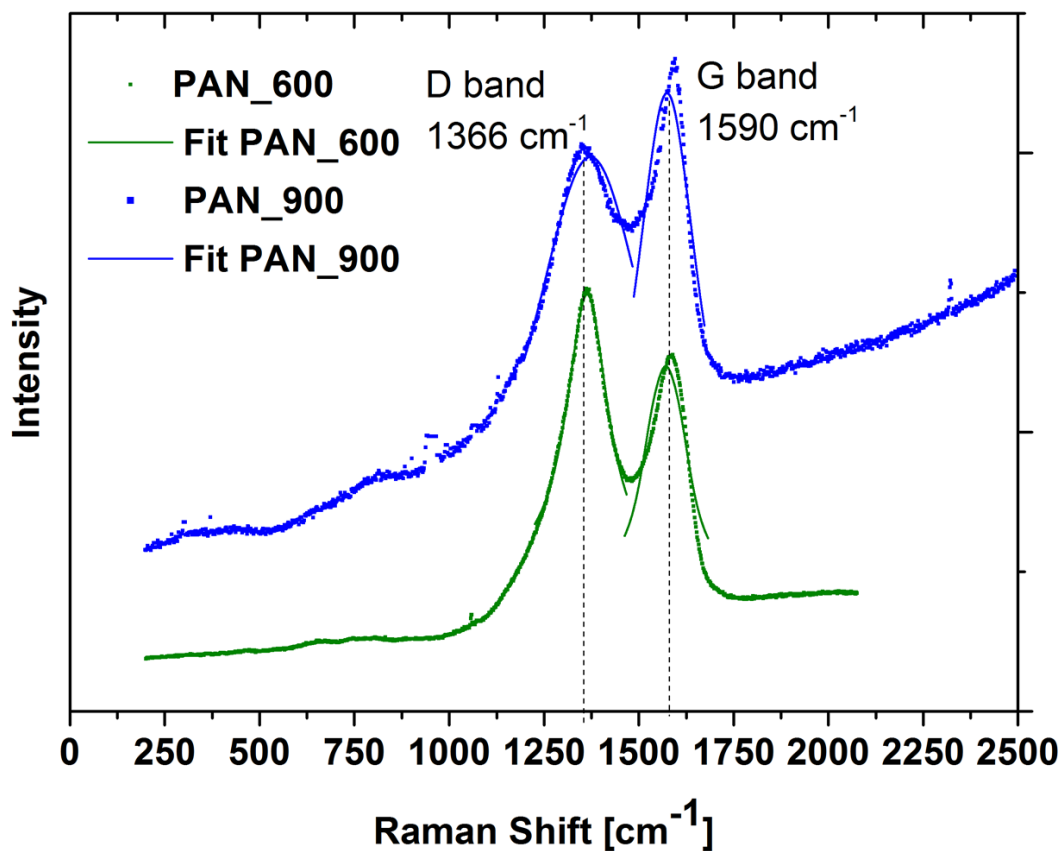


Figure 45 Raman Spectroscopy performed on the nanofibers pyrolyzed at 600°C and on PAN_900 samples. The definition of D-band and G-band confirm the presence of graphitic features in the mat of nanofibers; in particular, the degree of graphitization is higher in the PAN_900 than one obtained in the PAN_600 sample.

Finally, the electrical characterizations permit to define the conductivity of the carbon nanofibers, which increases as the pyrolysis temperature. The values of the electrical conductivity confirm all the physical characterizations performed on both 2 samples. In particular, the conductivity of PAN_600 closes to 1.16 mS/cm, results to be two orders of magnitude lower than that of PAN_900, equal to 520 mS/cm.

3.5.2 Electrochemical characterizations results

✓ Cyclic voltammetry (CV) results

The improvement of electro-catalytic properties of the carbon nanofibers, due to the high content of pyridinic nitrogen in the PAN_600 nanofibers, is emphasized by the cyclic voltammetry (CV) characterizations.

The key role of the nitrogen, needed for the improvement of electro-catalytic properties of carbon nanofibers, is emphasized by the cyclic voltammetry (CV) characterizations. The electrochemical characterizations are performed on PAN_600, PAN 900, with and without a biofilm interconnected with the materials [207, 208]. The carbon felt is used as the reference material during all tests. All the materials are defined as working electrode in the electrochemical cell, where the electrolyte contained hexacyanoferrate of potassium, as explained into the Experimental Section.

The CV characterizations conducted on PAN_600 (light blue curve in Figure 46) underline the presence of the current peaks, related to the oxidation (in correspondence of -0.2V) and to the reduction (at 0.65V) of hexacyanoferrate of potassium; while, on the contrary, the red and the green line, representing PAN_900 and CF respectively, does not show any current peak during CV tests. Nevertheless, the current flowing into PAN_900 and CF was one order of magnitude higher than that into PAN_600, underlining a better conductivity. The same observations can be done also for the samples interconnected with the biofilm.

These results confirmed the good electro-catalytic behaviours of the PAN_600; while the PAN_900 and CF were characterized by worse electro-catalytic behaviour.

Moreover, as shown in Figure 46 a) and b), the formation of biofilm on the nanofibers, treated at 600 °C (pink curve), induced an increment of the peak currents obtained, which varied from 0.45 to 0.6 mA, revealing a higher electroactive area of the samples. This result can be explained considering the combination between the active role of biofilm and nitrogen doping for the iron reduction process.

While, on the contrary, for PAN_900 the current peaks decrease from 6 mA to 2 mA when the biofilm is formed, as shown by the green curve. In this case the presence of the microorganisms seems to be a limiting factor for the catalytic activity.

The electroactive area is defined implementing Matsuda's Equation [207], represented by the Eq 59:

$$i_p = 0.4464 * 10^{-3} * \frac{n^{3/2} * F^3 * D^{1/2} * \nu^{1/2} * C * A}{R^{1/2} * T^{1/2}} \quad \text{Eq 59}$$

Where $n=1$ is the number of electron transferred, $F = 96487 \text{ C/mol}$ is Faraday's constant, $R = 8.314 \text{ J/mol} * K$ is the gas constant, T is the temperature, $C (\text{mol/cm}^3)$ is the initial ferrocyanide concentration and $\nu = 5 \text{ mV/s}$ is the scan rate. The effective diffusion coefficient of ferricyanide of potassium is equal to $D = 5.79 * 10^{-6} \text{ cm}^2/\text{s}$. Starting from the CV characterizations, the current peak is defined and consequently the surface electroactive area (A) is calculated. The electroactive area of an electrode is related to its surface and its determination is an essential step in order to characterize the electrochemical behaviour of materials. However, it is important to consider the geometric dimension of the electrodes (A_e) of both samples used during CV characterizations: A_e of PAN_600 is equal to 3.5 cm^2 and A_e of PAN_900 is 4 cm^2 . According to the Eq 59, PAN_600 carbon nanofibers have an electroactive surface area that is closed to 3.5 cm^2 , confirming thus that all surface area can be considered electroactive; while the electroactive surface area of PAN_900 carbon nanofibers is only 2.5 cm^2 and so 62,5% of A_e can be defined as electroactive area for this material. In conclusion, in this work in order to develop an anode, the final pyrolysis temperature equal to 600°C is selected thanks to all properties that the samples present. The PAN_600 carbon nanofibers intrinsically present the necessary content of nitrogen to optimize their electro-catalytic properties improving the interaction between the microorganisms and nanofibers. In the literature, these results with these kinds of functionalization were obtained only through the successive chemical treatments, such as ammonia treatments, steam activation [202, 203, 204, 205]. Moreover, as confirmed by all these characterizations, a proper surface chemistry and probably a positive surface charge of PAN_600 guarantee the good interactions between the nanofibers and bacteria, increasing the performances of SCMFCs.

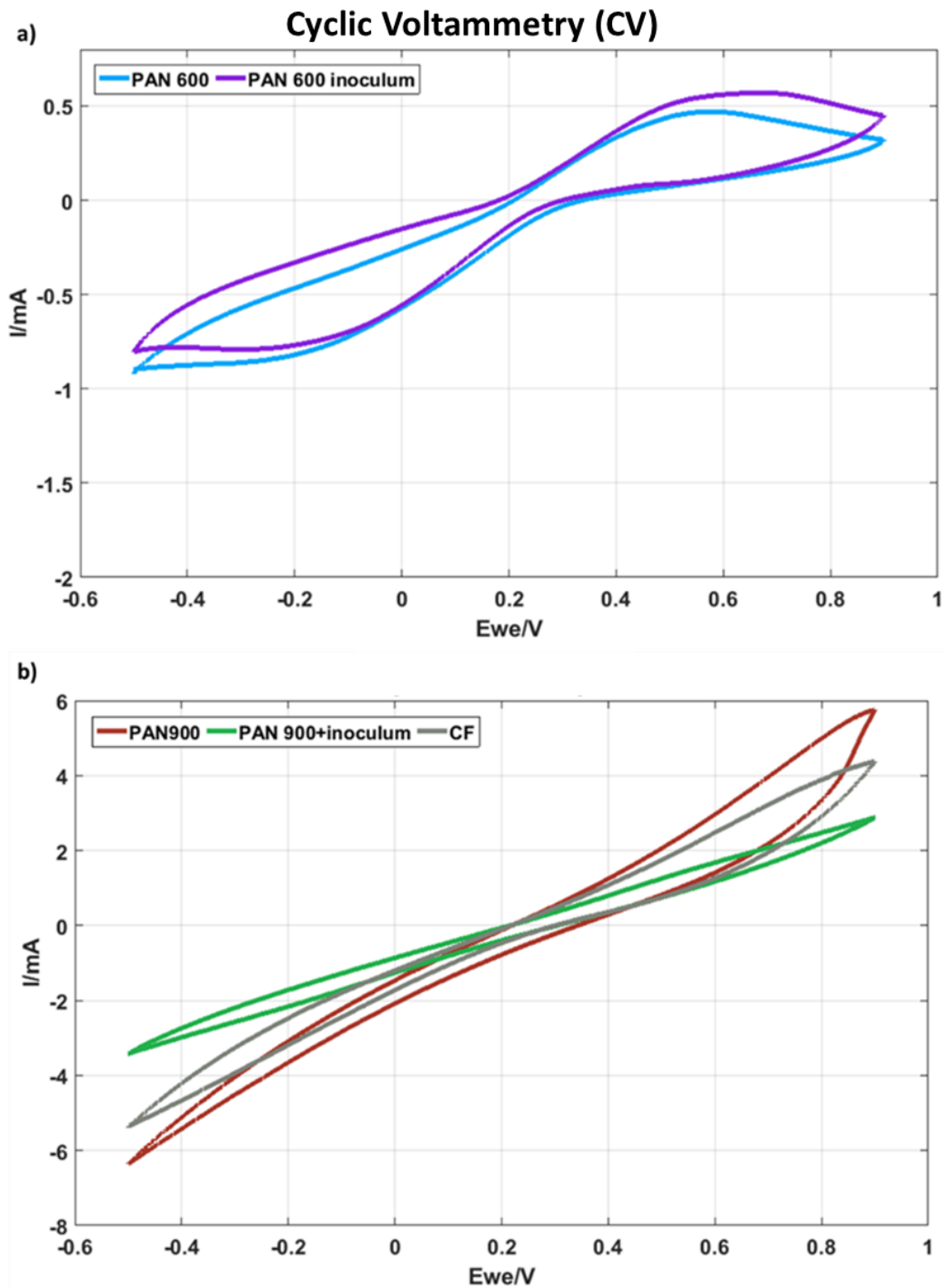


Figure 46 represent the Cyclic voltammetry conducted on the different samples. a) represents the comparison between the PAN_600 nanofibers (light blue curve) and the PAN_600 with the adhesion of microorganisms (pink curve); b) show the cyclic voltammetry conducted on the PAN_900 carbon nanofibers, with (green curve) and without (red curve) the biofilm formed on the carbon nanofibers. Finally, it is possible to confirm how the trends of CV's curves are similar to the curve characterizing the CF materials (Grey curve)

✓ **Rotating Ring Disk Electrode (RRDE) Results**

As explained in the experimental section, the RRDE technique allows validating the catalytic pathways of the proposed materials by using 4-electrodes measurements. In particular, the currents of disk and ring are measured; the disk current is related to the four-electrons ORR current of the analysed materials, while the current of the ring electrode is associated to the two electron ORR peroxide species [220].

Figure 47 shows the result for the samples under investigation. By applying Equations 1 and 2 defined in the Experimental section, the electron transfer number and the percentage of hydrogen peroxide species formation HO_2^- % can be defined. The curves built from these calculations were reported in Figure 47. Moreover, all the results were compared with the findings for platinum (black line), which guaranteed a number of electrons equal to 3.96.

In particular, the dark blue line represents the results for PAN_600, while the light blue one shows the results for PAN_900.

Regarding the carbon nanofibers PAN_900, the produced HO_2^- % species were found to be as low as about 10%, whereas n value was close to 3.9; the curve, moreover, the curve exhibits a very small dependency on the potential. On the contrary, the PAN_600 samples were characterized by larger peroxide percentages (as high as 50% at -0.4 V), and a lower electron transfer number, equal to 3.6. These electrochemical results demonstrate how the carbon nanofibers PAN_900 exhibits noticeable features for its application as an ORR catalyst, while, the PAN_600 carbon nanofibers are less performing as catalysts for the direct ORR. As deeply highlighted by XPS, however, PAN_600 is characterized by a good electrochemical activity, a high surface area and a high content of nitrogen, obtained without any successive treatment, which functionalize the surface chemistry of carbon nanofiber mats. It can be state that, in order to improve the performances of SCMFCs, the PAN_600 carbon nanofibers result to be a very performing 3D anode in SCMFCs, comparing them with the commercial carbon felt materials. While the PAN_900 nanofibers, which have been characterized by high electrochemical activity for ORR, are a good solution as cathode in the device.

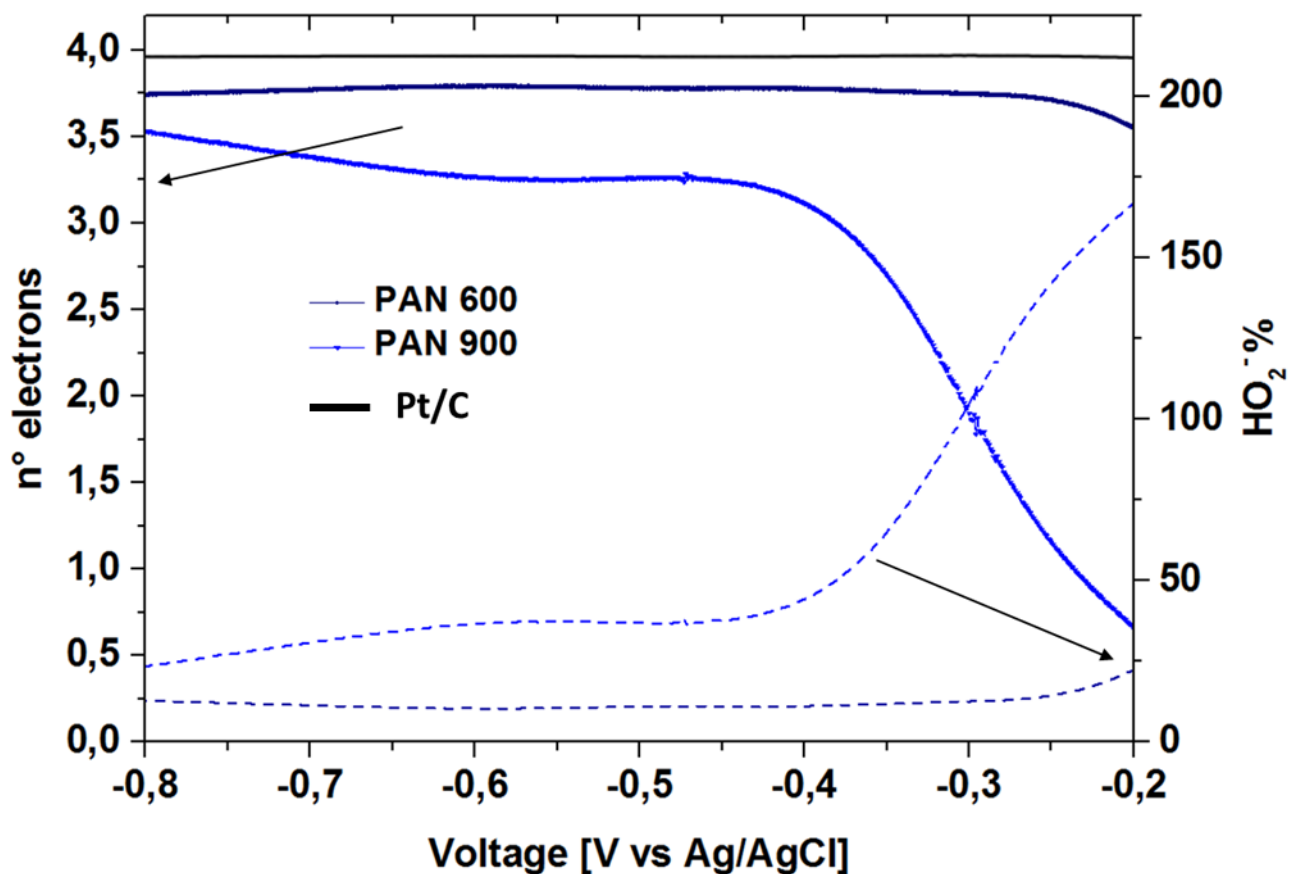


Figure 47 Comparison of electron transfer number (left axis) and peroxide percentage (right axis) evaluated from RRDE measurements of the different samples at 2500 rpm rotation speed and different potentials. The samples are respectively PAN_600 and PAN_900 nanofibers

3.5.3 Morphological properties of carbon nanofibers

Regarding the PAN_600 as anode in SCMFCs, the morphological properties must be investigated in order to define the porosity of the material, the diameter distribution and consequently the interaction between the nanofibers and the bacteria. All these studies were performed by FESEM characterization, on the material both with and without the interconnected biofilm, and compared with the results obtained by commercial carbon felt (CF). Figure 48 reports the morphological characterization of PAN_600 carbon nanofibers. In particular, Figure 48 a) and c) show the mat of nanofibers of PAN before and after the pyrolysis treatment respectively, underlying the maintenance of the nanostructures also after the heating treatment. Figure 48b) demonstrates the formation of bundled nanofibers with a certain degree of roughness, which are preserved also after

the pyrolysis, as shown in Figure 48d). Finally, Figure 48e) represents the morphological properties of Commercial carbon material (CF). Through the morphological characterizations, the distribution of diameters of nanofibers has been evaluated and it closes to 1 μm . It is possible to demonstrate how the diameter distribution of CF is quite higher than ones of carbon nanofibers (PAN_600). This characteristic should enhance the formation of densely interconnected biofilm on PAN_600 nanofibers.

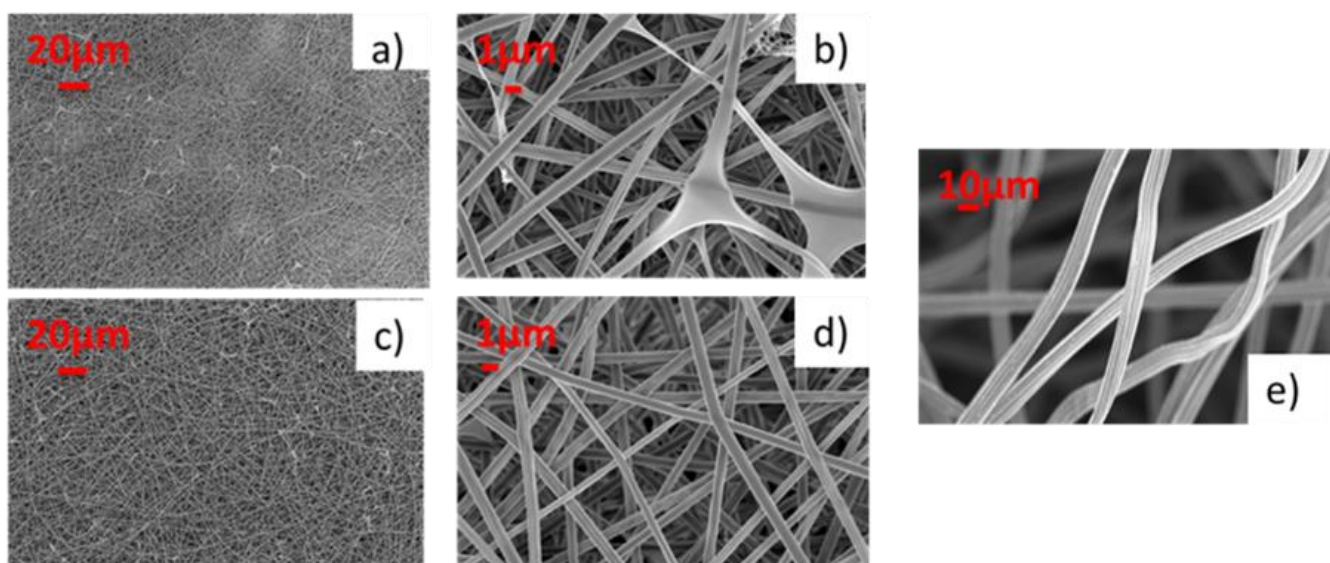
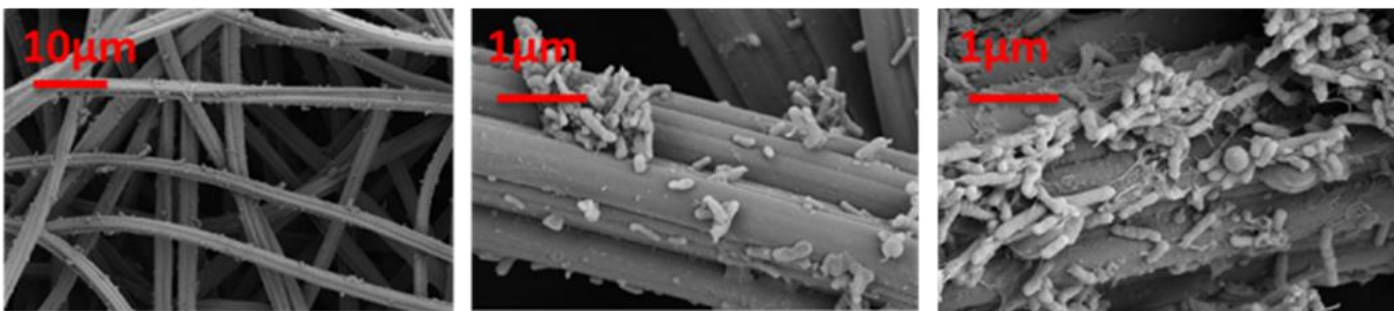


Figure 48 Morphological characterization of PAN_600 at different magnification. a) the mat of non woven nanofibers of PAN precursor before the heated treatment; b) a mat of nanofibers of PAN precursor with a higher magnification; c) mat of non woven pyrolyzed nanofibers; d) the mat of nanofibers of PAN_600 pyrolyzed with a higher magnification to evaluate the formation of bundled carbon nanofibers and e) the fibers of carbon felt.

In addition to all these characterizations conducted on PAN_600, it is needed to evaluate the cytotoxicity and the biofilm interaction with the mat of nanofibers in comparison with commercial electrode material CF. The cytotoxicity test was conducted inside Agar plates, as explained in experimental section. The inclusion of the material within a gel made of agar reveals no cytotoxicity as it can be observed by the bacteria proliferation and their uniform spread in all plates containing the nanofibers. While, in order to investigate the interaction between the materials and the bacteria through the morphological analysis performed by FESEM, all samples have been put for 1 month in

a solution, containing the inoculum and the feed for the microorganisms; then they were properly fixed with a specific protocol in order to investigate the morphological properties of the biofilm formed on the samples, as explained into the Experimental section. The FESEM images have demonstrated a very good interaction of bacteria with nanofibers of PAN_600, as represented in Figure 49. Figure 49 b) shows the biofilm growth on PAN_600 using an inoculum obtained from freshwater sediment, while Figure 49a) represents the interaction among the same inoculum and CF. The development of a densely connected biofilm results better in the mat of PAN_600 than in CF. The PAN_600 properties of higher porosity, lower values of diameters and a surface chemistry, proper to enhance the biocompatibility for microorganisms, influence clearly the biofilm growth.

a)



b)

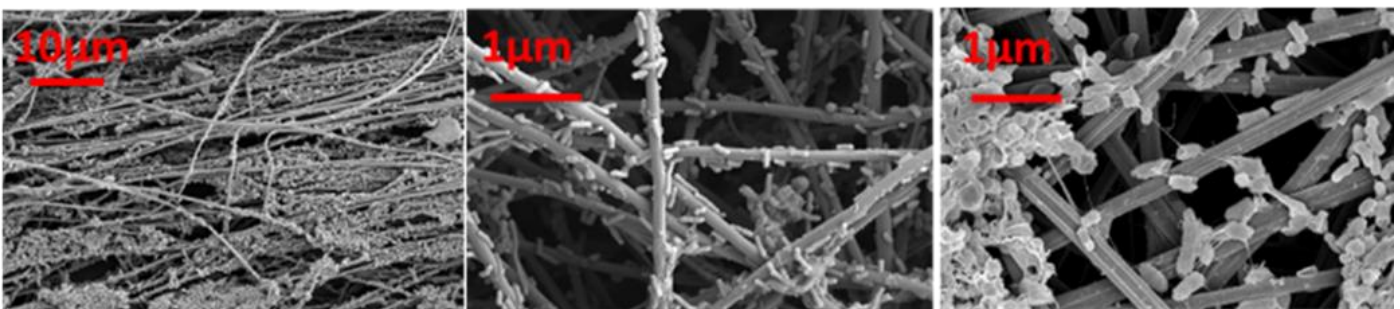


Figure 49 Field Scanning Electron Microscopy (FESEM) images related to the interconnected biofilm on respectively: a) shows the interaction between the bacteria, obtained from the fresh water sediment and CF b) shows the biofilm growth on PAN_600 using an inoculum obtained from freshwater sediment. The development of a densely connected biofilm results better in the mat of PAN_600 than in CF.

3.6 MFC performances evaluated with nanofibers as anode

In this study, as described in the experimental section, the performances of single chamber microbial fuel cells with anode electrodes based on PAN_600 were compared with the ones obtained with CF used as anodes. Both of SCMFCs have the same freshwater sediment inoculum, moreover two values of external loads, 47 Ω and 1k Ω have been applied. In this work a continuous feed mode with a flow rate of 0.3ml/h has been selected in order to ensure the biofilm formation, avoiding the microbial wash out, during the first phases of the experiments. The electrolyte, as described in Chapter 1, is made of 1g/l of sodium acetate as carbon-energy source, and by other compounds such as ammonium chloride as nitrogen source, and phosphate buffer saline solution (PBS) to maintain a neutral pH value. The performances have been evaluated for 1 month and the power density curves obtained in a single chamber MFCs are shown in Figure 50. To deeply investigate the effect of the tested material, the current density was defined normalizing the current values for the projected (geometric) area, which is close to 0.375 cm² for PAN_600 and close to 6.25 cm² for CF [202, 204]. The maximum current density value reached with PAN_600 is two orders of magnitude higher than the one obtained with CF, as summarized in the Table 7. It was also defined the trend of power density related to the acquisition time for both the anodic materials. Figure 50 confirms that the maximum power density obtained with PAN_600 (2153.6 \pm 11.6mW/m²) is one order higher than the CF one (120.6 \pm 1.9mW/m²), reached under an external load applied of 1k Ω . These high performances of SCMFCs obtained with 3D anode based on PAN_600 confirm the good electro-catalytic properties of the materials, due to the nitrogen doping on their surface and to its nanostructure. The cross linked nanofibers, which exhibit a surface charge and a chemistry surface proper for the interaction of microorganisms, provide an ideal habitat for the growth of the electroactive bacteria, leading to a high power density in the 3 weeks of experiment. The high micrometric porosity of the nanofibers equal to 98%, which is defined as the ratio between the volume of void space of material and the volume related to the bulk of nanofibers mat, maximizes the penetration of the bacteria in nanostructures and improves the diffusion of the feed substrate.

This consideration is confirmed by the morphological characterizations, demonstrating that the biofilm is more densely interconnected with PAN_600 than the biofilm on CF.

Samples	Defined	Current	Power
	Projected Area	Density	Density
	[cm ²]	[A/m ²]	[mW/m ²]
PAN_600	0.375	16.1±0.63	2153.6±11.6
CF	6.25	0.512±0.039	120.6±1.9

Table 7 summarizes maximum values of current density and power density reached with PAN_600 and CF used as anodic electrode

It is also important to underline that these high performances have been obtained with a mixed culture as inoculum; a pure and selected culture may further improve the performances but it is not suitable for the specific application of our MFCs.

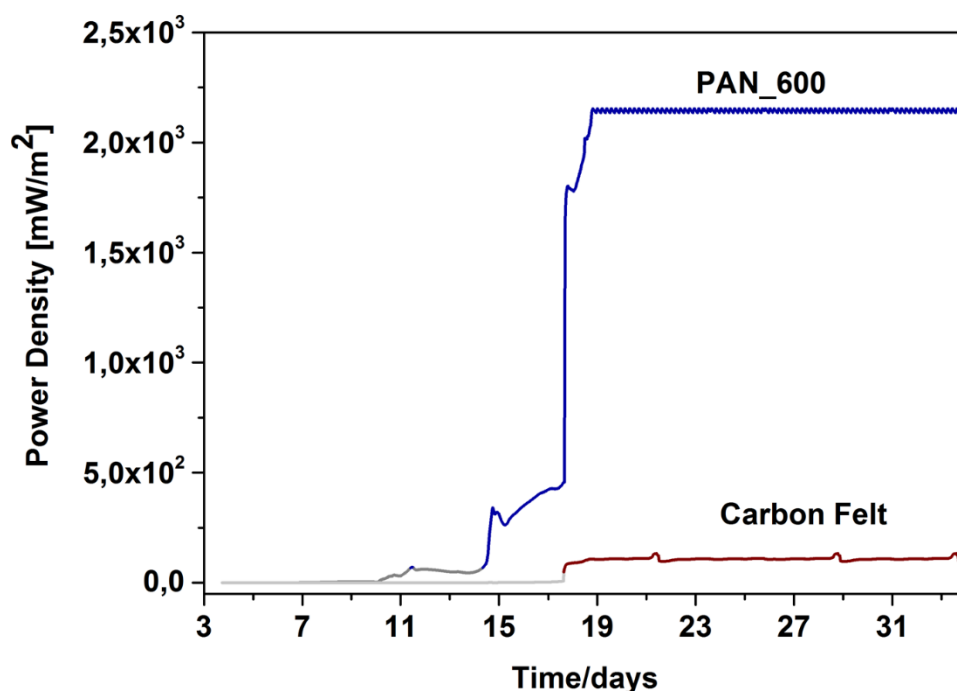


Figure 50 Power Density trends represented as function of time and normalized respect the projected area. a) represents the power density values obtained from PAN_600: dark grey line represents the power density reached with an external load of 47 Ω , while dark cyan one represents that reach under 1k Ω ; b) reports the power density curve obtained from CF material. The light grey line report the values of power density obtained with 47 Ω of external resistance and the blue one that reached under 1k Ω

Electrochemical Impedance Spectroscopy (EIS) has been performed to investigate the impedance measurements of the devices and, in particular, the internal resistance related to the charge transfer of the different anodic electrodes (R_{ct}). The Nyquist plot, defined as the real impedance Z_{real} (ohm) versus the imaginary one $-Z_{im}$ (ohm), is used to represent the data obtained.

In the EIS-Nyquist plot, reported in Figure 51, three different processes can be recognized. It is possible to define the value of Ohmic resistance (R_s) as the intersection between the x-axis and the projection of the first semi arch that belong in the high frequency region. The charge-transfer resistance of the different anodes (R_{ct}) is defined as the intersection of the projected second semi arch with the x-axis.

Finally, the straight line (on the right), that belong in the low frequency region, describes the resistance related to the interface between the electrolyte solution and the catalyst layer on cathode and the diffusion process. In Figure 51 the pink line represents the EIS curves of PAN_600 while the black one represents the EIS curve of CF. The equivalent electrical circuit in Figure 51 is defined to fit the EIS curves and to define the values of each parameters. The electrical circuit is based on the following elements:

- Ohmic series resistance R_s
- The first parallel, between the resistance and capacitance, models the interface between electrolyte and anode;
- The second parallel represents the interface between the electrolyte and cathode;
- The Warburg element (W) simulates from an electrical point of view the ionic species diffusion

Moreover, it is possible to evaluate the value of charge transfer resistance for PAN_600, which is of about 200Ω , smaller than the value obtained for the CF equal to 350Ω . A smaller charge transfer resistance is representative of the faster electron transfer rate of PAN_600 respect to the CF one. Additionally, the straight lines of PAN_600 electrodes are quite smaller with respect the CF electrode. The straight line defines the resistance to the ionic diffusion, occurring towards the electrolyte from anode to cathode; in particular, this results confirms that PAN_600 electrode enhance the ionic diffusion toward the cathode electrode surfaces.

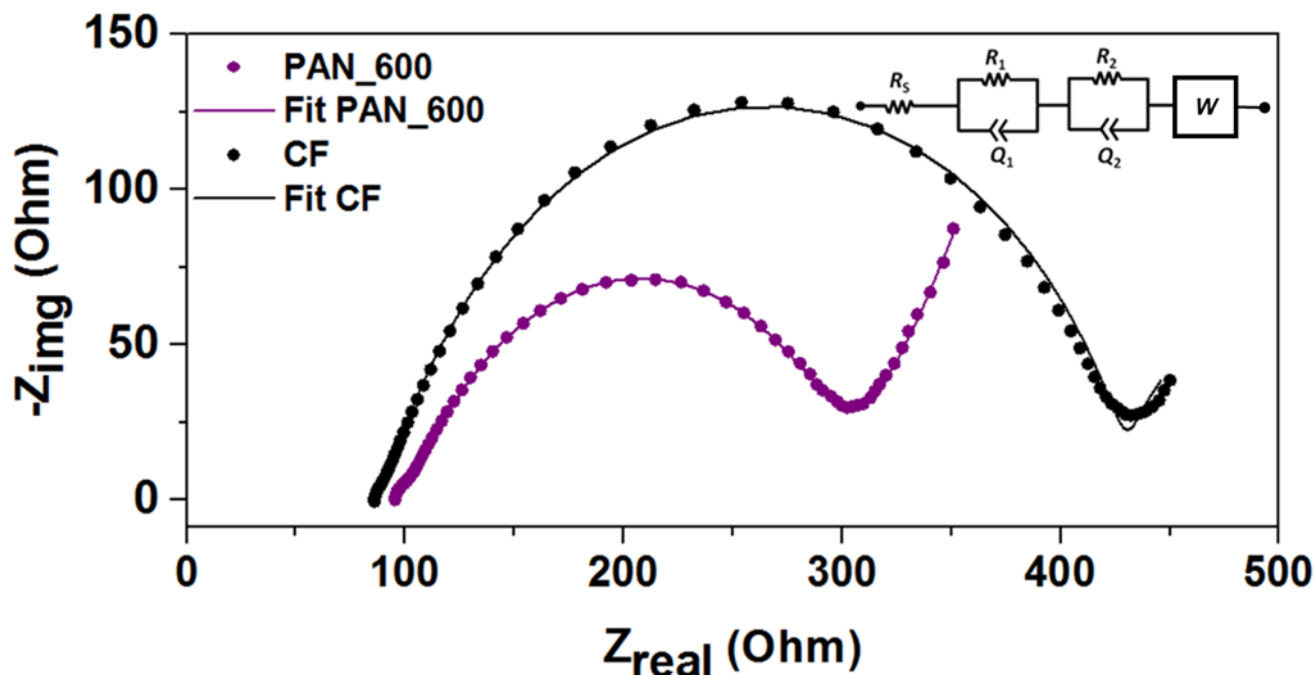


Figure 51 represents two different EIS related with two different SCMFCs with different anodes. The pink curve represented the EIS curve obtained with carbon nanofibers (PAN_600) used as anode, while the black one represents the EIS obtained with a CF anode electrode.

Linear Sweep Voltammetry (LSV) is performed in order to establish the polarization curves and the maximum power density achievable by the different anode electrodes, respectively based on carbon nanofibers and Carbon felt. Figure 52 represents the LSV results, which confirm that the maximum power reached for the SCMFCs containing the PAN_600 as anode is two order of magnitude higher than one obtained with CF as anode electrode. It is possible to evaluate that the short circuit current density for PAN_600 close to 10 A/m^2 , is one order of magnitude higher than one reached with CF anodes, equal to 1.25 A/m^2 .

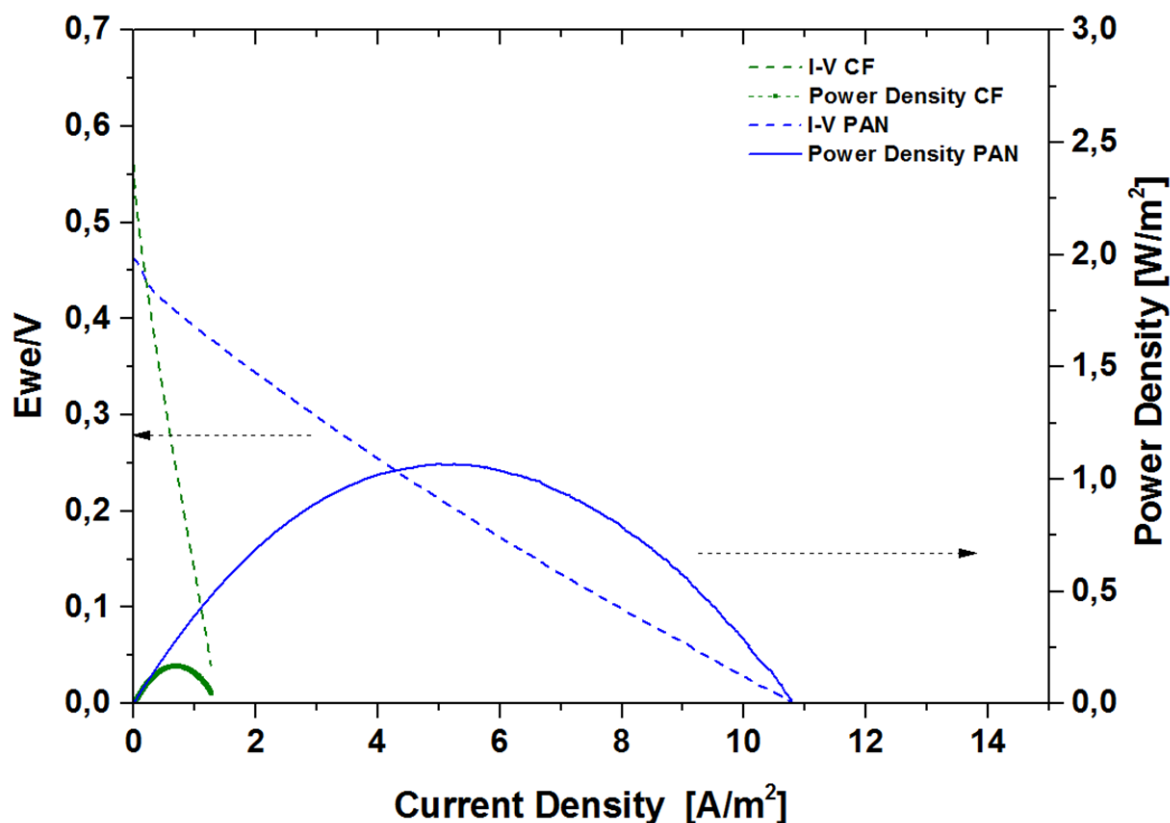


Figure 52 the LSV characterizations performed on PAN_600 and on CF materials, used as anode in SCMFCs. Moreover, assuming that the maximum power density occurs when the external resistance is equal to the internal resistance of the device, the LSV results confirm that maximum power density, reached by SCMFCs with PAN_600 nanofibers as anode, is obtained when the external resistance is equal to 1k Ω . This result is in line with the definition of power density trend of the devices, according to which it reaches a maximum value when the external resistance applied is equal to the value defined through the LSV.

3.7 MFC performances obtained with PAN_900 nanofibers as cathode

The catalyst cathode based on PAN_900 is designed depositing directly on carbon paper the nanofibers mat; moreover, the performances obtained with this electrode are compared with the ones reached with a commercial cathode based on carbon paper (CP) with a Pt layer on its side. The

two SCMFCs have the same carbon paper anode in order to have two different devices with the same anodes and consequently to demonstrate the effect of two catalysts on the device performances. Also in this case the inoculum is based on a mixed culture of bacteria, coming from the same freshwater sediment. Finally, an external load of 1 k Ω is applied. Differently from the previous test, in this work a feed batch mode was defined (explained in the Chapter 1), substituting the organic matter into device every two days. The performances have been evaluated for 1 month and the power density curves obtained from preliminary tests in a single chamber MFCs are shown in Figure 53.

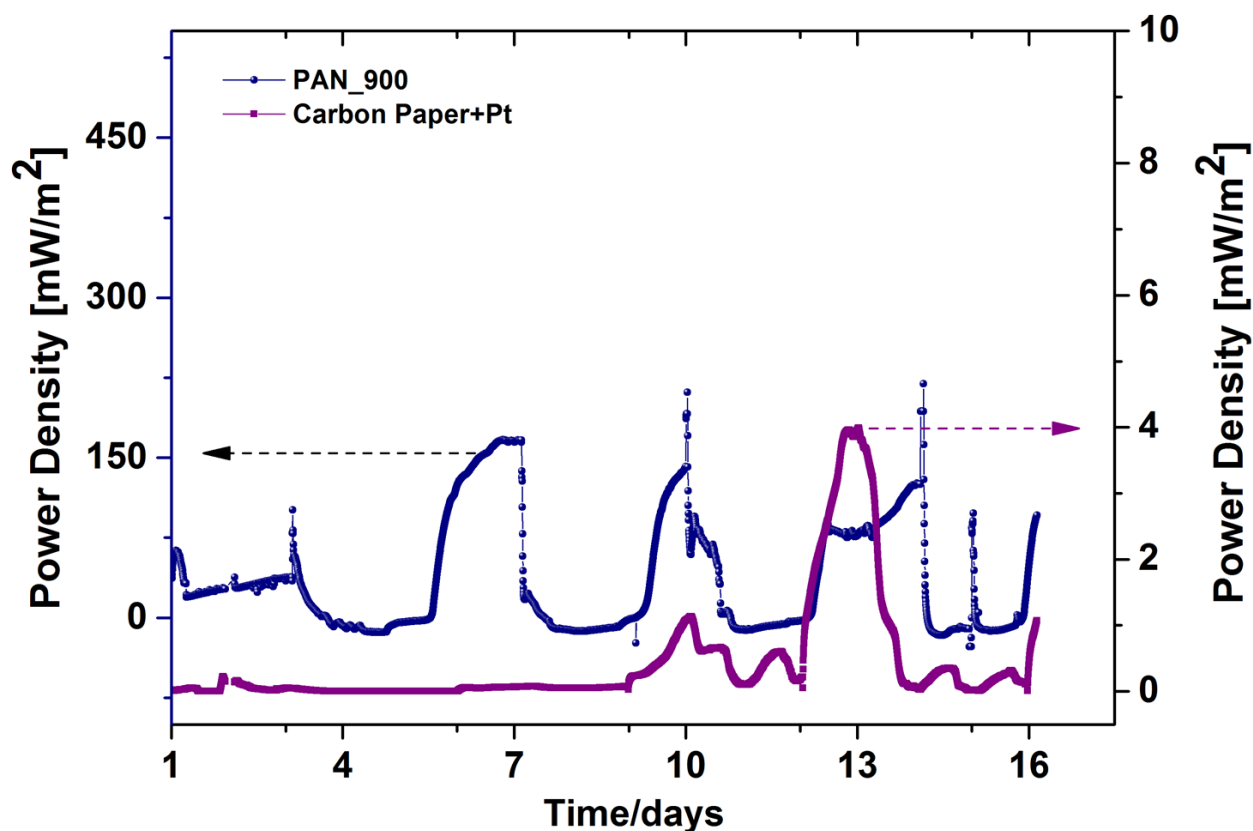


Figure 53 Power Density trends represented as function of time and normalized respect the projected area. a) represents the power density values obtained from PAN_900 catalyst cathode. The dark blue line represents the power density from the PAN_900, higher than one obtained with the CP modified with Pt as catalyst, represented by the pink curve.

Figure 53 demonstrates the high performances reached with the carbon nanofibers used as catalyst. The maximum power density obtained with PAN_900 catalyst cathode is close to 150mW/m², and

it is two orders of magnitude higher than the one obtained with Pt catalyst layer, which is equal to 4 mW/m².

3.8 Conclusion

A nonwovens mat of carbon nanofibers has been investigated as promising material used as electrodes in SCMFC.

In this work, two different kind of carbon nanofibers have been investigated. These samples were obtained starting from the same electrospun polymeric solution and then implementing two different pyrolysis treatments.

The obtained materials, called PAN_600 and PAN_900 nanofibers were then studied as innovative nanostructured electrodes in SCMFCs, comparing them with the commercial materials.

In this work, it has been demonstrated that the carbon nanofibers PAN_600 represent a promising and interesting material to build the 3D anodes in SCMFCs.

Indeed, the characterizations performed on this sample show nitrogen content able to increment the electro-catalytic properties of the PAN_600, to guarantee a surface charge and a proper chemical surface necessary to ensure a good adhesion between bacteria and nanofibers. The deeply interconnected biofilm formed on the materials leads to a maximum current density of 16.1 A/m², which is two order of magnitude higher than the current density reached with the CF anode.

It is important to underline again that this result was reached without any successive chemical treatment, such as ammonia treatment or stem activation, which are instead widely used in the literature in order to obtain the nitrogen doping, able to increment the power generation.

In this work this functionalization was ensured with a proper carbonization treatment conducted until a final temperature of 600°C.

In particular, as demonstrated through all chemical and physical analysis, the mat of PAN_600 is characterized by a higher content of pyridinic nitrogen bonds, which enhance its electro active surface area. Moreover, thanks to the high surface area of nanofibers to volume ratio and a higher porous structure, it has been evaluated the formation of deeply connected biofilm on nanofibers. The bacteria show a better proliferation in the sample of PAN_600, than that on CF, a commercial

material used as a reference material. All these results, reported in this work, demonstrate the possible application of the carbon nanofibers PAN_600 as anode in MFCs. Moreover, the performances of SCMFC reached for PAN_600 are higher with respect those obtained by commercial reference carbon material, CF. We can assert that the PAN_600 results to be a better bio-electrochemical system compared with the commercial material.

Regarding the development of new catalyst cathode, the carbon nanofibers PAN_900 were studied. The higher graphitic features were demonstrated through all physical characterizations. The PAN_900 showed a good electrical conductivity and in particular exhibited noticeable features for its application as an ORR catalyst, thanks to high amount of graphitic nitrogen and the high value of electrical conductivity.

The good electrochemical behavior, added to the all intrinsic properties of the nanostructures, permitted to apply this sample as cathodes in SCMFCs.

The obtained results demonstrated the increment of the performances with carbon nanofibers as cathode; the power density was an order of magnitude higher than the one reached with the commercial material.

4 Chapter 4

Mn_xO_y catalysts nanofibers for Oxygen Reduction Reaction using Multi Wall Carbon Nanotubes as conductive filler

4.1 Introduction

In order to develop a nanostructured material with a very high surface area, able to increase the number of catalytic sites exposed to the oxygen, a ceramic mat of nanofibers is investigated [63]. In particular, the manganese oxides are, among all the non-precious metal catalysts the most interesting material, given to their low cost, relatively high abundance, lower environmental impact and considerable electro-catalytic activity.

One of the aims of this work is to obtain mats of manganese oxide nanofibers, starting from a polymeric solution based on polyethylene oxide (PEO) and manganese acetate as the manganese (Mn) source. PEO is chosen as template in order to ensure the correct formation of the polymeric charged jet and, consequently, the deposition of nanofibers; moreover, PEO is one of the most environmental friendly material among all the common templating agents used to produce nanofibers, showing a very high biocompatibility and biodegradability. Indeed, PEO needs only water as solvent, differently from a widespread list of polymers which use less ecofriendly solvents. In order to demonstrate the possibility of the direct fabrication of electrodes for electrochemical devices, the carbon based material is used as a substrate for the synthesis of the ceramic nanofibers; in this way the manganese oxide (Mn_xO_y) nanofibers catalysts are deposited directly on the cathode electrode.

The catalytic behavior of the (Mn_xO_y) nanofibers with respect to the oxygen reduction reaction (ORR) is investigated through the Rotating Ring Disk Electrode (RRDE) electrochemical measurements and compared to the behavior of platinum, which is considered the standard material. A good result of 3.7 electrons is obtained for the ceramic nanofibers, which is not far from

the 3.96 obtained for the platinum. One of the main limit of these ceramic nanofibers is their very low electrical conductivity, which is in the order of few $\mu\text{S}/\text{cm}$. This property constrains the electro-catalytic properties of these materials and it is one of the most limiting factors for their final application as catalyst cathode in the device. In order to achieve a better electrical conductivity, a composite nanofibers based on manganese oxide and multi wall carbon nanotubes (MWCNTs) could be investigated. The multi wall carbon nanotubes are the conductive filler, which improve the electrical properties of the material but, at the same time, can intrinsically change the polymeric solution properties and consequently the electrospinning parameters process. In order to deeply investigate the effect of MWCNT on the optimal electrospinning conditions, and consequently on the final morphology of the nanofibers, a simplified solution, containing only PEO and MWCNTs without Mn precursor, is processed.

Therefore, it is then necessary to optimize the electrospinning parameters for the polymeric solutions containing a no conductive polymer, such as PEO, and a conductive filler like MWCNTs, in order to control, constrain and manage the formation of the secondary jet during the process. Moreover, many works in the literature underline the formation of secondary charged polymeric jet, derived from the principal one, depending on the distribution of the charges in the polymeric solutions or on the average weight of the polymer, as already explained into the Chapter 2. It is important to underline that this phenomenon is not always considered as a defect into the mat of nanofibers, while, on the contrary, could provide interesting features, improving the performances of the final mat.

Considering the composite mat of nanofibers based on polyethylene oxide (PEO) and the multiwall carbon nanotubes, (MWCNTs), the presence of secondary jet can improve the percolation path and consequently the conductivity of the nanofibers samples.

This event can be defined electrospinning/netting (ESN), which is an electro-hydrodynamic technique derived from the electrospinning technology. During the last decade these named electro-spinning/netting (ESN) technique has been identified as a unique approach for processing materials in hierarchical structures at the nanoscale [221, 222, 223]. ESN combines the conventional electrospinning (ES) process, that utilizes electrostatic forces to produce polymer nanofibers, and

the unique electro-netting (EN) technology [224, 225, 226, 227]. The result is the formation, with only one-step fabrication process, of ultrathin nanonets (NN) supported on the main electrospun nanofibers (NF) and it is known as Nanofibers/nets (NFN) [221, 222, 223].

Like conventional electrospinning, during ESN an electrostatic field is applied between a small size needle and a grounded substrate (or collector) to drive the assembly of NFN mats. Therefore, in contrast to conventional ES, during ESN the applied voltage must be very high, in order to enhance the instability of the Taylor cone [221].

Polymeric solutions of both natural and synthetic polymers have been successfully processed by the ESN technique, obtaining materials that overcome the traditional nanofibers created by ES, in terms of surface area, degree of porosity, and mechanical behavior [221, 222, 228]. Given the extremely high surface area to volume ratio and the superior set of properties usually shown by this class of nanostructures, a significant interest has raised on NFN, covering several scientific fields: from membranes for environmental applications as filtration and separation, to catalysis, sensing and tissue engineering [229, 230, 231].

In this work, the processability by electrospinning and electrospinning/netting of high molecular weight (hMw) poly(ethylene)oxide (PEO) and its nanocomposite based on MWCNTs are studied and compared; in particular, the main characteristics of the starting polymeric solutions and the control degree of the morphology of the resulting nanofibers by the fine tuning of the process parameters are investigated.

Moreover, it is demonstrated that the ESN can be performed adding MWCNTs to high molecular weight PEO. Up to now, in PEO based systems, ESN has been demonstrated in presence of cellulose nanocrystals (CNC) only [231], while MWCNTs have been demonstrated as an additive able to induce nanonetting into polyurethane (PU) solutions [232]. In this work, the first analysis of the effect of nanonets on the functional behavior of NFN functional composite (NFN-FC) material is analyzed.

Indeed, the electrical behaviour of high molecular weight (hMw) PEO/MWCNTs NFN composites is considered verifying the applicability of the percolation theory to describe the electrical behaviour

of the NFN composite, discussing the influence of NN on the percolation threshold and the values of the electrical conductivity above percolation.

Finally, as explained before, if the starting polymeric solutions contain the conductive filler (MWCNTS), the final samples are characterized by the presence of functional composite nanofibers nets (NFN-FC). The presence of nanonetting into the mat of nanofibers is well confirmed by transmission electron microscopy. The good quality of the interfaces inside the NFN-FC is also demonstrated by Raman spectroscopy and thermal gravimetric analysis (TGA).

Finally, the electrical conductivity of the NFN-FC increase when the nanofibers nets are denser, thanks to the formation of more efficient percolation paths.

Moreover, it is possible to evaluate also the different response of the final mat of composite nanofibers to the humidity variation taking advantage of the hygroscopic properties of PEO; the relative resistance of the nanofibers increases with the humidity. In particular, the relative differential resistance of NFN-FC is 4 times higher than ones fabricated using the standard composite NF. This different response of the humidity can be explained considering the increment of percolation paths into the mat of nanofibers-netting respect to the ones obtained into the nanofibers without netting. During my Ph.D. period, the mat of composite nanofibers, obtained starting from the polymeric solutions of hMw-PEO/MWCNTs, have been processed by the ESN technique applying high voltages values.

Furthermore, during this work Mn_xO_y nanofibers have been investigated in order to enhance the electro-catalytic behavior with respect the ORR. Moreover, since that the electrical conductivity of the ceramic nanofibers is very low, the Mn_xO_y nanofibers could be modified with the introduction of MWCNTs as conductive filler. Finally, in order to deeply understand the effects of MWCNTs addition, the composite nanofibers initially based on PEO and MWCNTs are studied.

Starting from the study and the analysis of both of these kinds of nanofibers mat, the future development will be represented by the possibility to develop a composite ceramic nanofibers characterized by Mn_xO_y and multiwall carbon nanotubes, and applying this final material as catalyst cathode in electrochemical devices, such as Microbial Fuel Cells.

4.2 Experimental section: materials and methods

4.2.1 Manganese oxide nanofibers synthesis

The nanofibers were obtained starting from an electrospun polymeric solutions containing 5wt% of (PEO) and 20wt% of manganese acetate, which were dissolved into deionized water. The polymer PEO was selected as template to ensure the nanofibers formation through the electrospinning process and the manganese acetate was selected as a precursor in order to have a final ceramic sample. During the electrospinning process, a voltage of about 14.5 kV was applied between the needle and the planar collector plate, covered with a substrate. The electrospun PEO/manganese acetate nanofibers were then dried in vacuum at 70°C for 24 h, in order to eliminate all the possible residues of solvent. Further on, the samples were calcinated by means of a vertical furnace (Carbolite, VST 12/300/3216) at 480°C for 3 h in air, with a heating rate of 2.5°C/min to ensure the complete decomposition of the PEO and guarantee the manganese acetate oxidation.

4.2.2 Composite nanofibers based on PEO and Multiwall carbon nanotubes synthesis

The polymeric solutions were based on a mixture of a fixed weight percentage (i.e., 5 wt%) of two PEOs having two different average molecular weights, i.e. 600 kDa and 1000 kDa (from Sigma Aldrich) in 12 ml of deionized (DI) water. The ageing of each solution was obtained overnight under continuous stirring at room temperature.

Different mass fraction of the conductive filler (MWCNTS, NC3100 by NANOCYL) was added into the polymeric solutions. The range of different weight percentage of MWCNTs is from 1 to 7 wt%. The dispersion of MWCNTs in DI water was ensured by the presence of surfactant poly(styrene)sulfonate (PSS, Sigma Aldrich), whose molar ratio is equal to 1 and was achieved through ultrasonic bath (2000U Digital Sonifier by Branson). After the addition of MWCNTS into the polymeric solution, the final mixture was aged under continuous stirring overnight at room temperature. The viscosity solution was evaluated by Rheometer analysis (MCR Rheometer series Anton Paar). The polymeric solution was loaded in a horizontal 6 mL syringe connected through a tube to spinneret vertically

aligned with the needle (27 Gauge x 15 mm) and positioned into a NANON 01A electrospinning apparatus (MECC., LTD). The spinneret, which constitutes the first electrode for the electrospinning process, was connected with a high positive voltage power supply (HVU-30P100) and a syringe pump setup operating with a flow rate ranging from 0.1 mL/h up to 99.9 mL/h. The high positive voltage power supply can work in the range of voltage from 0.5kV to 30 kV. During the process, a voltage of about 15kV was applied between the tip of the needle and the planar counter electrode plate, covered with a substrate. Normally, an aluminum foil can be used as the reference substrate during the electrospinner process.

4.3 Characterizations on the nanofibers

4.3.1 Morphological, optical and electrochemical characterizations performed on the Manganese oxide nanofibers

✓ **Morphological characterization**

The morphology of this sample was defined by means of Field Emission Scanning Electron Microscopy (FESEM, ZEISS, Merlin). Moreover, the samples for Transmission Electron Microscopy (TEM) were prepared by suspending a small quantity of material in ethanol, subsequently immersed in ultrasonic bath. A suspension droplet was then drawn and applied to a standard holey carbon TEM Cu grid, analyzing the specimen after the complete evaporation of the solvent. TEM observations were performed with a FEI Tecnai F20ST, equipped with a field emission gun (FEG) and operating at 200 kV.

✓ **Optical characterizations**

The X-ray diffraction spectroscopy was performed, establishing the oxides present into the mat of nanofibers. X-ray diffraction (XRD) with Bragg–Brentano symmetric geometry was then performed with an analytical X'Pert Pro instrument using Cu-K α (40 kV and 40 mA) radiation. The continuous scan mode was used to collect XRD data in a range of 10° to 74° and 0.02° as step size. The Rietveld analysis was performed in order to obtain each spectrum by using Topas Academic software (version 4.1). The convolution-based method was used where the source emission profiles with full axial

instrument contributions was modelled, while the background was fitted with a Chebyshev polynomial function with eight parameters. The average crystallite size was assumed to be isotropic in all cases and modelled by applying the integral breadth based method, whereas lattice strain was assumed to be zero as a consequence of the small crystal size found during the early refinement steps [233].

✓ **Electrochemical characterizations**

All the electrochemical measurements were carried out by means of a CH Instrument 760D electrochemical workstation and an ALS RRDE-3A rotating ring disk electrode apparatus, made of platinum. For all the measurements, the manganese oxide catalysts were deposited on the working electrode (a BioLogic glassy carbon disk/Pt ring) according to the following method. Before each catalyst deposition, the working electrode was properly polished with ethanol, then the catalyst (2 mg of active mass) was dispersed in a solution containing 25 μl of water, 175 μl of Nafion[®] solution and 100 μl of 2-propanol and finally the mixture was ultra-sonicated for 2 min to form a uniform black dispersion. 10 μl of this formulation were cast coated onto the disk surface to form a uniform film. The resulting deposition was dried at room temperature for one day.

For comparison purposes, commercial Pt/C paste was used as a reference catalyst and deposited on the disk electrode with the same procedure described above. The final Pt loading was 0.5 mg/cm². During the characterization, Pt wire was used as counter electrode and Ag/AgCl as reference one. The electrolyte used was 0.1 M KOH O₂-saturated aqueous solution and the experiments were conducted at room temperature. All the potentials are reported with respect to the Ag/AgCl electrode. For the (RRDE) measurements, the disk electrode was scanned from -0.2 V to -0.8 V, with a rate of 5 mV/s and a fixed rotating speed of 2500 RPM, while the ring electrode was maintained at a fixed potential of 0.2 V.

4.3.2 Characterizations performed on composite nanofibers PEO/MWCNTs

✓ Morphological, optical and physical characterizations

The morphology characterizations of the samples have been deeply performed through the Field Effect Scanning Electron Microscope (FESEM, Zeiss Merlin). To investigate the dispersion of MWCNTS into the composite nanofibers mat Raman Spectroscopy (Renishaw 1000 spectrometer equipped with a 514.5 nm laser excitation, through a microscope objective (50×)) and Transmission Electron Microscopy (TEM) were performed; in order to have the sample in a proper configuration for TEM analysis, we used directly on the counter electrode a standard holey carbon TEM Cu grid.

In this work a FEI Tecnai F20ST equipped with a field emission gun operating at 200 kV was used.

The thermal properties of hMw PEO/MWCNTs composite nanofiber/nets were measured by Thermo-Gravimetric-Analysis (Netzsch TG 209 F1) under inert atmosphere.

✓ Electrical characterizations

The optical glass slides were used as a proper substrate for the electrical characterizations.

Hard-masks, made of poly(methyl) methacrylate by column drill, are used to prepare the electrodes and to define the shape of the nanofibers mats for the characterizations. Four electrodes of platinum were obtained for each nanofibers strips, using a hard mask, by sputtering (Q150T ES by Quorum Technologies), applying a current of 50 mA for 120 s. Each platinum electrode has a thickness of about 100 nm, 1 mm wide and 5 mm long. Strips of nanofibers were prepared, having a length of 2 cm and a width of 2 mm. The thickness of the nanofiber strips was evaluated by a Tencor P-10 Surface Profiler and confirmed by FESEM analysis on samples analyzed in cross-section. The electrical characterization is performed by polarizing the samples applying different values of electrical voltage (V) and measuring the current (I) that flows through the sample by means of a Keithley 2635A Source unit measure. In particular, the presence of 4 platinum electrodes, under the nanofibers strips, allows to conduct a four points electrical characterization. The relation between voltage and current is exemplified by Ohm's Law, which permits the definition of bulk Resistance ($R(V)$) and consequently the conductance of the nanocomposite based on PEO and

different mass fraction of MWCNTs, defined as invers of resistivity of the sample. To characterize the response of the samples at the change of humidity, an electronic fast response digital thermo-hygrometer (DTH) is used to measure the relative humidity during the sensing tests. Humidity is generated by a Chiesi Clenny aerosol system, selected to avoid effect on temperature during the test. A vacuum pump by Dürr Technik GmbH was used for fine adjustment.

4.4 Results and Discussion

4.4.1 Manganese oxide nanofibers Results

✓ Results of the morphological characterizations

The morphological characterizations on the nanofibers mat have been performed before and after the calcination treatment, which is the most critical step to obtain the final manganese oxide nanofibers. Indeed, it is difficult to maintain the nanostructure after the totally removal of PEO and to convert at the same time the manganese acetate into the manganese oxides. Even if the manganese acetate oxidation occurred at lower temperature [234], the calcination treatment is conducted until 480°C in air, ensuring the completely removal of PEO.

As demonstrated by the TGA analysis, shown in Figure 54, the temperature, at which the PEO is completely removed, is about of 450°C.

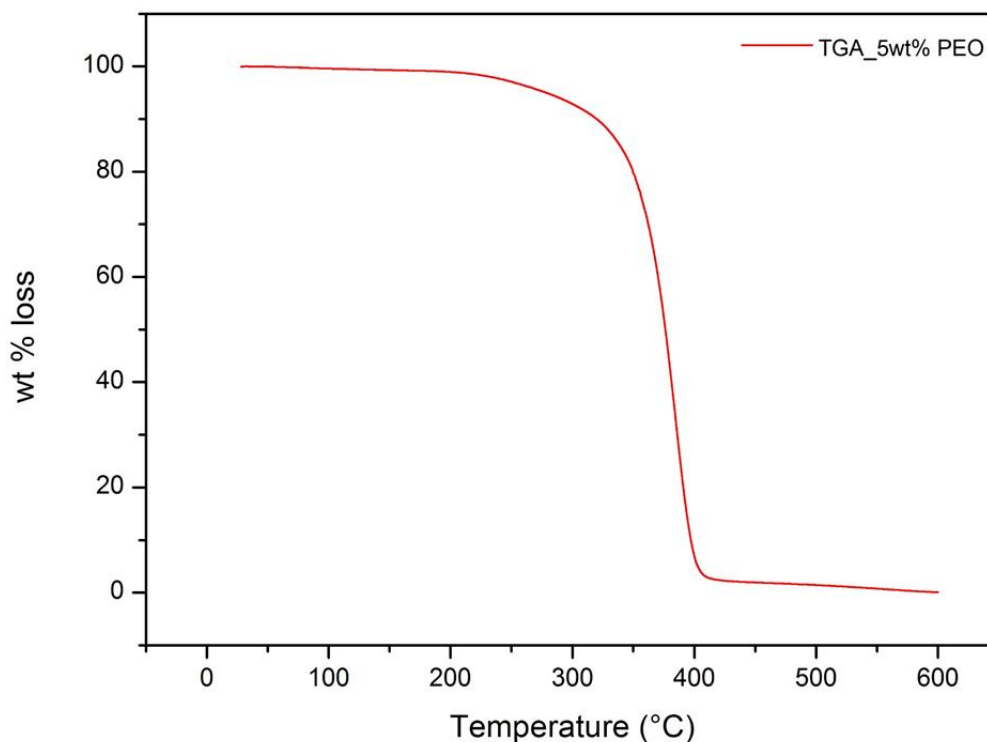


Figure 54 reports the TGA plot of a polymeric solution based on 5wt% PEO (Mw=600 kDa) dissolved into the deionized water

Figure 55a) shows the morphological properties of PEO/manganese acetate nanofibers, while, Figure 55b) represents the morphological aspects of ceramic nanofibers, when the polymer is completely removed and at the same time the manganese oxide is formed. In these images, it is possible to observe how the manganese oxide well retains the 1D fibrous morphology, exhibiting a nano-grain structure. The thermal treatment induced a slightly collapse of the nanofibers mats, as underlined by comparing Figure 55b) with Figure 55a).

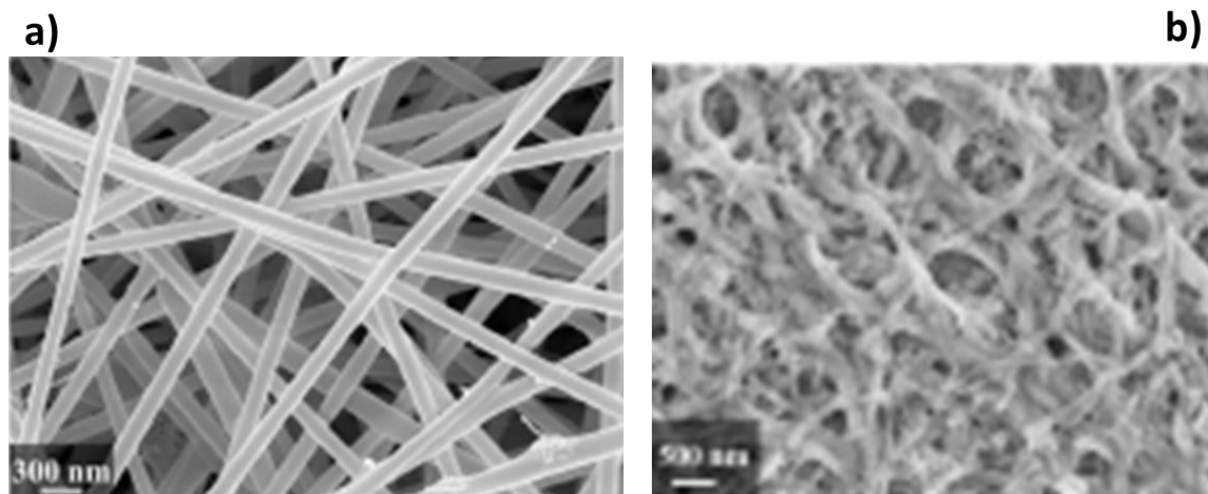


Figure 55 Morphological properties before and after the calcination treatment. In particular, a) shows the morphological properties of the PEO/manganese acetate nanofibers mat; b) show the morphological characteristics of Mn_xO_y nanofibers, when the PEO is completely removed.

The grain structure is further analyzed by the High Resolution (HR)TEM. Figure 56a) shows a Bright Field (BF) image of a nanofiber portion on the CU grid; this figure demonstrates the proper longed shape of the nanofibers characterized by the presence of very small grains. The Selected Area Electron Diffraction (SAED) pattern, defined for the same nanofibers portion, is composed by complete low intense rings, which are indexed as Mn₃O₄, as represented in Figure 56 B. The Dark Field (DF) image, reported in Figure 56 B), defines that the grains composing the fiber are actually round crystals with an average size of 10 nm, randomly distributed through the fiber. This DF image was obtained by selecting the electrons from one of the most intense ring on the SAED pattern, that corresponds to the {211} family planes for Mn₃O₄. Finally, Figure 56 C) and Figure 56 D) show an HRTEM image of one of these crystals (white frame denoted (i)) and its corresponding Fast Fourier Transform (FFT), respectively. The FFT was indexed as Mn₃O₄ along the [100] axis zone. The above result points out the polycrystalline structure of the electrospun nanofibers.

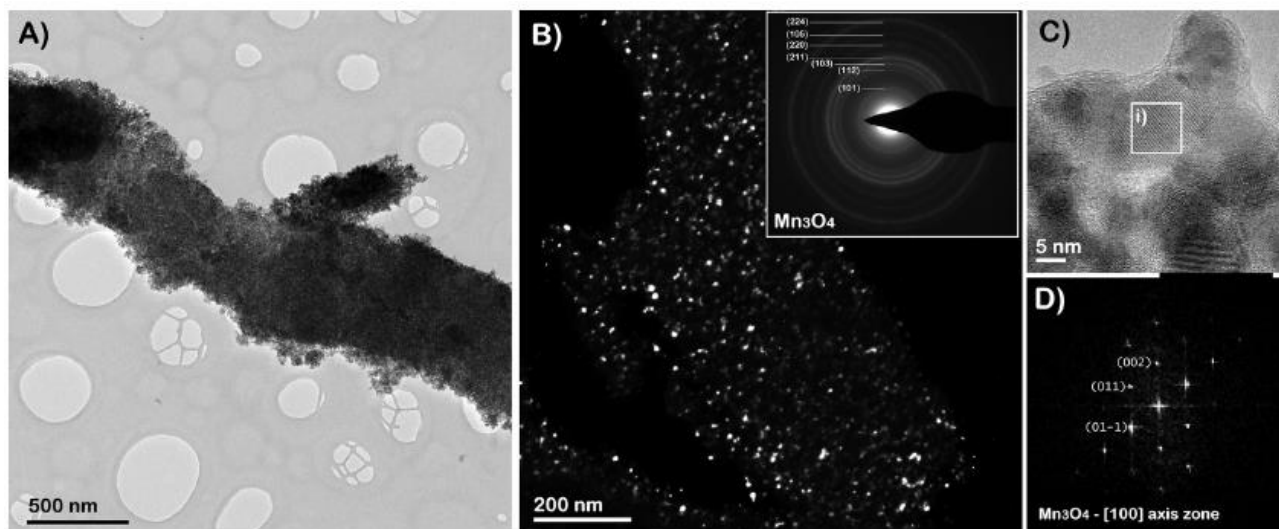


Figure 56 TEM images of the calcinated nanofibers in (A) bright field, (B) dark field, SAED pattern in the inset (C) (HR)TEM micrograph and its corresponding (D) FFT.

✓ Optical characterizations results

The presence of only phase Mn_3O_4 in the obtained nanofibers is also confirmed by the XRD characterizations, as underlined in Figure 57. Figure 57 shows the XRD spectrum obtained from manganese oxide nanofibers. The diffraction peaks at 28.9° , 32.5° and 36.1° (2θ) correspond to (112) (103) and (211) planes for Mn_3O_4 , with lattice parameters equal to $a = b = 5.764 \pm 0.002 \text{ \AA}$ and $c = 9.445 \pm 0.004 \text{ \AA}$. These results clearly indicate the monophasic nature of the sample, which is composed by Mn_3O_4 .

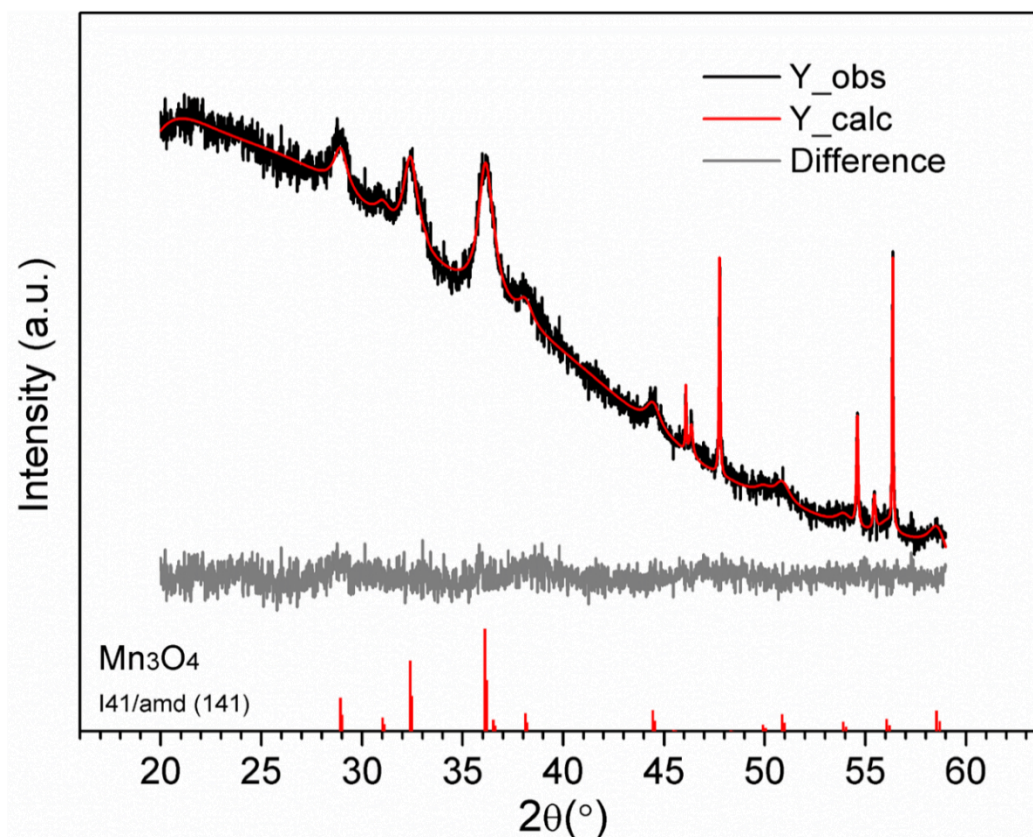


Figure 57 XRD pattern of the manganese oxide nanofibers supported on Si after calcination. In the graph are reported the experimental measure (black curve), the fitting results (red curve) and their difference (grey curve).

✓ **Electrochemical characterizations Results**

The catalytic performance of the presented manganese oxide-based materials was evaluated by means of the electrochemical technique. The RRDE technique allows the catalytic pathways of the proposed materials to be validated by using 4-electrodes measurements. While scanning the disk potential at fixed rotation rate, the current at disk and ring electrode is measured. The disk current is related to the four-electrons ORR current of the analyzed catalyst, while the ring current (whose potential is fixed at a large value) is associated to the two-electrons ORR (intermediate) peroxide species, as defined by the Eq 60 and Eq 61 widely investigated in the Chapter 3 [220]:

$$HO_2^- \% = 200 \times \frac{I_R/N}{I_D + I_R/N} \quad \text{Eq 60}$$

$$n = 4 X \frac{I_D}{I_D + I_R/N} \quad \text{Eq 61}$$

As represented in Figure 58, it is possible to estimate how the ring current for the nanofibers results very low in comparison with the corresponding disk current, as represented in Figure 58a) and Figure 58b) respectively. This confirms that the preferred reduction pathway depends on 4 electrons reaction, and consequently the current related to the two electrons reduction is very low. Considering these curves and the Eq 55 and Eq 56, the percentage of the peroxide formation (HO_2^- %) and the number of electrons involved in the ORR reaction can be estimated, as shown in Figure 58c). The green curve, related to the nanofibers, underlines how the current related to the 4 electrons remains quite constant in the range of potentials, defining an ensured number of electrons close to 3.7. At the same time the percentage of H_2O^- is lower than 30% into the same range of scanning potential. In conclusion it can be observed that the produced nanofibers rely mainly on the full reduction reaction, providing approximately four electrons for the reaction. These good results open the door to use the manganese oxide nanofibers as catalyst in MFC.

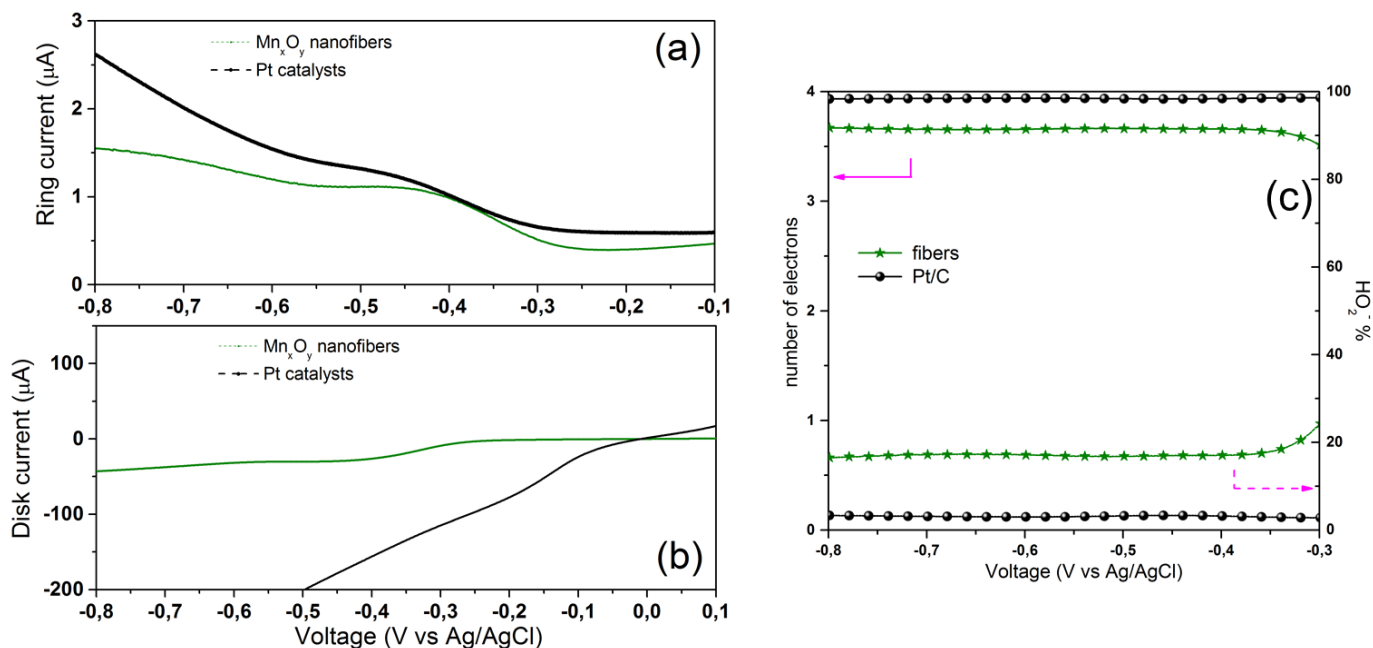


Figure 58 Ring current (a) and Disk current (b) obtained from the RRDE measurements of Mn₃O₄-based and reference Pt/C samples at a rotating speed of 2500 rpm and a potential of the ring electrode of 0.2 V. (c) Comparison of electron transfer number (left axis) and peroxide percentage (right axis) evaluated from RRDE measurements of manganese oxide-based samples and of the reference Pt/C catalyst at 2500 rpm rotating speed and different potentials.

By considering the high price of platinum, alternative catalysts are needed and manganese oxides (Mn_xO_y) can be considered promising substitutes. In conclusion, in order to prepare well-performing electrodes for electrochemical devices, it is, therefore, necessary to increase the manganese oxide nanofibers electrical conductivity. As introduced previously, in order to improve the electrical conductivity of the ceramic nanofibers, the adding of MWCNTs embedded into the nanofibers can be investigated. The following results permit to estimate how the presence of MWCNTs influences the morphological properties of the final mat of composite nanofibers, based on PEO/MWCNTs, and improves the electrical conductivity of the samples. All these finding information lead to the development of ceramic nanofibers functionalized with the MWCNTs adding as future developments.

4.4.2 Composite nanofibers based on PEO/MWCNTs

✓ **Morphological, Optical and Physical characterizations results**

The correlation between the intrinsic properties of the solutions and the electrospinning parameters is demonstrated by the following results. In general, the morphological properties of the mat of nanofibers are strictly dependent on both the process parameters, such as flow rate, electric field, and the intrinsic properties of the electrospun polymeric solution [224]. This is true for electro-spinning/netting too. It was possible to define a correlation between the polymer molecular weight (M_w) and the addition of different content of MWCNTs with the final morphology of nanofibers mat; in particular, the presence or no of nano-netting in the samples depends on both the molecular weight and the MWCNT content. Among other parameters, the viscosity and the electrical conductivity of the starting solution can be directly modified by the actual M_w of PEO and the content of MWCNTs. Indeed, the viscosity is not only strictly dependent on the polymer concentration and its molecular weight, but its value can further be changed by the presence of additives as MWCNTs. Moreover, the introduction of electrically conducting MWCNTs changes the electrical conductivity of the solution (σ_{sol}). Two molecular weights, 600 and 1000kDa, have been investigated, and two concentrations (1.5 and 3.5wt%) of MWCNTs have been analyzed. The PEO concentration has been kept fixed at 5wt%. The list of resulting solutions investigated in this work is reported in Table 8, indicating their composition, the electrical conductivity, and the average viscosity, η . The name of each sample has the general structure 5PEO_A_B, where A stands for the polymer M_w and B indicates the weight percentage of MWCNTs added into the solution.

Sample name	PEO [wt%]	Mw [kDa]	MWCNT [wt%]	σ_{sol} [μ S/cm]	η [Pa·s]
5PEO_600	5	600	0	4.2	23.8
5PEO_600_1.5	5	600	1.5	203	/
5PEO_600_3.5	5	600	3.5	405	68
5PEO_1000	5	1000	0	12.6	44.9
5PEO_1000_1.5	5	1000	1.5	240	/
5PEO_1000_3.5	5	1000	3.5	420	13.8

Table 8 The names and the main properties of the examined PEO based solutions are listed.

PEO is an insulating material, so using a higher molecular weight causes only a slight change of σ_{sol} , as shown in Table 8, while the introduction of MWCNTs induces significant σ_{sol} changes. At a fixed loading of MWCNTs, the value of σ_{sol} is almost the same for the two molecular weights: this can be explained considering that the contribution of the polymer to σ_{sol} is quite small.

The effects of both the filler and the M_w are quite noticeable on the average viscosity of the solution, whose values are reported in Table 8. Indeed, η increases when using a higher M_w , and a further increase is caused by the addition of MWCNTs. According to the literature, solutions, whose average shear viscosity belongs to the range between 0.02 and 300 Pa*s, are well suited for electrospinning [136]. For values below this range, nanofibers with several defects, as beads, are formed, while for too high values severe difficulties arise in managing the highly viscous solution during the process [226]. Based on the obtained values of the average apparent viscosity, all the four solutions are well suited for electrospinning from this viewpoint. Figure 59 shows the apparent viscosity of the PEO based solutions as a function of the shear rate. A Newtonian behavior can be observed for the 5PEO_1000 at low shear rates, while above 10 s^{-1} , the viscosity starts to decrease for increasing values of the shear rate. This behavior can be explained considering that high shear rates favor both the reduction of interactions among polymers chains and the breaking of the entanglements among them. The viscosity decreases of one order of magnitude as the M_w of PEO decreases, and the corresponding solution, 5PEO_600, exhibits a shear-thinning behaviour. This difference between

the two solutions is due to the relative easiness of the 600kDa PEO polymer chains to start aligning, if compared to the heavier PEO 1000kDa that exhibits a much higher effect of chains interactions and entanglements. When 3.5wt% MWCNTs is introduced in the two samples (i.e., the solutions named 5PEO_600_3.5 and 5PEO_1000_3.5, respectively), the viscosity increases. A typical shear-thinning behaviour is well visible. In this case the addition of MWCNTs helps to reduce the interactions among the polymer chains thereby granting an easier alignment.

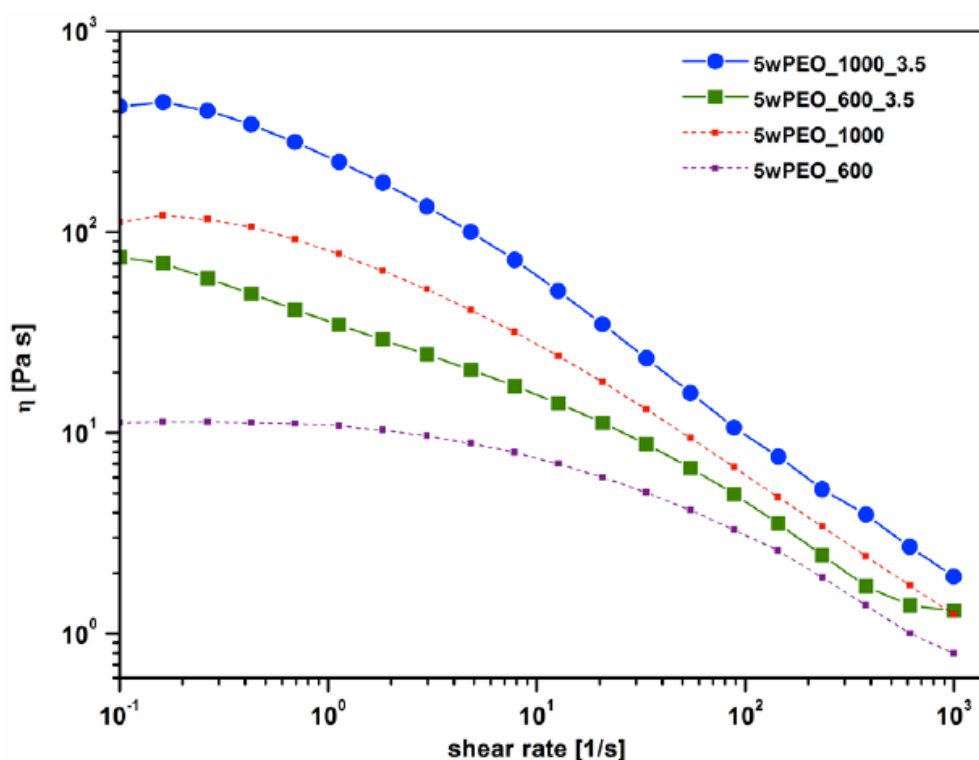


Figure 59 The shear viscosity is reported as a function of the shear rate. All the polymeric solutions have been analyzed, both with and without MWCNTs.

The morphology of the nanofibers, obtained by electrospun 5PEO_600 and 5PEO_1000 solutions, has been analyzed by field emission scanning electron microscopy (FESEM) and the results are shown in Figure 60a), where Figure 60a)-i and Figure 60a)-ii refer to 5PEO_600, and Figure 60a)-iii and Figure 60a)-iv refer to 5PEO_1000. Moreover, the first column in Figure 60a) shows the nanofibers fabricated at 18 kV, while the second one refers to samples processed at 23 kV. The obtained results underline that the morphology can be changed and modulated by varying the process parameters. It is interesting to notice that for all polymeric solutions without the MWCNTs no evidence of nano-

netting is present. The solution prepared with the 1000kDa PEO is too unstable to be electrospun with flow rates higher than 0.1 ml/h, so only the effect of voltage is analyzed in this case. As shown in Figure 60b), the diameter of the nanofibers reduces for increasing applied voltages, and the reduction is more appreciable for higher molecular weights. A correlation between the diameters distribution and the selected M_w can be defined: the higher the M_w , the higher the diameter of the resulting nanofibers. Moreover, increasing the molecular weight the instability of the jet can be strongly enhanced, inducing the spread of the diameters of the collected nanofibers: the higher the M_w , the more disperse the values of resulting diameters.

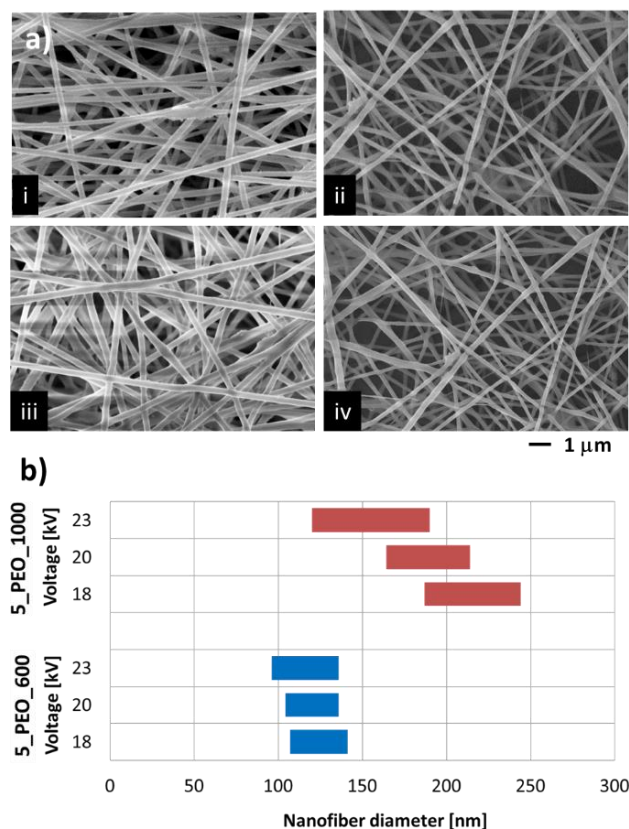


Figure 60 In a) FESEM images of nanofiber mats obtained from 600 kDa PEO in i) and ii), and from 1000 kDa PEO in iii) and iv). The mats have been processed at two different voltages: i) and iii) refer to 18 kV, while ii) and iv) to 23 kV. In b) the distribution of the diameters is analysed as a function of the M_w , the voltage and the flow rate (for 600 kDa PEO only).

Both the viscosity and the electrical conductivity of the solution significantly increase when adding MWCNTs into the hM_w-PEO based solutions, dramatically increasing the probability of jet instabilities during the process, that in turn can deeply change the morphology of the nanofiber mats. The FESEM characterizations of 5PEO_600 and 5PEO_1000 samples containing MWCNTs are reported in Figure 61a) and Figure 61b), respectively. For both the values of the polymer M_w, the diameters of the nanofibers reduce when MWCNTs are added: the higher the MWCNTs concentration (i.e., 3.5 vs. 1.5wt%) the lower the diameter, and a slight decrease is also caused by using higher voltages (i.e., 23 than 18 kV). By analysing in more details the 5PEO_1000 samples, it is possible to notice that a new morphology appears starting from 1.5wt% MWCNTs processed at 18 kV, as highlighted in yellow in Figure 61b)-i, with the creation of a secondary web, made of very small size nanofibers. This is the hybrid arrangement of nano-netting, made of the main nanofibers connected by the secondary, thin, nanoweb [221, 222, 223]. When the concentration of MWCNTs to 3.5 wt% increasing, the nanofiber/net morphology becomes even more complex. These results are in lie with the key finding in the literature, where the nanonets in PEO based composites have been previously reported for PEO/cellulose nanocrystals systems [231]. The morphology of the nanofiber/nets has been analysed by FESEM and the key images obtained are reported in Figure 61b). The nanofiber/nets are denser in the composite systems having a higher content of MWCNTs, and for increasing values of the working voltage. The structure of the nanonets found in this work is actually more complex to that reported in other materials [231], due to the presence of very small size beads along the nanonets (see Figure 61b)-ii); moreover, the density of beads into the nanonets increases as the MWCNTs content increases, as represented in Figure 61b)-ii and Figure 61b)-iv). The MWCNTs play a key role in determining the morphology of the nano-netting characterizing the mat of composite nanofibers based on PEO and MWCNTs.

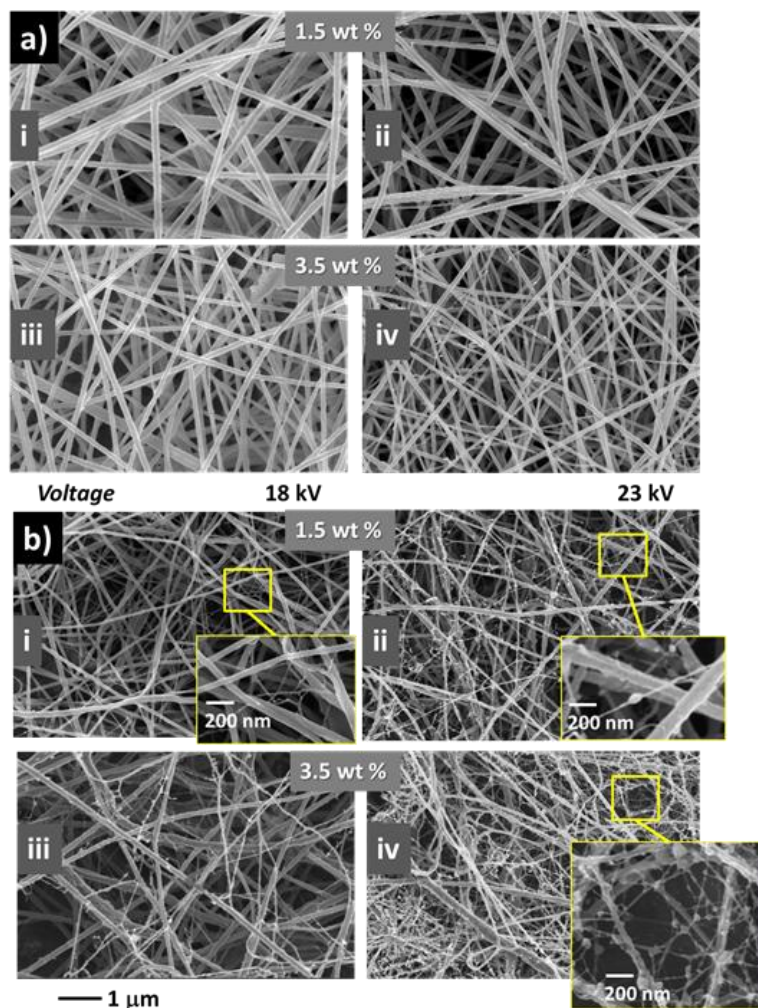


Figure 61 In a) and b) FESEM images of samples 5PEO_600 and 5PEO_1000 respectively, with different concentrations of MWCNTs. Two values are reported for each PEO Mw, i.e. 1.5 and 3.5 wt%, in the upper and lower line respectively of each picture. Morphology is investigated as function of voltage: pictures refers to 18 kV in the left column and 23 kV in the right column. Processing the 5PEO_1000 with MWCNTs nanonetting appears, as highlighted in b).

TEM analysis, shown in Figure 62, the MWCNTs well align to the nanofiber axis during ES, so that given their high dielectric polarizability, a strong dipole–dipole interaction is generated when several MWCNTs are present. Indeed, during electrospinning high electric fields are applied, so that each MWCNT experiences a polarization as sketched in Figure 4a), being the one oriented in the direction of the tube axis ($\vec{P}_{||}$) much larger than that across the diameter (\vec{P}_{\perp}) [235]. This causes a reduction

of the actual electric field in each region where MWCNTs are present, which in turns leads to the creation of an equivalent uncompensated charge distribution (Δq) in that area. Regions with different amounts of MWCNTs on adjacent nanofibers can exhibit different net charge distributions, leading to the creation of strong local secondary electric fields that can generate the secondary nanofiber net. A sketch of the resulting process is proposed in Figure 62a), showing the nano-nets bridging the main nanofibers thanks to the presence of MWCNTs driving the creation of the secondary nanostructure. Our hypothesis is consistent with the strict relation we observed between the NFN density and the MWCNTs content, and in line with the results proposed in other works discussing NN in the PU/MWCNTs composite [136].

Moreover, the presence of the nano-beaded into the nanofibers netting is due to the effect of MWCNTs. As deeply explained in the Chapter 2, beads can be formed during the travel of the fluid jet if the driving force elongating the nanofiber is reduced [236]. The same process to rule the creation of the nano-beaded-NN during the ESN process is considered, in which the MWCNTs alter the actual electric field acting on the small scale nanofibers and so contribute to the creation of the nano-beaded-NN as observed in this work.

TEM analyses were performed in order to analyse the actual distribution and the orientation of MWCNTs and gain a better understanding of the morphology of the hMw-PEO/MWCNTs NFN. A voltage value of 23 kV and a flow rate of 0.1 ml/h are considered as the reference electrospinning parameters, while the MWCNTs loading at 1.5wt% is fixed. Nanofiber/nets were directly collected on standard holey carbon TEM Cu grid. Figure 62a) and Figure 62c) help to confirm that the MWCNTs are aligned along the main axis of the nanofibers, in particular Figure 62b) well show that they are connected to one another in crossing areas among nanofibers. TEM characterization is crucial to confirm that the orientation of MWCNTs is preserved, even if the structure of the NFN is quite complex.

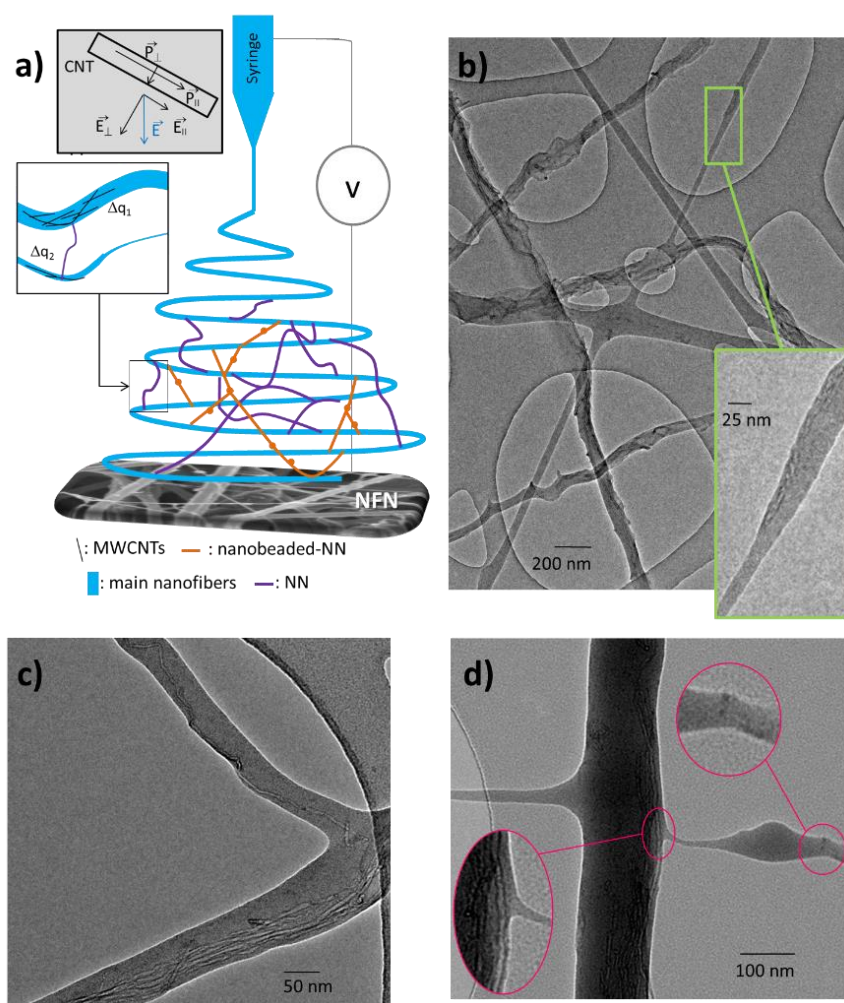


Figure 62 In a) the electrospinning/netting process due to MWCNTs is sketched, with both the NFN and the nanobeaded-NFN represented. In b) TEM analysis of nanocomposite nanofibers with 1.5 wt% MWCNTs is proposed, showing MWCNTs well aligned with the main axis of the nanofibers. In c) a TEM picture of NF and NFN is reported, showing MWCNTs present also in the very small size secondary nanofibers. In d) a TEM picture of a NFN a nanobeaded-NFN is shown.

Moreover, the zoomed detail highlighted in green in Figure 62b) helps showing the presence of MWCNTs even in very small nanofibers having diameters of about 25 nm. The ability of MWCNTs to get distributed not only into the main nanofibers but also into the secondary web is also confirmed by Figure 62c). This finding is of key importance to define the role of the NN on the final electrical behaviour of our composite NFN, as discussed later. In Figure 62d) the TEM analysis gives evidence of both the nano-nets described in this work: two thin fibers are shown, connected to a main nanofiber. In the left part of picture Figure 62d) a thin nanofiber is actually created at the outer part

of the main nanofiber, close to MWCNTS embedded in the main nanofiber [237]. On the right side of the picture, a small size bead is visible, which is slightly elongated: it is connected to the main nanofiber in the region highlighted in pink, where some MWCNTs are present; another MWCNT is visible after the bead, evidenced again with a pink circle in Figure 62d). This suggests a key role of MWCNTs in determining the final morphology observed in the hMw-PEO based composite NFN reported in this work.

A deeper investigation was performed, using Raman spectroscopy and thermal gravimetric analysis (TGA), on the nanocomposite nanofibrous materials made starting from 5PEO_1000 solution. The collected Raman spectra are shown in Figure 63a). The green and blue curves refer to the samples containing 1.5 and 3.5wt% of MWCTNs, respectively.

In line with the TEM analysis results, MWCNTs are confirmed to be actually present into the nanocomposite, by the D, G and the G' bands in the spectra. The D band, which is present in all graphite-like carbons, originates from structural defects and, in MWCTNs based composites, can be related to the stress induced on the carbon nanotubes by the hosting polymer when strong chemical-physical interaction is established among them. Increasing the amount of MWCNTs from 1.5wt% to 3.5wt% into the nanocomposite, the position of the D peak moves slightly to lower wavenumbers (from 1352 to 1348 cm^{-1} , respectively), which is in line with an increase of the stress induced on the MWCNTs [238]. The other peaks refer to the PEO matrix. In particular, in-plane CH deformations can be associated to the peak at 1122 cm^{-1} and at 1465 cm^{-1} CH₂ bending is visible, whereas at 2876, 2940 and 3074 cm^{-1} bands are present that can be assigned to C-H stretching modes [239].

The results of the thermogravimetric analysis are shown in Figure 63b). A reduction of the weight loss is well visible when MWCNTs are added into the samples. Moreover, the degradation temperature increases with the content of carbon nanotubes embedded into the nanofibers. This is consistent with the creation of a larger number of interfaces among the polymer chains and the MWCNTs when increasing their loading. These interfaces among the polymeric nanofibers and the MWCNTs improve the thermal stability of the nanofiber composite material.

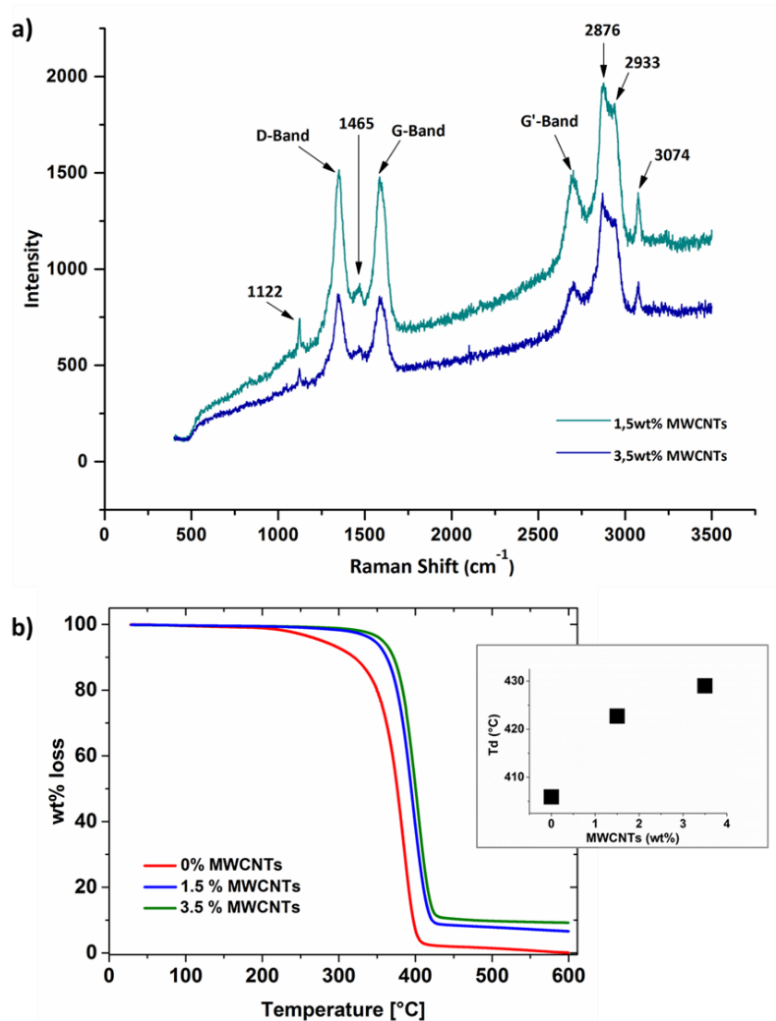


Figure 63 a) Raman spectra of nanofiber mats containing 1.5wt% and 3.5 wt% of MWCNTs. b) Thermogravimetric analysis (TGA) of samples with different MWCNTs loading. In the inserted graph the decomposition temperature (Td) is represented as a function of the concentration of MWCNTs: the higher the concentration, the higher the resulting Td.

✓ Electrical characterizations results

McCullen and colleagues demonstrate a percolation behaviour for the PEO/MWCNTs NF composite [240]. To investigate the role of NFN on the final electrical behaviour exhibited by the PEO/MWCNTs fibrous nanocomposites, samples were fabricated using 5PEO_600 and 5PEO_1000 solutions with defined mass fractions of MWCNTs. Indeed, the morphological characterizations demonstrate that no NFN has been observed for the 600kDa PEO allowing a comparison between standard NF and the NFN obtained using the 1000kDa PEO. Moreover, 5PEO_1000 samples were processed with two

different voltages, i.e. 18 and 23 kV, in order to fabricate samples with less or denser nano-nets, respectively, and consequently to define how the electrical conductivity increases as the nano-nets distribution changes.

The experimental values of the electrical conductivity as a function of the MWCNTs weight percentages (i.e., 0.75wt %, 1.5wt %, 2.5wt %, 3wt % and 3.5wt %) are represented, in logarithmic scale, in Figure 64a). The three sets of data are fitted with the percolation models, as reported in Eq 62 and in the Eq 63:

$$\sigma = \sigma_0(p - p_c)^t \quad \text{Eq 62}$$

$$\sigma = \sigma_d(p_c - p)^{-s} \quad \text{Eq 63}$$

These equations describe the electrical conductivity as a function of the filler content above and below the percolation threshold, respectively.

In the model p_c is the percolation threshold, σ is the electrical conductivity, p is the weight percentage of MWCNTs, and σ_0 , σ_d , t and s are fit parameters. The fitting curve for 5PEO_600 is represented in green, while the fitting curves for 5PEO_1000 samples processed at 18 kV are in blue for samples, while in red for those processed at 23 kV. The values of the percolation thresholds, p_c are 2.3 and 2.1wt% of MWCNTs for samples 5PEO_1000 processed at 23kV and 18kV, respectively and 1.5wt% for samples 5PEO_600. It is interesting to notice that the percolation threshold increases for increasing values of the polymer average molecular weight; moreover, for each MWCNTs concentration, the conductivity of the 5PEO_1000 processed at 18kV is lower than the conductivity of the samples with the same concentration of MWCNTs but fabricated with the 600kDa PEO. This behaviour can be explained considering the morphology of both the nanofibers and the nanofiber/nets. The consequence of the presence of less-dense NFN is therefore detrimental on the creation of a percolation path, so that higher concentration of MWCNTs are necessary to reach the threshold. Moreover, above the percolation threshold, for each

concentration of MWCNTs, the electrical conductivity remains lower than that of samples made with standard NF.

The red curve in Figure 64 refers to the 5PEO_1000 samples processed at 23 kV. When high voltage is used to fabricate the samples, a more ordered and compact NFN mat is created and, in particular, by increasing the amount of MWCNTs into the material, voids are progressively well occupied by the NN and the nanobeaded-NN. As confirmed by TEM analysis, the MWCNTs can be present into the secondary nanoweb. This turns in the progressive improvement of the percolation networks increasing the MWCNTs content, so incrementing the probability of charge transfer across the mat of nanofibers also thanks to the contribution of the nano-nets. The result is that dense NFN exhibit the onset of the electrical percolation at MWCNTs concentration close to the value found for the less dense NFN, but the exhibited electrical conductivity is significantly improved (Figure 64).

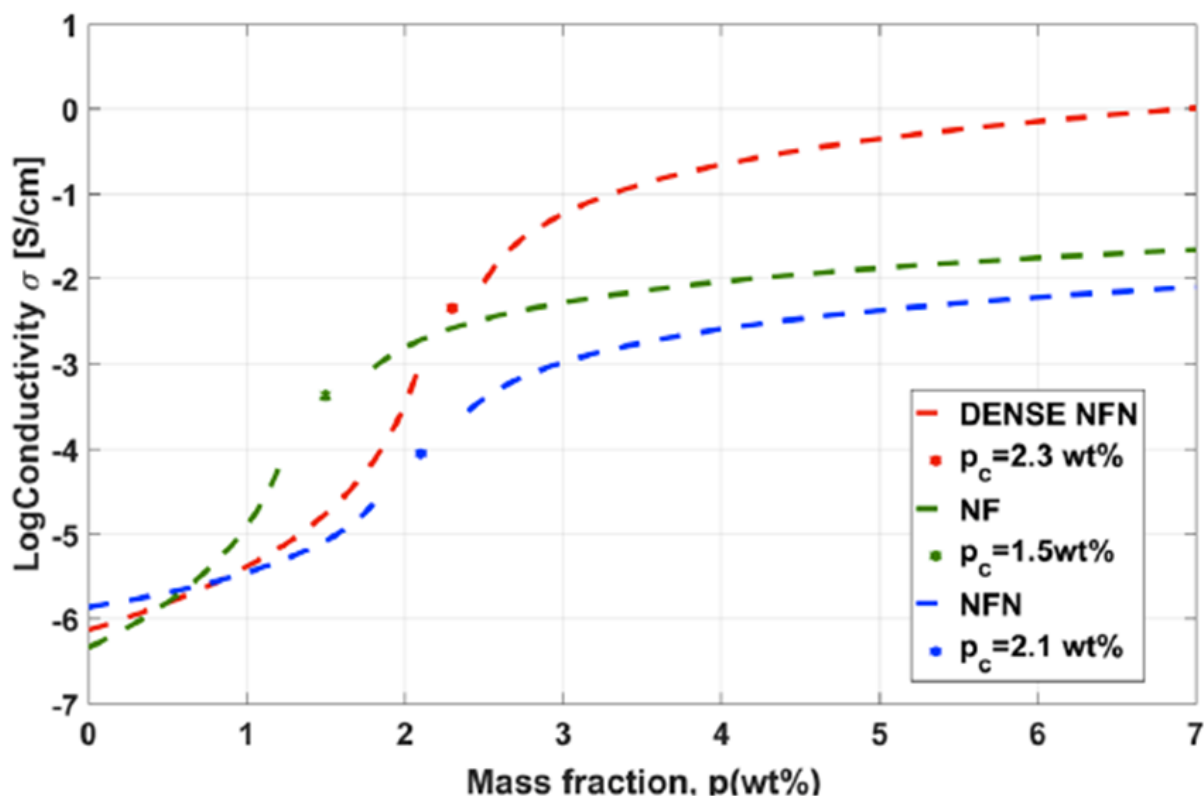


Figure 64 Experimental values of the electrical conductivity of composite nanofibers and nanofiber/nets for different concentration of MWCNTs. Three sets of samples are represented: red = 5PEO_600 with MWCNTs; blue = 5PEO_1000 with MWCNTs processed at 18 kV; red = 5PEO_1000 with MWCNTs processed at 23 kV.

Finally, regarding the intrinsically hygroscopic properties of the PEO, the different response, is investigated in terms of the relative resistance nanofibers increasing to the humidity; the correlation between this effect and the morphological properties of the samples is defined. Since exposure to humidity is expected to cause the polymer nanofibers to swell by water adsorption, if the concentration of MWCNTs is above the percolation threshold, the polymer swelling can directly affect the quality of the percolation path. The resulting sensing mechanism is a physical one, based on the increase of the material electrical resistivity due to the increase of the distance among the MWCNTs as caused by the polymer swelling [241, 242]. In other words, the percolation networks are reversibly worsened by water vapour adsorption. This implies that the worse is the quality of the percolation network, the lower will be the response of the sensor. Since, as well demonstrated in the previous sections, MWCNTs spontaneously align along the nanofibers during the electrospinning processes and also when the secondary jet is generated, the resulting composite materials can exhibit increased sensing properties respect to traditional ones. The tests using the same sample architecture, already used for the electrical characterizations of the material, are performed: the samples are directly exposed to a vapour flow in air generated by an aerosol system placed in proximity of them. An aerosol system is selected to avoid the effect of temperature on the samples during the tests. The test is conducted at room temperature (i.e., 23°C) and the lowest value of the relative humidity is the ambient one (i.e., 23%). A digital thermo-hygrometer (DTH) is placed in close proximity of the sample under investigation and it is possible to establish that 30 s are necessary to actually change the relative humidity from the lowest (23%RH) to the highest (60%RH) value, after that time the humidity remains constant at 60 %RH. The vapour is supplied to the sample according to following cycles: 30 s of exposure to humidity and 2 minutes of no exposure (recovery time). The results are shown in Figure 65, reporting the dimensionless relative differential resistance, $\Delta R/R_0$, defined in Eq 64

$$\Delta R/R_0 = (R - R_0)/R_0 \quad \text{Eq 64}$$

where R is the actual resistance and R_0 is the baseline resistance of the composite materials prior to exposure to the humidity change. Three sets of samples containing contained a 3.5 wt% of MWCNTs are analyzed: one made of NF only (i.e., 5PEO_600_3.5), one with the less dense NFN (i.e., 5PEO_1000_3.5 processed at 18kV) and the third with the dense NFN (i.e., 5PEO_1000_3.5 processed at 23kV). The good reversibility in the response of all the samples is well shown in Figure 65. Moreover, the results are impressively in line with the expected behaviour of these systems. Indeed, samples with a less dense NFN (blue curve) behaved worse than samples with NF only (green curve), but the dense NFN (red curve) significantly increased the response. Dense NFN had a 4 times higher value of $\Delta R/R_0$ than samples with standard NF mats.

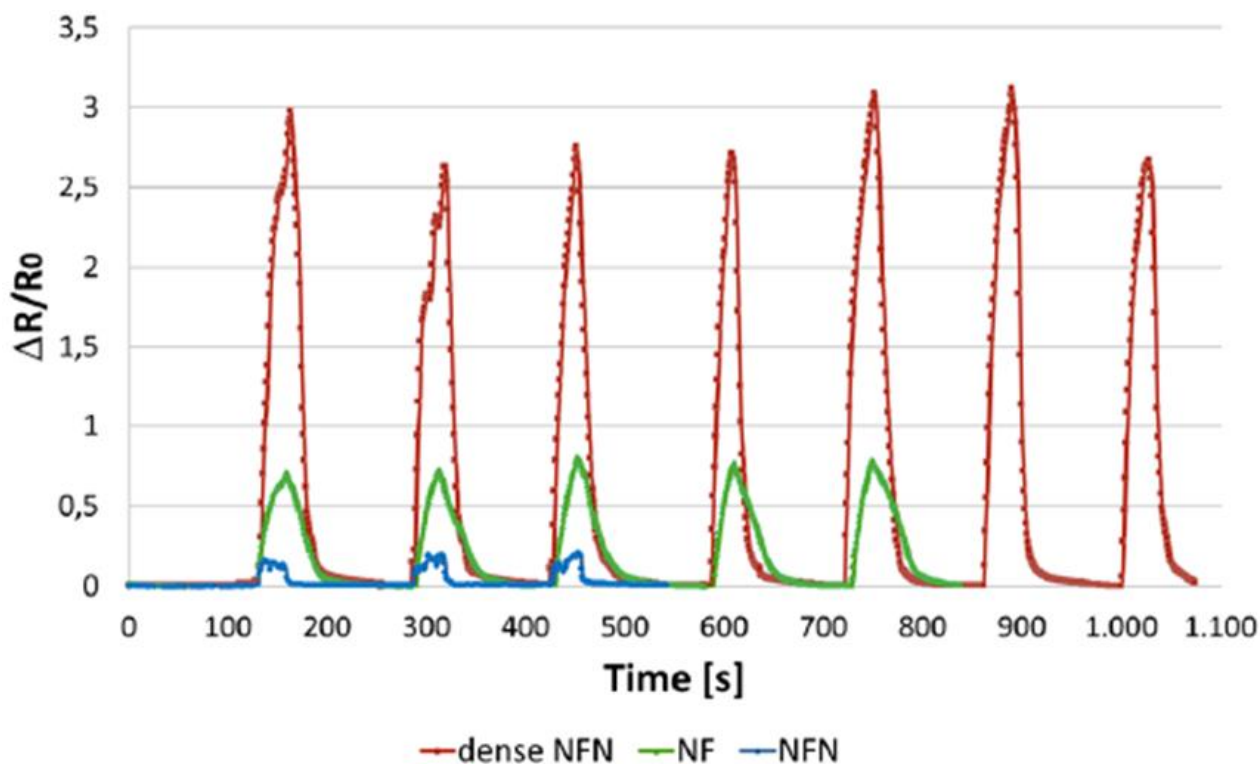


Figure 65 the relative differential resistance for the NF, NFN and dense NFN.

4.5 Conclusions

The nanostructured manganese oxides are prepared by using biocompatible and biodegradable precursors, by means of the electrospinning process. The final nanofibers Mn_3O_4 -based catalysts showed a good catalytic performance for the oxygen reduction reaction, with n values equal to 3.6,

at potentials lower than -0.4 V, which is in line with other cost-effective catalysts proposed in the literature. In order to improve these results, the electrical conductivity of ceramic nanofibers should be increased, leading to the increasing of the catalytic behaviour of these kind of materials. One of the possibilities is represented by the using of MWCNTs as a conductive filler into the ceramic mat of nanofibers. Due to the complexity of the electrospinning process and in order to better understand the correlation among the presence of MWCNTs, dissolved into a no conductive polymeric solution, and the final morphological properties of the nanofibers mat, a composite nanofibers based on PEO/MWCNTs have been investigated in this work. The obtained results demonstrate how the morphological aspects are modified by the adding of the MWCNTs and in particular how the electrical conductivity increases as the amount of MWCNTs increases. All these aspects allow to study, as future developments, the ceramic nanofibers starting from an initial electrospun polymeric solution, containing the PEO as a templating agents in order to obtain the final nanofibers, the manganese as the source of manganese oxide and the MWCNTs in order to improve the electrical conductivity of the nanofibers.

5 Thesis Conclusion

This thesis has widely explained the interconnection between the nanotechnology and energy production devices which use renewable energy sources; in particular, it has been demonstrated how the nanotechnology can improve the performances and the efficiency of these devices. The nanofibers, produced through the electrospinning technique, are developed in order to design new 3D innovative electrodes for bio-electrochemical devices, as Microbial Fuel Cells (MFCs).

It has been demonstrated that the nanostructured electrodes improve the efficiency of the Single Chamber Microbial Fuel cells (SCMFCs) thanks both to their low impedances and to their interaction with the microorganisms, considering the nanofibers as anode.

Furthermore, in this work the SCMFC architecture is widely described; the SCMFC is developed in order to ensure the oxygen reduction reaction into the cathode and, moreover, its architecture provides for the unique common electrolyte, since the proton exchange membrane is not used. The electrolyte contains the organic matter that is oxidized by the bacteria proliferated on the anode, the nitrogen source able to ensure an anaerobic environment into the devices, and the salts additives in order to maintain a neutral pH value quite constant. The SCMFC ensures, through an open air cathode configuration, the diffusion of the oxygen from the environment into the cell, leading to the oxygen reduction reaction (ORR) into the cathode compartment and, at the same time, minimizing the amount of oxygen near to the anode electrode, maintaining thus the anaerobic conditions as much as possible.

The carbon nanofibers are revealed the most promising material in the field of bio electrochemistry, satisfying all the main required properties for this device: high biofilm compatibility and good electrical conductivity. In particular, two different carbon nanofibers mats have been synthesized, starting from the same polymeric precursor solution but applying two different pyrolysis treatments in order to obtain a sample called PAN_600 and one defined PAN_900. The selected polymeric precursor is Polyacrylonitrile (PAN) thanks to its high carbonization yield; the polymer, dissolved in N-N DMF, ensures a proper solution viscosity value in order to guarantee the electrospinning process and the formation of final nanofibers mat.

The sample PAN_600 has been obtained through the definition of pyrolysis treatment conducted until a temperature of 600°C; on the contrary, the defined PAN_900 is treated until a temperature of 900°C; both of two treatments have been performed under inert atmosphere.

It has been demonstrated that PAN_600 carbon nanofibers satisfy all the mandatory properties of anode electrodes; while PAN_900 shows a high electro-catalytic behaviour, which, combined with its higher electrical conductivity, enhances the oxygen reduction reaction (ORR) occurred into the cathode.

It has been defined what properties make PAN_600 nanofibers the most innovative and promising structures in order to design an anode electrode for microbial fuel cells. It has been verified that the nanostructure provides an ideal habitat for the bacteria proliferations; in particular, the crosslinked nanofibers lead to the formation of 2D biofilm on them, which follows the connection among the nanofibers, improving the electron transfer from the bacteria to the electrode. Moreover, the high micrometric porosity of the materials, defined as the ratio between the volume of void spaces and the volume of bulk solid sample, enhances the penetration of bacteria and their proliferation, as deeply shown in the FESEM images into the Chapter 3. Through FESEM images, I have demonstrated that the bacteria proliferation is better on the sample of PAN_600 than that on carbon felt (CF), a commercial material used as anode reference material. Furthermore, the required high porosity improves the diffusion of chemical elements, which can be organic substrate, if the materials are used as anode, or oxygen, if the samples were applied as cathode.

PAN_600 carbon nanofibers, obtained optimizing the synthesis process in order to ensure a correct nitrogen content necessary to improve the electro-catalytic properties without any successive treatments, result to be a better bio-electrochemical system compared with the commercial material.

In particular, PAN_600 nanofibers show a partial protonated charge surface, which enhances the interaction with the microorganisms, thanks to the higher amount of pyridinic-N and pyrrolic-N, as established by all optical characterizations, such as X-ray Photoelectron Spectroscopy (XPS), Raman and Infrared Spectroscopy in Absorbance mode (ATR). While, as confirmed by Cyclic Voltammetry (CV) conducted on the samples, the electrochemical activity of PAN_600 is improved by pyridinic and pyrrolic nitrogen content.

Furthermore, it is important to underline again that this pyrolysis treatment guarantees a low cost process, able to ensure better morphological and chemical properties of PAN_600, without any successive chemical treatments, such as ammonia treatment or stem activation, which are widely used in the literature in order to obtain the required nitrogen doping [204].

Finally, these carbon nanofibers have a proper value of conductivity to guarantee the electron flow between biofilm and anode, and between anode and cathode through the external load applied.

Thanks to all these properties, PAN_600 carbon nanofibers have emerged as new 3D anode, leading to an improvement of the devices power density production, which is two order of magnitude higher than the ones obtained with the anode based on carbon felt (CF).

Regarding the development of new catalyst cathode material, in order to obtain a nanostructured material with a very high surface area, able to increase the number of catalytic sites exposed to the oxygen, and to substitute the platinum that until now is considered the ideal standard catalysts material, two different solutions have been developed. The first one is represented by carbon nanofibers (PAN_900), obtained through electrospinning technique and after a pyrolysis treatment until a final temperature of 900°C under inert atmosphere; while, the second one is based on manganese oxide nanofibers (Mn_xO_y), starting from an electrospun polymeric solution containing the manganese source and through the definition of proper calcination treatment. These two samples guarantee cheaper and eco friendlier materials if compared to the platinum catalyst.

As demonstrated by all physical, electrical and electrochemical characterizations performed on PAN_900 samples, both the high content of Graphitic-N and the high electrical conductivity, which is in the order of some mS/cm, improve the electro-catalytic behaviour respect to the oxygen reduction reaction (ORR). The electrochemical characterizations, carried out by ALS RRDE-3A rotating ring disk electrode apparatus, have defined the electron transfer number for PAN_900 equal to 3.9 and the percentage of peroxide species formation HO_2^- %, lower than 10%.

These finding results are quite similar to ones obtained for Platinum confirming the high electrochemical activity of PAN_900 carbon nanofibers. Good electrochemical behaviour, in addition to the all properties of the nanostructures, confirms the possibility to apply this kind of material as catalyst cathode thus upgrading the performances of the device.

The final cathode electrode is composed by two layers of PAN_900 electro-deposited directly on the carbon paper (CP) modified with a layer of PTFE on the opposite side; this cathode electrode has been compared with (CP), on which a catalyst layer of Platinum (Pt) and Nafion have been deposited, building thus the reference cathode electrode. The SCMFCs with catalyst carbon nanofibers reached a maximum power density close to 150mW/m^2 , two orders of magnitude higher than the one obtained with Pt catalyst layer, equal to 4mW/m^2 .

On the other hand, the manganese oxide (Mn_xO_y) nanofibers are obtained starting from a polymeric solution, based on Polyethylene oxide (PEO) as templating agent for the formation of nanofibers and manganese acetate as the manganese source (Mn). The final nanofibers mat has been calcinated until a final temperature of 480°C in order to guarantee the complete decomposition of PEO and the formation of manganese oxide nanofibers, as demonstrated by all characterizations performed on the final nanostructured samples. In particular, through X-ray Diffraction (XRD) spectroscopy and TEM characterizations, the presence of Mn_3O_4 , electrodeposited directly on the carbon based materials, is confirmed. The final Mn_3O_4 based catalyst showed good electro-catalytic properties for the oxygen reduction reaction with a number of electron transfer close to 3.7 at potentials lower than -0.4V , which is in line with other catalysts developed in the literature.

On the contrary, one of main limiting factors for the final application of Mn_3O_4 nanofibers as catalyst cathode into the device is represented by their low electrical conductivity, which can be increased adding a conductive filler into the final samples. Multi Wall Carbon Nanotubes (MWCNTs) are one of the possible conductive filler, increasing the percolation path and consequently the electrical conductivity of the final composite nanofibers mat.

Due to the influence of MWCTNs on the optimization of the electrospinning parameters and consequently on the final morphology of the nanofibers, a simplified polymeric solution, containing only PEO and MWCNTs, was initially investigated.

Indeed, it was mandatory to define the correct electrospinning parameters for the polymeric solutions containing a no conductive polymer (PEO) and a conductive filler, such as MWCNTs, in order to control the charge distribution into the polymeric solution, constraining and managing the formation of jet instabilities during the process.

The obtained results have demonstrated that the addition of the MWCNTs modifies the morphological aspects of the nanostructured samples, creating a secondary thinner web of nanofibers, which are in contact with the main nanofibers. As confirmed by FESEM and TEM characterizations, the MWCNTs are embedded into the nanofibers and, moreover, thanks to the formation of the secondary web, they are in contact one with each other. All these finding results have confirmed the improvement of the percolation paths for electrons, increasing the electrical conductivity of the composite nanofibers as the MWCNTs content increases.

The combinations of all these results, regarding good electro-catalytic properties of Mn_xO_y nanofibers and the increasing of electrical conductivity of composite nanofibers based on PEO/MWCNTs, lead to the investigation of ceramic nanofibers functionalized with MWCNTs as conductive filler as future developments.

In particular, the increment of electrical conductivity of composite nanofibers based on Mn_xO_y /MWCNTs should improve the electro-catalytic properties for ORR, ensuring its application as catalyst cathode in SCMFCs, substituting the more expensive platinum layer, thanks to their low cost, relatively high abundance of manganese oxide and its lower environmental impact.

In wider terms, to further enhance the performances of bio-anodes and bio-cathodes, a set of properties are required to be optimized, such as a proper surface morphology and chemistry, good biofilm adhesion and electron transfer, and a good electrical conductivity.

All the obtained results have demonstrated that the electrospun nanofibers own all the necessary properties, revealing themselves as the most innovative and promising structures for the design of anodes and cathodes in microbial fuel cells.

6 References

- [1] W. Luther, Application of Nanotechnologies in the energy sector, Wiesbaden Germany, 2008.
- [2] «US Energy Information Administration (EIA),» April 2016. [Online].
- [3] A. Akella, R. Saini e M. Sharma, «Social, economical and environmental impacts of renewable energy systems,» *Renewable Energy*, vol. 34, pp. 390-396, 2009.
- [4] «KYOTO PROTOCOL TO THE UNITED NATIONS FRAMEWORK CONVENTION ON CLIMATE CHANGE,» 2005.
- [5] E. Commissions, «Renewable Energy Moving Towards a low carbon economy,» 2016.
- [6] W. Bank, «http://www.worldbank.org/html/fpd/energy/e4_files/rural.pdf,» Meeting the challenge for rural energy and development, 1999. [Online].
- [7] J. Wendorff, S. Agarwal e A. greiner, *Electrospinning: Materials, Processing and Applications*, Weinheim: Wiley, 2008.
- [8] Z. Huang, Y. Zang, M. Kotaki e K. Ramakrishna, «A review on polymer nanofibers by electrospinning and their applications in nanocomposites,» *Composites Science and Technology*, vol. 63, p. 2223–2253, 2003.
- [9] B. Logan, *Micorbial Fuel Cells*, Wiley interscience, 2007.
- [10] S. Chen, H. Hou, F. Harnisch, S. Patil, A. Carmona Martinez, S. Agarwal, Y. Zhang, S. Ray, A. Yarin, A. Greiner e U. Schroeder, «Electrospun and solution blown three-dimensional carbon fiber nonwovens for application as electrodes in microbial fuel cells,» *Energy and Environmental Science*, vol. 4, pp. 1417-1421, 2011.
- [11] A. Ghenciu, «Review of fuel processing catalysts for hydrogen production in PEM fuel cell systems,» *Current Opinion in Solid State and Materials Science*, vol. 6, n. 5, pp. 389-399, 2002.
- [12] A. Qi, B. Peppley e K. Karan, «Integrated fuel processors for fuel cell application: A review,» *Fuel Processing Technology*, vol. 88, n. 1, pp. 3-22, 2007.

References

- [13] J. Larminie e A. Dicks, «Fuel cell systems explained,» *John Wiley & Sons*, 2000.
- [14] B. Logan, P. Aelterman, B. Hamelers, R. Rezendal, U. Schroeder, J. Keller, S. Freguia, W. Verstraete e K. Rabaey, «Microbial fuel cells: methodology and technology,» *Environmental Science and Technology*, vol. 40, pp. 5181-5192, 2006.
- [15] B. Logan, *Microbial Fuel Cells*, John Wiley & Sons Inc, 2008.
- [16] Lewis e Nocera, «Powering the planet: chemical challenges in solar energy utilization,» *PNAS*, vol. 103, pp. 15729-15735, 2006.
- [17] «<https://www.iea.org/>,» [Online].
- [18] R. Allen e H. Bennetto, «Microbial Fuel Cells: Electricity production from carbohydrates,» *Appl. Biochemical Biotechnology*, vol. 39, pp. 27-40, 1993.
- [19] B. Kim, D. Park, P. Shin, I. Chang e H. Kim, «Mediator-less biofuel cell,» *U.S patent 5976719*, 1999.
- [20] K. Rabaey e R. Rozendal, «Microbial Electrosynthesis-revisiting the electrical route for microbial production,» *Applied and industrial microbiology*, vol. 8, pp. 706-716, 2010.
- [21] W. t. f. encyclopedia, «<https://en.wikipedia.org/wiki/Biofilm>,» [Online].
- [22] F. Harnisch, F. Aulenta e U. Shroeder, «Microbial Fuel Cells and Bioelectrochemical Systems: Industrial and environmental Biotechnologies based on extracellular electron transfer,» Elsevier, 2011, pp. 644-659.
- [23] J. Babuata, R. Renslow, Z. Lewandowski e H. Beyenal, «electrochemically active biofilms: facts and fiction. A review,» *Biofouling*, vol. 28, n. 8, pp. 789-812, 2012.
- [24] M. Hernandez e D. Newman, «Exacellular Electron Transfer,» *CMLS CELL MOL LIFE SCI*, vol. 58, 2001.
- [25] K. Rabaey, N. Boon e al, «Biofuel cells select for microbial consortia that self-mediate electron transfer,» *Appl Environ Microbiol*, vol. 70, pp. 5373-5382, 2004.
- [26] K. Rabaey, N. Boon, M. Hofte e W. Verstraete, «Microbial phenazine production enhances electron transfer in biofuel cells,» *Appl Environ Microbiol*, vol. 70, n. 9, pp. 5373-5382, 2005.

- [27] Y. Gorbi e al, «Electrically conductive bacterial nanowires produced by shewanella oneidensis strain MR-1 and other microorganisms,» *PNAS*, vol. 103, n. 30, pp. 11358-11363, 2006.
- [28] G. Reguera e al., «Extracellular electron transfer via microbial nanowires,» *Nature*, vol. 435, pp. 1098-1101, 2005.
- [29] «<https://pubchem.ncbi.nlm.nih.gov/compound/phenazine-1-carboxamide#section=Top>,» [Online].
- [30] «pubchem.ncbi.nlm.nih.gov,» [Online].
- [31] «<http://encyclopedia2.thefreedictionary.com/inoculum> The Free Dictionary,» farlex. [Online].
- [32] F. Harnish e U. Schroeder, «From MFC to MXC:chemical and biological cathodes and their potential from microbial bioelectrochemical systems,» *Chem Soc Rev*, vol. 38, pp. 4433-4448, 2010.
- [33] Kim, H. Yang e R. Hensley, «Effective control of chlorination and dechlorination at wastewater treatment plant using redox potential,» *water environment research*, vol. 69, pp. 1008-1014, 1997.
- [34] H. Liu, R. Ramnarayan e B. Logan, «Production of electricity during wastewater treatment using a single chamber microbial fuel cell,» *Environmental Science and Technology*, vol. 38, pp. 2281-2285, 2004.
- [35] B. Logan, B. Hamelers, R. Rozendal, U. Schroder, J. Keller, S. Freguia, P. Aelterman, W. Verstraete e K. Rabaey, «Microbial Fuel Cells: Methodology and Technology,» *Environmental Science Technology*, vol. 40, n. 17, pp. 5181-5192, 2006.
- [36] C. Song e J. Zhang, «Electrocatalytic oxygen reduction reaction,» in *PEM Fuel Cell Electrocatalysts and Catalyst layers*, London, Springer-Verlag, 2008, pp. 89-134.
- [37] S. Cheng, H. Liu e B. Logan, «Increased performance of single chamber microbial fuel cells using an improved cathode structure,» *Electrochemistry Communications*, vol. 8, pp. 489-494, 2006.

- [38] S. Cheng, H. Liu e B. Logan, «Increased performnace of single chamber microbial fuel cells using an improved cathode structure,» *Electrochemistry Communications*, vol. 8, pp. 489-494, 2006.
- [39] S. Cheng, H. Liu e B. Logan, «Power densities using different cathode cataalysts (Pt and CoTMPP) and polymer binders (Nafion and PTFE) in single chamber microbial fuel cells,» *Environmental Science and Technology*, vol. 40, pp. 364-369, 2006.
- [40] S. Oh e B. Logan, «Proton exchange membrane and electrode surface areas as factors that affect power generation in microbial fuel cell,» *Appl. Microbiol. Biotechnol.*, vol. 72, pp. 162-169, 2006.
- [41] S. You, Q. Zhao, J. Jiang e S. Zhao, «A microbial fuel cell using permanganate as the cathodic electron acceptor,» *Journal of Power Sorcues*, vol. 162, n. 2, pp. 1409-1415, 2006.
- [42] P. Aelterman, K. Rabaey, N. boon e W. Vestraete, «Continuous electricity generation at high voltages and currents using stacked microbial fuel cells,» *Environmental Science and Technology*, vol. 40, pp. 3388-3394, 2006.
- [43] J. Menicucci, H. Beyenal, E. Marsili, R. Veluchamy, G. Demir e Z. Lewandowski, «Procedure for determining maximum sustainable power generatted by microbial fuel cells,» *Environmental Science and Technology*, vol. 40, pp. 716-721, 2006.
- [44] B. Logan, S. W. Hermanowicz e G. Estadt, «Graphite fiber brush anodes for increased power production in air cathode microbial fuel cells,» *Environmental and Science technology*, vol. 41, pp. 3341-3346, 2007.
- [45] J. Heilman e B. Logan, «Production of electricity from proteins using a single chamber microbial fuel cell,» *Water Environ Res*, vol. 78, pp. 531-537, 2006.
- [46] B. Conway e J. Bockris, *The Modern aspects of electrochemistry*, New York: Kluwer Academic Publisher, 2002.
- [47] F. Lisdat e D. Shafer, «The use of electrochemical impedance spectroscopy for biosensing,» *Springer Anal. Bioanal.Chem*, vol. 39, pp. 1555-1567, 2008.

- [48] S. Chaudhuri e D. Lovley, «Electricity generation by direct oxidation of glucose in mediatorless microbial fuel cells,» *Nat Biotechnol*, vol. 21, pp. 1229-1232, 2003.
- [49] Y. Ahn e B. E. Logan, «Effectiveness of domestic wastewater treatment using microbial fuel cells at ambient and mesophilic temperatures,» *Bioresource and Technology*, vol. 101, pp. 469-475, 2010.
- [50] Zhou e al, «An Overview of electrode materials in microbial fuel cells,» *journal of power sources*, vol. 196, pp. 4427-4435, 2011.
- [51] Y. Feng, X. Wang e B. Logan, «Brewery wastewater treatment using air cathode microbial fuel cells,» *water science technology*, vol. 57, pp. 1117-1121, 2008.
- [52] Logan e al., «Graphite fiber brush anodes fro increment of power production in Air cathode Microbial Fuel Cell,» *environmental Science technology*, vol. 41, pp. 3341-3346, 2007.
- [53] K. C e al., «synthesis and characterization of porous carbon nanofibers with hollow cores through the thermal treatment of electrospun copolymer nanofibers web,» *Small*, vol. 3, pp. 91-95, 2007.
- [54] C. Kim, B. Ngoc, K. Yang, M. Kojima, Y. Kim, Y. Kim, M. Endo e S. Yang, «Self sustained thin webs consisting of porous carbon nanofibers via electrospinning of polyacrylonitrile solutions containing zinc chloride,» *Advanced materials*, vol. 19, pp. 2341-2346, 2007.
- [55] S. Chen, G. He, A. Martinez, S. Agarwal, H. Hou e U. Schroeder, «Electrospun carbon fiber mat with layered architecture for anode in microbial fuel cells,» *Electrochemistry communications*, vol. 13, n. 10, pp. 1026-1029, 2011.
- [56] Manickam e al, «activated carbon nanofibers andoes for microbial fuel cells,» *Carbon*, vol. 53, pp. 19-28, 2013.
- [57] S. Chen e U. Schroeder, «Electrospun and solution blow three dimensional carbon fiber nonwoven for application as electrodes in microbial fuel cells,» *Energy and Environmental Science*, vol. 4, pp. 1417-1421, 2011.

- [58] S. Cheng e B. E. Logan, «ammonia treatment of carbon cloth anodes to enhance power generation of microbial fuel cells,» *Electrochemistry communications*, vol. 9, pp. 492-496, 2007.
- [59] M. Kannan e G. Kumar, «Current status, key challenges and its solutions in the design and development of graphene based ORR catalysts for the microbial fuel cell applications,» *Biosensors and Bioelectrtonics*, vol. 77, pp. 1208-1220, 2016.
- [60] D. Park e J. Zeikus, «Impact of electrode composition on electricity generation in a single compartment fuel cell using *Shewanella putrefaciens*,» *Appl Microbiol Biotechnol*, vol. 59, pp. 58-61, 2002.
- [61] H. Park e J. Zeikus, «Improvred fuel cell and electrode designs for producing electricity from microbial degradation,» *Biotechnology Bioengineering*, vol. 81, n. 3, pp. 348-355, 2003.
- [62] F. Zhao, F. Harnisch, U. Schroeder, F. Scholz, P. Bogdanoff e I. Hermann, «Application of pyrolysed iron (II) phtalocyanine and CoTMPP based oxygen reduction cataalysts as cathode materials in microbial fuel cells,» *Electrochemistry Communications*, vol. 7, pp. 1405-1410, 2005.
- [63] L. DelMondo, G. Massaglia, G. Salvador, J. Tabares, A. Sacco, N. Garino, M. Castellino, M. Gerosa, A. Chiodoni e M. Quaglio, «Nanostructured Mn_xO_y for oxygen reduction reaction,» *Applied surface Science*, vol. 388, pp. 631-639, 2016.
- [64] Q. Wen, S. Wang, J. Yan, L. Cong, Z. Pan, Y. Ren e Z. Fan, « MnO_2 - grpahene hybrid as an alternative cathodic catalyst to platinum in microbial fuel cells,» *Journal of Power Sources*, vol. 216, pp. 187-191, 2012.
- [65] P. Clauwaert, K. Rabaey, P. Aelterman e al, «Biological denitrification in microbial fuel cells,» *Environmental SCience and Technology*, vol. 41, n. 9, pp. 3354-3360, 2007.
- [66] A. Bergel, D. Feron e A. Mollica, «Catalysis of oxygen reduction in PEM fuel cell by seawater biofilm.,» *electrochemistry communications*, vol. 7, n. 9, pp. 900-904, 2005.

- [67] K. Rabaey, G. Lissens, S. Sicilian e W. Verstraete, «A microbial fuel cell capable of converting glucose to electricity at high rate and efficiency,» *Biotechnol Lett*, vol. 25, n. 18, pp. 1531-1535, 2003.
- [68] D. Park e J. Zeikus, «Electricity generation in microbial fuel cells using neutral red as an electronophore,» *Appl Environ Microbiol*, vol. 66, n. 4, pp. 1292-1297, 2000.
- [69] H. Liu e B. Logan, «Electricity generation using an air cathode single chamber microbial fuel cell in the presence and absence of a proton exchange membrane,» *Environmental Science and Technology*, vol. 38, n. 14, pp. 4040-4046, 2004.
- [70] K. Rabaey e al, «Microbial fuel cells for sulfide removal,» *Environmental Science and Technology*, vol. 40, n. 17, pp. 5218-5224, 2006.
- [71] J. Jang e al, «Construction and operation of a novel mediator and membrane less microbial fuel cell,» *Process Biochem*, vol. 39, n. 8, pp. 1007-1012, 2004.
- [72] H. Moon e al, «Residence time distribution in microbial fuel cell and its influence on COD removal with electricity generation,» *Biochem Eng J*, vol. 27, n. 1, pp. 59-65, 2005.
- [73] Z. He e al, «Electricity generation from artificial wastewater using an upflow microbial fuel cell,» *Environmental and Science Technology*, vol. 37, n. 14, pp. 5262-5267, 2005.
- [74] S. Oh e B. Logan, «Hydrogen and electricity production from a food processing wastewater using fermentation and microbial fuel cell technology,» *Water Res*, vol. 39, n. 19, pp. 4673-4682, 2005.
- [75] B. Min, J. Kim, S. Oh, J. Regan e B. Logan, «Electricity generation from swine wastewater using microbial fuel cells,» *Water Res*, vol. 39, n. 20, pp. 4961-4968, 2005.
- [76] Y. Zhou, P. Maness e B. Logan, «Electricity production from steam exploded corn stover biomass,» *Energy & Fuels*, vol. 20, n. 4, pp. 1716-1721, 2005.
- [77] J. Kim, B. Min e B. Logan, «Evaluation of procedures to acclimate a microbial fuel cell for electricity production,» *Appl. Microbiol Biotechnol*, vol. 68, n. 1, pp. 23-30, 2005.

- [78] L. Tender e al, «Harnessing microbially generated power on the seafloor,» *Nat Biotechnol*, vol. 20, n. 8, pp. 821-825, 2002.
- [79] E. DeLong e P. Chandler, «Power from the deep,» *Nature Biotechnology*, vol. 20, pp. 788-780, 2002.
- [80] I. Ieropolous, J. Greenman e C. Melhuish, «Imitating metabolism:energy autonomy in biologically inspired robots,» in *Second International Symposium on Imitation in Animals and Artifacts*, Aberystwyth, Wales, 2003.
- [81] Ieropolous e al, «Ecobot-II: an artificial agent with a natural metabolism,» *Journal of Advanced Robotic Systems*, vol. 2, n. 4, pp. 295-300, 2005.
- [82] S. Wilkinson, «“Gastrobots” —Benefits and Challenges of Microbial Fuel Cells in FoodPowered Robot Applications,» *Autonomous Robots*, vol. 9, pp. 99-111, 2000.
- [83] Chai, 2002.
- [84] L. Chen, C. Lin, J. Zuo, L. Song e C. Huang, «First spectroscopic observation of peroxocarbonate/peroxodicarbonate in molten carbonate,» *The journal of physical Chemistry B*, vol. 108, n. 23, pp. 7553-7556, 2004.
- [85] H. Kim, D. Choi, M. Hyun e S. Nam, «Method and device for detecting toxic material in water using microbial fuel cell». Brevetto 10/5090718, 2003.
- [86] M. Di Lorenzo, A. Thomson, K. Schrneider, P. CAmeron e I. Ieropoulos, «A small scale air cathode microbial fuel cell for on-line monitoring of water quality,» *Biosensors and bioelectronics*, vol. 62, pp. 182-188, 2014.
- [87] K. H. Kim, J. Jang, T. Pham, H. Moon, I. Chang e B. Kim, «A microbial fuel cell with improved cathode reaction as a low biochemical oxygen demand sensor,» *Biotechnology Letters*, vol. 25, n. 16, pp. 1357-1361, 2003.
- [88] N. Stein, H. Hamelers e C. Buisman, «Stabilizing the baseline current of a microbial fuel cell-based biosensor through overpotential control under non-toxic conditions,» *Bioelectrochemistry*, vol. 78, n. 1, pp. 87-91, 2010.

References

- [89] I. Chang, J. Jang, G. Gil, M. Kim, H. Kim, B. Cho e B. Kim, «Continuous determination of biochemical oxygen demand using microbial fuel cell type biosensor,» *Biosensors and Bioelectronics*, vol. 19, n. 6, pp. 607-613, 2004.
- [90] H. Liu, S. Grot e B. Logan, «Electrochemically assisted microbial production of hydrogen from acetate,» *Environmental Science Technology*, vol. 39, n. 11, pp. 4317-4320, 2005.
- [91] «Wikipedia the free Enciclopedia,» [Online]. Available: [http://www.tikp.co.uk/knowledge/technology/fiber and filament production](http://www.tikp.co.uk/knowledge/technology/fiber%20and%20filament%20production).
- [92] S. Lee, S. Park e Y. Kim, «Effect of the concentration of sodium acetate (SA) on crosslinking of chitosan fiber by epichlorohydrin (ECH) in a wet spinning system,» *Carbohydrate Polymers*, vol. 70, n. 1, pp. 53-60, 2007.
- [93] Y. Ohzawa, Y. Nagano e T. Matsuo, «Studies on dry spinning. I. Fundamental equations,» *Applied Polymer*, vol. 13, n. 2, pp. 257--283, 1969.
- [94] J. Samon, J. Schultz e al, «Study of the structure development during the melt spinning of nylon 6 fiber by on-line wide-angle synchrotron X-ray scattering techniques,» *Polymer Physics*, vol. 37, n. 12, pp. 1227-1287, 1999.
- [95] J. Wendorff, S. Agarwal e A. Greiner, *Electrospinning: Materials, Processing and Applications*, Singapore: Wiley-CH, 2012.
- [96] W. Gilbert, *De Magnete, Magneticisque Corporibus, et de Magno Magnete Tellure*, London: Peter Short, 1628.
- [97] C. Boys, «On the Production, Properties, and some suggested Uses of the Finest Threads,» *Proceeding of the physical Society*, vol. 9, pp. 8-19, 1887.
- [98] Formhals, «US patent». Brevetto 1,975,504;2,160,962;2,187,306, 1934-1940.
- [99] Simons. Brevetto 3,280,229, 1966.
- [100] G. Taylor, «Properties of liquid marbles,» *Proceeding of the Royal Society*, vol. 462, n. 2067, pp. 973-999, 1964.
- [101] G. Taylor, «Conical free surfaces and fluid interfaces,» *Applied Mechanism Springer*, 1966.

- [102] G. I. Taylor, « Electrohydrodynamics: a review of the role of interfacial shear stresses,» *Annual Review of Fluid mechanics*, vol. 313, pp. 453-475, 1969.
- [103] P. Baumgardt, «Electrostatic spinning of acrylic microfibers,» *J Colloid Interface Science*, vol. 36, pp. 71-79, 1971.
- [104] L. Larrondo e R. Manley, «Electrostatic fiber spinning from polymer melts. III. Electrostatic deformation of a pendant drop of polymer melt,» *Polymer Physics*, vol. 19, n. 6, pp. 933-940, 1981.
- [105] S. Reznik, A. Therom e E. Zussman, «Transient and steady shapes of droplets attached to a surface in a strong electric field,» *Journal of fluid mechanics*, vol. 516, pp. 349-377, 2004.
- [106] M. Hohman, G. Ruletdge e M. Brenner, «Electrospinning and electrically forced jets.,» *Physics of Fluids*, vol. 13, n. 8, p. 2221, 2001.
- [107] G. Srinivasa e D. Reneker, «Structure and morphology of small diameter electrospun aramid fibers,» *Polymer International*, vol. 36, n. 2, pp. 195-201, 1995.
- [108] D. Reneker e I. Chun, «Nanometre diameter fibres of polymer, produced by electrospinning,» *Nanotechnology*, vol. 7, n. 3, pp. 216-223, 1996.
- [109] H. Fong, I. Chun e D. Reneker, «Beaded nanofibers formed during electrospinning,» *Polymer*, vol. 40, n. 16, pp. 4585-4592, 1999.
- [110] C. Thompson, G. Chase C e D. Reneker, «Effects of parameters on nanofiber diameter determined from electrospinning model,» *Polymer*, vol. 48, n. 23, pp. 6913-6922, 2007.
- [111] H. Hou e D. Reneker, «Carbon nanotubes on carbon nanofibers: a novel structure based on electrospun polymer nanofibers,» *2004*, vol. 16, n. 1, pp. 69-73, *Advanced Materials*.
- [112] Z. Huang, Y. Zhang, M. Kotaki e S. Ramakrishna, «A review on polymer nanofibers by electrospinning and their applications in nanocomposites,» *Composite Science and Technology*, vol. 63, n. 15, pp. 2223-2253, 2003.

- [113] X. Zhou, C. Shang, L. Gu e al, «Mesoporous Coaxial Titanium Nitride-Vanadium Nitride Fibers of Core-shell Structures for High-Performance Supercapacitors,» *Applied Materials & Interfaces*, vol. 3, n. 8, pp. 3058-3063, 2011.
- [114] R. Sahay, P. Kumar, R. Stridhar, S. Ramakrishna e al, «Electrospun composite nanofibers and their multifaceted applications,» *Journal of material chemistry*, vol. 22, pp. 12953-12971, 2012.
- [115] J. Ge, H. Hou, Q. Li, M. Graham, A. Greiner, D. Reneker, Harris, W. F e Z. Cheng, «Assembly of well-aligned multiwalled carbon nanotubes in confined polyacrylonitrile environments: electrospun composite nanofiber sheets,» *Journal of the American Chemical Society*, vol. 126, n. 48, pp. 15754-15761, 2004.
- [116] H. Jiang, Y. Hu, P. Zhao, K. Zhu e W. Chen, «A facile technique to prepare biodegradable coaxial electrospun nanofibers for controlled release of bioactive agents,» *Journal of controlled release*, vol. 108, n. 2-3, pp. 237-243, 2005.
- [117] A. Yarin, «Coaxial electrospinning and emulsion electrospinning of core-shell fibers,» *Polymers for Advanced Technologies*, vol. 22, n. 3, pp. 310-317, 2011.
- [118] E. Ghadiri e al., «Enhanced electron collection efficiency in dye-sensitized solar cells based on nanostructured TiO₂ hollow fibers,» *Nanoletters*, vol. 10, n. 5, pp. 1632-1638, 2010.
- [119] D. Li e Y. Xia, «Electrospinning of nanofibers: reinventing the wheel?,» *Advanced materials*, vol. 16, p. 1151, 2004.
- [120] W. Teo e S. Ramakrishna, «A review on electrospinning design and nanofibre assemblies,» *Nanotechnology*, vol. 17, pp. 89-106, 2006.
- [121] D. Li, G. Ouyang, J. McCann e Y. Xia, «Collecting Electrospun Nanofibers with Patterned Electrodes,» *Nanoletters*, vol. 5, n. 5, pp. 913-916, 2005.
- [122] S. Ramakrishna, T. Lim e W. Teo, «An introduction to electrospinning and nanofibers,» *World Scientific Pub*, 2005.

- [123] Y. Filatov, A. Budyka e Kirinchenko, *Electrospinning of Micro and Nanofibers, Fundamentals in Separation and filtration process*, Minneapolis: Donaldson Co., 2007.
- [124] A. Greiner e J. Wendorff, «Electrospinning: A Fascinating Method for the Preparation of Ultrathin Fibers,» *Angewandte Chemie*, vol. 46, n. 30, pp. 5670-5703, 2007.
- [125] A. Greiner e J. Wendoff, «Functional self assembled nanofibers by electrospinning in self assembled nanomaterials,» *Advanced Polymer Science*, vol. 219, 2007.
- [126] H. Fong e D. Reneker, Hanser Publishing , 2000.
- [127] A. Yarin, S. Koombhongse e D. Reneker, «Taylor cone and jetting from liquid droplets in electrospinning of nanofibers,» *J. Applied Physics*, vol. 20, 2001.
- [128] D. Reneker e A. Yarin, «Electrospinning jets and polymer nanofibers,» *Polymer*, vol. 49, pp. 2387-2425, 2008.
- [129] M. Hohman, M. Shin, RutledgeG e M. Brenner, «Electrospinning and electrically forced jets: stability theory,» *Physics of Fluids*, vol. 13, p. 2201, 2001.
- [130] Y. Shin, M. Hohman, M. Brenner e G. Rutledge, «Experimental characterization of electrospinning: the electrically forced jet instabilities,» *Polymer*, vol. 42, p. 9955, 2001.
- [131] D. Reneker, A. Yarin, H. Fong e Koombhongse, «Bending instabilities of electrically charged jets of polymer solution in electrospinning,» *J Appl Physics*, vol. 87, n. 9, pp. 4531-4547, 2000.
- [132] J. Deitzel, J. Kleinmeyer, D. Harris e N. Beck Tan, «The effect of processing variables on the morphology of electrospun,» *Polymer*, vol. 42, pp. 261-272, 2001.
- [133] S. Earnshaw, «On the nature of the molecular forces which regulate the constitution of the luminiferous ether,» *Trans Camb Phil Soc*, vol. 7, pp. 97-112, 1842.
- [134] W. Scott, «Who was Earnshaw,» *American Journal of Physics*, p. 4127, 1959.
- [135] D. Reneker, A. Yarin, E. Zussman e H. Xu, «Electrospinning of nanofibers from polymer solutions and melts,» *Advances in applied mechanics*, vol. 41, pp. 44-195, 2007.
- [136] J. Wendorff, S. Agarwal e A. Greine, *Electrospinning: Materials, Processing and Applications*, Weiheim Germany: Wiley-VCH, 2012.

- [137] L. Huang, S. Manickam e R. McCutcheon, «Increasing strength of electrospun nanofiber membranes for water filtration using solvent vapor,» *Journal of Membrane Science*, vol. 436, n. 1, pp. 213-220, 2013.
- [138] E. Boland, G. Wnek, D. Simpson, K. Pawlowski e G. Bowlin, «Tailoring tissue engineering scaffolds using electrostatic processing techniques: a study of poly (glycolic acid) electrospinning,» *Journal of Macromolecular Science*, vol. 38, n. 12, pp. 1231-1243, 2001.
- [139] J. Matthews, G. Wnek, D. Simpson e G. Bowlin, «Electrospinning of collagen nanofibers,» *Biomacromolecules*, vol. 3, n. 2, pp. 232-238, 2002.
- [140] S. Fennessey e R. Farris, «Fabrication of aligned and molecularly oriented electrospun polyacrylonitrile nanofibers and the mechanical behavior of their twisted yarns,» *Polymer*, vol. 45, pp. 4217-4225, 2008.
- [141] R. Dersch, T. Liu, A. Schaper, A. Greiner e J. Wendorff, «Electrospun nanofibers: Internal structure and intrinsic orientation,» *Journal of Polymer Science*, vol. 41, n. 4, pp. 545-553, 2003.
- [142] A. Baji, Y. Mai, S. Wong, M. Abtahi e P. Chen, «Electrospinning of polymer nanofibers: effects on oriented morphology, structures and tensile properties,» *Composites Science and Technology*, vol. 70, n. 5, pp. 703-718, 2010.
- [143] D. Li, Y. Wang e Y. Xia, «Electrospinning nanofibers as uniaxially aligned arrays and layer-by-layer stacked films,» *Advanced materials*, vol. 16, n. 4, pp. 361-366, 2004.
- [144] S. Fridrikh, J. Yu, M. Brenner e G. Rutledge, «Controlling the fiber diameter during electrospinning,» *Physical Review Letter*, vol. 90, 2001.
- [145] S. Theron, E. Zussman e A. Yarin, «Experimental investigation of the governing parameters in the electrospinning of polymer solutions,» *Polymer*, vol. 45, n. 6, pp. 2017-2030, 2004.
- [146] W. Son, J. Youk, T. Lee e W. Park, «The effects of solution properties and polyelectrolyte on electrospinning of ultrafine polyethylene oxide fibers,» *Polymer*, vol. 45, pp. 2959-2966, 2004.

- [147] S. Talwar, J. Hinestroza, B. Pourdeyhimi e S. Khan, «Associative Polymer Facilitated Electrospinning of Nanofibers,» *Macromolecules*, vol. 41, n. 12, pp. 42755-4283, 2008.
- [148] S. Fridrikh, J. Yu, M. Brenner e G. Rutledge, «Controlling the Fiber Diameter during Electrospinning,» *Physich Review Letters*, vol. 90, n. 14, 2003.
- [149] B. Min, G. Lee, S. Kim, Y. Nam, T. Lee e W. Park, «Electrospinning of silk fibroin nanofibers and its effect on the adhesion and spreading of normal human keratinocytes and fibroblasts in vitro,» *Biomaterials*, vol. 25, n. 7-8, pp. 1289-1297, 2004.
- [150] Q. Pharm, U. Sharma e A. Mikos, «Electrospinning of polymeric nanofibers for tissue engineering applications: a review,» *Tissue Engineering*, 2006.
- [151] Y. Zhang, C. Lim e S. Ramakrishna, «Recent development of polymer nanofibers for biomedical and biotechnological applications,» *Journal of Materials Science:Materials in Medicine*, vol. 16, n. 10, pp. 933-946, 2005.
- [152] M. Brewster, G. Verreck, I. Chun, J. Rosenblatt e al, «The use of polymer-based electrospun nanofibers containing amorphous drug dispersions for the delivery of poorly water-soluble pharmaceuticals,» *Journal of Pharmaceutical Sciences*, vol. 59, n. 5, pp. 387-391, 2004.
- [153] D. Liang, B. Hsiao e B. Chu, «Functional electrospun nanofibrous scaffolds for biomedical applications,» *Advanced Drug Delivery Reviews*, vol. 59, n. 14, pp. 1392-1412, 2007.
- [154] D. Katti, K. Robinson, F. Ko e C. Laurencin, «Bioresorbable nanofiber-based systems for wound healing and drug delivery: Optimization of fabrication parameters,» *Journal of Biomedical Materials Research Part B: Applied Biomaterials*, vol. 70, n. 2, pp. 286-296, 2004.
- [155] T. McCall e A. Baichwall, *Modified-Release Drug Delivery Technology*, Rathbone,M,J, 2003.
- [156] C. Saw, M. Olivo e P. Heng, «Delivery of hypericin for photodynamic applications,» *Cancer Letters*, vol. 241, n. 18, pp. 23-30, 2006.
- [157] U. Patent.Brevetto 4,855,326, 1988.

- [158] G. Verreck, I. Chun, J. Rosenblatt e Al, «Incorporation of drugs in an amorphous state into electrospun nanofibers composed of a water-insoluble, nonbiodegradable polymer,» *Journal of controlled release*, vol. 92, n. 3, pp. 349-360, 2003.
- [159] F. Zeng, J. Liu e C. Allen, «Synthesis and Characterization of Biodegradable Poly (ethylene glycol)-b lock-poly (5-benzyloxy-trimethylene carbonate) Copolymers for Drug Delivery,» *Bio Macromolecules*, vol. 5, n. 5, pp. 1810-1817, 2004.
- [160] Comyn, Introduction to polymer permeability and the mathematics of diffusion, Leicester: Chapman & Hall, 1985, pp. 1-10.
- [161] E. Luong-Van e al, «Controlled release of heparin from poly(ϵ -caprolactone) electrospun fibers,» *Biomaterials*, vol. 27, n. 9, pp. 2042-2050, 2006.
- [162] L. Youxin e T. Kissel, «Synthesis and properties of biodegradable ABA triblock copolymers consisting of poly(l-lactic acid) or poly (l-lactic-co-glycolic acid) A-blocks attached to central poly (oxyethylene) B-blocks,» *Journal of controlled release*, vol. 27, pp. 247-257, 1993.
- [163] J. Zeng, X. Xu e al, «Biodegradable electrospun fibers for drug delivery,» *Journal of Controlled Release*, vol. 92, n. 3, pp. 227-231, 2003.
- [164] Y. Zamg, X. He, Z. Li, Z. Miao e F. Huang, «Fabrication and ethanol-sensing properties of micro gas sensor based on electrospun SnO₂ nanofibers,» *Sensors and Actuators B: Chemical*, vol. 132, n. 1, pp. 67-73, 2008.
- [165] A. Andry, Science and technology of polymer nanofibers, John Wiley and Science, 2008.
- [166] H. Jia e al, «Enzyme-carrying polymeric nanofibers prepared via electrospinning for use as unique biocatalysts,» *Biotechnology Progress*, vol. 18, n. 5, pp. 1027-1032, 2005.
- [167] Subbiah e al, «Selective Capacitive Sensor for Ammonia Hydroxide at Room Temperature,» *IEEE Sensors Journal*, vol. 13, n. 7, pp. 2757 - 2762, 2013.
- [168] L. Wang, Y. Yun, P. Chen e C. Chen, «Electrospun carbon–cobalt composite nanofiber as an anode material for lithium ion batteries,» *Scripta Materialia*, vol. 58, n. 5, pp. 405-408, 2008.

- [169] F. Quan e M. Whittingham, «Electrospun manganese oxide nanofibers as anodes for lithium-ion batteries,» *Electrochemical and Solid State Letter*, vol. 10, n. 3, pp. 48-51, 2007.
- [170] L. Ji e X. Zhang, «Manganese oxide nanoparticle-loaded porous carbon nanofibers as anode materials for high-performance lithium-ion batteries,» *Electrochemistry Communication*, vol. 11, n. 4, pp. 795-798, 2009.
- [171] L. Ji e al., «Recent developments in nanostructured anode materials for rechargeable lithium-ion batteries,» *Energy & Environmental Science*, vol. 4, pp. 2682-2699, 2011.
- [172] H. Han e al, «Nitridated TiO₂ hollow nanofibers as an anode material for high power lithium ion batteries,» *Energy Environ. Science*, vol. 4, pp. 4532-4536, 2011.
- [173] J. Kong e al, «Silicon nanoparticles encapsulated in hollow graphitized carbon nanofibers for lithium ion battery anodes,» *Nanoscale*, vol. 5, pp. 2967-2973, 2013.
- [174] G. Zheng e Al, «Hollow carbon nanofiber-encapsulated sulfur cathodes for high specific capacity rechargeable lithium batteries,» *Nanoletters*, vol. 11, n. 10, pp. 4462-4467, 2011.
- [175] A. Cao e al, «Self-Assembled Vanadium Pentoxide (V₂O₅) Hollow Microspheres from Nanorods and Their Application in Lithium-Ion Batteries,» *Angewandte chemie*, vol. 44, n. 28, pp. 4391-4395, 2005.
- [176] S. Molla e V. Compan, «Polyvinyl alcohol nanofiber reinforced Nafion membranes for fuel cell applications,» *Journal of Membrane Science*, vol. 372, n. 1-2, pp. 191-200, 2011.
- [177] R. Bajon, S. Balaji e S. Guo, «Electrospun Nafion Nanofiber for Proton Exchange Membrane Fuel Cell Application,» *Journal of Fuel Cells Technology*, vol. 6, n. 3, 2009.
- [178] S. Molla e V. Compan, «Performance of composite Nafion/PVA membranes for direct methanol fuel cells,» *Journal of Power Sources*, vol. 196, n. 5, pp. 2699-2708, 2011.
- [179] Y. Zhai, H. Zhang, J. Hu e B. Yi, «Preparation and characterization of sulfated zirconia (SO₄²⁻/ZrO₂)/Nafion composite membranes for PEMFC operation at high temperature/low humidity,» *Journal of Membrane Science*, vol. 280, n. 1-2, pp. 148-155, 2006.

- [180] M. Adachi e al., «Highly Efficient Dye-Sensitized Solar Cells with a Titania Thin-Film Electrode Composed of a Network Structure of Single-Crystal-like TiO₂ Nanowires Made by the “Oriented Attachment” Mechanism,» *journal of the American chemical society*, vol. 126, n. 45, p. 14943–14949, 2004.
- [181] D. Zhang e al., «Low-Temperature Fabrication of Efficient Porous Titania Photoelectrodes by Hydrothermal Crystallization at the Solid/Gas Interface,» *Advanced materials*, vol. 15, n. 10, pp. 814-817, 2003.
- [182] B. Liu e al., «Growth of Oriented Single-Crystalline Rutile TiO₂ Nanorods on Transparent Conducting Substrates for Dye-Sensitized Solar Cells,» *Journal of america Chemical society*, vol. 131, n. 11, p. 3985–3990, 2009.
- [183] H. Kim e al., «Effect of Electrolyte in Electrospun PEO/TiO₂ Composite Fibers,» *Journal molecular crystals and liquid crystals*, vol. 464, n. 1, 2007.
- [184] J. Sundaramurthy, N. Li, P. Kumar e S. Ramakrishna, «Perspective of electrospun nanofibers in energy and environment,» *Biofuel Research journal*, vol. 1, n. 2, pp. 44-54, 2014.
- [185] L. Francis e al., «Fabrication and characterization of dye-sensitized solar cells from rutile nanofibers and nanorods,» *Energy*, vol. 36, n. 1, pp. 627-632, 2011.
- [186] F. Bella, A. Sacco, G. Massaglia, A. Chiodoni, C. Pirri e M. Quaglio, «Dispelling clichés at the nanoscale: the true effect of polymer electrolytes on th performances of DSSC,» *Nanoscale*, vol. 7, pp. 12010-12017, 2015.
- [187] Zhou e al., «An Overview of electrode materials in microbial fuel cells,» *Journal of Power sources*, vol. 196, pp. 4427-4435, 2011.
- [188] H. Liu, R. Ramnarayan e B. Logan, «Production of electricity during wastewater treatment using a single chamber microbial fuell cell,» *Environmental Science and Technology*, vol. 38, pp. 2281-2285, 2004.
- [189] Y. Ahn e B. Logan, *Bioresource and Technology*, vol. 101, pp. 469-475, 2010.

- [190] Y. Feng, X. Wang e B. Logan, «Brewery wastewater treatment using air cathode microbial fuel cells,» *Water Science and Technology*, vol. 57, pp. 1117-1121, 2008.
- [191] T. Saito, B. Logan e al., «Effect of nitrogen addition on the performance of microbial fuel cell anodes,» *Bioresource Technology*, vol. 102, pp. 395-398, 2011.
- [192] Y. Feng, Q. Yang, X. Wang e B. Logan, «Treatment of carbon fiber brush anodes for improving power generation in air cathode micorbial fuel cells,» *Journal of power sources*, vol. 195, pp. 1841-1844, 2010.
- [193] S. Cheng e B. logan, «Ammonia treatment on carbon cloth anodes to enhance power generation of microbial fuel cells,» *Electrochemistry Communications*, vol. 9, pp. 492-496, 2007.
- [194] T. Zhang e al, «Improved cathode materials for microbial electrosynthesis,» *Energy and Environmental Science*, vol. 6, pp. 217-224, 2013.
- [195] M. Kannan e G. Kumar, «Current status, key challenges and its solutions in the design and development of graphene based ORR catalysts for the microbial fuel cell applications,» *Biosensors and Bioelectronics*, vol. 77, pp. 1208-1220, 2016.
- [196] C. Song e J. Zhang, «Electrocatalytic Oxygen REduction Reaction,» in *PEM Fuel Cell Electrocatalysts And Catalysts Layers*, Zhang,J, 2008, p. 1137.
- [197] E. Yu, S. Cheng, K. Scott e B. Logan, «Microbial fuel cell with non Pt cathode catalysts,» *Journal of Power Sources*, vol. 171, pp. 275-281, 2007.
- [198] Q. Wen, S. Wang, J. Yan, L. Cong, Z. Pan, Y. Ren e Z. Fan, «MnO₂-graphene hybrid as an alternative cathodic catalyst to platinum in microbial fuel cells,» *Journal of Power Sources* , vol. 216, pp. 187-191, 2012.
- [199] L. Feng, Y. Chen e L. Chen, «Easy to operate and low temperature synthesis of gram scale nitrogen doped graphene and its application as cathode catalyst in microbial fuel cells,» *ACS NANO*, vol. 5, n. 12, pp. 9611-9618, 2011.

- [200] L. Qu, Y. Liu, J. Baek e L. Dal, «Nitrogen doped graphene as efficient metal free electrocatalyst for oxygen reduction reaction in fuel cells,» *ACS NANO*, vol. 4, n. 3, pp. 1321-1326, 2010.
- [201] C. Kim e al., «Synthesis and characterization of porous carbon nanofibers with hollow cores through the thermal treatment of electrospun copolymeric nanofiber webs,» *Small*, vol. 3, n. 1, pp. 91-95, 2006.
- [202] S. Chen e al, «electrospun and solution blow three dimensional carbon fiber nonwovens for applications in microbial fuel cells,» *Energy and Environmental Science*, vol. 4, pp. 1417-1421, 2011.
- [203] S. Chen, U. Schroeder e al, «electrospun carbon nanofibers with layered architecture for anode in microbial fuel cells,» *electrochemistry communications*, vol. 13, pp. 1026-1029, 2011.
- [204] S. Manickam, U. Karra, L. Huang, N. Bui, B. Li e R. McCutcheon, «Activated carbon nnaofiber anodes for microbial fuel cells,» *Carbon*, vol. 53, pp. 19-28, 2013.
- [205] U. Karra, S. Manickam, J. McCutcheon, N. Patel e B. Li, «Power generation and organics removal form wastewater using activated carbon nanofiber (ACNF) microbial fuel cells (MFCs),» *International Journal Of Hydrogen Energy*, vol. 38, pp. 1588-1597, 2013.
- [206] D. Yang, S. Chaudari, P. Rajesh e J. Yu, «Preparation of Nitrogen-Doped Porous Carbon Nanofibers and the Effect of Porosity, Electrical Conductivity, and Nitrogen Content on Their Oxygen Reduction Performances,» *CHEMCATCHEM*, Vol. %1 di %21236-1244, p. 6, 2014.
- [207] X. Wang, S. Cheng, Y. Feng, M. Merrill, T. Saito e B. Logan, «Use of carbon mesh anodes and the effect of different pretreatment methods on power produciton in microbial fuel cells,» *environmental science and technology*, vol. 43, n. 17, pp. 6870-6874, 2009.
- [208] Y. Liu, F. Harnischa, K. Frickea, U. Schröder, V. Climent e J. Feliu, «The study of electrochemically active microbial biofilms on different,» *Biosensors and Bioelectronics*, vol. 25, pp. 2167-2171, 2010.
- [209] A. Kashi e al., «How to Prepare Biological Samples and Live Tissues for Scanning Electron Microscopy (SEM),» *Galen Medical Journal*, vol. 3, n. 2, pp. 63-80, 2014.

- [210] M. Kalab, A. Yang e D. Chabot, «Conventional Scanning Electron Microscopy of Bacteria,» *Infocus*, n. 10, pp. 44-6, 2008.
- [211] B. Logan, *Microbial Fuel Cells*, Pennsylvania: Wiley Inter science, 2008.
- [212] J. McGann, M. Zhong, E. Kim, S. Natesakhawat, M. Jaroniec, J. Whitacre, K. Matyjaszewski e T. Kowalwski, «Block copolymer templating as a path ton porous nanostructured carbons with highly accessible nitrogens for enhanced electro chemical performance,» *Macomolecular chemistry and physics*, vol. 213, pp. 1078-1090, 2012.
- [213] K. Cong e al, «Electrochemical stability of the polymer-derived nitrogen-doped: an elusive goal?,» *Mater Renew Sustain Energy*, pp. 4-11, 2015.
- [214] G. Liu, X. Li, P. Ganesan e B. Popov, «Development of non-precious metal oxygen-reduction catalysts for PEM fuel cells based on N-doped ordered porous carbon,» *Applied Catalysis B: Environmental*, vol. 93, pp. 156-165, 2009.
- [215] «<http://www.mdpi.com>,» [Online].
- [216] M. Jing, C. Wang, Q. Wang, Y. Bai e B. Zhu, «Chemical structure evolution and mechanism during pre carbonization of PAN-based stabilized fiber in the temperature range of 350°C-600°C,» *Polymer Degradation and stability*, vol. 92, pp. 1737-1742, 2007.
- [217] Z. Wangxi, L. Jie e W. Gang, «Evolution of structure and properties of PAN precursors during their conversion to carbon nanofibers,» *Carbon*, vol. 41, pp. 2805-2812, 2003.
- [218] Y. Wang, S. Serrano e J. Aviles, «Raman characterization of carbon nanofibers prepared using electrospinning,» *synthetic metals*, vol. 138, pp. 423-427, 2003.
- [219] C. Kim, S. Park, J. Cho, D. Lee, T. Park, W. Lee e K. Yang, «Raman spectroscopic evaluation of polyacrylonitrile-based carbon nanofibers prepared by electrospinning,» *Journal of Raman Spectroscopy*, vol. 35, pp. 928-933, 2004.
- [220] M. Orazem e B. Tribollet, *Electrochemical impedance spectroscopy*, Hoboken, New Jersey: Wiley, 2008.

- [221] B. Ding, C. Li, O. Miyauchi, Kuwaki e S. Shiratori, «Formation of novel 2D polymer nanowebs via electrospinning,» *Nanotechnology*, vol. 17, n. 15, pp. 3685-3691, 2006.
- [222] B. Ding, M. Wang, J. Yu e G. Sun, «Electrospun nanomaterials for ultrasensitive sensors,» *Materials Today*, vol. 13, n. 11, pp. 16-27, 2010.
- [223] X. Wang, B. Ding, G. Sun, M. Wang e J. Yu, «Electrospinning/netting: a strategy for the fabrication of three-dimensional polymer nano-fiber/nets,» *Progress in Materials Science*, vol. 58, n. 8, pp. 1173-1243, 2013.
- [224] W. Teo, E e S. Ramakrishna, «A review on electrospinning design and nanofibre assemblies,» *Nanotechnology*, vol. 17, pp. 89-106, 2006.
- [225] N. Bhardwaj e S. Kundu, «Electrospinning: a fascinating fiber fabrication technique,» *Biotechnology Advances*, vol. 28, n. 3, pp. 325-347, 2010.
- [226] C. Feng, K. Khulbe e T. Matsuura, «Recent progress in the preparation, characterization, and applications of nanofibers and nanofiber membranes via electrospinning/interfacial polymerization,» *Journal of Applied Polymer Science*, vol. 115, n. 2, pp. 756-776, 2010.
- [227] D. Reneker e A. Yarin, «Electrospinning jets and polymer nanofibers,» *Polymer*, vol. 49, n. 10, pp. 2387-2425, 2008.
- [228] R. Nirmala, R. Navamathavan, S. Park e H. Kim, «Recent progress on the fabrication of ultrafine polyamide-6 based nanofibers via electrospinning: a topical review,» *Nano Micro Letters*, vol. 6, n. 2, pp. 89-107, 2014.
- [229] K. Yoon, B. Hsiao e B. Chu, «Functional nanofibers for environmental applications,» *Journal of Materials Chemistry*, vol. 18, pp. 5326-5334, 2008.
- [230] X. Wang, J. Wang, Y. Si, B. Ding, J. Yu, G. Sun, W. Luo e G. Zheng, «Nanofiber-net-binary structured membranes for highly sensitive detection of trace HCl gas,» *Nanoscale*, vol. 4, pp. 7585-7592, 2012.

- [231] C. Zhou, R. Chu, R. Wu e Q. Wu, «Electrospun polyethylene oxide/cellulose nanocrystal composite nanofibrous mats with homogeneous and heterogeneous microstructures,» *Biomacromolecules*, vol. 12, n. 7, pp. 2617-2625, 2011.
- [232] S. Parvee e S. Sahoo, *Clin Pharmacokinet*, vol. 45, pp. 965-988, 2006.
- [233] W. R. A. a e Coehlo, «Axial divergence in a conventional X-Ray powder diffractometer,» *Appy Crystallogr*, vol. 31, pp. 862-868, 1998.
- [234] L. X e W. G, «Flexible supercapacitor based on MnO₂ nanoparticles via electrospinning,» *Journal of mateiral and chemistry A1*, pp. 10103-10106, 2013.
- [235] C. Martin, J. Sandler, A. Windle e al, «Electric field-induced aligned multi-wall carbon nanotube networks in epoxy composites,» *Polymer*, vol. 46, n. 3, pp. 877-886, 2005.
- [236] H. Fong, I. Chun e D. Reneker, «Beaded nanofibers formed during electrospinning,» *Polymer*, vol. 40, n. 16, pp. 4585-4592, 1999.
- [237] D. Kimmer, P. Slobodian, D. Petras, M. Zatloukal, R. Olejnik e P. Saha, «Polyurethane/multiwalled carbon nanotube nanowebs prepared by an electrospinning process,» *Journal of Applied Polymer Science*, vol. 111, n. 6, pp. 2711-2714, 2009.
- [238] D. Chipara, J. Macossay, A. Ybarra, A. Chipara, T. Eubanks e M. Chipara, «Raman spectroscopy of polystyrene nanofibers—Multiwalled carbon nanotubes composites,» *Applied Surface Science*, vol. 275, n. 15, pp. 23-27, 2013.
- [239] G. Socrates, *Infrared and Raman Characteristic Group Frequencies:Table and Charts*, NJ, USA: Wiley, Hoboken, 2001.
- [240] S. McCullen, D. Stevens, W. Roberts, S. Ojha, L. Clarke e R. Gorga, «Morphological, electrical, and mechanical characterization of electrospun nanofiber mats containing multiwalled carbon nanotubes,» *Macromolecules*, vol. 40, n. 4, pp. 997-1003, 2007.
- [241] I. Fratoddi, A. Bearzotti, I. Venditti, C. cametti e M. Russo, «Role of nanostructured polymers on the improvement of electrical response-based relative humidity sensors,» *Sensors and Actuators B: Chemical*, vol. 225, pp. 96-108, 2016.

References

- [242] E. Lobet, «Gas sensors using carbon nanomaterials: A review,» *Sensors and Actuators B: Chemical*, vol. 179, pp. 32-45, 2013.
- [243] P. o. E. d. W. T. U. a. S. C. M. F. Cell, «Liu,H;Ramnarayanan,R;Logan,B,E,» *Environmental Science and Technology*, vol. 38, n. 7, pp. 2281-2285, 2004.